International Hydrological Programme

Precipitation and Water Resources

—The Textbook for Twelfth IHP Training Course in 2002—

Edited by Eiichi Nakakita and Hiroshi Uyeda

Hydrospheric Atmospheric Research Center, Nagoya University

United Nations Educational Scientific and Cultural Organization

Prepared for the Twelfth IHP Training Course on Precipitation and Water Resources,
23 February - 8 March, 2003, Nagoya and Kyoto, Japan

Working Group for IHP Training Course,
Sub-Committee for IHP,
Japan National Commission for UNESCO
  Chairperson: Prof. K. Nakamura, Nagoya University
  Secretariat:
    Mr. T. Imura, Ministry of Education, Culture, Sports, Science and Technology
    Ms. M. Sakogawa, Ministry of Education, Culture, Sports, Science and Technology
    Mr. T. Katsukawa, Nagoya University
  Members:
    Prof. K. Takeuchi, Yamanashi University
    Prof. Y. Fukushima, Research Institute for Humanity and Nature
    Mr. T. Sonoda, Ministry of Land, Infrastructure and Transport
    Dr. A. Iseki, Japan Meteorological Agency
    Dr. T. Kishii, National Research Institute for Earth Science and Disaster Prevention
    Dr. H. Ohno, National Institute for Agro-Environmental Sciences
    Dr. K. Kazahaya, National Institute of Advanced Industrial Science and Technology
    Prof. Y. Iwasaka, Nagoya University
    Prof. T. Kitada, Toyoyashi University of Technology
    Dr. S. Hatakeyama, National Institute for Environmental Studies
    Prof. Y. Ishizaka, Nagoya University
    Prof. H. Uyeda, Nagoya University
    Prof. I. Tamagawa, Gifu University
    Prof. E. Nakakita, Kyoto University

Published in 2004 by the Hydrospheric Atmosheric Research Center, Nagoya University and United Nations Educational Scientific and Cultural Organization

Printed by Nagoya University COOP
ISBN: 4-9980619-4-1
Cover : Three-dimensional radar image of a localized heavy rainfall which occurred in the northern part of Kanto region, Japan in 1998.
Back Cover : Radar image of a localized heavy rainfall which occurred around Nagoya City, Japan in 2000.

Preface

The objective of the Training Course is to help participants to deepen their basic knowledge on the hydrological system and to develop their skills to understand hydrological problems, which are now crucial in many countries. The course is part of UNESCO International Hydrological Programme (IHP) and is held every Japanese fiscal year that starts in April. The participants mainly from Asia-Pacific regions are given a series of lectures and practical trainings for about two weeks. Until 1996, the course was mainly focused on general hydrology and later concentrated on specified themes such as: snow hydrology (1998), remote sensing (1999), limnology (1999), hydrology related to head water management (2000) and hydrogen and oxygen isotopes in hydrology (2002).

This year, the Twelfth IHP Training Course with a theme of "Precipitation and Water Resources" will be held from 23 February to 8 March, 2003 at Nagoya, and Kyoto with many lectures and practices. This IHP short course will focus on understanding mechanism and prediction of heavy rainfall and flood runoff including river basin management. The topic on draught in senses of phenomena and management will be included as a typical topic of water resources. The problems of water resources and ways of solving them depend much on features of nature and human activity in the field people are living. In this sense, participants can get essential and comprehensive idea of ways of planning, managing and monitoring problems on water resources of their own countries including precipitation.

The Twelfth course will be conducted by contributions from professionals/experts in universities and research institutes led by Prof. Kenji Nakamura, Prof. Hiroshi Uyeda, Prof. Kazuhisa Tsuboki, Dr. Taro Shinoda, Nagoya University, Prof. Ichiro Tamagawa, Gifu University, Prof. Eiichi Nakakita, Prof. Tomoharu Hori, Prof. Yasuto Tachikawa, Dr. Yutaka Ichikawa, and Dr. Kenji Tanaka, Kyoto University.

The course would not have been possible to conduct without management supports. Dr. Giuseppe Arduino and his staff in UNESCO Jakarta Office worked for the arrangement for the participants. The IHP Training Course is under continuous support from the Ministry of Education, Culture, Sports, Science, and Technology.

21 February, 2003

Kenji Nakamura
Chairperson of Working Group for IHP Training Course
Director, Hydrospheric Atmospheric Research Center,
Nagoya University

Acknowledgements

We would like to take this opportunity to thank all the authors for their great contributions to this textbook. Without their considerable efforts, this textbook would not have been published. The editing work was done with help from Ms. Mayumi Tsuji and Mr. Shinichi Akamatsu, Kyoto University. The English proof reading was accomplished by Prof. Thomas T. Wilheit, Jr., Texas A & M University and Mr. Paul J. Smith, Kyoto University. Thanks are extended to Prof. Kenji Nakamura, the chairperson of the Working Group of the IHP Training Course and the Director of the Hydrospheric Atmospheric Research Center, Nagoya University.

The Japan National Commission for UNESCO, Sub-committee for IHP led by Prof. Takeuchi, Yamanashi University, and the Working Group for IHP Training Course supported the activity. Mr. Imura and Ms. Sakogawa, Ministry of Education, Culture, Sports, Science and Technology and Mr. Katsukawa, Nagoya University, share the role of secretariat. Local arrangements are accomplished by Ms. Junko Banno, Mineko Kano and Saori Haga from Hydrosheric Atmospheric Research Center, Nagoya University, and Ms. Miho Konno and Michiyo Kai, Department of Global Environment Engineering, Kyoto University.

February, 2004
Eiichi Nakakita and Hiroshi Uyeda
Co-Editors

List of the contributors

Chapter 1 Basics of Meteorology on Precipitation
H. Uyeda
Chapter 2 Basics on Mesoscale Meteorology and Radar Meteorology
H. Uyeda
Chapter 3 Boundary Layer
I. Tamagawa
Chapter 4 Rain Observation from Satellites
K. Nakamura
Chapter 5 Basics on Numerical Simulation
K. Tsuboki
Chapter 6 Land Surface Processes
K. Tanaka
Chapter 7 Radar Hydrology
E. Nakakita
Chapter 8 Water Resources Planning and Management
T. Hori
Chapter 9 Catchment Hydrology
Y. Tachikawa
Chapter 10 Distributed Runoff Modeling
Y. Ichikawa

Practices
P1 Cloud Resolving Model
T. Shinoda
P2 Short-term Rainfall Prediction Using Radar
E. Nakakita
P3 Flood Runoff Prediction
Y. Tachikawa
Technical Tours
T1 Meteorological Office & Observatory
H. Uyeda
T2 In-situ Observation sites for Land Surface Processes
K. Tanaka and I. Tamagawa
T3 Offices and Facilities for River Basin Management
E. Nakakita

Current addresses of the contributors (alphabetical order)

T. Hori .... Graduate School of Global Environmental Studies, Kyoto
University
E-mail: tomo@mbox.kudpc.kyoto-u.ac.jp

Y. Ichikawa........ Graduate School of Global Environmental Studies, Kyoto
University
E-mail: ichikawa@wr.kuciv.kyoto-u.ac.jp

E. Nakakita .... Urban and Environment Engineering, Faculty of Engineering,
Kyoto University
E-mail: nakakita@eie.gee.kyoto-u.ac.jp

K. Nakamura...... Hydrospheric Atmospheric Research Center, Nagoya
University
E-mail: nakamura@hyarc.nagoya-u.ac.jp

T. Shinoda.......... Hydrospheric Atmospheric Research Center, Nagoya
University
E-mail: shinoda@ rain.hyarc.nagoya-u.ac.jp

Y. Tachikawa ... Disaster Prevention Research Institute, Kyoto University
E-mail: tatikawa@rdp.dpri.kyoto-u.ac.jp

I. Tamagawa ...... River Basin Research Center, Gifu University
E-mail: tama@cive.gifu-u.ac.jp

K. Tanaka .... Disaster Prevention Research Institute, Kyoto University
E-mail: tanaka@wrcs.dpri.kyoto-u.ac.jp

K. Tsuboki .... Hydrospheric Atmospheric Research Center, Nagoya
University
E-mail: tsuboki@rain.hyarc.nagoya-u.ac.jp

H. Uyeda .... Hydrospheric Atmospheric Research Center, Nagoya
University
E-mail: uyeda@rain.hyarc.nagoya-u.ac.jp

Contents

I Textbook

Part I

Textbook

Chapter 1

Basics of Meteorology on Precipitation

Hiroshi Uyeda
Hydroshperic Atmospheric Research Center, Nagoya University
Furo-cho, Chikusa-ku, Nagoya 464-8601, JAPAN
phone: +81-52-789-3492, fax: +81-52-789-3436
e-mail: uyeda@rain.hyarc.nagoya-u.ac.jp

1.1 Introduction

Meteorology is an indispensable basis for developing knowledge of hydrological systems and their sensitivity to climate changes. Knowing the background of hydrology and meteorology one can put the knowledge to practical use: forecasting of heavy rainfall and flooding, river controls, and solving problems of water resources.

In this chapter, the meaning of the basic equations in meteorology is explained. The role of precipitation in the water and energy circulation in the atmosphere is understood based on the equations. For better understanding of precipitation, methods to measure the distribution of precipitation are explained. This chapter is the entrance to mesoscale meteorology and radar meteorology in Chapter 2.

1.2 Equations

The foundation for expressing weather phenomena is a set of conservation principles. For synoptic scale phenomena, those principles are

(1) conservation of mass,
(2) conservation of heat,
(3) conservation of motion, and
(4) conservation of water,
(5) conservation of other gaseous and aerosol materials.

These principles form a coupled set of relations that must be satisfied simultaneously and that include sources and sinks in the individual expression. The corresponding mathematical representations of these principles for atmospheric applications are explained in textbooks, Atkinson (1981), Cotton, and Anthes (1989), Pielke (1984), Houghton (2002) and others. For simplicity and for practical use in weather phenomena associating precipitation, the equation of conservation of gaseous and aerosol materials is ignored.
A set of equations is listed as follows.

$$\partial \rho / \partial t = -(\nabla \cdot \rho \boldsymbol{V}), \tag{1.1}$$

$$\partial \theta / \partial t = -\boldsymbol{V} \cdot \nabla \theta + S\theta, \tag{1.2}$$

$$\partial \boldsymbol{V} / \partial t = -\boldsymbol{V} \cdot \nabla \boldsymbol{V} - (1/\rho)\, \nabla p - g\mathbf{k} - 2\boldsymbol{\Omega} \times \boldsymbol{V}, \tag{1.3}$$

$$\partial q_{\mathrm{n}} / \partial t = -\boldsymbol{V} \cdot \nabla q_{\mathrm{n}} + Sq_n, \qquad n = 1,2,3, \tag{1.4}$$

$$\partial \chi_{\mathrm{m}} / \partial t = -\boldsymbol{V} \cdot \nabla \chi_{\mathrm{m}} + S\chi_{\mathrm{m}}, \qquad m = 1,2,\ldots,M. \tag{1.5}$$

Here, ρ, θ, V, q_{n}, and χ_{m} are density, potential temperature, wind velocity, water substances and chemical species respectively. $\boldsymbol{\Omega}$ is the constant angular velocity of the earth's rotation. S_θ represents the sources and sinks of heat as expressed by changes in potential temperature. Sq_1, Sq_2 and Sq_3 are the sources and sinks of the amount (in g per 1 m^3 of air) of water vapor, liquid water (cloud and rain), and solid water (cloud ice and snow) respectively.

In utilizing these equations in textbooks and manual of numerical models, it is convenient to adopt the formalism of tensor notation.

Using the tensor notation, along with the requirement that the independent spatial variables $x_i = (x, y, z)$ are mutually orthogonal other at all locations, (1.1) – (1.4) can be rewritten as

$$\partial \rho / \partial t = - \partial \rho u_j / \partial x_j, \qquad (1.6)$$

$$\partial \theta / \partial t = - u_j (\partial \theta / \partial x_j) + S_\theta, \qquad (1.7)$$

$$\partial u_i / \partial t = - u_j (\partial u_i / \partial x_j) - (1/\rho)(\partial p / \partial x_i) - g\delta_{i3} - 2\varepsilon_{ijk} \Omega_j \times u_k, \qquad (1.8)$$

$$\partial q_n / \partial t = - u_j (\partial q_n / \partial x_j) + S q_n, \qquad n = 1,2,3, \qquad (1.9)$$

1.3 Role of precipitation on circulation

Precipitation and its effects are included in equations (1.7) and (1.9) as source and sink terms, Sq_n and S_θ. If the amount of cloud and rain Sq_2 increases in a unit volume by condensation of vapor and coagulation of cloud, latent heat will be released to increase the heat S_θ in (1.7). This change drives the circulation through (1.6)-(1.9). Rainfall amount on the ground is the accumulation of rain formed above the ground which reaches the ground. Rainfall amount and rainfall intensity vary depending on the environmental circulation of clouds which include rain. In order to understand and forecast rainfall, it is essential to develop knowledge of precipitation systems and circulation in and around the system. It is also essential to understand precipitation types in the precipitating system and cloud physical processes in the precipitating clouds. Cloud physical processes as shown in Fig. 1.1 are necessary to consider for better understanding of the precipitation systems. However, measurement tools are also necessary for operational use in meteorology. Before we examine precipitation systems, methods to measure precipitation intensity should be introduced.

1.4 Measurement of precipitation

Rain gauges have been used to measure rainfall amount and rainfall intensity. A rain gauge network is very useful to measure rainfall on the ground however it has limitations. To cover wider ranges, a weather radar network is used to observe and monitor rainfall (Atlas, 1986). The lowest elevation angle of radar scan provides the rainfall intensity closest to the ground for operational use. Recent advances of computer technology made it possible to have of three-dimensional rain data set by radar in order to make an accurate estimation of the rainfall distribution on the ground (Ray, 1986; Rinehart, 1990)

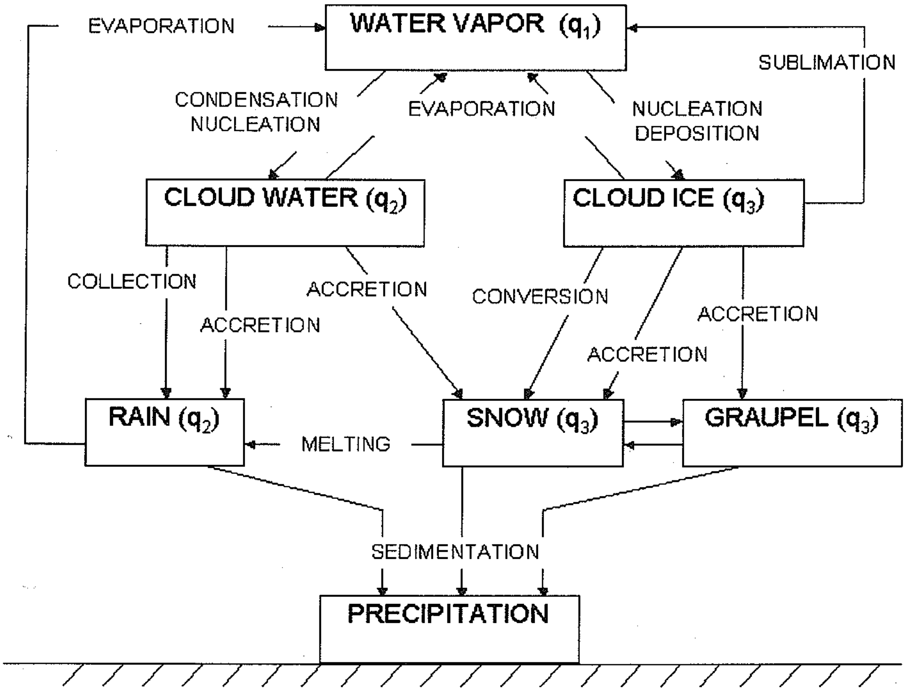

Figure 1.1: Processes in clouds. Major processes are shown by arrows. Mixing ratios, q_1, q_2, and q_3, correspond to that of equations (1.6) – (1.9).

From the point of view of equations (1.6)-(1.9), three dimensional rainfall intensity (or mixing ratio of rain amount) are required to measure. Although the measurement of three-dimensional distributions of water vapor and cloud amount is very difficult, nevertheless the measurement of rain is essential for understanding weather phenomena.

1.5 Concluding remarks

Recent advance in radar meteorology made the monitoring and short term forecasting of rainfall a reality. However radar can measure the rainfall intensity after the formation of raindrops. Prediction of the development of convective cloud and precipitation system is required to forecast rainfalls as early as possible. For those who are concerned about water and water circulation, knowledge of radar meteorology and mesoscale meteorology would be useful. Further details on these topics will be given in Chapter 2.

References

Atkinson, B. W., 1981: Meso-scale atmospheric circulations. *Academic Press*, 495 pp.

Atlas, D., 1986: Radar in meteorology. *American Meteorological Society.* 806pp.

Cotton, W. R. and R. A.,1989: Storm and Cloud dynamics. *Academic Press,* 883 pp.

Houghton, J., 2002: The physics of atmosphere. *Cambridge University Press.* 320pp.

Pielke, R. A., 1984: Mesoscale meteorological modeling. *Academic Press,* 612pp.

Ray, P. S., 1986: Mesoscale meteorology and forecasting. *American Meteorological Society.* 793pp.

Rinehart, R. E., 1990: Radar for meteorologists. *Rinehart Publications.* 428pp.

Chapter 2

Basics of Mesoscale Meteorology and Radar Meteorology

Hiroshi Uyeda
Hydroshperic Atmospheric Research Center, Nagoya University
Furo-cho, Chikusa-ku, Nagoya 464-8601, JAPAN
phone: +81-52-789-3492, fax: +81-52-789-3436
e-mail: uyeda@rain.hyarc.nagoya-u.ac.jp

2.1 Introduction

For understanding and forecasting the rainfall, as was mentioned in Chapter 1, it is essential to develop the knowledge of precipitation systems and circulation in and around the system. For better understanding precipitation systems, mesoscale meteorology, which deals weather phenomena in the horizontal scale from 20 km to 2000 km, provides useful aspect and approach. In mesoscale meteorology, a tool to reveal three-dimensional distribution of precipitation, weather radar, plays an important role. In this chapter a brief introduction to mesoscale meteorology and radar measurement of precipitation intensity is given.

2.2 Mesoscale meteorology

A major problem in atmospheric science, including precipitation, is a full explanation of atmospheric motion. This problem has confronted physical scientists for several centuries and even today is not fully solved. The general atmospheric circulation has been shown to be exceedingly complicated. In the face of such complexity, meteorologists have attempted to "break down" the global atmosphere into parts that may be more easily examined and understood. These "parts" are frequently known as "motion systems", configurations of motion which have different sizes and lifetimes or alternatively different scales, as was introduced by Fujita (1981). This appreciation of scale soon became recognized as vital to any real understanding of atmospheric circulation.

Recently many meteorologists are following the classification by Orlanski (1975): micro-α,β,γ, meso-α,β,γ, and macro-α,β, as shown in Fig.2.1. Weather phenomena with precipitation are in meso-α,β,γ scales with horizontal scales of 2000-200 km, 200-20 km, and 20-2 km. Fronts and hurricanes are in meso-α scale, squall lines and cloud clusters are in meso-β scale, and thunderstorms are in meso-γ scale. The abscissa of Fig.2.1 indicates the time scale relating to the dynamics of the earth and the atmosphere. For further understanding on mesoscale meteorology, see textbooks (Pielke, 1984; Ray, 1986; Cotton and Anthes, 1989; Houze, 1993). Based on the atmospheric dynamics, the formation and development of precipitation systems in the scale of meso-α,β,γ are expressed by the equations (1.6) - (1.9) in Chapter 1.

For understanding and estimation of rainfall, the source and sink terms Sq_2 and Sq_3 of (1.9) in Chapter 1 must be known. Radar can detect a bulk of precipitation particles. Common wave lengths of weather radar are about 3 cm, 5 cm and 10 cm. These radars can detect and measure rain drops, snow particles and graupel particles. However the wave lengths of weather radar can not detect cloud droplets because they are too large to sense the small droplets. Thus, a radar can detect the rain part of q_2.

Besides amount of precipitation, wind fields in clouds are retrieved with Doppler radar. However the methods to measure wind fields are not major concern in this chapter. For operational application we can

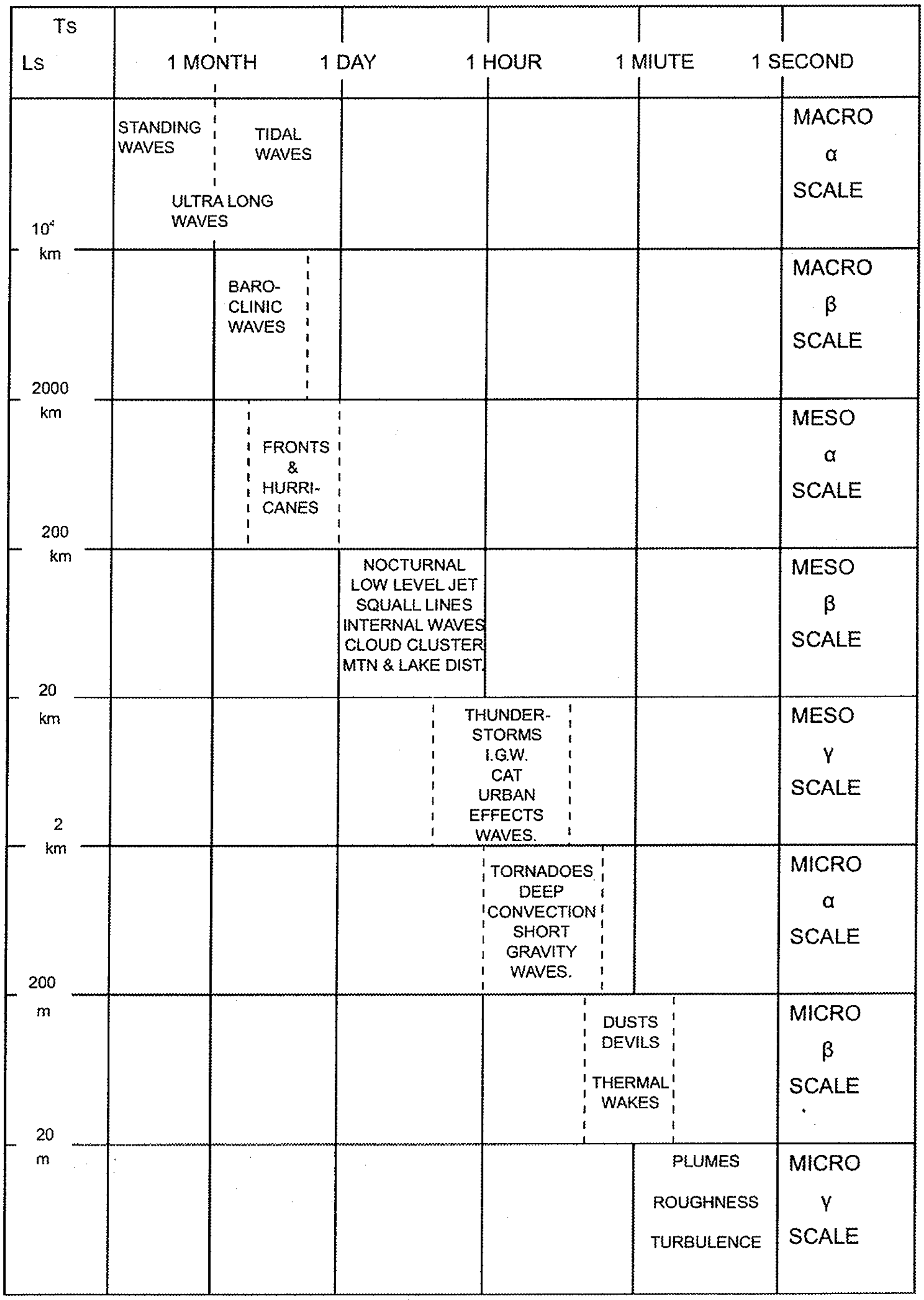

Figure 2.1: Scale definitions and different processes with characteristic time and horizontal scales. (Simplified the figure of Orlanski, 1975)

estimate the rainfall intensity in the troposphere directly by using weather radar instead of solving the equations (1.6) - (1.9) in Chapter 1.

2.3 Radar for precipitation measurement

The word "radar" suggests its origin in radio: "Radio Detection And Ranging" (Fig.2.1). Radar has long history to learn up to now (Battan, 1959; Atlas, 1986; Rinehart, 1990; Sauvageot, 1992). After the war it became available for civilian use. Improvements have been made in all components of radar, from the transmitters to the antennas, receivers, displays and processors. The application of computers to radar made it useful for monitoring and forecasting of weather with precipitation.

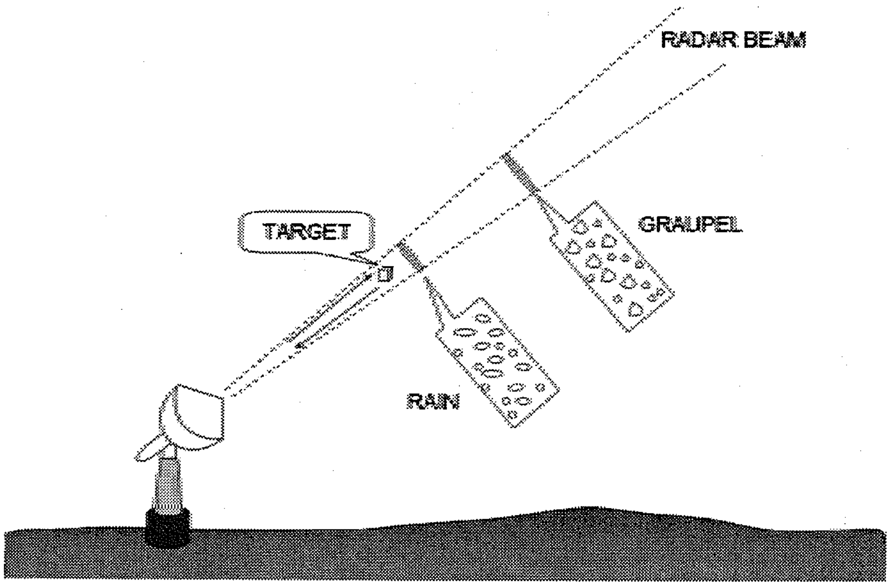

Figure 2.2: A radar looking in the direction of an target. Within the short pulse of the sampling volume, a certain number of rain, graupel and snow particles are expected in weather measurement. Also shown is a short pulse of energy traveling outward at the speed of light. Note that nothing in this drawing is to scale!

An example of transportable radar set is shown in Fig. 2.3. Radar basically consists of four main components (Fig. 2.4). These include a transmitter to generate the high-frequency signal, an antenna to send the signal into space and to receive the echo from the target, a receiver to detect and amplify the signal so it is strong enough to measure and some kind of display system.

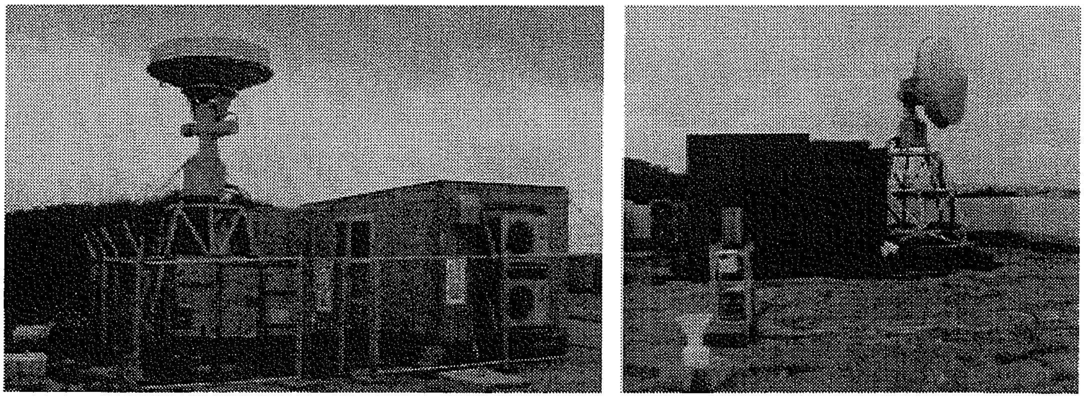

Figure 2.3: Transportable radar sets of Nagoya University.

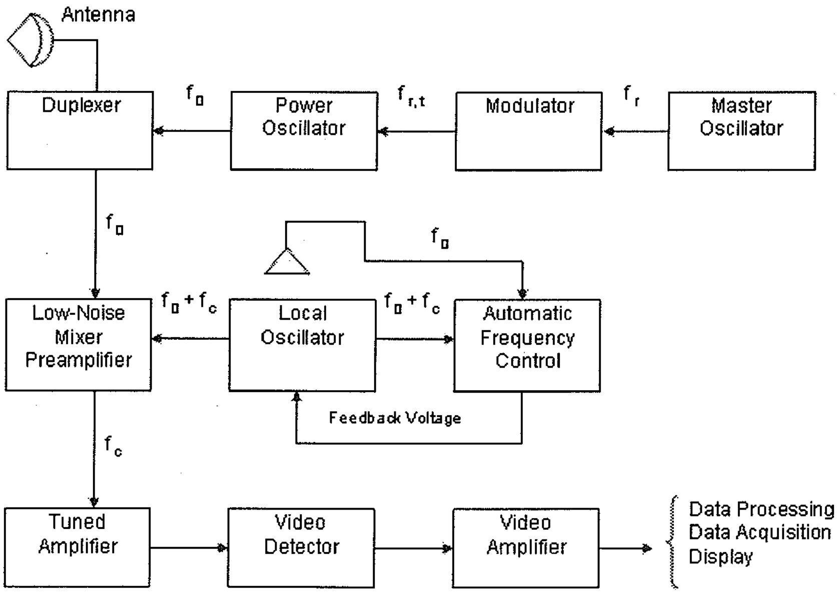

Figure 2.4: Block diagram of noncoherent pulse radar.

Modern weather radars use a single antenna. Weather radars send out short pulses of energy and then wait so the signal can travel out at the speed of light, hit a target, and return to the antenna. After an appropriate wait, another pulse is sent out. The energy travels out at the speed of light (3×10^8 ms^{-1}), so it does not take very long for the signal to travel a few hundred kilometers.

The antenna of the radar usually rotates about a vertical axis, scanning the horizontal in all directions around the radar site. Even though, the antenna may be scanning at a speed from 10 degree/s to, as much as 70 degree/s. It only takes 2 ms (milliseconds) for a radar signal to travel out 300 km and back. If the antenna is rotating at 10 rpm, the antenna will move less than a tenth of a degree during this time. So, from the human perspective, the signal went out and back with the antenna virtually stationary. The radar repeats its transmission/listening cycle several hundred to a couple of thousand times each second. So, we mere mortals watch the antenna moving smoothly and fairly rapidly, but we often do not appreciate the fact that the signal is going out and back very long distances at speeds that are almost incomprehensible to the human mind. We see the radar painting echoes smoothly as the trace sweeps along on the radar display, and it looks like it is not doing much. In reality, it is doing thousands of times more things than we can see happen. For giving rough image of radar display, an explanation of PPI (Plan Position Indicator) and RHI (Range Height Indicator) is shown in Fig. 2.5.

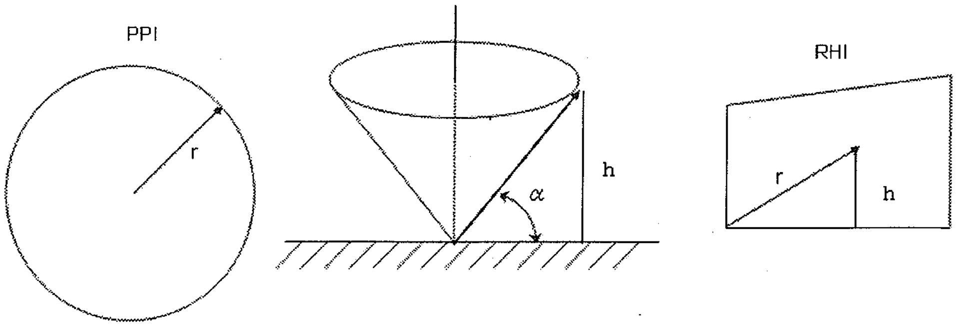

Figure 2.5: Illustration of plan view (left), PPI (Plan Position Indicator), and vertical cross section (right), RHI (Range Height Indicator) for a scan at the elevation angle of α (center).

An actual example of PPI is shown in Fig. 2.6 in order to show the relation between cloud systems seen by geostationary satellite infrared image and by weather radar. The radar echo of 2 July 1998 over Huaihe River Basin, China has a range of 500 km in diameter.

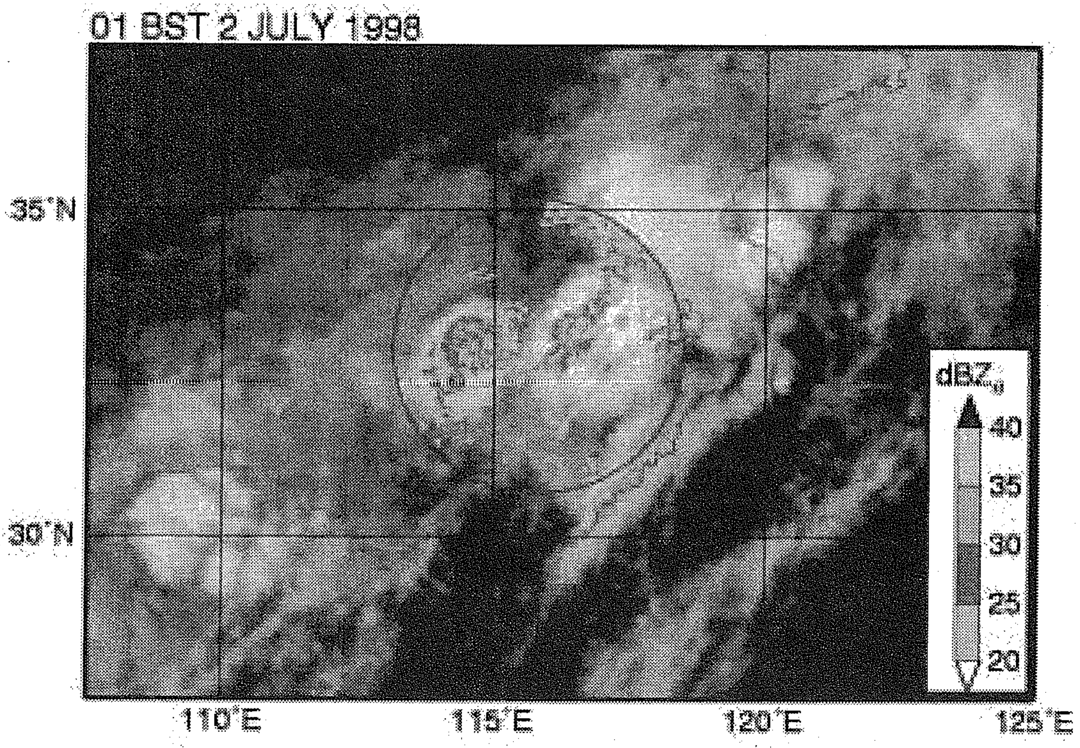

Figure 2.6: PPI image of the echo of 2 July 1998 over Huaihe River Basin, China in the range of 500 km in diameter. The radar range is in between Yangtze River and Yellow River. Cloud systems seen by geostationary satellite infrared image are superposed (from the courtesy of Dr. Maesaka).

Weather radar to see rainfall (precipitation), measures radar reflectivity and convert it to rainfall intensity. The radar equation is known as follows,

$$P_r = (\pi^3 P_t g^2 \theta \varphi h\,[\mathrm{K}]^2 \textstyle\sum D_i^6)/(1024 \ln(2) \lambda^2 r^2). \qquad (2.1)$$

Here, P_r is received power (mW) and P_t is transmitted power (mW). The θ, φ and h are radar constants. The constant $[K]^2$ is a parameter related to the complex index of refraction of the material. D_i are rain drop diameters. λ is the wave length of the radar. The distance of the target from the radar is expressed by r. As rain drops have a size distribution (Fletcher, 1969; Pruppacher and Klett, 1997), we usually use radar reflectivity factor

$$Z = \sum D_i^{\,6}. \qquad (2.2)$$

Because of the tremendous range of values the Z can have, it is convenient to compress this over a smaller range of numbers. We can define the logarithmic radar reflectivity factor Z as follows

$$Z = 10 \log_{10} (\mathrm{Z}/1\mathrm{mm}^6\mathrm{m}^{-3}). \qquad (2.3)$$

The logarithmic radar reflectivity Z in dB is used as a measure of the rainfall intensity. An empirical conversion from Z to rainfall intensity R (mm/h) is made by using the following relation

$$Z = \mathrm{BR}^{\beta}. \qquad (2.4)$$

Here B and β are constants (Battan, 1959).

The equations to convert Z to rainfall intensity are empirically introduced. For better estimation of rainfall intensity with radar, polarimetric radar is one of the most plausible equipments. Polarimetric radar can tell the shape of precipitation particles.

2.4 Concluding remarks

Recent development of Doppler radar made it possible to retrieve wind fields in precipitation systems (Doviak and Zrnic', 1993; Mahapatra, 1999). Furthermore polarimetric radar can reveal precipitation types and its size distribution in clouds (Sauvageot, 1992; Doviak and Zrnic', 1993). With the aid of mesoscale numerical models, we can reveal three-dimensional structure of precipitation systems. Estimation of rainfall amount in catchment basins and forecasting of rainfall are becoming reality. However, conventional weather radar is still useful for rain measurements with a wide range and with certain accuracy, when we think about cost performance. A plausible use of conventional weather radar is for monitoring of precipitation and climate change in rainy areas where radar is essential for disaster prevention at the present day. International collaboration for measurement and monitoring of world wide precipitation is expected for understanding climate change.

References

Atlas, D., 1986: Radar in meteorology. *American Meteorological Society.* 806pp.

Battan, L. J., 1959: Radar observation of the atmosphere. *The University of Chicago Press.* 324pp.

Cotton, W. R. and R. A. Anthes, 1989: Storms and cloud dynamics. *Academic Press.* 883pp.

Doviak. R. J. and D. S. Zrnic', 1993: Doppler radar and weather observations. *Academic Press.* 562pp.

Fletcher, N. H., 1969: The physics of rain clouds. *Cambridge University Press.* 390pp.

Fujita, T. T., 1981: Tornadoes and downbursts in the context of generalized planetary scales. *J. Atmos. Sci.*, **38**, 1511-1534.

Houze Jr., R. A., 1993: Cloud dynamics. *Academic Press.* 573pp.

Mahapatra, P., 1999: Aviation weather surveillance systems. *The Institution of Electrical Engineers.* 453pp.

Orlanski, I., 1975: A rational subdivision of scales for atmospheric processes. *Bull. Amer. Meteor. Soc.*, **56**, 527-530.

Pielke, R. A., 1984: Mesoscale meteorological modeling. *Academic Press,* 612pp.

Pruppacher, H. R. and J. D. Klett, 1997: Microphysics of clouds and precipitation. *Academic Publishers.* 954pp.

Ray, P. S., 1986: Mesoscale meteorology and forecasting. *American Meteorological Society.* 793pp.

Rinehart, R. E., 1990: Radar for meteorologists. *Rinehart Publications.* 428pp.

Sauvageot, H., 1992: Radar meteorology. *Artech House.* 280pp.

Chapter 3

Boundary Layer

Ichiro TAMAGAWA
River Basin Research Center, Gifu University
1-1 Yanagido, Gifu, 501-1193, JAPAN
phone/fax: +81-58-293-2430
e-mail: tama@cive.gif-u.ac.jp
WWW: http://tama.cive.gifu-u.ac.jp/~tama/

3.1 Introduction

The 'Boundary Layer' is discussed in this chapter. What do we mean by 'boundary'? Webster's II dictionary explains that boundary is 'something that marks a limit or border.' In our context, 'boundary' is the lower limit of the atmosphere. It is the 'lower' limit of the atmosphere, because the other limits are undefinable or unclear. Here the 'Boundary Layer' is the lowest part of the atmosphere. Through it, momentum, heat, water vapor, and other materials, are exchanged between the earth's surface and the atmosphere. We often call it 'atmospheric boundary layer' to distinguish from the one in fluid mechanics.

3.1.1 Boundary layer in fluid mechanics

Some readers know the word 'boundary layer' from hydraulics, fluid dynamics or fluid mechanics. It is the same idea as the one in meteorology but they are sometimes introduced in a different way.

In the past, fluid mechanics mainly treated water movement, especially water in pipes, channels, tanks or rivers for engineering purposes. Water can be treated as incompressible fluid, in which the density is not changed by pressure.

The movement can be described by the Navier-Stokes equation:

$$\frac{\partial \mathbf{u}}{\partial t} + (\mathbf{u} \cdot \nabla)\, \mathbf{u} = -\frac{1}{\rho} \nabla p + \mathbf{f} + \nu \nabla^2 \mathbf{u} \tag{3.1}$$

where:

$\mathbf{u}$: velocity vector
∇ : $\left(\frac{\partial}{\partial x}, \frac{\partial}{\partial y}, \frac{\partial}{\partial z}\right)$
ρ : density
p : pressure
$\mathbf{f}$: force to unit mass .

The last term of Eq.3.1 represents viscosity. In many cases, the viscosity term is not important except the region very near a boundary such as a wall. The region is boundary layer. In the other parts, the viscosity term can be neglected. There is the powerful potential theory that can be applied to solve for the flow.

When the Reynolds number of the flow is large enough, that is, the speed of the flow is high and/or the spatial scale of it is large, the flow becomes turbulent. The turbulent flow shows irregular and unsteady motion. The turbulent motion has a similar effect as viscosity on the mean flow. It transports momentum and smooths the flow pattern. Even in such a case, the equation of mean flow can be expressed in similar form as

$$\frac{\partial \mathbf{u}}{\partial t} + (\mathbf{u} \cdot \nabla)\, \mathbf{u} = -\frac{1}{\rho} \nabla p + \mathbf{f} + \nu_t \nabla^2 \mathbf{u} \tag{3.2}$$

where ν_t is turbulent viscosity coefficient. The value of ν_t is much larger than ν and is not constant but the function of the flow itself. But the form of Eq.3.2 is still the same as Eq.3.1 so that the boundary layer is also formed along the wall.

In boundary layer, the following approximations are applied with good accuracy.

- The flow (velocity vector) is parallel to the surface.
- The difference of the velocity (gradient of the velocity) exist only the direction normal to the surface.
- The flow is almost steady.

Those can be understood from the thinness of the boundary layer. The flow in the thin layer along the surface can not avoid going along the surface. Its velocity varys from zero at surface into some value at the outer limit of the thin layer. Therefore the gradient normal to the surface is large enough to permit us to neglect those in the other two directions. The thin layer quickly reaches the equivalent state to the outer flow due to its small mass.

3.1.2 Boundary layer in meteorology

Motion in the atmosphere

In meteorology, we consider 'air' as the fluid. The air is a compressible fluid. Its density varys both by pressure and temperature. And also air is mixed gas so that its density can change by the amount of water vapor[1] In meteorological conditions, the following three features of compressibility are enough usually.

One is the density change due to the vertical pressure change of hydrostatic balance, as the readers know the air density decreases as the height increases. The second is the change due to the temperature change. Hot air is lighter than cold air, as the readers know. The last is due to water vapor content.

Other than the density change, the effect of the earth rotation, which is called Colioris effect, must be included in the equation of motion especially in large scale motion. The Reynolds number of the atmospheric boundary layer flow is very large. The equation of motion must include the effect of turbulence as mentioned later. Turbulent motion of the air has important role especially in the boundary layer. That is almost same as the definition of boundary layer.

Thermal stratification

First let us consider the density change. Meteorologists prefer to use 'virtual potential temperature' rather than density itself. It can treat the three kinds of density change together. Start the discussion from dry air. The potential temperature is defined as the temperature that the air will have after moving to the reference pressure level (1000hPa) without heat exchange between the moving air and its environment[2]. Potential temperature is conserved in kinetic processes. 'No-heat exchange' is good approximation to the motion in atmosphere.

The equation showing the potential temperature (θ) of the air with pressure p (hPa) and temperature T (K) is

$$\theta = T\left(\frac{p_0}{p}\right)^{R/C_p} \tag{3.3}$$

where p_0 is the reference pressure (1000hPa), R is the gas constant of the air (287 $\mathrm{N\,m\,kg^{-1}K^{-1}}$) and C_p is the specific heat at constant pressure (1005 $\mathrm{J\,kg^{-1}K^{-1}}$).

To add the effect of water vapor, the virtual temperature T_v is used instead of T. T_v is defined as

$$T_v = T\left\{1 + \left(\frac{1}{\varepsilon} - 1\right)q\right\} \sim T(1 + 0.61q) \tag{3.4}$$

---

[1] The mass of water molecule is lighter than nitrogen or oxygen.

[2] It is called 'adiabatic condition'

where ε is the ratio of the molecular mass of water vapor to that of dry air (0.622) and q is specific humidity(kg kg^{-1}), which is the ratio of water vapor mass to the total air mass including water vapor in same volume. T_v is the temperature that dry air of the same density and at the same pressure as the air considered would have. When T_v is used in Eq.3.3 instead of T for moist air,

$$\theta_v = T_v \left(\frac{p_0}{p}\right)^{R/C_p} = T(1+0.61q)\left(\frac{p_0}{p}\right)^{R/C_p} \tag{3.5}$$

is obtained.

θ_v is a very good indicator of the density of moving air. Using it, air densities at different altitudes can be compared directly. If the θ_v of lower air is smaller than that of upper air, the lower air would be heavier than the upper one after moving to same altitude. In such a case, the vertical motion of air is very suppressed, because the rising air becomes heavier than the surrounding air and feels negative buoyancy (downward force). And descending air feels positive buoyancy (upward force) in the same way. Therefore vertical motion has a wave form and can not grow much. A layer with this thermal stratification is called a stable layer. And if θ_v of the lower air is larger than the upper, the vertical motion is enhanced. The rising air feels positive buoyancy and rises more and descending air feels negative buoyancy and so on. A vertical motion becomes active convection. Such a layer is called an unstable layer. Table 3.1 shows the above relationship. These stability conditions are called as thermal stratification.

	stability	motion
$\frac{\partial\theta_v}{\partial z} > 0$	stable	wave, inactive turbulence
$\frac{\partial\theta_v}{\partial z} = 0$	neutral	
$\frac{\partial\theta_v}{\partial z} < 0$	unstable	convection, active turbulence

Table 3.1: thermal stratification and stability

The atmosphere is stable almost everywhere, because the convection in the unstable layers transports heat and water vapor, with release of latent heat, to reduce unstability making the layer into a neutral or stable layer. The temperature of atmosphere usually decreases as altitude becomes large, but the potential temperature increases. The boundary layer near land surface in daytime is a rare sample of unstable layer.

3.2 Structure

The atmospheric boundary layer changes its depth and characteristics with time. The heat from surface has a large effect through the modification of the thermal stratification. The details of heat exchange at the surface will be discussed later. The atmosphere is cooled or heated from the bottom, according to the surface cooling (in nighttime) or heating (in daytime).[3] The above is typical for the boundary layer in fine day over land. The water vapor and low altitude clouds may play main role over the ocean, because of the weak heating/cooling and copious water vapor supply from the surface. Strong cloud convection like cumulonimbus causes strong winds and turbulence in the layer near surface. In such a case, the boundary layer can not be distinguished with cloud system. Here the boundary layer on a clear day over land will be discussed for simplicity. It will provide the basic physical idea for understanding actual boundary layer.

If a one dimensional boundary layer is considered, that is, the horizontal inhomogeneity can be neglected, the conceptual boundary layer structure over land is following:

- the surface layer lays near the surface.
- the nocturnal boundary layer lays over the surface layer in nighttime.
- the mixed layer lays over the surface layer in daytime.
- the mixed layer becomes the residual layer in nighttime.

The schematic picture is Fig.3.1.

Surface layer

In the air near surface, typically less than several tens meter above the ground, the vertical motion of the air is suppressed by the surface, and surface friction causes a large decrease of wind speed near surface. Small scale turbulence, mainly caused by wind speed vertical difference (called wind shear) is dominant in the flow. Thermal stratification modifies the turbulence by buoyancy effect. The surface layer will be discussed in a later section.

Mixed layer

In the daytime, the surface is heated by the solar radiation. The heat through the surface layer increases the θ_v of the upper part of the boundary layer from its bottom side. Then the stability of the surface layer becomes super-adiabatic (unstable) and that of the upper boundary layer becomes neutral by the active

---

[3] And above air is always cooled by radiation.

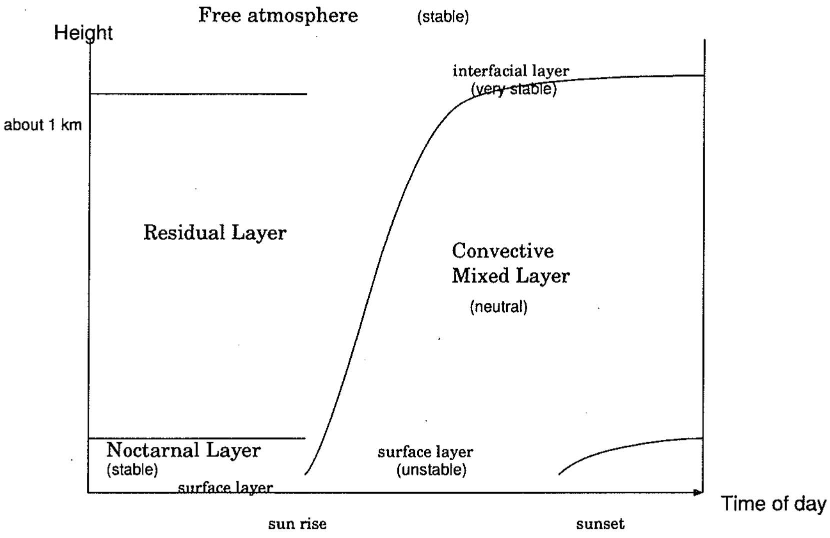

Figure3.1: Schematic picture of one dimensional boundary layer structure. This figure is simplified from a similar figure in Stull 1988 or Garratt 1992.

convection in the layer. The latter is called as a convective boundary layer, which is characterized as a well mixed layer.

Heated air at bottom moves upward but it will meet warmer (or lighter) air at some altitude because the upper atmosphere has a higher θ_v. That limits convective motion to some height. The air goes to even more higher altitude than the equilibrium level using its inertia and entrains the upper air of outer region into the convective boundary layer. The entrained air will be well mixed in the boundary layer. A sharp difference between the boundary layer and the atmosphere outside is formed at the top of the convective boundary layer. This is called an interfacial layer, which forms the upper edge of the convective boundary layer. The thermal stratification is very stable. It is sometimes called a capping inversion.[4] It spreads out horizontally with undulating form like hummocks from updrafts the underneath.

The buoyancy energy supply from the bottom and also the upper entrainment contribute to the growth of the convective boundary layer. In the convective boundary layer, the air inside is well mixed by the convection. The slab model, in which u, θ_v and other variables are constant, is often used in simple theoretical discussion. The well mixed feature is sometimes illustrated by the behavior of the smoke from a tall chimney.

---

[4] 'inversion' is used to mention about the state that temperature (not θ_v) increases as altitude become large. The situation is inverse to usual case.

Nocturnal layer and residual layer

On a clear night, the air is cooled from the bottom. θ_v decreases from the bottom, then the layer becomes stable. Turbulence and its mixing are suppressed. Wind in the layer becomes weak by decreasing the momentum transfer from the upper air. The lower air becomes cooler and more humid, because of reducing heat and water vapor transfer into upper layer.

Wave motion can be seen with intermittent turbulence. Pure wave motion does not transfer heat, momentum and so on. The vertically moved air returns to its original height without mixing. Sporadically occurring unstabilities may contribute their transfer process. The transfer process remains unclear until now. And also, radiative heat transfer becomes more important when turbulent transfer is weak.

The nocturnal layer decouples the surface below and the air above by its weak mixing due to stable stratification. Sometime it contributes a nocturnal jet or drainage flow on slopes.

The turbulent energy of the former mixed layer air decreases after decreasing or stopping the buoyancy supply from surface. This layer is called as a residual layer. It has caps on the top and bottom. It is characterized by decaying turbulent motion.

3.2.1 Observed data

Fig. 3.2 is an observed potential temperature change at Kinomoto near Lake Biwa, Japan during the intensive observation period of 2002 of the Lake Biwa project. It was measured by HyARC of Nagoya University using radiosodes. The weather was clear on the day of observation. The above mentioned features can be seen. Please compare Fig.3.2 with Fig.3.1. The points are:

- A nocturnal layer below a few hundred meters formed after 16 JST.
- A convective boundary layer reaching about 700m formed after 10 JST.
- At the same time, an unstable stratified surface layer formed below about 200m.

3.3 Turbulent transport

Except in very stable cases, the flow in the boundary layer is turbulent. Let the variables such as u, w, T and q be divided into the mean and fluctuation (turbulence) as

$$x = \overline{x} + x'$$

where x represents u, w, and so on. In the discussion of surface layer, u is usually set into the mean wind direction for simplicity. The $\overline{x}$ shows some

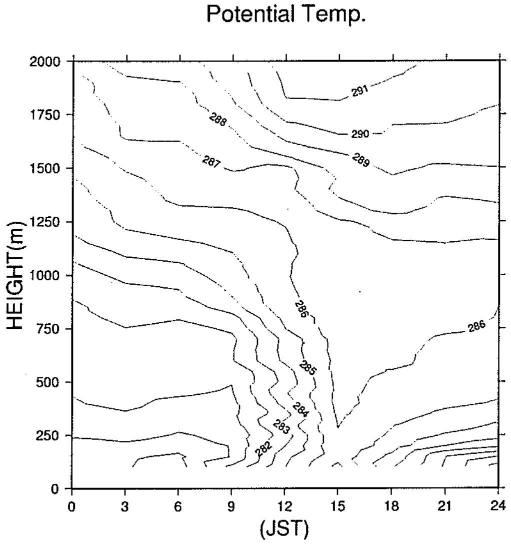

Figure 3.2: Potential temperature distribution measured at Kinomoto, Shiga prefecture, Japan in 17 November 2002 by HyARC, Nagoya University during the intensive observation period of 2002 of the Lake Biwa project.

kind of average of x. The way of average should be defined appropriately, such as ensemble averaging, time averaging, and space averaging, according to its context. $\overline{x'}$ is zero in the usual definitions.

The averaged form of the second term of Eq.3.1 becomes

$$\overline{(\mathbf{u}\cdot\nabla)\,\mathbf{u}} = (\overline{\mathbf{u}}\cdot\nabla)\,\overline{\mathbf{u}} + \begin{pmatrix} \nabla\cdot\overline{\mathbf{u}'u'} \\ \nabla\cdot\overline{\mathbf{u}'v'} \\ \nabla\cdot\overline{\mathbf{u}'w'} \end{pmatrix} \tag{3.6}$$

The equation of continuity is used to deduce Eq.3.6 and u, v, w are the components of $\mathbf{u}$. The terms $\overline{u'u'}$, $\overline{u'v'}$, $\overline{u'w'}$ and so on are called Reynolds stress terms, which are the direct expressions of eddy viscosity or turbulent viscosity. They show the contribution of turbulence to mean flow by transporting the momentum. Their convergence accelerates the mean velocity. The same kinds of turbulent transports exist for scalar variables such as heat, water vapor, CO_2, and so on.

For example, the averaged equation of potential temperature can be deduced from the equation of conservation. The conservation equation is

$$\frac{\partial\theta}{\partial t} + (\mathbf{u}\cdot\nabla)\,\theta = S \tag{3.7}$$

where S shows the effect of non adiabatic heating, such as molecular diffusion, the convergence of radiation flux, heat conduction from surface, and so on. Then both sides of the equation are averaged into

$$\frac{\partial\overline{\theta}}{\partial t} + (\overline{\mathbf{u}} \cdot \nabla)\,\overline{\theta} = -\nabla\overline{\theta'\mathbf{u}'} + S_\theta \tag{3.8}$$

Also that for specific humidity q is

$$\frac{\partial\overline{q}}{\partial t} + (\overline{\mathbf{u}} \cdot \nabla)\,\overline{q} = -\nabla\overline{q'\mathbf{u}'} + S_q \tag{3.9}$$

where S_q is the source for water vapor such as evaporation.

Turbulent motion is characterized by its irregularity. Only the statistical features are required to be known for many purpose. They are described in the next section for a very simple surface layer.

3.3.1 Surface layer turbulence

The discussion here is limited to a very simple case. The following are assumed.

- The surface is so homogenous that we can ignore the horizontal variation of all variables in the surface layer.
- The surface layer reaches equilibrium with the environment quickly so that it is in equilibrium and its time change can be ignored.
- There is no convergence of radiation, no phase change of water or no floating obstacles (rain drop, snow flake, sand, and so on) in the surface layer.
- The Coriolis force can be ignored in comparison to the other terms.

The equations of mean state can be reduced into

$$\frac{\partial\overline{u'w'}}{\partial z} = 0 \tag{3.10}$$

$$\frac{\partial\overline{w'\theta'}}{\partial z} = 0 \tag{3.11}$$

$$\frac{\partial\overline{w'q'}}{\partial z} = 0 \tag{3.12}$$

The above equations show that $\overline{u'w'}$, $\overline{w'\theta'}$ and $\overline{w'q'}$ are constant in the surface layer. The $\overline{x'w'}$ ($x = u$, θ or q) shows the amount of x transported by turbulence per unit time and per unit area of horizontal plane. This kind of quantity is called flux. Eqs.3.10 – 3.12 show that the flux is constant in the surface layer.

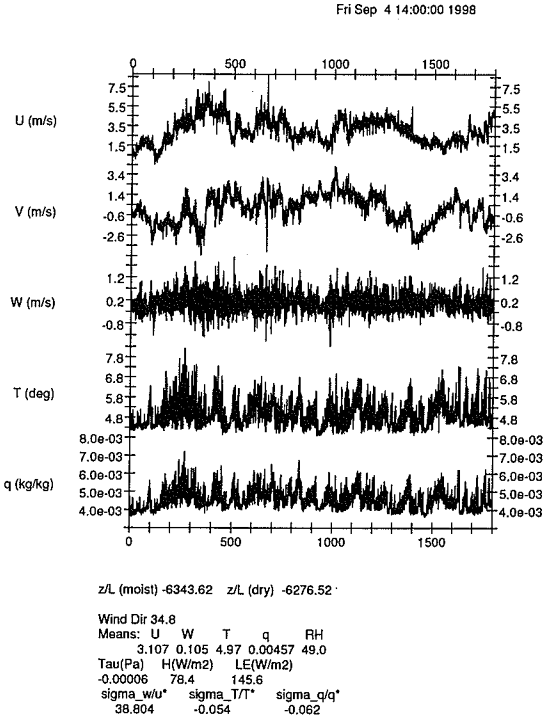

```
z/L (moist) -6343.62   z/L (dry)  -6276.52

Wind Dir 34.8
Means:  U     W      T    q       RH
     3.107  0.105  4.97  0.00457  49.0
Tau(Pa)    H(W/m2)    LE(W/m2)
-0.00006    78.4       145.6
sigma_w/u*   sigma_T/T*    sigma_q/q*
  38.804       -0.054        -0.062
```

Figure 3.3: Sample of turbulence measurement and results. The data were taken over the Tibetan plateau in China during the intensive observation period of GAME/Tibet 1998. The values are explained in the figure. ‘sigma’ is the standard deviation.

The assumption used here might be thought to be an oversimplification, but the results with the constant flux assumption are a good approximation for the fluxes over flat terrain. The flux from (or into) the surface passes through the surface layer with small loss. The fluxes in Eqs.3.10 – 3.12 have the relationships to shearing stress(τ), heat flux(H) or surface evaporation(E) as

$$
\begin{aligned}
\tau &= -\rho\overline{u'w'} && (3.13)\\
H &= \rho C_p \left(\frac{p}{p_0}\right)^{R/C_p} \overline{w'\theta'} && (3.14)\\
E &= \rho\overline{w'q'} && (3.15)
\end{aligned}
$$

where p is pressure at the surface and turbulent fluctuations of p and ρ are ignored. The reader should remember that the heat H causes a temperature change $H/(\rho C_p)$ at constant pressure condition to understand the factor in Eq.3.14. τ, H and E are the averaged value.

The turbulent fluctuations (u', w', θ' and q') can be measured with fast response sensors. A Sonic anemometer-thermometer is a standard sensor used to measure wind velocity and temperature. The measurement is based on the fact that the velosity of a sound wave is the vector sum of that in static air and the wind velocity. It was developed during late 1960s. Now very stable and accurate sensors are manufactured by several companies. For humidity fluctuation, an optical sensor using the absorption of water vapor in infrared or ultraviolet band is used. The humidity sensors were unstable. they required much care about their calibrations or maintain. Recently a few stable sensors were started to use, and they need a little care about sensor calibration.

The measured turbulent fluctuations are used to evaluate surface fluxes with Eqs.3.13–3.15. This technique is called the eddy covariance (or correlation) method. It is thought to be reliable because it is a direct measurement. It is usually done with about 10Hz sampling rate and about 30 minutes averaging. The duration of 30 minutes is supported by the spectral gap around 1 hour, but not always and everywhere. The quarity of the flux estimation depends on the applicability of the assumptions mentioned before under the measurement condition. Fig.3.3 is a sample of turbulence measurement and fluxes by the eddy covariance technique. The data were taken at Amdo over Tibetan plateau during the GAME/Tibet project.

Recently, the eddy covariance observation has become popular and is even applied over forests or city buildings. In such a case, sometimes a correction is required due to its departure from an ideal horizontally homogeneous and statistically steady condition. The discussion based on the integratation of Eqs.3.8 and 3.9 is necessary in such a case.

3.4 Logarithmic law and Monin-Obukhov similarity

There are many statistical theories about turbulence. A few of them are introduced below.

In the surface layer, the fluxes ($\overline{u'w'}$, $\overline{w'T'}$ and so on) are important, because they are constant and the mean states are balanced with them.

The neutral surface layer is simple because it has no buoyancy. In this case, the vertical distribution of the mean wind speed is known to be expressed with a logarithmic function of the height from the surface. This is explained as follows.

The magnitude of $\overline{u'w'}$ is estimated by thinking that the fluctuations are caused by eddy mixing of the profile of mean wind as follows:

$$\overline{u'w'} \sim |u'||w'| \qquad (3.16)$$

$$|u'|,|w'| \quad \sim \quad \ell\frac{\partial\overline{u}}{\partial z} \tag{3.17}$$

where ℓ shows the representative size of eddies, that is a representative length scale of turbulent mixing. ℓ must be affected by the distance to the surface. So $\ell \propto z$. Then

$$|\overline{u'w'}| = -\overline{u'w'} = \left(kz\frac{\partial\overline{u}}{\partial z}\right)^2 \tag{3.18}$$

where k is a constant, which is called the 'von Kármán' constant. The experimental value of k is about 0.4. The scaling parameter of turbulent velocity $u* = \sqrt{|\overline{u'w'}|}$ is often used, which is called the friction velocity. Using $u*$, Eq.3.18 becomes

$$u* \quad = \quad kz\frac{\partial\overline{u}}{\partial z} \tag{3.19}$$

$$\overline{u} \quad = \quad \frac{u*}{k}\log\left(\frac{z}{z_0}\right) \tag{3.20}$$

Here z_0 is an integral constant called the roughness length. z_0 indicates the height at which the logarithmic wind would become zero if the logarithmic law could be applied. z_0 is usually treated as a constant which is determined by surface condition. Kondo 1994 shows z_0 as follows:

	z_0(m)		z_0(m)
bare soil	10^{-4}	water (2ms^{-1} wind)	0.27×10−4
grass land (0.1m∼1m)	0.01∼0.15	forest	0.3 ∼ 1
rural town	0.2∼0.5	city	1 ∼ 5

For a thermally stratified surface layer, that is for a stable or unstable layer, a correction to the buoyancy effect is necessary. The turbulent kinetic energy equation is used to obtain an adequate stability parameter for describing turbulent statistics. The turbulent kinetic energy equation reduced by the surface layer assumption used here is as follows:

$$\frac{\partial e}{\partial t} = -\overline{u'w'}\frac{\partial\overline{u}}{\partial z} + \frac{g}{\theta_v}\overline{w'\theta_v'} - \frac{\partial\overline{w'e}}{\partial z} - \frac{1}{\rho}\frac{\partial\overline{p'w'}}{\partial z} - \text{(viscous dissipation)} \tag{3.21}$$

Here e indicates turbulent kinetic energy ($e = \overline{\frac{u'^2+v'^2+w'^2}{2}}$). The right side should be zero due to the steady state of the surface layer. The first term of the left side of the equation indicates turbulence production by wind shear. And the second term represents production or destruction by buoyancy. The third and fourth terms show turbulent transport of e and redistribution of e, respectively. The first two terms are important for describing turbulent statistics. The second term vanishes in neutral layer, that is, the logarithmic law theory considers the first one only. The second term adds energy production in unstable conditions and the produced energy is consumed by viscous dissipation. In stable conditions, the buoyancy term also reduces the turbulent kinetic energy produced by the first term. Therefore the ratio of the two terms can be a good non-dimensional parameter. The following parameters are used to evaluate the ratio as a stability parameter.

$$Ri = \frac{g}{\overline{\theta_v}} \frac{\frac{\partial \overline{\theta_v}}{\partial z}}{\frac{\partial \overline{u}}{\partial z}} \tag{3.22}$$

$$\frac{z}{L} = \frac{kz \frac{g}{\theta_v} \theta_v *}{u*^2} \tag{3.23}$$

where $\theta_v * = -\overline{w'\theta'_v}/u*$. Ri is called the Richardson number, and z/L is called the Monin-Obukhov stability.

Ri can be evaluated only by mean variables. It is convenient to use to compute turbulent statistics from mean values. However z/L includes turbulent parameters $u*$ and $\theta*$. Nevertheless, z/L is widely used in describing turbulent characteristics with $u*$, $\theta*$ and other scaling parameters. Both Ri and z/L become negative value in unstable condition, zero in neutral and positive in stable condition.

The logarithmic law is expanded by including the stability parameter Ri or z/L, which is found by Monin and Obukhov during 1940s and 1950s. The relationship was experimentally confirmed during late 1960s and 1970s by several intensive observations.

Eq.3.19 can be arranged as

$$\frac{kz}{u*} \frac{\partial \overline{u}}{\partial z} = 1 \tag{3.24}$$

Eq.3.24 can be read as follows: the shear of the mean flow can be non-dimensionalized by $u*$ and z.

Then Eq.3.24 can be expanded as

$$\frac{kz}{u*} \frac{\partial \overline{u}}{\partial z} = \phi_m \left(\frac{z}{L} \right) \tag{3.25}$$

where ϕ_m is a non-dimensional function of stability, called the non-dimensional shear function of wind speed[5].

In the same way, the shear of θ and q can be expressed as

$$\frac{kz}{\theta*} \frac{\partial \overline{\theta}}{\partial z} = \phi_h \left(\frac{z}{L} \right) \tag{3.26}$$

---

[5] This kind of discussion is called dimensional analysis. It is widely used in treating complicated phenomena.

$$\frac{kz}{q*}\frac{\partial\overline{q}}{\partial z} = \phi_e\left(\frac{z}{L}\right) \tag{3.27}$$

where $\theta*$ and $q*$ are the scaling parameters for the turbulent fluctuations of potential temperature and of specific humidity, defined $\theta* = \overline{w'\theta'}/u*$ and $q* = \overline{w'q'}/u*$. The subscripts $_m$, $_h$ $_e$ indicate momentum, heat and evaporation respectively. The functional forms and parameters of ϕ_m, ϕ_h and ϕ_e can not determined by theory. They need to be determined by experiments.

The form in Eqs.3.28 and 3.29 is the so-called Businger-Dyer type expression. The constants are slightly different among observations. Here the values are taken from the summary in the textbook by Garratt (Garratt 1992).

$$\phi_m = \begin{cases} 1+5\frac{z}{L} & \left(0 \le \frac{z}{L} < 1\right) \\ \left(1-16\frac{z}{L}\right)^{1/4} & \left(-5 < \frac{z}{L} < 0\right) \end{cases} \tag{3.28}$$

$$\phi_h = \begin{cases} 1+5\frac{z}{L} & \left(0 \le \frac{z}{L} < 1\right) \\ \left(1-16\frac{z}{L}\right)^{1/2} & \left(-5 < \frac{z}{L} < 0\right) \end{cases} \tag{3.29}$$

for q and other scalar variables, the form of non-dimensional shear function is said to be same, but there are few observational results. In many case, the assumptions (horizontal homogeneity and steadiness) used here are not appropriate. For very unstable conditions ($\frac{z}{l} \ll -1$), the energy of turbulence is supplied only from the buoyancy force. Therefore $u*$ is no longer a good parameter for non-dimensional shear functions. In such a case, dimensional analysis leads the following relationships: $\phi_m \propto \left(\frac{z}{L}\right)^{\frac{1}{3}}$ and $\phi_h \propto \left(\frac{z}{L}\right)^{-\frac{1}{3}}$. Kadar and Yaglom 1989 recommended as follows:

$$\phi_m = 0.4\left(\frac{z}{L}\right)^{\frac{1}{3}} \tag{3.30}$$

$$\phi_h = 0.5\left(\frac{z}{L}\right)^{-\frac{1}{3}} \tag{3.31}$$

and H is directly related to the temperature difference as

$$H = \rho C_p A_h \left(\overline{\theta}(z) - \overline{\theta}(surface)\right)^{1+a} \tag{3.32}$$

As the parameters in Eq.3.32, Kondo 1994 said $(A_h, a) = (1.2 \times 10^{-3}, 1/3)$ for $z = 1$m, and Tamagawa 1996 said $(2.7\times10^{-3}, 0.4)$ for $z = 20$m. According to the laboratory experiment on heat transfer, the following relationship is obtained

$$Nu = A\,Ra^{1/3\sim0.4} \tag{3.33}$$

Nu and Ra are the Nusselt number and the Rayleigh number respectively. Details should be referred to a textbook on heat transfer mechanics. In any case, both values above are consistent. This kind of consideration of free convection is sometimes necessary to estimate H under strong heating.

Here the relationships between mean values and turbulence with Monin-Obukhov similarity are described. Integrating Eqs.3.25–3.26 with the constant flux approximation, the difference between two altitude can be expressed as

$$\begin{aligned}
\overline{u}(z_2) - \overline{u}(z_1) &= \int_{z_1}^{z_2} \phi_m \left(\frac{z}{L}\right) dz \\
&= \frac{u*}{kz} \left\{ \log\left(\frac{z_2}{z_1}\right) + \psi_m \left(\frac{z_2}{L}\right) - \psi_m \left(\frac{z_1}{L}\right) \right\} \qquad (3.34) \\
\overline{\theta}(z_2) - \overline{\theta}(z_1) &= \int_{z_1}^{z_2} \phi_h \left(\frac{z}{L}\right) dz \\
&= \frac{\theta*}{kz} \left\{ \log\left(\frac{z_2}{z_1}\right) + \psi_h \left(\frac{z_2}{L}\right) - \psi_h \left(\frac{z_1}{L}\right) \right\} \qquad (3.35) \\
\overline{q}(z_2) - \overline{q}(z_1) &= \int_{z_1}^{z_2} \phi_e \left(\frac{z}{L}\right) dz \\
&= \frac{q*}{kz} \left\{ \log\left(\frac{z_2}{z_1}\right) + \psi_e \left(\frac{z_2}{L}\right) - \psi_e \left(\frac{z_1}{L}\right) \right\} \qquad (3.36)
\end{aligned}$$

where ψ_m, ψ_h and ψ_e are defined as $\psi_x = \int \frac{\phi_x - 1}{\frac{z}{L}} d\left(\frac{z}{L}\right)$ (x indicates m, h or e). Integrating from parametric heights indicating surface, such as z_0 in Eq.3.20, to height z,

$$\begin{aligned}
\overline{u}(z) &= \int_{z_0}^{z} \phi_m \left(\frac{z}{L}\right) dz \\
&= \frac{u*}{kz} \left\{ \log\left(\frac{z}{z_0}\right) + \psi_m \left(\frac{z}{L}\right) - \psi_m \left(\frac{z_0}{L}\right) \right\} \qquad (3.37) \\
\overline{\theta}(z) - \overline{\theta}(surface) &= \int_{z_T}^{z} \phi_h \left(\frac{z}{L}\right) dz \\
&= \frac{\theta*}{kz} \left\{ \log\left(\frac{z}{z_T}\right) + \psi_h \left(\frac{z}{L}\right) - \psi_h \left(\frac{z_T}{L}\right) \right\} \qquad (3.38)
\end{aligned}$$

where z_T indicates the height where θ would have the surface value assuming non-dimensional shear function to be applicable. However, for water vapor, the surface value can not be defined except over a water surface. The β, indicating water availability or evaporation efficiency, is introduced as

$$\begin{aligned}
\beta\left(\overline{q(z)} - q_{s0}\right) &= \int_{z_q}^{z} \phi_e \left(\frac{z}{L}\right) dz \\
&= \frac{q*}{kz} \left\{ \log\left(\frac{z}{z_q}\right) + \psi_e \left(\frac{z}{L}\right) - \psi_e \left(\frac{z_q}{L}\right) \right\} \qquad (3.39)
\end{aligned}$$

where q_{s0} indicates the saturation specific humidity at the surface mean temperature. In Eqs.3.34–3.39, $\psi_{m,h,e}\left(z/z_{0,T,q}\right)$ usually set to be zero and $z_q = z_T$. β set to be 1 on a water surface and 0 on a non-evaporating surface.

Using Eqs.3.34 – 3.36 or Eqs.3.37 – 3.39, $u*$, $\theta*$ and $q*$ can be estimated from the differences of mean wind speed, potential temperature and specific humidity at two observation levels or from one observation and adequate parameters.

> For example, if the observed mean values at z_1 and z_2 are obtained, tentative values of $u*$, $\theta*$, $q*$ can be obtained by assuming $z/L = 0$ in Eq.3.34–3.36. And z/L can be calculated by using the so-obtained $u*$ and so on using Eq.3.23. Then use Eq.3.34–3.36 again but with the newly obtained z/L to get refined values of $u*$, $\theta*$ and so on. The parameters $u*$, $\theta*$, $q*$ will show no change after several iterations.

$u*$, $\theta*$ and $q*$ can be easily converted into shearing stress τ, sensible heat flux H and water vapor flux E by

$$\begin{aligned} \tau &= \rho u*^2 && (3.40) \\ H &= -\rho C_p \left(\frac{p}{p_0}\right)^{R/C_p} u*\,\theta* && (3.41) \\ E &= -\rho u*\,q* && (3.42) \end{aligned}$$

Therefore the relationship between the profiles and fluxes are obtained. The observation of profiles of wind, temperature and humidity can be used to estimate heat balance at the surface, but the required accuracy of the observation is very high. The small errors that is not a problem to measure the variables themselves often cause serious errors in obtaining the differences in Eqs.3.34–3.36. Careful calibration of the sensors is required. The observer should remember the fact that the direct measurement of Eqs.3.13–3.15 is sometimes easier, especially for H, although the cost of turbulent measuring sensors is much higher than the usual sensors for mean values.

3.4.1 Surface heat budget

On an idealized plane surface, the energy coming into the surface having zero depth must go upwards or downwards because the surface can not store energy due to zero depth. In such a case, heat budget equation:

$$(1-\alpha)Q_s + Q_l \downarrow - Q_l \uparrow = H + \lambda E + G \qquad (3.43)$$

is applied to the surface. Here, Q_s is the short wave (visible) radiation downward flux, $Q_l \downarrow$ and $Q_l \uparrow$ are the infrared radiation fluxes coming into and going up from the ground respectively, α is reflectivity of the surface (albedo), λ is the latent heat of vaporization of water and G is heat flux into ground. The left side of the equation is often called the net radiation ($Q_n = (1-\alpha)Q_s + Q_l \downarrow - Q_l \uparrow$). This equation gives the boundary conditions to energy equations both for the atmosphere and the ground. For example, the stability of boundary layer is affected by surface conditions (α, z_0 and so on) by limiting the available energy through Eq.3.43. Meteorological simulation models include the same kind of equation.

In non-ideal cases such as city or forest, one more layer called the canopy layer is considered in modeling. The heat storage term of the canopy should be added to Eq.3.43. Recent numerical models treat the complicated surface conditions as a layer or several layers called canopy layer or surface model.

3.5 For more study

A very rough sketch of the boundary layer and a little detail of the surface boundary layer are described above. The textbooks listed below are recommended for more study of the boundary layer and also as reference for this chapter.

R. S. Stull An introduction to boundary layer meteorology, Kluwer Academic Publishers, 1988

J. R. Garratt The atmospheric boundary layer, Cambridge university press, 1992

The aboves are comprehensive textbooks of atmospheric boundary layer. Many observational results and discussions are found in them.

R. G. Fleagle and J. A. Businger An introduction to atmospheric physics (2nd ed.), Academic press, 1980

This is a textbook for whole atmospheric physics but the discussion about surface layer and observational instruments are very educative.

J. C. Kaimal and J. J. Finnigan Atmospheric boundary layer flows, Oxford university press, 1994

This book has detail discussion surface layer flow and measurement techniques and instruments. It is good for surface layer observational researcher.

Other references

J. Kondo 水環境の気象学 (Meteorology of water environment), Asakura corp. 1994 (in Japanese).

I. Tamagawa Turbulent Characteristics and Bulk Transfer Coefficients over the Desert in the HEIFE Area, Boundary-Layer Meteorology, **77**, pp.1–20, 1996.

B. A. Kadar and A. M. Yaglom Mean fields and fluctuation moments in unstable stratified turbulent boundary layers, Journal of fluid mechanics, **212**, pp.637–662, 1990.

Chapter 4

Rain Observation from Satellites

Kenji Nakamura
Hydrospheric Atmospheric Research Center, Nagoya University
Furocho, Chikusaku, Nagoya 464-8601, JAPAN
phone: +81-52-789-5439, fax: +81-52-789-3436
e-mail: nakamura@hyarc.nagoya-u.ac.jp

4.1 Introduction

Rainfall is one of the major components of the Earths climate. Precipitation is a result of the water vapor condensation which releases latent heat energy to the atmosphere. This latent heat energy drives the general circulation. Over the tropical regions, especially the tropical west Pacific Ocean and maritime continent, vigorous convection occurs. Thus, this region is a strong driving force of the Hadley and Walker circulations. The importance of precipitation is not only to the climate system but also in the society. Almost all countries in the world, precipitation is the primary source of the fresh water. Even a small change of precipitation greatly affects daily life and impacts to society. Vulnerability of society to the water resource variation is not only in the developing countries but also in the developed countries, where the fresh water is fully utilized. Recently global warming has attracted great attentions. One of the most important issues is the future precipitation variation. Many model simulations show that the global precipitation will increase as the global warming progresses. This is primarily because the saturated water vapor pressure increases as a result of the low level atmospheric temperature increase. The change is roughly 5 % in the future 50 years (e.g. Wetherald and Manabe[1]). The precipitation has increased over land in the last 100 years also by a few percent (Climate Change[2]). While the temperature increase is rather uniform with high increase in northern high latitude areas, the increase of precipitation varies greatly. Also the natural (unforced) variation is high. Thus, the current documentation and future prediction of precipitation are a difficult task. On the other hand, precipitation is a very good index to evaluate general circulation models, since the high precipitation is a very sensitive to the model parameterizations. The Tropical Rainfall Measuring Mission (TRMM) was successfully launched in November 1997 (Kummerow *et al.*[3]). Since then more than nearly six years of data have been accumulated. TRMM is equipped with the first spaceborne rain radar (PR) along with a microwave radiometer (TMI) and a visible/infrared radiometer (VIRS). Those sensors observe precipitation system nearly simultaneously, and give us a unique opportunity to study the precipitation system over the tropical and sub-tropical regions (Fig. 4.1). Thus, TRMM showed its unique and invaluable ability in many reports. In addition to progress in rain/cloud system studies, algorithm development is also one of the fruitful results (Iguchi *et al.*[4]). The PR is the first spaceborne rain radar and the algorithms for the PR are very successful. Though the PR is a simple single wavelength radar with a slightly high frequency of 13.8 GHz, the so-called surface reference technique which utilizes strong signature from the surface works well. This technique is peculiar to the down-looking radar. Various investigations of the PR algorithm opened a new field of 'radar rain estimate from space'. This field will naturally extend to the future dual-wavelength radar algorithms. The comparison of TMI-derived rainrate and PR-derived rainrate helped to improve both algorithms (e.g., Viltard *et al.*[5], Prabhakara *et al.*[6]). For example, a problem in the rain height assumption in the TMI algorithm is found to be one of the causes of the discrepancies (Masunaga *et al.*[7], Ikai and Nakamura[8]). The brightness temperatures of TMI high frequency channels show the signature of solid particles in the cloud/precipitation system. Incorporating PR and TMI data, and also with the Lightning Imaging Sensor (LIS) onboard TRMM, addressing the precipitation system has been much improved. For example, the difference of the precipitation systems over land and over ocean was revealed as the system over land is generally more vigorous and may have more suprercooled water (Nesbitt *et al.*[9], Toracinta *et al.*[10], Cecil and Zipser[11], Cecil *et al.*[12]). Research on temporal and spatial variation of precipitation has also been performed. The well-known variation of precipitation distribution for El Niño and La Niña is a good example (Adler *et al.*[13]). An interesting difference of rain estimates between TMI, the Global Precipitation Climatology Project (GPCP) and PR has also been shown. It is said that rain over the ocean increases during an El Niño. The PR, however, shows no such indication while TMI and GPCP showed the increase. Nearly six years have passed since the TRMM launch, and data accumulation continues. Using the data over several years, we now have a unique opportunity to address the inter-annual variation of precipitation in space and time over tropical and sub-tropical regions. TRMM observations are focused on the rain over tropical and sub-tropical regions. TRMM observations also cover up to near 40 degree latitude covering some of the mid-latitude regions. In the mid-latitude region, baroclinic disturbances are strong and the precipitation is usually associated with those disturbances. Precipitation might take somewhat smaller role than in the tropical or sub-tropical regions but still has a big impact to the disturbances through the latent heat release. Some comparisons of rain distributions derived by GPCP, TRMM and others have been done (e.g., Kodama and Tamaoki[14]), but it is not intensive. One obstacle is the solid precipitation. The PR rain estimate for the solid precipitation has a problem. For the wet snowfall, the equivalent rainrate estimate accuracy is very problematic. In the data analysis, this issue should be taken into consideration.

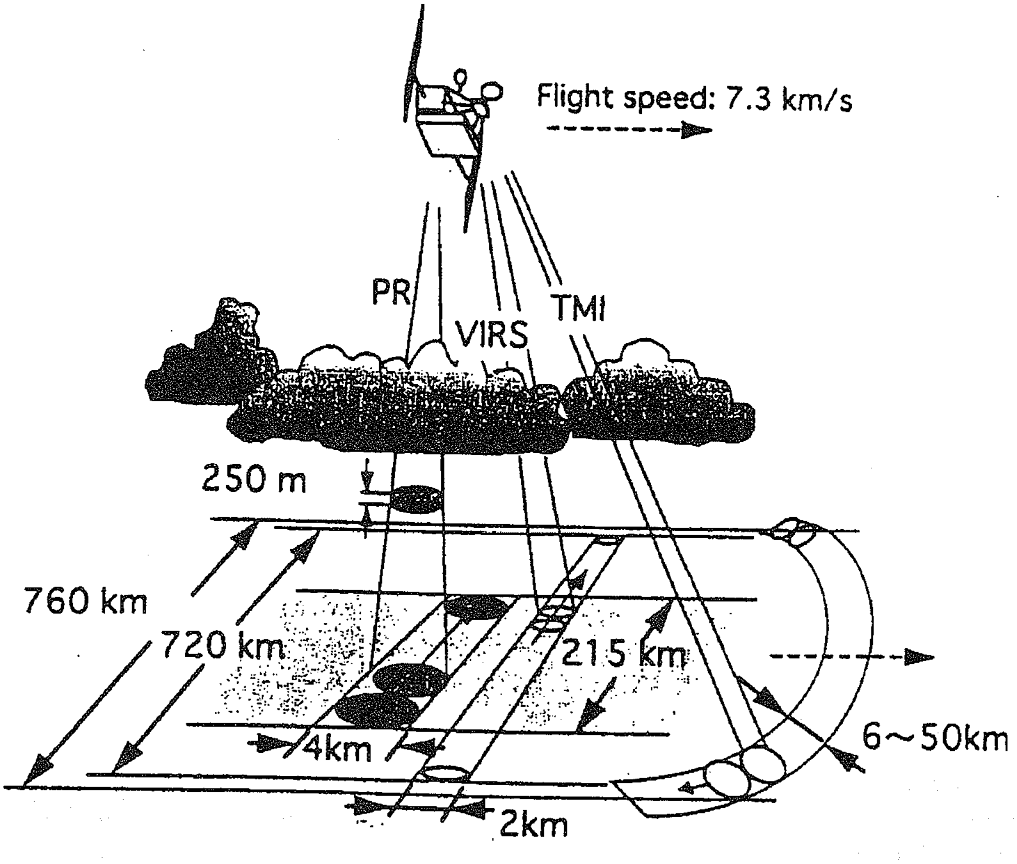

Figure 4.1: TRMM observation.

4.2 Brief history of TRMM

NASA Goddard Space Flight Center devised the concept for TRMM in 1986. At that time reliable precipitation data were not obtained using spaceborne microwave radiometers. At the same time, it was recognized that precipitation in the tropical regions plays an important role as a heat source that drives the overall atmospheric general circulation For this reason, the science community strongly desired to observe precipitation from space on a global basis, and developing a spaceborne precipitation radar was essential to meet the mission requirements. Advancements in precipitation observation were made once the Special Sensor Microwave/Imager (SSM/I) was launched. It is now possible to obtain accurate precipitation data using existing microwave radiometers at least over ocean. In fact, SSM/I data on the precipitation distribution yielded extremely good results. Visible-infrared radiometers are also used as a spaceborne precipitation observation sensor, measuring the brightness temperature of cloud tops. In this advancement, the meaning of PR changed from an essential and only sensor for rain observation to an essential sensor to observe three-dimensional rain structure. PR's value is also in the capability to train microwave radiometer rain retrievals.

4.3 Current and future research

4.3.1 Algorithm and validation

To utilize fully the PR data, we need to know the PR rain echo characteristics. Another example is a comparison of TRMM PR rain estimates and others over Africa (Kummerow *et al.*[3], Adler *et al.*[13], Adeyewa and Nakamura[15]). One example is the mirror echo of rain. Over the ocean, the PR observes the mirrored echo of rain because the ocean surface is a good microwave reflector. The mirror echo characteristics were investigated and the effect of the radar receiver noise and rain attenuation was clarified (Li and Nakamura[16]).

4.3.2 Rain characteristics

Convective/stratiform distributions

The convective/stratiform rain distribution is easy to obtain using Level 3 data (gridded monthly statistics). The difference in El Niño and La Niña has already documented. However, the characteristics of each year has not yet fully addressed. During the El Niño episode, the deep convection region shifts to the central Pacific Ocean. The activity of the deep convection slightly reduces and the fraction of stratiform rain increases. This characteristics appear not only in the convective/stratiform rain fraction but also in the rain estimate difference in the TMI and the PR. This may also affect the so-called GOES Precipitation Index (GPI) type rain estimate. Over land, the distribution of the convective/stratiform rain fraction is affected by orography. In the southern part of Himalayan region, the eastern part is likely to have stratiform rain, but the western part is likely to have convective rain. It is interesting to investigate the reasons of this type of difference. Precipitation systems are different over ocean and over land. Generally, the precipitation is vigorous over land. The systems are characterized as over ocean shallow (Fig. 4.2). We have shown the global distribution of the shallow convection using the TRMM Level 3 data (Short and Nakamura[17]). The upward increasing and upward decreasing profile were characterized as land type and ocean type rain systems, respectively. The former dominated tropical land regions and the latter over tropical ocean regions. The ocean type profile, however, migrates onto land in India region during Asian monsoon period (Hirose and Nakamura[18]). Similar trend appears over Africa in rainy season.

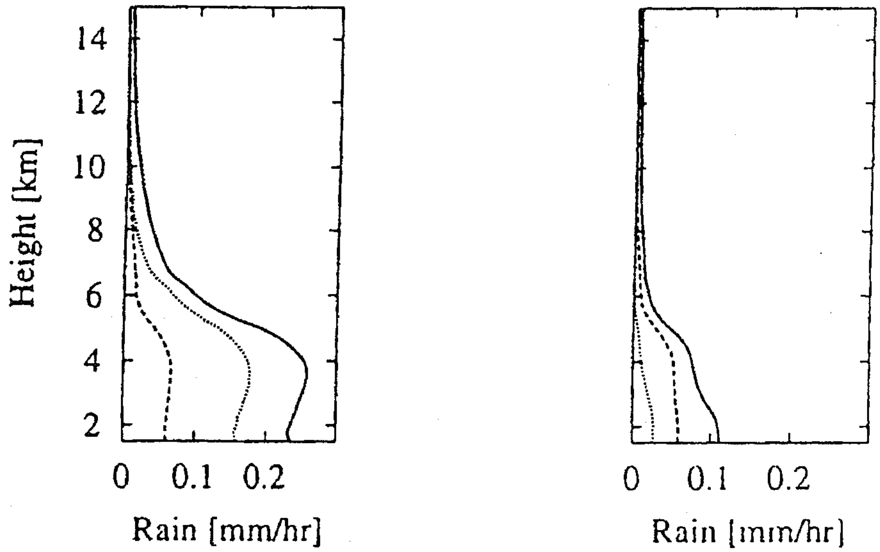

Figure 4.2: Typical vertical rain profiles over land and ocean in the tropics.

Storm height distribution over ocean

It is well known that shallow convection is common over open oceans. Shallow convection capped by the trade wind inversion dominates over eastern Pacific Ocean where in the subsiding leg of the Walker circulation. Over the west

Pacific Ocean where rising leg of the Walker circulation exists, deep convections is common but still shallow convection exists. The boundary between the rising and subsiding legs of the Walker circulation seems to clearly appear by the storm height distribution (Fig. 4.3). The effect of the Walker circulation also appears in the sea surface temperature (SST) vs. storm height statistics. Generally, storm height has a good correlation with SST. There, however, are deviations from the averaged relationship between SST and the storm height. One of the causes of this deviation is the Walker circulation. SST can also be obtained from the TMI. The TMI can observe SST through clouds (Sengupta *et al.*[19], Stammer *et al.*[20]), while infrared technique use mosaics of data with clear sky. Thus, infrared-derived SST might have a bias for the cloudy regions. In addition, TMI-derived SST has a high temporal resolution, which helps to obtain precise SST-storm height relationship.

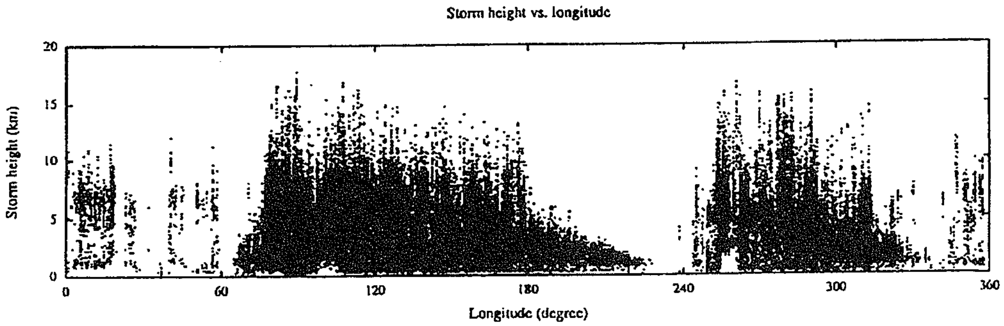

Figure 4.3: Storm height distribution for 20–25N for August 1999.

Precise rain distribution

One of the unique characteristics of the PR is its high spatial resolution. At nadir, the pixel size of the PR is about 4.3 km. Thanks to this advantage, we can obtain a precise rain distribution. So far, many studies using visible/infrared radiometer data have been performed. The visible/infrared radiometer data have an advantage in its very high sampling if the radiometer is onboard a geostationary satellite. On the other hand, the visible/infrared radiometer observes cloud instead of rain. Clouds are blown by high level wind and easily spread. So, the actual precipitation region is hard to determine. The detailed rain distribution is closely related with surface topography. This is especially true for mountainous regions, such as the Himalaya. From the visible/infrared data analysis, topography affects diurnal variation of rain in a scale of 100 km (Kuwagata *et al.*[21]) The relationship between rain total and surface elevation is another interesting issue. Kuraji *et al.*[22] reported that rain increases with surface elevation up to 1500 m MSL. A preliminary study in the southern slope of Himalaya mountain range shows that the rain increase up to 1500 m MSL is not clear, but above 1500 m, rain clearly decreases with surface elevation. In the Irawaddy River basin, study shows that rain is nearly constant up to about 2000 m. These apparent discrepancies may be due to the wind direction. Wind facing slopes might show a clear rain-surface elevation relationship. It is desirable to investigate more details. One of the applications of this relationship is river basin areal rain total estimate. Rain estimates by visible/infrared radiometer have a poor spatial resolution but a high temporal resolution. The poor spatial resolution rain map may be refined by the low level wind and the topography.

Diurnal variation of rain

Thanks to the non-sun synchronous orbit of TRMM, diurnal variation of rain can be revealed. The diurnal variation is significant in tropical land and tropical ocean near land. For example, the maritime continent shows very clear diurnal variation of rain (Fig. 4.4). The diurnal variation is nearly reversed over land versus over ocean near the coast. That is, afternoon rain dominates over land, while morning rain dominates over ocean. Over the open ocean, a weak morning rain peak is reported. If we looked at more detail, the afternoon rain peak over land is not universal. Generally speaking, night rain peak appears in deep mountainous regions, e.g., in the Himalayan region or high region in Borneo Island, Indonesia. The land-sea breeze and the valley wind seem to cause the general characteristics of the diurnal variation of rain over land. Even over land, some areas show morning enhanced rain. The southern foothills of the Himalayan mountain region shows early morning enhanced rain clearly. This morning rain band extends further east and almost to Vietnam (Ohsawa *et al.*[23], Barros and Lang[24]). The morning rain band shift southward through the morning. This morning rain seems due to strong valley wind. The same feature appears in the eastern foothills of the Andes mountain range. It is interesting to see whether the same shift (maybe eastward) appears in the Andes mountain regions. For a suitable size ocean, there is a possibility of an enhanced afternoon rain region. Over the South China Sea near Malaysia between Thailand and Indonesia, there seems to be an enhanced afternoon rain region. The secondary flow due to the strong morning rain in the regions near Thailand and near Indonesia might cause the afternoon enhancement.

Precipitation over islands

In the maritime continent, it was found that the rain total over islands is bigger than over the ocean. The difference is bigger for larger island. On the other

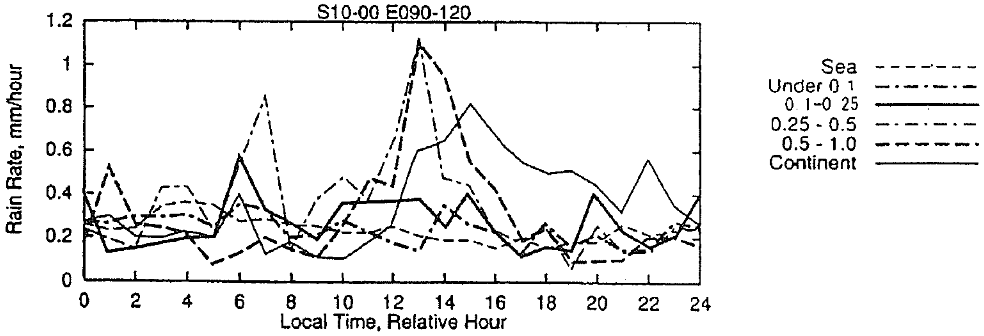

Figure 4.4: Averaged rain rate for each local hour over the maritime continent (10–00S, 120–150E) over two years (1998 and 1999).

hand, for very small islands, such as many islands in the south Pacific Ocean, there is no obvious rain enhancement. Using the six year accumulated data, more accurate characteristics of island rain could be obtained. Even for a small island, rain is thought to be enhanced over islands. Only a few years data was insufficient to detect rain enhancement over islands.

Precipitation in the mid-latitudes

The main target region is around the Japan Islands. In winter, east of Japan is the origin of the strong winter depressions some of which are called 'bomb depression'. TRMM observes part of southern edge of this region. Preliminary study shows that part of the precipitation profile in the east of Japan in winter is similar with that over the Japan Sea. That is, the so-called the Contoured Frequency by Altitude Diagram (CFAD) is very similar. On the other hand, the depression part shows more deep convections. This fact suggests that the precipitation in the east of Japan consists of shallow convection due the warm SST but suppressed by the general subsidence. The comparison of rain estimates from TMI and PR also showed that a systematic discrepancy exists in the east of Japan in winter (Ikai and Nakamura[8]).

4.4 Current TRMM

TRMM is on orbit and in good health except for CERES (Clouds and Earth's Radiant Energy System). The designed life time of TRMM was three years, but the currently expected life time is much longer. Recently, a reentry problem was recognized and it was found that much more fuel is required for a controlled reentry. NASA and NASDA decided to put TRMM satellite in a higher orbit of 402 km. The higher orbit allows the satellite to use less fuel consumption for orbit maintenance. We recognize that the higher orbit causes a sensitivity reduction for the PR. We, however, understood that the primary three year mission of TRMM has successfully conducted, and the longer observation period will contribute much on studies of interannual rain distribution. The current plan is for TRMM to re-enter in September 2004.

4.5 Future global precipitation observation mission

4.5.1 GPM

The U.S. has proposed the Global Precipitation Mission (GPM)[1] which consists of a core satellite and several small satellites (constellation) equipped with small microwave radiometers. An objective of GPM is to observe global precipitation distribution every three hours. The mission should continue over twenty years. A short-term observation of precipitation is strongly demanded by the hydrological research community. The data must also contribute much to the short-term weather forecast by assimilation. The TRMM follow-on satellite which was called ATMOS-A1 in Japan is supposed to the core satellite. The ATMOS-A1 can provide precise and accurate rain measurements including three dimensional precipitation structure for the microwave radiometer rain retrievals. The constellation remedies the limited sampling frequency of ATMOS-A1 and also gives a possibility of studying precipitation evolution. Now, ATMOS-A1 is the core satellite of GPM. The basis of the discussion is the heritage of TRMM, not only the mission collaboration itself but also the mutual understanding between Japan and US. As ATMOS-A1 concept emerged as a TRMM follow-on mission, this base is very natural. TRMM is very successful. TRMM not only improved our understanding of the rain total distribution but also clarified the three-dimensional rain structure of precipitation system. The latter is thanks to the unique power of the TRMM precipitation radar. Considering the fast development of Atmospheric General Circulation Models (AGCM) which are expected to have less than 10 km spatial resolution with non-hydrostatic physics and reproduce directly rain, the climatological data of the three dimensional rain structure must play a crucial role in validation of AGCMs. After confirmation of the TRMM capability, it is very natural that we desire to extend the TRMM-like observations to the whole globe. The TRMM PR is the

---

[1] Websites for TRMM and GPM
Japan Aerospace Exploration Agency (JAXA):
http://www.jaxa.jp/missions/projects/sat/eos/trmm/index_e.html
National Space and Aeronautics Administration (NASA):
http://trmm.gsfc.nasa.gov and http://gpm.gsfc.nasa.gov/

first spaceborne precipitation radar and we could improve the PR capability more based on the PR development heritage. We also noted that new sensors are the strong and essential tools for new findings. Thus, we required a significant improvement in the PR capability. The improvements should be in 1) rain estimate accuracy, 2) sensitivity and 3) liquid/solid hydrometeor discrimination. To meet the requirements, we concluded that the suitable PR is the dual-wavelength radar (DPR).

The current concept of the GPM core satellite is as follows:
Launch year: 2007
Mission life: 5 years
Orbit inclination: 65–70 degrees
Orbit altitude: about 400 km
Core sensors: dual-wavelength radar, TMI-like microwave radiometer (now called GMI)
The roles of Japan and the U.S. could follow the TRMMs path as:
Japan: radar, rocket launching
US: satellite bus, microwave radiometer

4.5.2 Specifications of DPR

Beside the science objectives and operational utilization, we investigated the specifications of DPR. The specifications include: the sensitivity, the swath, the range resolution, etc. We would like to keep nearly the same performance of TRMM PR for the lower frequency radar (14 GHz Ku-band radar). One of the big decision is the nominal range resolution in the Ka-band radar (the higher frequency part of DPR) which was chosen to be 500 m, though the TRMM PR and the 14 GHz radar of DPR has 250 m range resolution. The main reason is to attain the minimum sensitivity of nearly 10 dBZ. We thought that a significant sensitivity improvement is required for the light snow observation and for detection of very light rain or highly rain-attenuated rain signatures. Making half the range resolution gives 6 dB improvement of sensitivity. Though very shallow rain/snow may be missed by the degraded range resolution, such shallow rain/snow is hard to be detected even with 250 m range resolution due to range smearing and ground clutter. The swath of the Ka-band radar was another issue and our choice is about a half of the TRMM PR, that is, about 100 km. There are hardware difficulties to get the same swath as the TRMM PR (220 km). The minimum swath may be the maximum pixel size (about 40 km) of the microwave radiometer onboard the same core satellite. Another requirement may be: the swath should be wide enough to cover the core rain area. Figure 4.5 shows the 30 dBZ core rain area length statistics obtained by the TRMM PR for August 1998 for the rectangular area of 120–150E and 10–20N. One pixel corresponds to about 4.5 km. The figure shows that more

than 95 % of the core rain areas have less than 100 km characteristic length.
The current major parameters of DPR are:
Frequency: 13 and 35 GHz (dual-wavelength)
Range resolution: 250 m (14 GHz), 250/500 m (35 GHz)
Swath: about 220 km (14 GHz), about 100 km (35 GHz)
Horizontal resolution: about 5 km at nadir
Sensitivity: nearly 10 dBZ

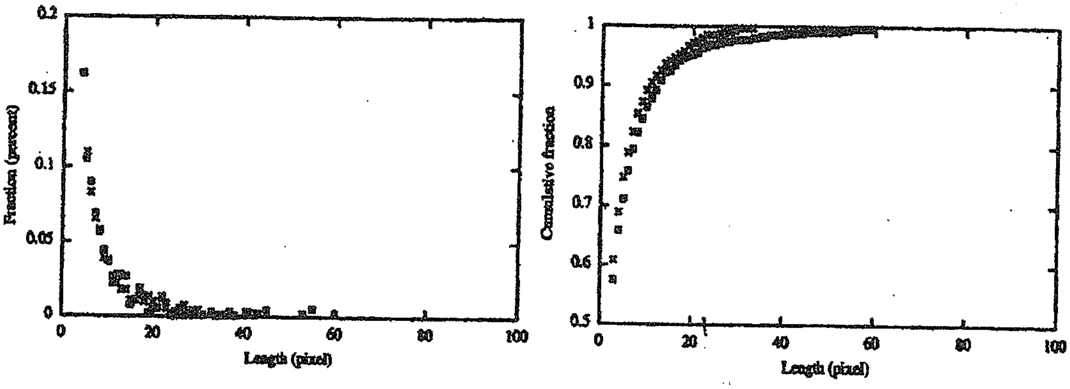

Cumulative distribution (square: along track, cross: cross track)

Figure 4.5: Pixel length of core rain area measured by TRMM PR for 10–20N, 120–150E in August 1998. Above: frequency distribution, below: cumulative distribution.

4.5.3 Algorithms

Algorithm development for DPR is essential for the success of DPR and is also interesting. Even for TRMM, the PR algorithm is complicated, and the DPR algorithm is expected much more complicated. The algorithms are for Ku-only, Ka-only, Ku-Ka combined for Ka-swath, Ku-Ka combined for Ku-swath and others. The Ku-only algorithm may be nearly the same as the TRMM PR algorithm. A similar algorithm for Ka-only may be developed. Since the rain attenuation is 6–7 times bigger than for the Ku-band, the rain attenuation correction effect must be much different from the PR case. The applicability and accuracy of the so-called surface reference technique must also be different. The conventional dual-wavelength technique can be applied for Ku-Ka combined for Ka-swath where both Ku and Ka radar data are available. The dropsize distribution variation issue which is one of the major issues in TRMM PR algorithm will be elucidated. While improvement of rain estimate using DPR was shown by a simulation (Adhikari and Nakamura[25]), we need more experimental studies. Any algorithm for the Ku-Ka combined for the Ku-swath is yet to be proposed. The whole DPR algorithm is yet fully developed either. The combination of DPR and microwave radiometer will also be complicated. Snow estimation from space is another issue. Solid hydrometers have more ambiguities than liquid ones: the size, the density, the shape, melting rate, etc. Though several studies have already been performed, we need much more to study the performance of each algorithm.

4.5.4 Validation

Validation is another issue. Validation strategy is closely related to algorithms. As TRMM PR validation experiences told us that a simple comparison between ground-measured rain and TRMM PR rain estimate is never enough for instantaneous nor climatological rain totals. Each algorithm has its own assumptions/models including rain system structures. The Z-R relationship still remains to be validated. We would like to estimate rainrate in radiometrically consistent manner for both radars and radiometers. Even for this, we again need comprehensive data on the precipitation system. US is now considering the 'supersites'. In Japan, we have one excellent ground validation site which is the Communications Research Laboratory's (CRL) Okinawa Subtropical Environment Remote-Sensing Center. There, CRL installed a fully polarimetric Doppler radar, 400 MHz/1.3 GHz windprofiler radars, a sodar and ground insitu measuring sensors as rain gauges and a disdrometer.

4.6 Future precipitation observation

It is out of question that the satellite observation could be the only major player in global precipitation measurements. The ground-based measurement will still remain important but its role may become as validation. The ground-based observation network will possibly be reduced worldwide due to its labor costs, etc. In the case of TRMM validation, space measurement was so good that the accuracy of ground validation was not sufficient except in a few cases, such as, simultaneous rain observation using a well-calibrated ground-based radars. In fact, it was found that the reasons of many discrepancies between PR and ground-based radar observations which were at first expected for ground validations were on the ground-based radar side. Measurements from space are very clean. They are free from anomalous propagation, topographic effect, etc. In addition, the instruments are generally very well maintained and calibrated. Different sensors give independent rain estimates, which reduce the ambiguity range. It certainly occurred in TRMM, that is, PR and TMI provide independent rain estimates and the similarity of the results confirmed the absolute accuracy of both. Though current global precipitation distribution measurement is a combination of space measurements and ground-based measurements, future precipitation distribution measurements may be based on only space measurements

References

[1] Wetherald, R. T., and S. Manabe, 2002: Simulation of hydrologic changes associated with global warming. J. Geophys. Res., 107(D19), 10.1029/2001JD001195.

[2] Climate Change 2001: The science basis. Eds. J. T. Houghton *et al.*, 2001, Cambridge Univ. Press. 881pp.

[3] Kummerow, C. and coauthors, 2000: The status of the Tropical Rainfall Measuring Mission (TRMM) after two years in orbit, J. Applied Meteor., 39, 1965–1982.

[4] Iguchi, T., T. Kozu, R. Meneghini, J. Awaka, and K. Okamoto, 2000: Rain-profiling algorithm for the TRMM precipitation radar. J. Appl. Meteor., 39, 2038–2052.

[5] Viltard, N., C. Kummerow, W. S. Olson, and Y. Hong, 2000: Combined use of the rdar and radiometer of TRMM to estimate the influence of drop size distributiononrain retrievals. J. Appl. Meteor., 39(12), 2103–2114.

[6] Prabhakara, C., R. Iacovazzi, Jr., and J. M. Yoo, 2002: TRMM precipitation radar and microwave imager observations of convective and stratiform rain over land and their theoretical implications. J. Meteor. Soc. Japan, 80(5), 1183–1197.

[7] Masunaga, H., T. Iguchi, R. Oki, and M. Kachi, 2002: Comparison of rainfall products derived from TRMM microwave imager and precipitation radar. J. Appl. Meteor., 41, 849–862.

[8] Ikai, J. and K. Naikamura, 2003: Comparison of rain rates over the ocean derived from TRMM microwave imager and precipitation radar. J. Atmos. Oceanic Technol., 20, 1709–1726.

[9] Nesbitt, S. W., E. J. Zipser, and D. J. Cecil, 2000: A census of precipitation features in the tropics using TRMM: radar, ice scattering, and lightning observations. J. Climate, 13(23), 4087–4106.

[10] Toracinta, E. R., D. J. Cecil, E. J. Zipser, and S. W. Nesbitt, 2002: Radar, passive microwave, and lightning characteristics of precipitating systems in the tropics. Mon. Wea. Rev., 130(4), 802–824.

[11] Cecil, D. J. and E. J. Zipser, 2002: Reflectivity, ice scattering, and lightning characteristics of hurricane eyewals and rainbands. Part II: Intercomparison of observations. Mon. Wea. Rev., 130(4), 785–801.

[12] Cecil, D. J., E.J.Zipser, and S. W. Nesbitt, 2002: Reflectivity, ice scattering, and lightning characteristics of hurricane eyewals and rainbands. Part I: Quantitative description. Mon. Wea. Rev., 130(4), 769–784.

[13] Adler, R. F., G. J. Huffman, D. T. Bolvin, S. Curtis, and E. J. Nelkin, 2000: Tropical rainfall distribution determined using TRMM combined with other satellite and rain gauge information. J. Appl. Meteor., 39(12), 2007–2023.

[14] Kodama, Y. M. and A. Tamaoki, 2002: A re-examination of precipitation activity in the subtropics and the mid-latitudes based on satellite-derived data. J. Meteor. Soc. Japan, 80(5), 1261–1278.

[15] Adeyewa, Z. D. and K. Nakamura: Validation of TRMM radar rainfall data over major climatic regions in Africa, J. Applied Meteor. 42, 331–347, 2003.

[16] Li, J. and K. Nakamura, 2002: Characteristics of the mirror image of precipitation observed by the TRMM precipitation radar. J. Atmos. Oceanic Technol., 19(2), 145–158.

[17] Short, D and K. Nakamura: TRMM radar observation of shallow precipitation over the tropical oceans, J. Climate, 13 (23), 4107–4124.

[18] Hirose, M. and K. Nakamura, 2002: Spatial and seasonal variation of rain profiles over Asia observed by spaceborne precipitation radar, J. Climate, 15 (23), 3443–3458.

[19] Sengupta, D., B. N. Goswami, and R. Senana, 2001: Coherent intraseasonal oscillations of ocean and atmosphere during the Asian summer monsoon. Geophys. Res. Lett., 28(21), 4127–4130.

[20] Stammer, D., F. Wentz, and C. Gentemann, 2003: Validation of microwave sea surface temperature measurements for climate purposes. J. Climate, 16(1), 73–87.

[21] Kuwagata, T., A. Numaguti, and N. Endo, 2001: Diurnal variation of water vapor over the central Tibetan Plateau. J. Meteor. Soc. Japan, 79(1B), 401–418.

[22] Kuraji, K, K. Punyatrong, and M. Suzuki, 2001: Altitudinal increase in rainfall in the Mae Chaem watershed, Thailand. J. Meteor. Soc. Japan, 79(1B), 353–363.

[23] Ohsawa, T., H. Ueda, T. Hayashi, A. Watanabe, and J. Matsumoto, 2001: Diurnal variations of convective activity and rainfall in Tropical Asia. J. Meteor. Soc. Japan, 79, 333–352.

[24] Barros, A. and T. J. Lang, 2002: Monitoring the monsoon in the Himalaysa: Observations in central Nepal, June 2001. Mon. Wea. Rev., 131, 1408–1427.

[25] Adhikari, N. B. and K. Nakamura, 2003: Simulation-based analysis of rainrate estimation errors in dual-wavelength precipitation radar from space. Radio Sci., 38, 1066, doi:10.1029/2002RS002775.

Chapter 5

Basics of Numerical Simulation

Kazuhisa Tsuboki
Hydrospheric Atmospheric Research Center, Nagoya University
Furo-cho, Chikusa-ku, Nagoya, 464-8601 JAPAN
phone: 052-789-3493, fax: 052-789-3436
tsuboki@rain.hyarc.nagoya-u.ac.jp

5.1 Introduction

A numerical cloud model is indispensable for both understanding clouds and precipitation and their forecasting. Convective clouds and their organized storms are highly complicated systems determined by the fluid dynamics and cloud microphysics. In order to simulate evolution of a convective cloud storm, the calculation should be performed in a large domain with a very high resolution grid to resolve individual clouds. It is also required to formulate cloud physical processes as well as the fluid dynamic and thermodynamic processes accurately. A detailed formulation of cloud physics requires many prognostic variables even in a bulk method such as cloud, rain, ice, snow, hail and so on. Consequently, large-scale parallel computing with a huge memory is necessary for this type of simulation.

Cloud models have been developed and used for study of cloud dynamics and cloud microphysics since 1970's (e.g., Klemp and Wilhelmson, 1978; Ikawa, 1988; Ikawa and Saito, 1991; Xue et al., 1995; Grell et al., 1994). These models employed the non-hydrostatic and compressible equation systems with a fine-grid. Since the computation of cloud models was very large, they have been used for research with a limited domain.

Recent progress in high performance computer, especially a parallel computers is extending the potential of cloud models widely. It enables us to perform simulations of mesoscale storms using a cloud model. For four years, we have been developing a cloud resolving numerical model which was designed for parallel computers including "the Earth Simulator".

The purposes of this study are to develop the cloud resolving model and its parallel computing to simulate convective clouds and their organized storms. Thunderstorms which are organizations of convective clouds produce many types of severe weather: heavy rain, hail, downbursts, tornadoes and so on. The simulation of thunderstorms will clarify the characteristics of dynamics and evolution and will contribute to the mesoscale storm prediction.

The cloud resolving model which we are now developing was named "the Cloud Resolving Storm Simulator" (CReSS). In this paper, we will describe the basic formulation and characteristics of CReSS in detail. Some results of numerical experiments using CReSS will be also presented.

5.2 Description of CReSS

5.2.1 Characteristics of *CReSS*

CReSS is a cloud resolving model to perform a simulation of cloud scale and mesosccale phenomena. The importatnt characteristics of ***CReSS*** are as follows.

- ***CReSS*** is designed for a parallel processor and enables large-scale computation. On the other hand, a serial version of ***CReSS*** can be run on a PC-UNIX.
- Detailed cloud microphysics is implemented. On the other hand, a simulation of the fluid dynamics is possible in the dry configuration.
- It is possible to perform not only a numerical experiment of cloud but also a prediction experiment or a simulation of a real phenomenon with a time dependent lateral boundary condition and real terrain.
- The code is written in the standard FORTRAN77 (with some extension functions) and easy to read. ***CReSS*** can be used on most computers.

The characteristics of ***CReSS*** are summarized here.

- ***CReSS*** is formulated in the non-hydrostatic and compressible equation system.

- The coordinate system is terrain-following in a two or three dimensional geometry.
- The prognostic Variables are
  - three-dimensional velocity components,
  - perturbation of pressure,
  - perturbation of potential temperature,
  - subgrid-scale turbulent kinetic energy (TKE),
  - and mixing ratios for water vapor and several types of hydrometeors.
- Finite difference method for the spatial discretization (explicit both in horizontal and vertical or explicit in horizontal and implicit in vertical).
- Leap-frog time integration with the Asselin time filter for time integration.
- Advection is a forth order scheme.
- Turbulence is the first order closuer and 1.5 order closuer with TKE.
- Divergence damping term for suppress acoustic waves.
- Cloud physics is formulated by a bulk method for cold rain. Prognostic variables are mixing ratios for
  - water vapor,
  - cloud water,
  - rain water,
  - cloud ice,
  - snow
  - and graupel.
- Cloud radiation is not included.
- Numerical smoothing is the second or forth order computational mixing.
- Initial conditions are
  - Horizontal uniform field from upper air sounding or theoretical function.
  - Three-dimensionally inhomogeneous data.
- Lateral boundary conditions are
  - rigid wall, periodic, zero normal gradient,

  - wave-radiating,
  - and externally forced time-dependent condition.

- Cumulus parameterization is not included.
- The n-th layer Ground model and surface process have been implemented. The radiation is calculated in the ground temperature scheme.
- Parallel processing is performed by the Message Passing Interface (MPI).

5.2.2 Basic equations

The coordinate system of CReSS is the Cartesian coordinates in the horizontal (x, y) and a terrain-following curvilinear coordinate in the vertical (ζ) to include the effect of orography. Using height of the model surface $z_s(x, y)$ and top height z_t, the vertical coordinate $\zeta(x, y, z)$ is defined as,

$$\zeta(x, y, z) = \frac{z_t[z - z_s(x, y)]}{z_t - z_s(x, y)}. \tag{5.1}$$

If we use a vertically stretching grid, the effect will be included in (5.1). Computation of CReSS is performed in rectangular linear coordinate transformed from the curvilinear coordinate. The transformed velocity vector will be

$$\begin{aligned} U &= u, && (5.2)\\ V &= v, && (5.3)\\ W &= (uJ_{31} + vJ_{32} + w) \Big/ G^{\frac{1}{2}}. && (5.4) \end{aligned}$$

where variable components of the transform matrix are defined as

$$\begin{aligned} J_{31} &= -\frac{\partial z}{\partial x} = \left(\frac{\zeta}{z_t} - 1\right) \frac{\partial z_s(x, y)}{\partial x} && (5.5)\\ J_{32} &= -\frac{\partial z}{\partial y} = \left(\frac{\zeta}{z_t} - 1\right) \frac{\partial z_s(x, y)}{\partial y} && (5.6)\\ J_d &= \frac{\partial z}{\partial \zeta} = 1 - \frac{z_s(x, y)}{z_t} && (5.7) \end{aligned}$$

and the Jacobian of the transformation is

$$G^{\frac{1}{2}} = |J_d| = J_d \tag{5.8}$$

In this coordinate system, the governing equations of dynamics in CReSS are formulated as follows. The dependent variables of dynamics are three-dimensional velocity components (u, v, w), perturbation pressure p' and perturbation of potential temperature θ'. For convenience, we use the following variables to express the equations.

$$\begin{gathered}\rho^* = G^{\frac{1}{2}}\bar{\rho}, \quad u^* = \rho^* u, \quad v^* = \rho^* v \\ w^* = \rho^* w, \quad W^* = \rho^* W, \quad \theta^* = \rho^* \theta'.\end{gathered}$$

where $\bar{\rho}$ is the density of the basic field which is in the hydrostatic balance.

Using these variables, the momentum equations are

$$\begin{aligned}\frac{\partial u^*}{\partial t} = & \underbrace{-\left(u^*\frac{\partial u}{\partial x} + v^*\frac{\partial u}{\partial y} + W^*\frac{\partial u}{\partial \zeta}\right)}_{\text{[rm]}} \\ & \underbrace{-\left[\frac{\partial}{\partial x}\left\{J_d\left(p' - \alpha Div^*\right)\right\} + \frac{\partial}{\partial \zeta}\left\{J_{31}\left(p' - \alpha Div^*\right)\right\}\right]}_{\text{[am]}} \\ & + \underbrace{\left(f_s v^* - f_c w^*\right)}_{\text{[rm]}} + \underbrace{G^{\frac{1}{2}}\text{Turb.}u}_{\text{[physics]}},\end{aligned} \tag{5.9}$$

$$\begin{aligned}\frac{\partial v^*}{\partial t} = & \underbrace{-\left(u^*\frac{\partial v}{\partial x} + v^*\frac{\partial v}{\partial y} + W^*\frac{\partial v}{\partial \zeta}\right)}_{\text{[rm]}} \\ & \underbrace{-\left[\frac{\partial}{\partial y}\left\{J_d\left(p' - \alpha Div^*\right)\right\} + \frac{\partial}{\partial \zeta}\left\{J_{32}\left(p' - \alpha Div^*\right)\right\}\right]}_{\text{[am]}} - \underbrace{f_s u^*}_{\text{[rm]}} + \underbrace{G^{\frac{1}{2}}\text{Turb.}v}_{\text{[physics]}},\end{aligned} \tag{5.10}$$

$$\begin{aligned}\frac{\partial w^*}{\partial t} = & \underbrace{-\left(u^*\frac{\partial w}{\partial x} + v^*\frac{\partial w}{\partial y} + W^*\frac{\partial w}{\partial \zeta}\right)}_{\text{[rm]}} \underbrace{-\frac{\partial}{\partial \zeta}\left(p' - \alpha Div^*\right)}_{\text{[am]}} \\ & -\rho^* g\left(\underbrace{\frac{\theta'}{\bar{\theta}}}_{\text{[gm]}} - \underbrace{\frac{p'}{\bar{\rho}c_s^2}}_{\text{[am]}} + \underbrace{\frac{q_v'}{\epsilon + \bar{q}_v} - \frac{q_v' + \sum q_x}{1 + \bar{q}_v}}_{\text{[physics]}}\right) + \underbrace{f_c u^*}_{\text{[rm]}} + \underbrace{G^{\frac{1}{2}}\text{Turb.}w}_{\text{[physics]}},\end{aligned} \tag{5.11}$$

where αDiv^* is an artificial divergence damping term to suppress acoustic waves, f_s and f_c are Coriolis terms, c_s^2 is square of the acoustic wave speed, q_v and q_x is mixing ratios of water vapor and hydrometeors, respectively.

The equation of the potential temperature is

$$\frac{\partial \theta^*}{\partial t} = \underbrace{-\left(u^*\frac{\partial \theta'}{\partial x}+v^*\frac{\partial \theta'}{\partial y}+W^*\frac{\partial \theta'}{\partial \zeta}\right)}_{\textbf{[rm]}} \underbrace{-\bar{\rho} w\frac{\partial \bar{\theta}}{\partial \zeta}}_{\textbf{[gm]}} + \underbrace{G^{\frac{1}{2}}\text{Turb}.\theta}_{\textbf{[physics]}} + \underbrace{\rho^*\text{Src}(\theta}_{\textbf{[physics]}},12) \quad (5.12)$$

and the pressure equation is

$$\begin{aligned}\frac{\partial G^{\frac{1}{2}}p'}{\partial t} &= \underbrace{-\left(J_3u\frac{\partial p'}{\partial x}+J_3v\frac{\partial p'}{\partial y}+J_3W\frac{\partial p'}{\partial \zeta}\right)}_{\textbf{[rm]}} + \underbrace{G^{\frac{1}{2}}\bar{\rho} g w}_{\textbf{[am]}} \\ & \underbrace{-\bar{\rho}c_s^2\left(\frac{\partial J_3u}{\partial x}+\frac{\partial J_3v}{\partial y}+\frac{\partial J_3W}{\partial \zeta}\right)}_{\textbf{[am]}} + \underbrace{G^{\frac{1}{2}}\bar{\rho}c_s^2\left(\frac{1}{\theta}\frac{d\theta}{dt}-\frac{1}{Q}\frac{dQ}{dt}\right)}_{\textbf{[am]}} \quad (5.13)\end{aligned}$$

where Q is diabatic heating, terms of "Turb." is a physical process of the turbulent mixing and term of "Src." is source term of potential temperature.

Since the governing equations have no approximations, they will express all type of waves including acoustic waves, gravity waves and Rossby waves. These waves have very wide range of phase speeds. The fastest wave is the acoustic wave. Although it is unimportant in meteorology, its speed is very large in comparison with other waves and limits the time increment of integration. We, therefore, integrate the terms related to the acoustic waves and other terms with different time increments. In the equations (5.9)~(5.13), **[rm]** is indicates terms which are related to rotational mode (the Rossby wave mode), **[gm]** the divergence mode (gravity wave mode), and **[am]** the acoustic wave mode, respectively. Terms of physical processes are indicated by **[physics]**.

5.2.3 Computational scheme and parallel processing strategy

In numerical computation, a finite difference method is used for the spatial discretization. The coordinates are rectangular and dependent variables are set on a staggered grid: the Arakawa-C grid in horizontal and the Lorenz grid in vertical (Fig.5.6). The coordinates x, y, ζ are defined at the faces of the grid boxes. The velocity components (u, v, w) are defined at the same points of the coordinates x, y, ζ, respectively. The metric tensor J_{31} is evaluated at a half interval below the u point and J_{32} at a half interval below the v point. All scalar variables (p', θ', q_v, q_x), the metric tensor J_d and the transform Jacobian are defined at the center of the grid boxes. In the computation, an averaging operator is used to evaluate dependent variables at the same points. All output variables are obtained at the scalar points.

As mentioned in the previous sub-section, the governing equations include all types of waves and the acoustic waves severely limits the time increment. In order to avoid this difficulty, CReSS adopted the mode-splitting technique (Klemp and Wilhelmson, 1978) for time integration. In this technique, the terms related to the acoustic waves in (5.9) $\sim$ (5.13) are integrated with a small time increment ($\Delta\tau$) and all other terms are with a large time increment (Δt). Figure 5.6 shows a schematic representation of the time integration of the mode-splitting technique. CReSS has two options in the small time step integration; one is an explicit time integration both in horizontal and vertical and the other is explicit in horizontal and implicit in vertical. In the latter option, p' and w are solved implicitly by the Crank-Nicolson scheme in the vertical. With respect to the large time step integration, the leap-frog scheme with the Asselin time filter is used for time integration. In order to remove grid-scale noise, the second or forth order computational mixing is used.

A large three-dimensional computational domain (order of 100 km) is necessary for the simulation of a thunderstorm with very high resolution (order of less than 1km). For parallel computing of this type, CReSS adopts a two dimensional domain decomposition in the horizontal (Fig.5.6). Parallel processing is performed by the Message Passing Interface (MPI). Communications between the individual processing elements (PEs) are performed by data exchange of the outermost two grids.

The performance of the parallel processing in CReSS was tested by a simulation whose grid size was 67 × 67 × 35 on HITACHI SR2201. With increase of the number of PEs, the computation time decreased almost linearly (Fig.5.6). The efficiency was almost 0.9 or more if the number of PEs was less than 32. When the number of PEs was 32, the efficiency decreased significantly. Because the number of grids was too small to use the 32 PEs. The communication between PEs became relatively large. The results of the test showed a sufficiently high performance of the parallel computing by CReSS.

5.2.4 Initial and boundary conditions

Several types of initial and boundary conditions are optional in CReSS. For a numerical experiment, a horizontally uniform initial field provided by a sounding profile will be used with an initial disturbance of a thermal bubble or random noise. Optional boundary conditions are rigid wall, periodic, zero normal-gradient, and wave-radiation type of Orlanski (1976).

CReSS has an option of being nested within a coarse-grid model and performs a prediction experiment. In this option, the initial field is provided by interpolation of grid point values and the boundary condition is provided by the coarse-grid model.

izontal grid spacing of order of 100 m or less. In order to simulate the supercell and the associated tornado by a cloud model, a huge memory and high speed CPU are indispensable.

To overcome this difficulty, Wicker and Wilhelmson (1995) used an adaptive grid method to simulate tornado-genesis. The grid spacing of the fine mesh was 120 m. They simulated a genesis of tornadic vorticity. Grasso and Cotton (1995) also used a two-way nesting procedure in a cloud model and simulated tornadic vorticity. These simulations used a two-way nesting technique. Nesting methods include complication of the communication between the coarse-grid model and the fine-mesh model through the boundary. On the contrary, the present research does not use any nesting methods. We attempted to simulate both the supercell and the tornado using a uniform grid. In this type of simulation, there is no complication of the boundary communication. The computational domain of the present simulation was about 50 × 50 km and the grid spacing was 100 m. The integration time was about 2 hours.

The basic field was given by a sounding at Shionomisaki, Japan at 00 UTC, 24 September 1999 (Fig.5.6). The initial perturbation was given by a warm thermal bubble placed near the surface. It caused an initial convective cloud. After one hour from the initial time, a quasi-stationary super cell was simulated by CReSS (Fig.5.6). The hook-shaped precipitation area and the bounded weak echo region (BWER) which are characteristic features of supercells were formed in the simulation. An intense updraft occurred along the surface flanking line. At the central part of BWER or of the updraft, a tornadic vortex was formed at 90 minutes from the initial time.

The close view of the central part of the vorticity (Fig.5.6) shows closed contours. The diameter of the vortex is about 500 m and the maximum of vorticity is about 0.1 s^{-1}. This corresponds well to the observed tornado. The pressure perturbation (Fig.5.6) also shows closed contours which corresponds to those of vorticity. This indicates that the flow of the vortex is in cyclostrophic balance.

The vertical cross section of the vortex (Fig.5.6) shows that the axis of the vorticity and the associated pressure perturbation is inclined to the left hand side and extends to a height of 2 km. At the center of the vortex, the downward extension of cloud is simulated.

While this is a preliminary result of the simulation of the supercell and tornado, some characteristic features of the observation were simulated well. The important point of this simulation is that both the supercell and the tornado were simulated in the same grid size. The tornado was produced purely by the physical processes formulated in the model. A detailed analysis of the simulated data will provide important information about tornado-genesis within the supercells.

5.5 Simulation of squall line

A squall line is a significant mesoscale convective system. It is usually composed of an intense convective leading edge and a trailing stratiform region. An intense squall line was observed by three Doppler radars on 16 July 1998 over China during the intensive field observation of GAME / HUBEX (the GEWEX Asian Monsoon Experiment / Huaihe River Basin Experiment). The squall line extended from the northwest to the southeast with a width of a few tens kilometers and moved northeastward at a speed of 11 m s^{-1}. Radar observation showed that the squall line consisted of intense convective cells along the leading edge. Some of cells reached a height of 17 km. Rear-inflow was present at a height of 4 km which descended to cause intense lower-level convergence at the leading edge. After the squall line passed over the radar sites, stratiform precipitation extended behind the convective leading edge.

The experimental design of the simulation experiment using CReSS is as follows. Both the horizontal and vertical grid sizes were 300 m within a domain of 170 km × 120 km. Cloud microphysics was the cold rain type. The boundary condition was the wave-radiating type. An initial condition was provided by a dual Doppler analysis and sounding data. The inhomogeneous velocity field within the storm was determined by the dual Doppler radar analysis directly while that of outside the storm and thermodynamic field were provided by the sounding observation. Mixing ratios of rain, snow and graupel were estimated from the radar reflectivity while mixing ratios of cloud and ice were initially set to zero. A horizontal cross section of the initial field is shown in Fig.5.6.

The simulated squall line extending from the northwest to the southeast moved northeastward (Fig.5.6). The convective leading edge of the simulated squall line was maintained by the replacement of new convective cells and moved to the northeast. This is similar to the behavior of the observed squall line. Convective cells reached a height of about 14 km with large production of graupel above the melting layer. The rear-inflow was also simulated as the observation. A stratiform region extended with time behind the leading edge. Cloud extended to the southwest to form a cloud cluster. The result of the simulation experiment showed that CReSS successfully simulated the development and movement of the squall line.

5.6 Summary and future plans

We are developing a cloud resolving numerical model, CReSS, for numerical experiments and simulations of clouds and storms. Parallel computing is indispensable for large-scale simulations. In this paper, we described the basic formulations and important characteristics of CReSS. We also showed some results of the numerical experiments: Kelvin-Helmholtz billows, mountain waves, a tornado within a supercell and a squall line. These results showed that the CReSS has a capability to simulate thunderstorms and related phenomena.

In the future, we will include detailed cloud microphysical processes which resolve size distributions of hydrometeors. The parameterization of turbulence is another important physical process in cloud. The large eddy simulation is expected to be used in the model. We will develop CReSS to enable two-way nesting within a coarse-grid model for a simulation of a real weather system. Four-dimensional data assimilation of Doppler radar is also our next target, because initial conditions are essential for a simulation of mesoscale storms.

CReSS can be used for numerical experiments of clouds and storms. CReSS has been tested on a several computers: HITACHI SR2201, HITACHI SR8000, Fujitsu VPP5000, NEC SX4. We expect that CReSS will be run on the Earth Simulator and make a large-scale parallel computation to simulate a details of clouds and storms.

Acknowledgements

This study is a part of a project led by Professor Kamiya, Aichi Gakusen University. The project is supported by the Research Organization for Information Science and Technology (RIST). The simulations and calculations of this work were performed using HITACHI S3800 super computer and SR8000 computer at the Computer Center, the University of Tokyo and Fujitsu VPP5000 at the Computer Center, Nagoya University. The Grid Analysis and Display System (GrADS) developed at COLA, University of Maryland was used for displaying data and drawing figures.

References

Cotton, W. R., G. J. Tripoli, R. M. Rauber and E. A. Mulvihill, 1986: Numerical simulation of the effects of varying ice crystal nucleation rates and aggregation processes on orographic snowfall. *J. Climate Appl. Meteor.*, **25**, 1658–1680.

Grasso, L. D., and W. R. Cotton, 1995: Numerical simulation of a tornado vortex. *J. Atmos. Sci.*, **52**, 1192–1203.

Grell, G., J. Dudhia and D. Stauffer, 1994: A description of the fifth-generation of the Penn State/NCAR mesoscale model (MM5). *NCAR Technical Note*, 138pp.

Ikawa, M., 1988: Comparison of some schemes for nonhydrostatic models with orography. *J. Meteor. Soc. Japan*, **66**, 753–776.

Ikawa, M. and K. Saito, 1991: Description of a nonhydrostatic model developed at the Forecast Research Department of the MRI. *Technical Report of the MRI*, **28**, 238pp.

Klaassen, G. P. and W. R. Peltier, 1985: The evolution of finite amplitude Kelvin-Helmholtz billows in two spatial dimensions. *J. Atmos. Sci.*, **42**, 1321–1339.

Klemp, J. B., and R. B. Wilhelmson, 1978: The simulation of three-dimensional convective storm dynamics. *J. Atmos. Sci.*, **35**, 1070–1096.

Klemp, J. B., and R. Rotunno, 1983: A study of the tornadic region within a supercell thunderstorm. *J. Atmos. Sci.*, **40**, 359–377.

Lin, Y.-L., R. D. Farley and H. D. Orville, 1983: Bulk parameterization of the snow field in a cloud model. *J. Climate Appl. Meteor.*, **22**, 1065–1092.

Louis, J. F., M. Tiedtke and J. F. Geleyn, 1981: A short history of the operational PBL parameterization at ECMWF. *Workshop on Planetary Boundary Layer Parameterization 25–27 Nov. 1981*, 59–79.

Murakami, M., 1990: Numerical modeling of dynamical and microphysical evolution of an isolated convective cloud — The 19 July 1981 CCOPE cloud. *J. Meteor. Soc. Japan*, **68**, 107–128.

Murakami, M., T. L. Clark and W. D. Hall 1994: Numerical simulations of convective snow clouds over the Sea of Japan; Two-dimensional simulations of mixed layer development and convective snow cloud formation. *J. Meteor. Soc. Japan*, **72**, 43–62.

Orlanski, I., 1976: A simple boundary condition for unbounded hyperbolic flows. *J. Comput. Phys.*, **21**, 251–269.

Smagorinsky, J., 1963: General circulation experiments with the primitive equations. I. The basic experiment. *Mon. Wea. Rev.*, **91**, 99–164.

Weisman, M. L., and J. B. Klemp, 1982: The dependence of numerically simulated convective storms on vertical wind shear and buoyancy. *Mon. Wea. Rev.*, **110**, 504–520.

Weisman, M. L., and J. B. Klemp, 1984: The structure and classification of numerically simulated convective storms in directionally varying wind shears. *Mon. Wea. Rev.*, **112**, 2478–2498.

Wicker, L. J., and R. B. Wilhelmson, 1995: Simulation and analysis of tornado development and decay within a three-dimensional supercell thunderstorm. *J. Atmos. Sci.*, **52**, 2675–2703.

Wilhelmson, R. B., and J. B. Klemp, 1978: A numerical study of storm splitting that leads to long-lived storms. *J. Atmos. Sci.*, **35**, 1974–1986.

Xue, M., K. K. Droegemeier, V. Wong, A. Shapiro and K. Brewster, 1995: Advanced Regional Prediction System, Version 4.0. *Center for Analysis and Prediction of Storms, University of Oklahoma*, 380pp.

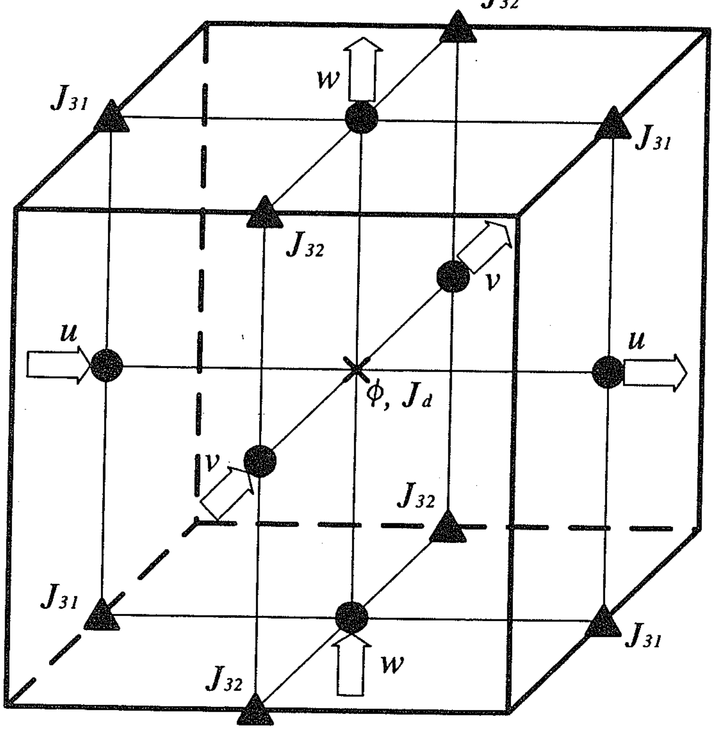

Figure 5.1: Structure of the staggered grid and setting of dependent variables.

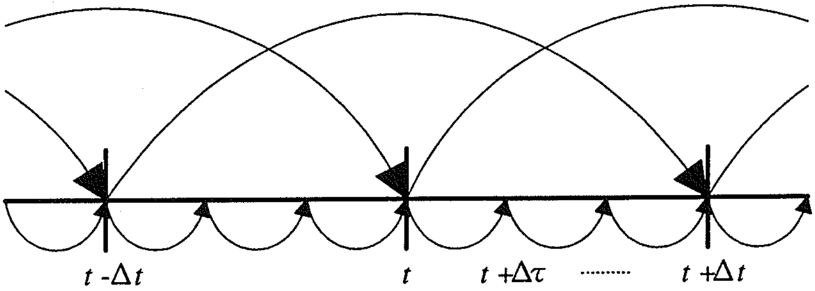

Figure 5.2: Schematic representation of the mode-splitting time integration method.

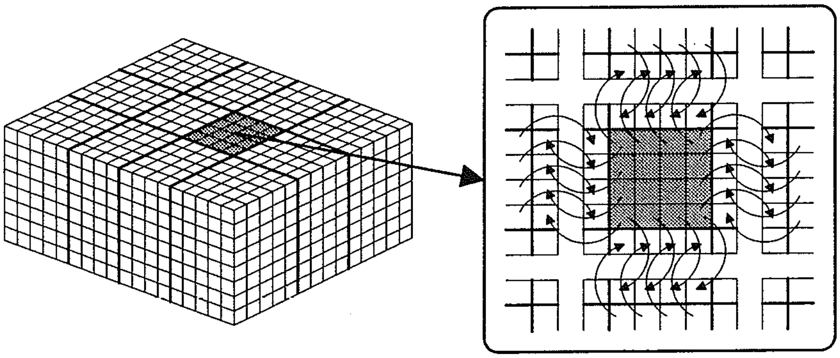

Figure 5.3: Schematic representation of the two-dimensional domain decomposition and the communication strategy for the parallel computing.

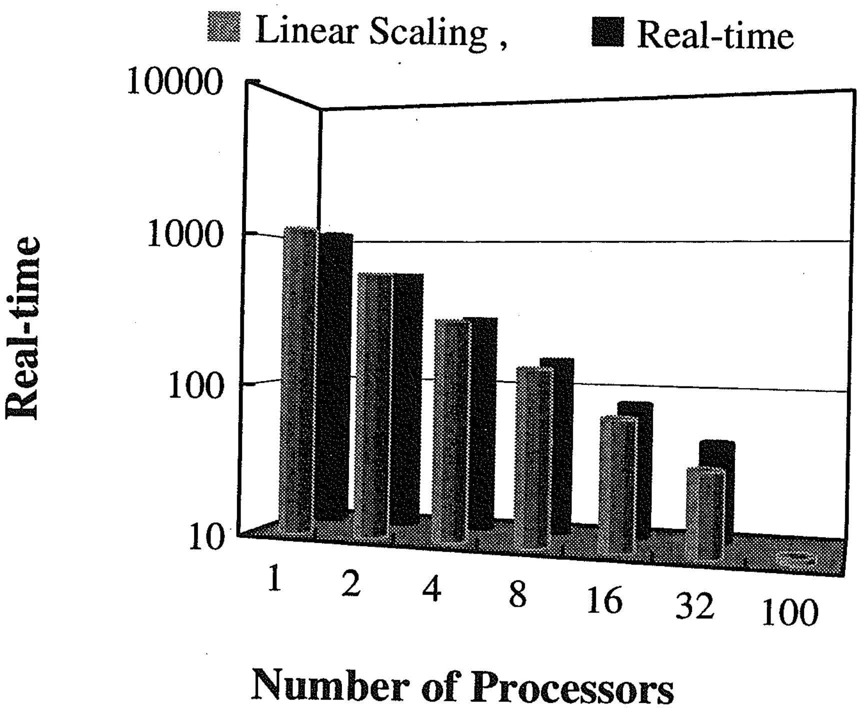

Figure 5.4: Computation time of parallel processing of a test experiment. The model used in the test had 67×67×35 grid points and was integrated for 50 steps on HITACHI SR2201.

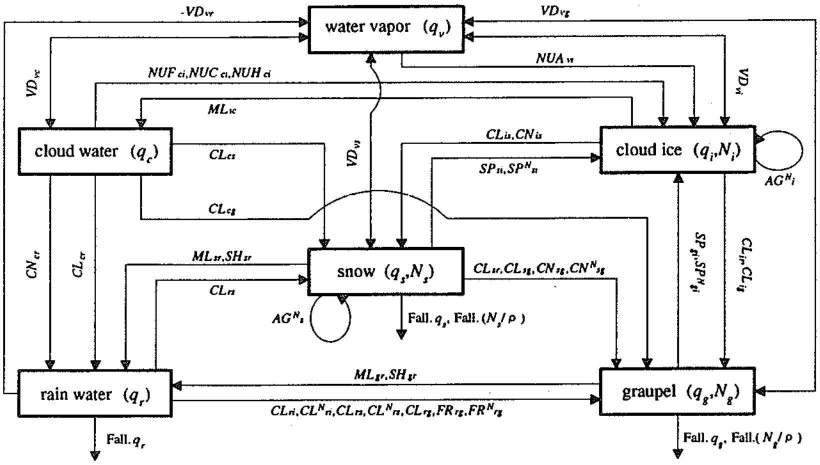

Figure 5.5: Diagram describing of water substances and cloud microphysical processes in the bulk model.

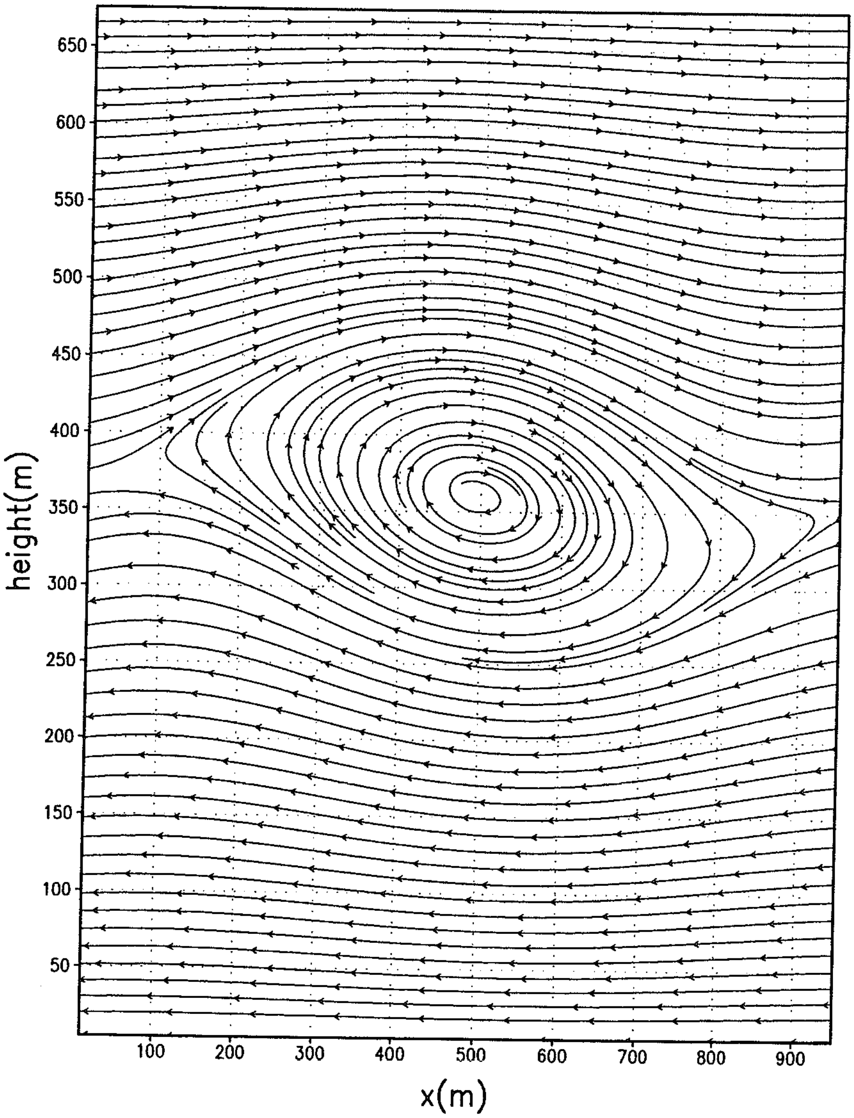

Figure 5.6: Stream lines of the Kelvin-Helmholtz billow at 240 seconds from the initial simulated in the two-dimensional geometry.

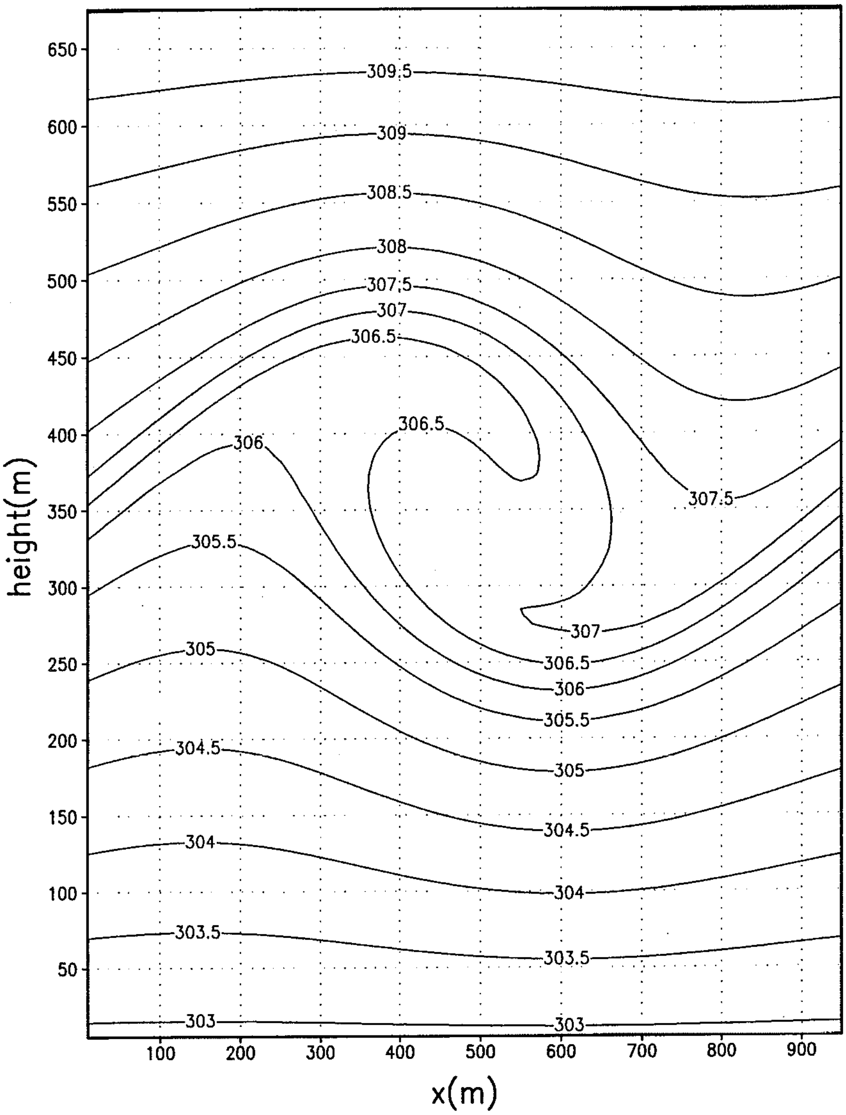

Figure 5.7: Same as Fig.5.6, but for potential temperature.

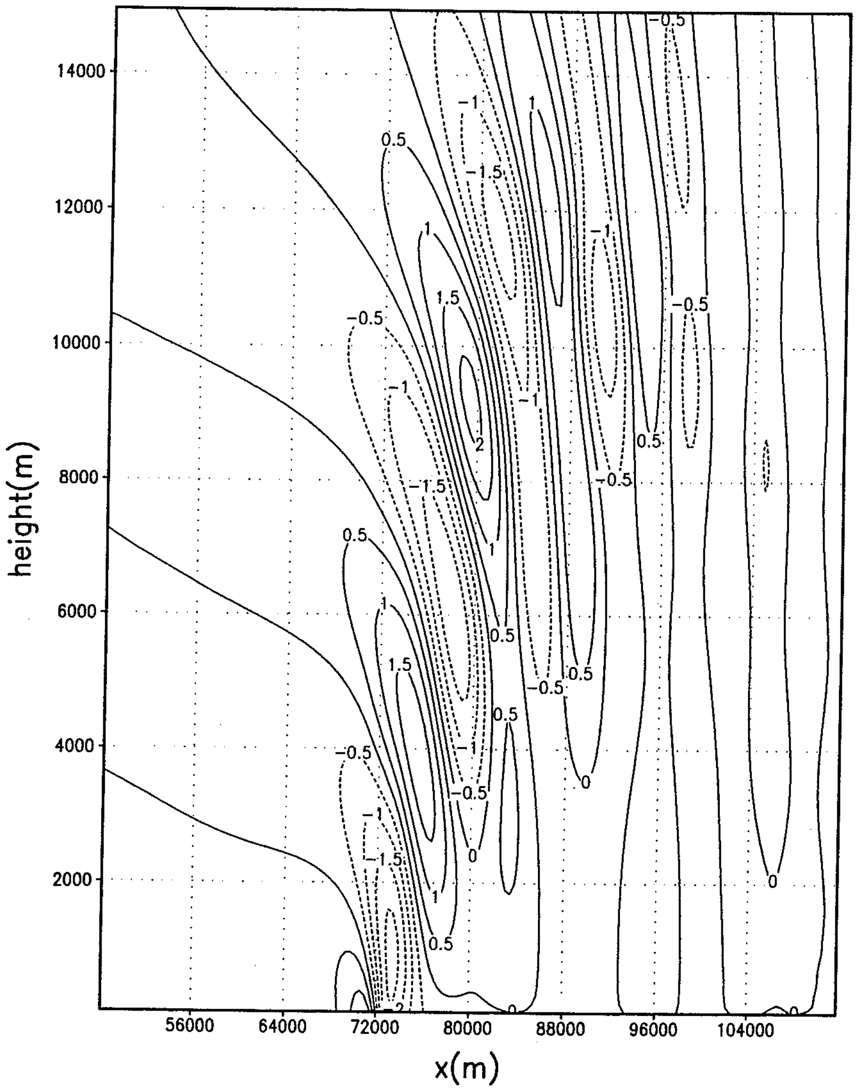

Figure 5.8: Vertical velocity at 9000 seconds from the initial obtained by the mountain wave experiment.

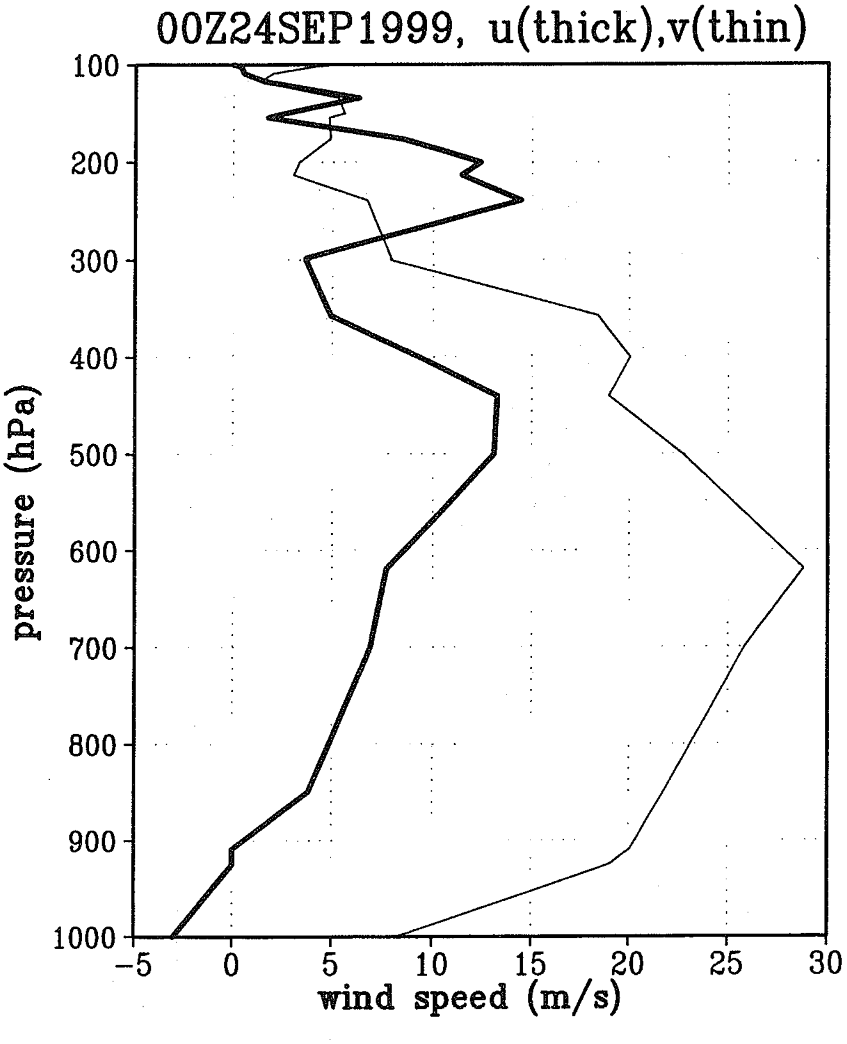

Figure 5.9: Vertical profiles of zonal component (thick line) and meridional component (thin line) observed at Shionomisaki at 00 UTC, 24 September 1999.

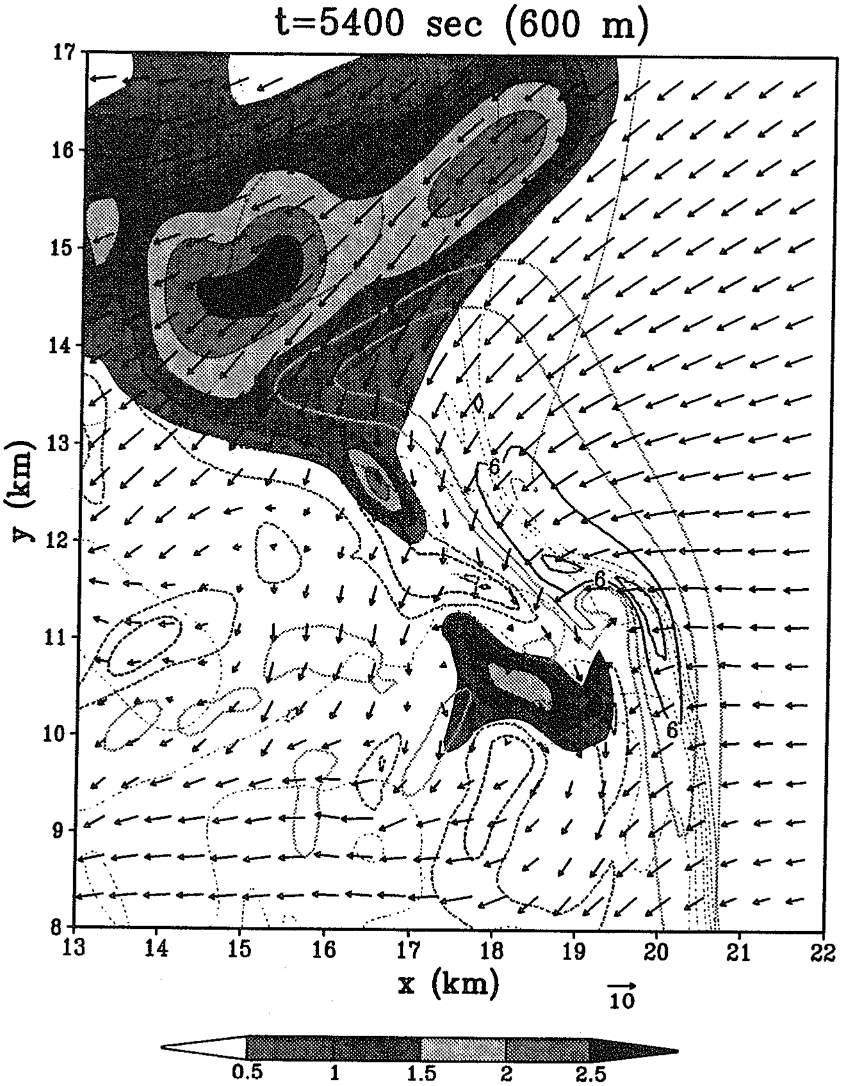

Figure 5.10: Horizontal display at 600 m of the simulated supercell at 5400 seconds from the initial. Mixing ratio of rain (gray scales, g kg^{-1}), vertical velocity (thick lines, m s^{-1}), the surface potential temperature at 15 m (thin lines, K) and horizontal velocity vectors.

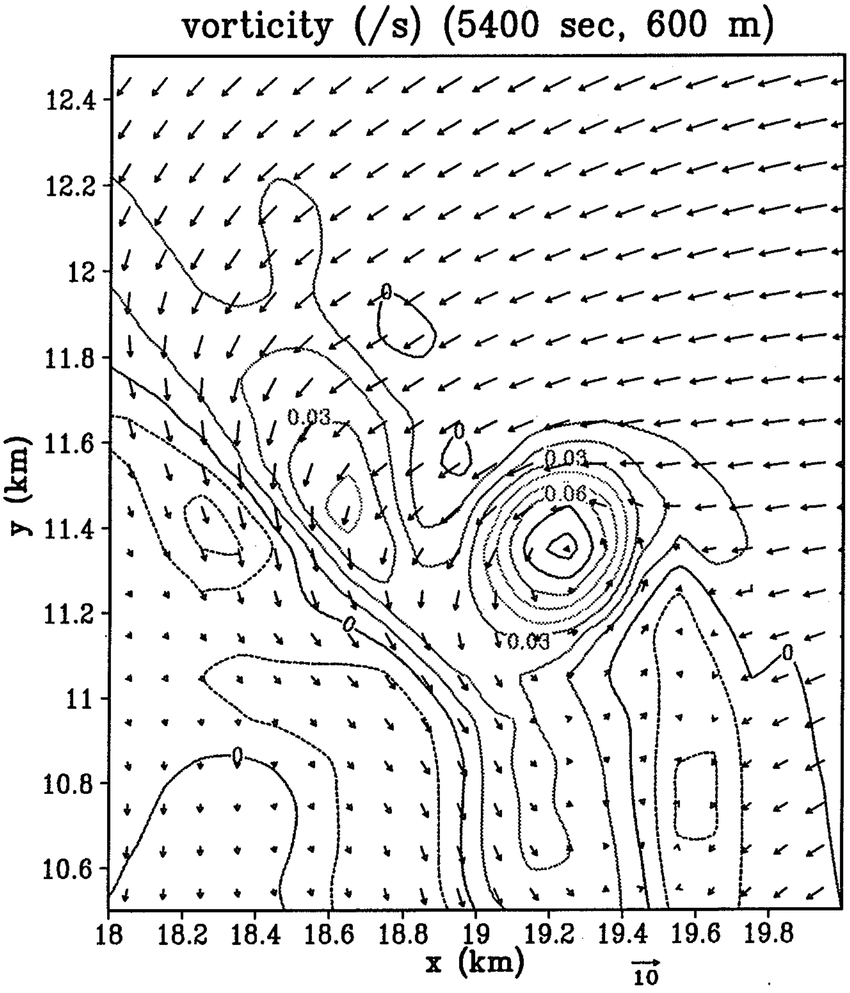

Figure 5.11: Close view of the simulated tornado within the supercell. The contour lines are vorticity (s^{-1}) and the arrows are horizontal velocity. The arrow scale is shown at the bottom of the figure.

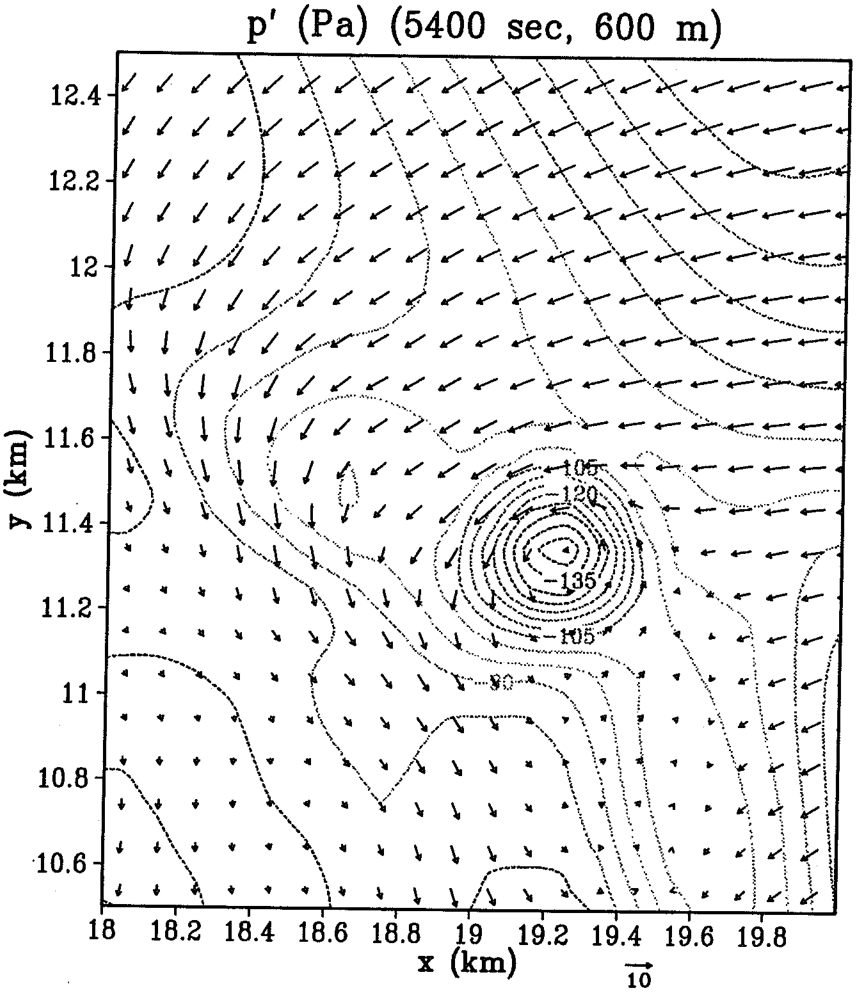

Figure 5.12: Same as Fig.5.6, but for pressure perturbation.

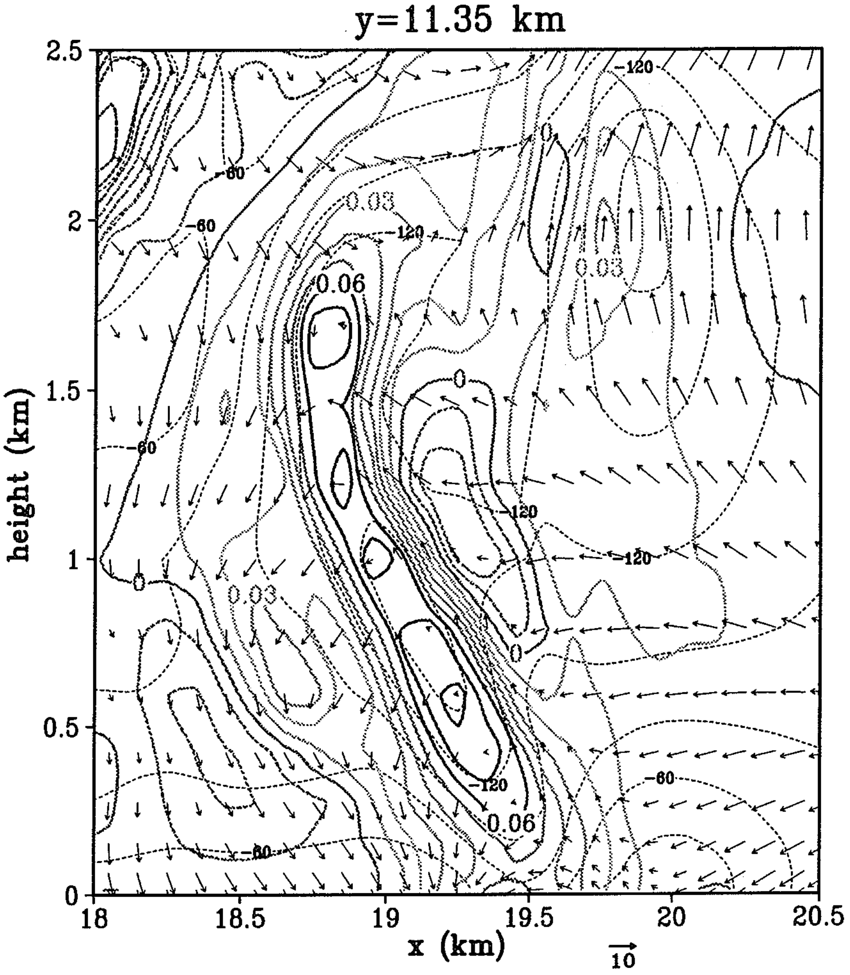

Figure 5.13: Vertical cross section of the simulated tornado. Thick lines are vorticity (s^{-1}), dashed lines are pressure perturbation and arrows are horizontal velocity.

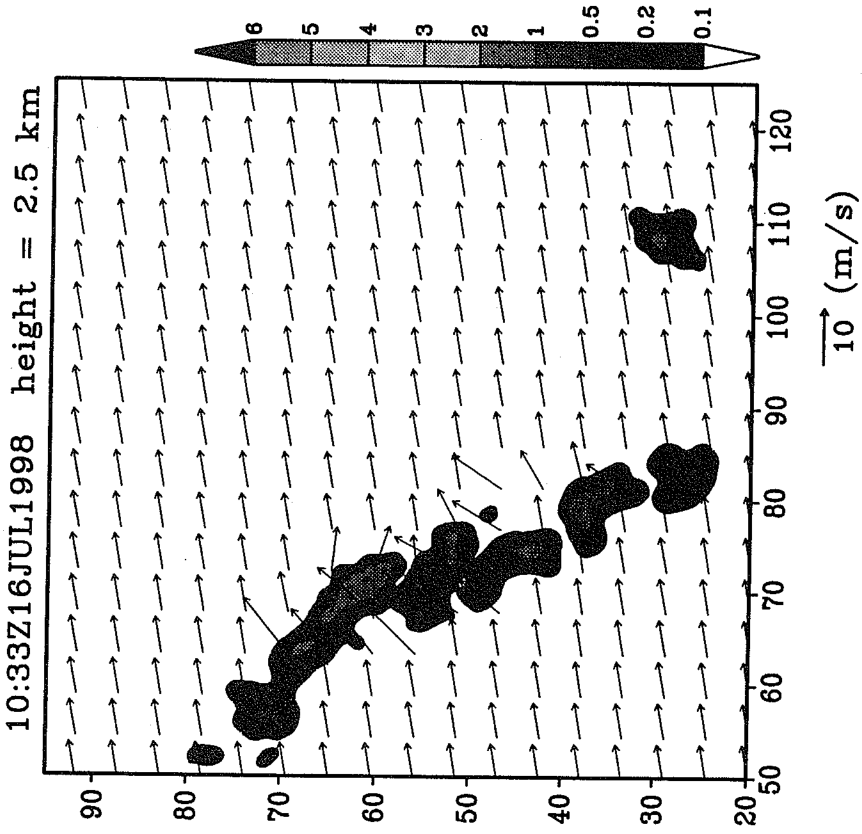

Figure 5.14: Horizontal cross section of the initial field at a height of 2.5km at 1033 UTC, 16 July 1998. The color levels mixing ratio of rain (g kg^{-1}). Arrows show the horizontal velocity obtained by the dual Doppler analysis and sounding.

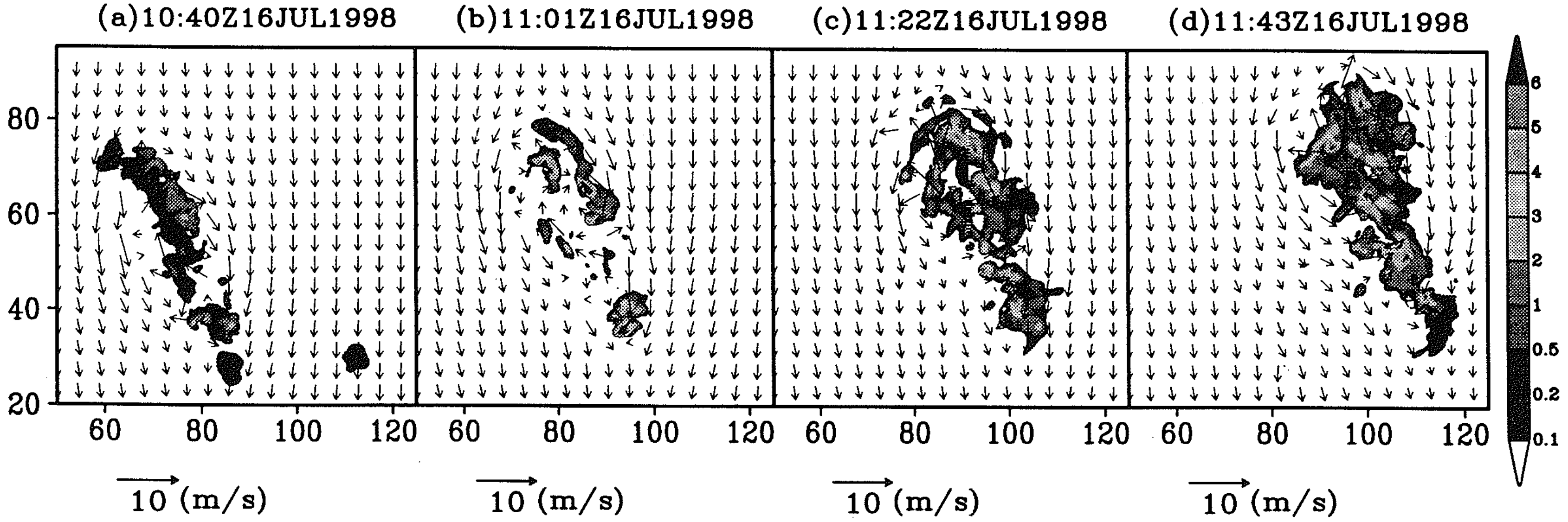

Figure 5.15: Time series of horizontal displays (upper row) and vertical cross sections (lower row) of the simulated squall line. Color levels indicate total mixing ratio (g kg^{-1}) of rain, snow and graupel. Contour lines indicate total mixing ratio (0.1, 0.5, 1, 2 g kg^{-1}) of cloud ice and cloud water. Arrows are horizontal velocity.

Chapter 6

Land Surface Processes

Kenji Tanaka
Disaster Prevention Research Institute, Kyoto University
Gokasho, Uji, Kyoto, 611-0011, JAPAN
phone: +81-774-38-4246, fax: +81-774-32-3093
e-mail: tanaka@wrcs.dpri.kyoto-u.ac.jp

6.1 Introduction

In this chapter, fundamental and important features of land surface processes are briefly documented. Then, some aspects of the land surface scheme are described to see how these processes are expressed in the so-called SVAT(Soil-Vegetation-Atmosphere Transfer) schemes. Also, field measurement of the land surface processes currently implemented in the Lake Biwa Basin Japan is introduced to see how the energy budget is observed and how these datasets are utilized to develop and improve the land surface scheme. Before starting this lecture, I want to introduce the description by Bill Crosson (NASA MSFC) to get a basic idea about what land-surface processes are.

"Land surface processes are those associated with the exchange of water and energy between the land surface and the atmosphere and are, therefore, integral components of hydrologic and atmospheric sciences."

6.2 Basic components of land surface processes

Roughly speaking, land surface processes consist of three budget equations - radiation budget, energy budget, and water budget. Here, important terms which appear in these budget equations are defined.

6.2.1 Radiation budget

All surfaces receive short-wave radiation during daylight and exchange long-wave radiation continuously with the atmosphere. Here, short-wave radiation means the radiation emitted from the sun, and this radiation has a wavelength interval less than 4μ m. Long-wave radiation means the radiation emitted from the earth's surface or atmosphere, and this radiation has a wavelength interval greater than 4μ m.

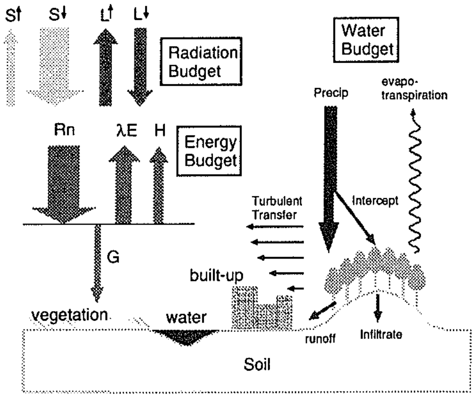

Figure 6.1: Three budgets in land-surface processes

$$R_n = (1 - \alpha)S_d + L_d - L_u \tag{6.1}$$

R_n is the net amount of radiation received by the surface. S_d is the amount of downward short-wave radiation reaching the surface. α is reflectance (albedo) of the surface. L_d is downward long-wave radiation emitted from the atmosphere/cloud. L_u is upward long-wave radiation emitted from the surface.

If the radiation budget is treated in a sophisticated SVAT scheme like SiB [11] which describes physiological characteristics of vegetation, S_d is partitioned into two wavelength intervals, visible(VIS) and near-infrared(NIR), as the spectral properties of green leaves exhibit a sharp change at around 0.72 μ m. S_d is further partitioned into diffuse and direct beam components because the absorption and transmittance coefficients of vegetation canopies are highly dependent upon the angle of the incident flux.

6.2.2 Energy budget

The radiative energy absorbed from the sun and the atmosphere is partitioned into fluxes of sensible, latent, and gound heat, and this partitioning (redistribution of absorbed energy) is strongly dependent on both the land cover characteristics and its hydrological state.

$$R_n = H + \lambda E + G \tag{6.2}$$

H is the energy flux exchanged between surface and atmosphere, and it directly warms or cools the lower part of the atmosphere. E is water vapor flux exchanged between surface and atmosphere. As water changes from one form to another (liquid to gas, solid to liquid, etc.), there is an associated transfer of energy. The energy absorved for evaporating water is released when water vapor condenses to form raindrops. In this sense, latent heat warms the middle part of the atmosphere. In the case of snow processes, additional energy is needed to melt snow (sublimation). G is the energy flux absorbed/released to warm/cool the surface itself. The energy for soil moisture freezing/melting is included in G. This term produces a time lag between radiation budget and energy budget.

6.2.3 Water budget

Water is exchanged between the atmosphere and the land surface through the processes of precipitation, evaporation, and transpiration. Also water is exchanged between the land surface and ocean/lake through runoff processes.

$$\Delta S = P - E - R \tag{6.3}$$

P is precipitation (rain/snow) input from the atmosphere. E is water vapor flux by evaporation and transpiration. R is runoff flux by river system and ground water system. ΔS is change in the surface water (interception/snowpack) and soil moisture storage.

When the surface is expressed by more than two components (vagetation and soil, etc.), the above three budget equations should be taken into account for each component.

6.3 Heterogeneity and "mosaic" approach

At the grid resolution of atmospheric models, land-surfaces are very heterogeneous. This can be easily understood by looking at maps of soil, vegetation, topography, land-use patterns, etc. Figure 6.2 shows a land-use map around the Lake Biwa Basin, Japan. The domain of this area is 1 degree × 1 degree. Water surface and urbanized area are shown in white and blue color respectively.

In the NWP(Numerical Weather Prediction) models and GCM(Global Climate Model), the size of grid element is usually decided from the need of high accuracy and high computational efficiency.

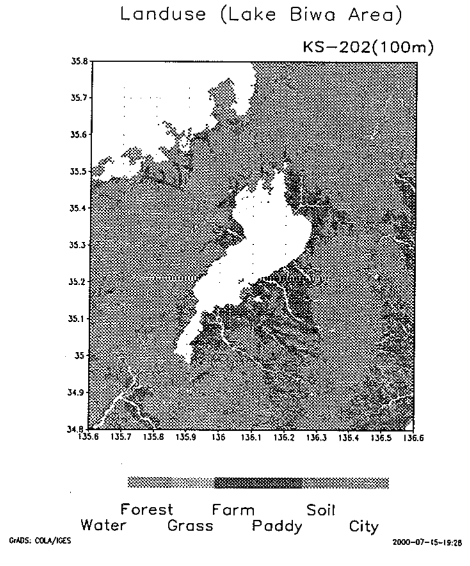

Figure 6.2: Land-use of the Lake Biwa Basin

If the grid size is selected to eliminate the heterogeneity of land-surface, in another words, if the grid size is selected according to the 'minimum' size of land-use patch, it will become extremely small, and the number of grid elements will become enormous. Therefore, the problem of heterogeneity, off course, must be treated in LSS (Land-Surface Scheme).

One solution is to find effective parameters to generate representative values of the whole grid square. A great deal of work has already been done on aggregation research (Michaud and Shuttleworth, 1997[9]). Sometimes such a parameter aggregation is not possible because of high non-linearity between parameters and resulting fluxes.

Another way is to apply a "mosaic" type parameterization (Avissar and Pielke, 1989[1] ; Kimura, 1989[8]). Such approach independently couples each land-use patch of the grid element to the atmosphere. The grid averaged surface fluxes are obtained by averaging the surface fluxes over each land-use weighted by its fractional area.

The SiBUC (Simple Biosphere including Urban Canopy)[15] model, which was developed at DPRI Kyoto University, uses a "mosaic" approach to incorporate all kinds of land-use into LSS. In the SiBUC model, the surface of each grid area is divided into three landuse categories and five components.

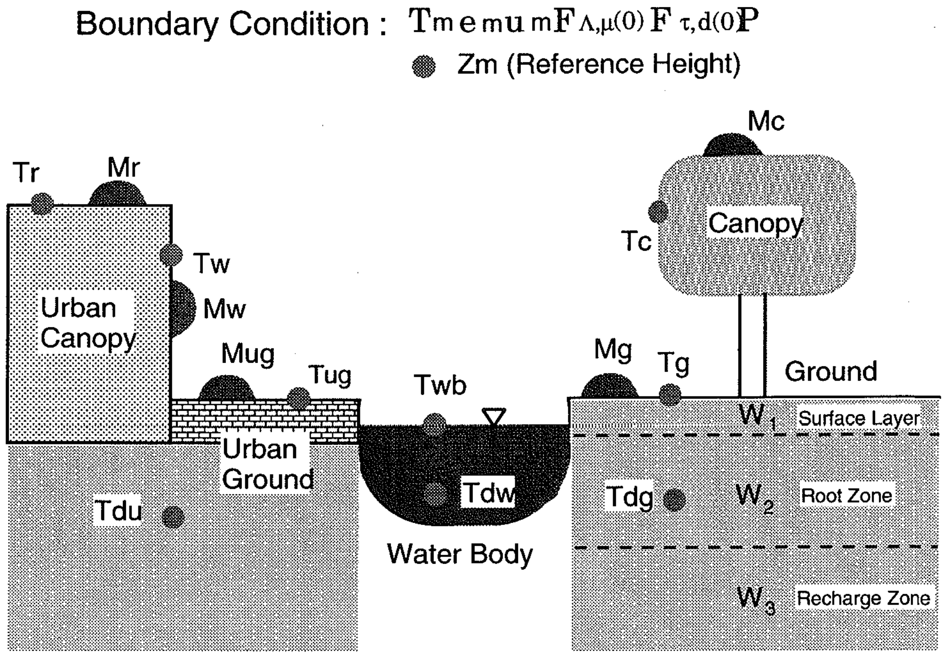

Figure 6.3: Schematic image of surface elements in SiBUC.

- **green area (vegetation canopy(c), ground(g))**
  This is a natural land surface area (forest, grassland, bare soil, etc.), and it is usually treated in most LSS. For the vegetation scheme, SiB[11] is adopted. Some modification from the original SiB was done.

- **urban area (urban canopy(uc), urban ground(ug))**
  This is an artificial unpermeable surface (buildings, houses, pavement, etc.). A new urban canopy scheme which can account for the complex structure of canyon geometry has been developed. In the urban area, each roughness element is expressed by a square prism. All prisms are assumed to have the same width and to be evenly spaced, while they have their own roof heights.

- **water body (wb)**
  This is inland water surfaces (ponds, rivers, lakes) or the ocean surface. The water body scheme is based on the force-restore model. Both diurnal and seasonal cycles of water temperature are reproduced by this model.

All the surface elements that are included in the same category are lumped and treated as "unit tiles". Each gridbox has specified fixed fractions of these three land-uses (V_{ga}, V_{ua}, V_{wb}, respectively). Also canopy fractions within green area and urban area are also specified (V_c, V_{uc}, respectively).

$$V_{ga} + V_{ua} + V_{wb} = 1 \quad , \quad V_{ga} \geqq 0, \quad V_{ua} \geqq, \quad V_{wb} \geqq 0 \tag{6.4}$$

$$0 \leqq V_c \leqq 1 \quad , \quad 0 \leqq V_{uc} \leqq 1 \tag{6.5}$$

Sensible heat, latent heat, and momentum fluxes are calculated separately by each sub-model (green area, urban canopy, water body). And the grid averaged surface fluxes are obtained by averaging the surface fluxes over each land-use weighted by its fractional area.

$$[F]_{total} = \sum_i [F]_i V_i = [F]_{ga} V_{ga} + [F]_{ua} V_{ua} + [F]_{wb} V_{wb} \tag{6.6}$$

When the grid size is small, the arrangement and size of each land-use within grid areas has only a small effect on heat fluxes, and only the fractional area must be considered to express the land-use heterogeneity. But when the grid size is large, the land-use scale effects may appear, and the arrangement and size of each land-use should be considered too.

For the moment, the SiBUC model only uses "mosaic" parameterization to calculate the grid average fluxes, and its application is limited to "basin-scale".

6.4 Description of the green area model

In this section, as an example of a SVAT scheme, the green area model is described to see how land surface processes are formulated numerically. Physical constants are listed in Table 6.1. Variables and parameters are listed in Table 6.2 and 6.3. The description of the snow process is omitted for simplicity.

As mentioned above, the green area model is basically the same as the SiB. In designing the SiB, the philosophy was to model the vegetation itself and thereby calculate the radiation, momentum, heat and water vapor transfer properties of the surface in a consistent way. The morphological and physiological characteristics of the vegetation are used to derive coefficients and resistances which govern the fluxes between the surface and the atmosphere.

6.4.1 Atmospheric boundary conditions

The green area model, which was designed for use within NWP models and GCMs, requires the same kind of upper boundary conditions as other SVAT schemes.

- Air temperature, vapor pressure and wind speed of the lowest model layer (reference height), — T_m, e_m, u_m
- The solar zenith angle, — μ
- Five components of the incident radiation, — $F(0)$

$F_{v,b(0)}$	Visible or PAR ($< 0.72\mu$ m) direct beam radiation
$F_{v,d(0)}$	Visible or PAR ($< 0.72\mu$ m) diffuse radiation
$F_{n,b(0)}$	Near infrared (0.72 - 4.0 μ m) direct beam radiation
$F_{n,d(0)}$	Near infrared (0.72 - 4.0 μ m) diffuse radiation
$F_{t,d(0)}$	Thermal infrared (8.0 - 12.0 μ m) difuse radiation

- Precipitation rates, — P

The reference height (z_m) is selected within the atmospheric boundary layer (usually the upper side of surface layer, 30 - 50(m)). μ can be calculated from the location (latitude, longitude), date, and time. The propotions of the various spectral and angular fractions of short-wave incoming radiation are estimated from the scheme of Goudriaan (1977)[6], since they are not usually provided by atmospheric models.

6.4.2 Structure of the green area model

SiB has two vegetation layers for canopy and ground-cover. In the green area model, vegetation layer is reduced to one as in SiB2[14]. It was necessary to

Table 6.1: List of physical constants

symbol	definition	unit
λ	latent heat of vaporization	J kg^{-1}
c_w	specific heat of water (= 4.18×10^6)	J m^{-3}K^{-1}
σ	Stephan-Boltsman constant (= 5.6698 × 10^{-8})	Wm^{-2}K^{-4}
ρ	density of air (= 1.2)	kg m^{-3}
ρ_w	density of water (=1000)	kg m^{-3}
C_p	specific heat of air (= 1010)	J kg^{-1}K^{-1}
γ	psychrometric constant (= 0.662)	mb K^{-1}
ω	angular frequency of diurnal cycle ($2\pi/86400$)	s^{-1}
κ	von Karman's constant (= 0.4)	

Table 6.2: List of variables used in the green area model

Symbol	Definition
Rn_c, Rn_g	absorbed net radiation absorbed
H_c, H_g	sensible heat flux
$\lambda E_c, \lambda E_g$	latent heat flux
C_c, C_g, C_d	effective heat capacity
k_s	soil thermal conductivity
c_s	soil heat capacity
E_s	direct evaporation of water from the surface soil layer
$E_{dc,1}, E_{dc,2}$	abstraction of soil moisture by transpiration
E_{wc}, E_{wg}	rate of evaporation of water from wet portions
P_c, P_g	rate of precipitation interception
D_c, D_g	water drainage rate
P_1	infiltration of precipitation into the upper soil layer
$Q_{1,2}, Q_{2,3}$	flow between soil layer
Q_3	gravitational drainage from recharge layer
K_i	hydraulic conductivity of ith layer
ψ_i, ψ_r	soil moisture potential of ith layer and root zone
ψ_l	leaf water potential
r_b	bulk canopy boundary layer resistance
r_d	aerodynamic resistance between ground and canopy
r_a	aerodynamic resistance between canopy and z_m
r_c	bulk canopy resistance
r_{surf}	bare soil surface resistance

The subscript c refers to the canopy, g to the ground, and d to the deep soil.

Table 6.3: List of parameters used in the green area model

Symbol	Definition
	Time-invariant vegetation parameters
z_2, z_1	height of canopy top/bottom
z_c	inflection height for leaf-area density
z_s	ground roughness length
χ_L	Ross-Goudriaan leaf-angle distribution factor
G_1, G_4	momentum transfer coefficient parameters
l_w, l_l	leaf dimension (width, length)
$D_1, D2, D3$	depth of soil layer
D_d	root length density
α_V, α_N	leaf reflectance for visible/near infra-red
δ_V, δ_N	leaf transmittance for visible/near infra-red
C_l	drag coefficient of a canopy leaf
C_s	heat/vapor transfer coefficient of a canopy leaf
a_2, b_2, c_2	light dependent stomatal response parameters
T_l, T_h, T_o	lowest, highest, and optimum temperatures
h_5	stomatal response parameter for vapor pressure
ψ_{c1}, ψ_{c2}	stomatal response parameter for ψ_l
r_{plant}	resistance imposed by plant vascular system
R	root resistance per unit area
	Time-varying vegetation parameters
L_T	total leaf area index
V_c	canopy cover fraction
N	canopy greenness fraction
	Soil physical properties
ψ_s	soil water potential at saturation
K_s	soil hydraulic conductivity at saturation
B	soil wetness parameter
θ_s	soil water content at saturation (porosity)
$\alpha_{s,V}, \alpha_{s,N}$	soil reflectance for visible/near infra-red

reduce these to one layer in SiB2 to incorporate the iterative photosynthesis-conductance model and to make use of satellite data to describe surface parameters. The green area model also uses satellite data to calculate time-varying vegetation parameters such as leaf area index and canopy coverage. Therefore, both "canopy" and "ground cover" in SiB are refered to as "canopy" and treated together in this model. The schematic image of surface elements of the green area model is shown in Figure 6.4.

The roots are assumed to access the soil moisture from the second layer of a three-layer soil model, while the third layer acts as a source for hydrological baseflow and upward recharge of the root zone. The uppermost thin soil layer can act as a significant source of direct evaporation when the soil surface is wet.

Each vegetation type is assigned a set of time-invariant parameters. These include (i) morphological parameters; (ii) optical properties; and (iii) physiological properties. These properties are treated as constants for each vegetation type. Time-varying quantities such as leaf area index are combined with these parameters to produce further quantities.

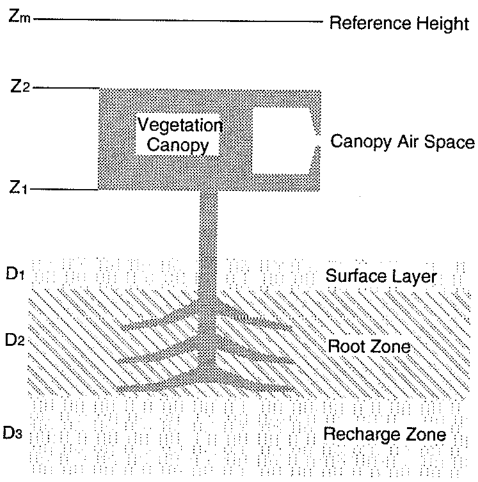

Figure 6.4: Structure of the green area model. (Reproduced from *Sellers et al.,1996*)

If there is a need to identify two vegetation types within one grid area, we can further divide the green area into two areas (mosaic of two tiles), that is :

$$V_{ga} = V_{ga,1} + V_{ga,2} \tag{6.7}$$

where $V_{ga,1}$ and $V_{ga,2}$ are the fractional areas of "type 1" and "type 2" vegetation, respectively. In the same way, it is possible to assign up to ten kinds of vegetation classes within one gridbox (fully mosaic approach). Since the main concern of SiBUC is a heterogeneity between natural vegetation and urbanized area and water body, one green area (one tile for green area) is just a default setting of the green area model.

6.4.3 Prognostic equations of the green area model

The prognostic physical-state variables of the green area model is basically the same as SiB. The difference in the definition of prognostic variables between SiB and our model is the treatment of ground cover.

Governing equations for temperatures

In the case of the green area model, two surface temperatures (T_c, T_g) are predicted to calculate the surface fluxes. Heat transport in the soil is described by the force-restore model of Deardorff (1977)[4]. The force-restore approximation relies on the analytical solution of the heat conduction equation under periodic forcing, which is used to parameterize the almost periodic daily ground heat flux. In this way, a very simple and efficient but reasonably accurate description of the temperature dynamics can be achieved. Since the the heat conduction term through the step of vegetation is negligible, the prognostic equation for T_c does not have a restoring term. Therefore, the governing equations for the three temperatures are expressed as follows.

$$
\begin{aligned}
C_c \frac{\partial T_c}{\partial t} &= Rn_c - H_c - \lambda E_c && (6.8)\\
C_g \frac{\partial T_g}{\partial t} &= Rn_g - H_g - \lambda E_g - \omega C_g (T_g - T_d) && (6.9)\\
C_d \frac{\partial T_d}{\partial t} &= Rn_g - H_g - \lambda E_g && (6.10)
\end{aligned}
$$

The heat capacity of the diurnally responsive upper soil (C_g) is defined after the work of Camilo and Schmugge (1981)[2], who formulated expressions for soil thermal conductivity (k_s) and specific heat (c_s) as functions of porosity and soil moisture content.

$$
\begin{aligned}
C_c &= 0.0001\, L_T\, C_w\, \rho_w,\quad C_g = \left(\frac{c_s k_s}{2\omega}\right)^{1/2},\quad C_d = \sqrt{365} C_g && (6.11)\\
k_s &= 0.4186 \frac{1.5(1-\theta_s) + 1.3\theta_s W_1}{0.75 + 0.65\theta_s - 0.4\theta_s W_1} && (6.12)\\
c_s &= [0.5(1-\theta_s) + \theta_s W_1] C_w \rho_w && (6.13)
\end{aligned}
$$

In eq.(6.11), the thickness of canopy leaves are assumed to be 0.1(mm). As for C_d, heat capacity is propotional to the square root of cycle. T_d is defined as the mean value of T_g over one day, and T_d is expected to have a seasonal cycle (one year). The effective heat capacity is impotant for reproducing the amplitude and phase of the diurnal cycle.

Governing equations for interception water stores

The governing equations for the two interception water stores are expressed in the same formula.

$$
\begin{aligned}
\frac{\partial M_c}{\partial t} &= P_c - D_c - \frac{E_{wc}}{\rho_w} && (6.14)\\
\frac{\partial M_g}{\partial t} &= P_g - D_g - \frac{E_{wg}}{\rho_w} && (6.15)
\end{aligned}
$$

This is a simple water budget equation for the water store. The interception and evaporation of precipitation stored on the canopy and the ground is modeled simply. Figure 6.5 shows the schematic image of the precipitation interception and water budget in the green area model. The maximum values for water store (S_c and S_g) are set to each story. If the water store (M_c or M_g) exceeds the maximum value, drainage (D_c or D_g) occurs.

The rate of inflow (interception) and outflow (drainage) for the canopy are given as follows.

$$
\begin{aligned}
P_c &= PV_c(1-e^{-L_T K_c}) && (6.16)\\
D_c &= 0 \quad \text{if } M_c < S_c \\
&= P_c \quad \text{if } M_c = S_c && (6.17)
\end{aligned}
$$

The water actually captured by the canopy is $P_c - D_c$, Therefore, the effective precipitation for the ground surface is given by

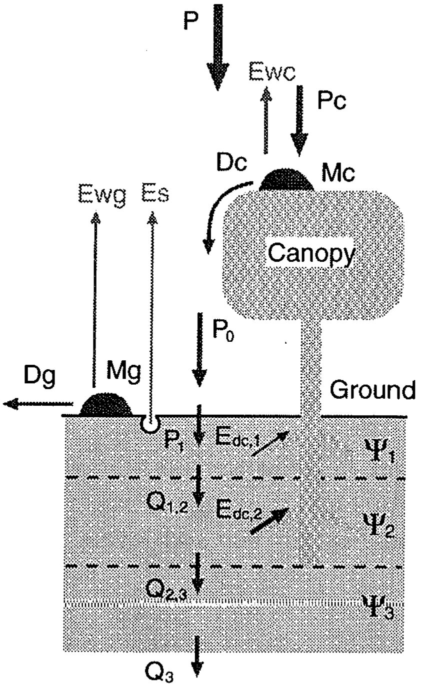

Figure 6.5: Schematic image of interception and water budget

$$P_0 = P - (P_c - D_c) \tag{6.18}$$

Some of the effective precipitation can infiltrate into the surface soil layer. When P_0 is stronger than the hydraulic conductivity at saturation (K_s), 'infiltration excess' runoff occurs. And if the surface soil layer is saturated, 'saturation excess' runoff occurs.

$$
\begin{aligned}
P_1 &= P_0 && \text{if } P_0 \leqq K_s \ \mathit{and} \ W_1 < 1 \\
&= K_s && \text{if } P_0 > K_s \ \mathit{and} \ W_1 < 1 \\
&= 0 && \text{if } W_1 = 1 && (6.19)
\end{aligned}
$$

Now $P_0 - P_1$ becomes the inflow to the surface water store (M_g).

$$
\begin{aligned}
P_g &= P_0 - P_1 && && (6.20)\\
D_g &= 0 && \text{if } M_g < S_g \\
&= P_g && \text{if } M_g = S_g && (6.21)
\end{aligned}
$$

Governing equations for soil moisture stores

The governing equations for the three soil moistures are based on Richards' equation with forcing terms of evapotranspiration ($E_s, E_{dc,1}, E_{dc,2}$) and infiltration (P_1).

$$\begin{aligned}
\frac{\partial W_1}{\partial t} &= \frac{1}{\theta_s D_1}\left(P_1 - Q_{1,2} - \frac{1}{\rho_w}(E_s + E_{dc,1})\right) \\
\frac{\partial W_2}{\partial t} &= \frac{1}{\theta_s D_2}\left(Q_{1,2} - Q_{2,3} - \frac{E_{dc,2}}{\rho_w}\right) \\
\frac{\partial W_3}{\partial t} &= \frac{1}{\theta_s D_3}(Q_{2,3} - Q_3)
\end{aligned}$$

A three-layer isothermal model is used to calculate the hydraulic diffusion and gravitational drainage of water in the soil. The equation used to describe vertical exchanges between soil layers is expressed by Darcy's law.

$$Q_{i,i+1} = K\left(\frac{\partial \psi}{\partial z} + 1\right) = \overline{K}\left(\frac{2(\psi_i - \psi_{i+1})}{D_i + D_{i+1}} + 1\right) \quad (i = 1, 2) \qquad (6.22)$$

$$\overline{K} = \frac{D_i K_i + D_{i+1} K_{i+1}}{D_i + D_{i+1}} \qquad (6.23)$$

In eq.(6.22), the term "1" accounts for gravitational drainage. When $Q_{i,i+1}$ is positive, flow is downward. As for the relationship between soil physical properties, Clapp and Hornberger(1978)[3] is used.

$$K_i = K_s W_i^{2B+3}, \qquad \psi_i = \psi_s W_i^{-B} \qquad (6.24)$$

The flow out of the bottom of the soil column to create base flow is determined by gravitational drainage only.

$$Q_3 = \sin \oslash_s \, K_s \, W_3^{2B+3} \qquad (6.25)$$

Therefore, the total runoff from the green area (R_{ga}) is given by summing surface runoff (D_g) and baseflow (Q_3).

$$R_{ga} = D_g + Q_3 \qquad (6.26)$$

Where $\oslash_s$ is defined as "mean topographic slope". However, is is almost meaningless if the grid size is larger than the size of actual slope of the mountain. The infiltration of liquid water (P_1) is assumed to be zero when the ground temperature (T_g) is below the freezing point of water.

6.4.4 Radiative transfer (two-stream approximation)

The two-stream approximation model (Dickinson, 1983)[5] was extended by Sellers (1985)[10] to describe the interception, reflection, transmission, and absorption of radiation by vegetation and soil. The radiation model used in the green area model is the same as for SiB2. Since there is only one vegetation layer, a single set of calculations for the canopy-soil system (one for each radiation component) is performed for each time step. Following the solution of the two-stream approximation model for the canopy-ground system, the canopy reflectances, absorbances, and transmittances are specified and the radiation absorbed by the canopy and soil from each incident component is calculated. Reflected and emitted fluxes are used as lower boundary conditions for the atmospheric radiation submodel. The original equations as specified by Dickinson (1983) are as follows.

$$-\overline{\mu}\frac{dI^{\uparrow}}{dL} + [1-(1-\beta)(\alpha+\delta)]I^{\uparrow} - (\alpha+\delta)\beta I^{\downarrow} = (\alpha+\delta)\overline{\mu}K\beta_0 e^{-KL} \tag{6.27}$$

$$\overline{\mu}\frac{dI^{\downarrow}}{dL} + [1-(1-\beta)(\alpha+\delta)]I^{\downarrow} - (\alpha+\delta)\beta I^{\uparrow} = (\alpha+\delta)\overline{\mu}K(1-\beta_0)e^{-KL} \tag{6.28}$$

$I^{\uparrow}, I^{\downarrow}$ = upward and downward diffuse radiative fluxes
K = optical depth of the direct beam per unit leaf area
$\overline{\mu}$ = average inverse diffuse optical depth per unit leaf area
β, β_0 = upscatter parameters for the diffuse and direct beams
L = cumulative leaf area index

The values of the parameters $K, \overline{\mu}$ are functions of canopy geometry, specifically the leaf angle distribution function. The values of the upscatter parameters β and β_0 are functions of both canopy geometric and optical properties.

The two equations (6.27) and (6.28) are solved using the incident (above canopy) radiation flux and the upwelling diffuse flux reflected by the soil as upper and lower boundary conditions, respectively. The calculation is performed for each of the four solar radiation components with a different simplified calculations for the exchanges of thermal infrared radiation.

Figure 6.6 describes each term of the radiation components for direct beam, diffuse and thermal-infrared radiation. The downward flux of diffuse radiation in the canopy $I^{\downarrow}$ has three components : 1) a component resulting from interception and rescattering of the direct beam radiation, 2) an exponentially extinguished downward flux resulting from downward scattering in the canopy, 3) an exponentially attenuated upwards flux resulting from upward scattering of radiation by canopy leaves and soil. The upward diffuse flux ($I^{\uparrow}$) also has similar components. $I^{\uparrow}(0)$ can be used as the canopy-soil system hemispherical reflectance, while $I^{\downarrow}(L_T/V) + e^{-KL_T/V}$ defines the spectral transmittance of the vegetation.

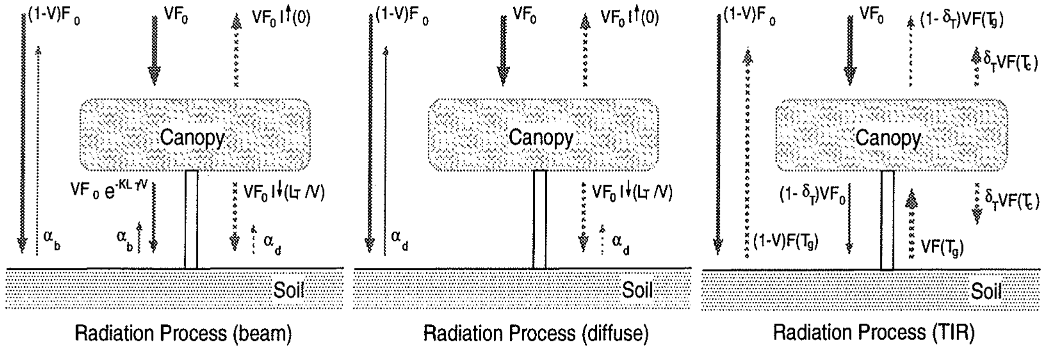

(a) direct beam **(b) diffuse** **(c) thermal infrared**

Figure 6.6: Schematic image of radiative transfer model

The direct beam and diffuse solar radiations absorbed by the canopy and ground are given as follows.

$$
\begin{aligned}
F_{\Lambda,b(c)} &= V[1 - I^{\uparrow}(0) - (1-\alpha_{\Lambda,b})e^{-KL_T/V_c} && (6.29)\\
&\quad -(1-\alpha_{\Lambda,d})I^{\downarrow}(L_T/V_c)]F_{\Lambda,b(0)} && (6.30)\\
F_{\Lambda,b(g)} &= [(1-V_c)(1-\alpha_{\Lambda,b}) + V_c((1-\alpha_{\Lambda,b})e^{-KL_T/V_c} \\
&\quad +(1-\alpha_{\Lambda,d})I^{\downarrow}(L_T/V_c))]F_{\Lambda,b(0)} && (6.31)\\
F_{\Lambda,d(c)} &= V_c\left[1 - I^{\uparrow}(0) - (1-\alpha_{\Lambda,d})I^{\downarrow}(L_T/V_c)\right]F_{\Lambda,d(0)} && (6.32)\\
F_{\Lambda,d(g)} &= \left[(1-V_c)(1-\alpha_{\Lambda,d}) + V_c(1-\alpha_{\Lambda,d})I^{\downarrow}(L_T/V_c)\right]F_{\Lambda,d(0)} && (6.33)
\end{aligned}
$$

The net absorbed thermal radiation fluxes are given by

$$
\begin{aligned}
F_{T,d(c)} &= \delta_T V_c F_{T,d(0)} - 2\delta_T V_c \sigma T_c^4 + \delta_T V_c \sigma T_g^4 && (6.34)\\
F_{T,d(g)} &= (1-\delta_T V_c)F_{T,d(0)} + \delta_T V_c \sigma T_c^4 - \sigma T_g^4 && (6.35)
\end{aligned}
$$

where

$F_{\Lambda,\mu(0)}$ = incident solar energy of wavelength Λ and direction μ
$\delta_T V_c$ = fraction of incident TIR absorbed by canopy

The net radiation fluxes for canopy and ground are given by the total of the absorbed flux components.

$$
\begin{aligned}
Rn_c &= \sum F_{\Lambda,\mu(c)} = F_{V,b(c)} + F_{N,b(c)} + F_{V,d(c)} + F_{N,d(c)} + F_{T,d(c)} && (6.36)\\
Rn_g &= \sum F_{\Lambda,\mu(g)} = F_{V,b(g)} + F_{N,b(g)} + F_{V,d(g)} + F_{N,d(g)} + F_{T,d(g)} && (6.37)
\end{aligned}
$$

6.4.5 Turbulent transfer and aerodynamic resistances

The aerodynamic resistance model of SiB describes the turbulent transfer processes above, within, and below a vegetation canopy. The scheme has been modified to describe height-varying leaf area densities (Sellers et al.,1989)[13]. In this modified form, the first-order closure model provided much better descriptions of z_0, d_0, and the wind profile. This improved version of the turbulent transfer scheme is used in the green area model. Figure 6.7 shows the different turbulent transfer regimes considered in the first-order closure model.

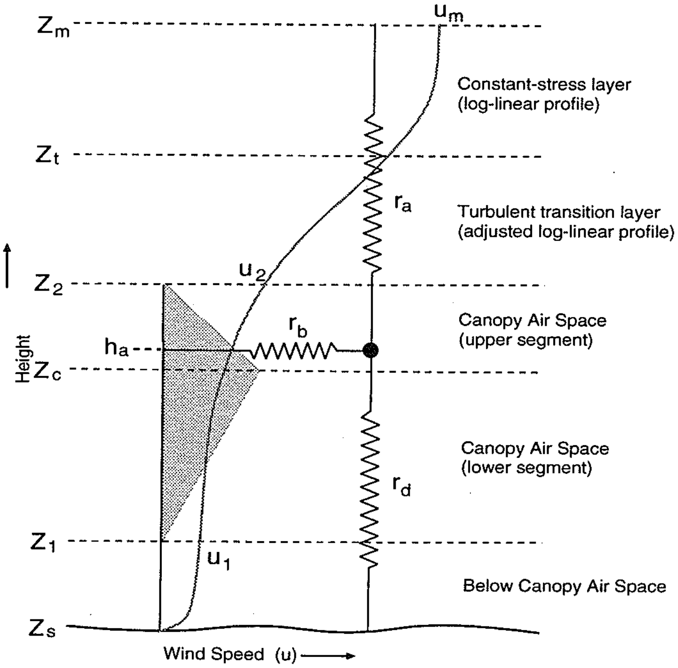

Figure 6.7: Turbulent transfer regimes considered in the first-order closure model. (Reproduced from *Sellers et al.,1996*)

Above the transition layer ($z_t \leqq z \leqq z_m$)

A conventional log-linear profile is assumed to be valid, and shear stress is assumed to be constant.

$$\tau = \rho K_m \frac{\partial u}{\partial z} \tag{6.38}$$

$$K_m = K_m^* = \kappa\ u_*(z - d_0) = \frac{\kappa^2 u(z - d_0)}{\log\left(\frac{z - d_0}{z_0}\right)} \tag{6.39}$$

Within the transition layer ($z_2 \leqq z \leqq z_t$)

Shear stress is assumed to be constant (eq.6.38), but the actual value of the momentum transfer coefficient (K_m) varies linearly with height from a value higher than K^*_m (log-linear extrapolated value of K_m) at z_2 to $K_m = K^*_m$ at z_t. This treatment of K_m is intended to take account of the intense local turbulence generated by roughness elements at the top of the canopy.

$$K_m = K^*_m \left(1 + (G_1 - 1)\left(\frac{z_t - z}{z_t - z_2}\right)\right) \tag{6.40}$$

To maintain constant shear stress throughout the same layer, the wind velocity gradient must shift away from the log-linear profile.

Within the canopy air space (CAS) ($z_1 \leqq z \leqq z_2$)

Leaf area density (L_d) increases with height from z_1 to z_c, after which it decreases linearly with height to z_2, giving a triangular profile of L_d (see Figure 6.7). Shear is absorbed by drag force interaction with the canopy leaves.

$$\frac{\partial \tau}{\partial z} = \rho \frac{C_l L_d}{P_s} u^2 \tag{6.41}$$

The shelter factor P_s was first introduced by Thom (1972) and is still not well understood. It accounts for the observation that the drag coefficient of an ensemble of densely clustered leaf elements is less than the sum of their individual drag coefficients, presumably due to mutual sheltering effects.

K_m is assumed to be a product of local wind (u) and mixing length (l_m). The local wind speed profile within the canopy is expressed by an exponential function.

$$K_m = l_m u \qquad u = u_2 \exp\left(-a_w\left(1 - \frac{z}{z_2}\right)\right) \tag{6.42}$$

Below the canopy ($z_s \leqq z \leqq z_1$)

A log-linear wind profile with constant shear stress links the soil surface to the flow at z_1. The shear stress is a function of ground roughness (z_s).

$$\tau_1 = \rho \left(\frac{\kappa\ u_1}{\log(z_1/z_s)}\right)^2 \tag{6.43}$$

Thom (1971)[16] defined the zero plane displacement height(d_0) as being equivalent to the moment height of momentum absorption by the surface.

$$d_0 = \frac{\int_{z_1}^{z_2} \frac{L_d C_l}{p_s} u^2 z\ dz}{\int_{z_1}^{z_2} \frac{L_d C_l}{p_s} u^2\ dz + \frac{\tau_1}{\rho}} \tag{6.44}$$

τ = shear stress $\mathrm{kgm^{-1}s^{-2}}$
K_m = local momentum transfer coefficient $\mathrm{m^2s^{-1}}$
u_* = friction velocity $\mathrm{ms^{-1}}$
u = local wind speed $\mathrm{ms^{-1}}$
d_0 = zero plane displacement height m
z_0 = roughness length m
C_l = leaf drag coefficient —
P_s = shelter factor of a canopy leaf —

Solution of momentum transfer equation set

z_0 and d_0 are independent of wind speed at reference height (u_m). Firstly, the local wind speed at the canopy top is assumed ($u_2 = 1$). Then, the wind profile within the canopy, u_1, τ_1, d_0, and u_* are specified. Next, z_0 is calculated assuming the log-linear profile above the canopy.

$$z_0 = \exp\left(\log(z_2 - d_0) - \frac{\kappa\ u_2}{u_*}\right) \tag{6.45}$$

Using z_0, d_0, u_*, and u_m, wind speed at canopy top (u_2) is specified, and τ, u_* are modified from the "temporal" values.

$$u_2 = u_m \frac{\log[(z_2 - d_0)/z_0]}{\log[(z_m - d_0)/z_0]} \tag{6.46}$$

$$\tau = \tau u_2^2 \qquad u_* = u_* u_2 \tag{6.47}$$

Now the profile of wind speed (u) and momuntum transfer coefficient (K_m) can be specified from the ground surface (z_s) to the reference height (z_m). These calculated profiles of u and K_m are then used to derive the aerodynamic resistances.

Aerodynamic resistances

The bulk canopy boundary-layer resistance (under neutral conditions) is given by the following expression.

$$r_b = \left(\int_{z_1}^{z_2} \frac{L_d u^{1/2}}{P_s C_s} dz\right)^{-1} = \frac{C_1}{u_2^{1/2}} \tag{6.48}$$

The transfer coefficient for heat-mass transfer (C_s) is less than that for momentum (C_l) since C_l incorporates both bluff-body and viscous forces, while C_s describes only viscous transfer.

The ground to canopy air space (CAS) resistance is defined as in SiB.

$$r_d = \int_{z_s}^{h_a} \frac{1}{K_s} dz = \int_{z_s}^{h_a} \frac{1}{K_m} dz = \frac{C_2}{u_2} \tag{6.49}$$

The heat-water vapor transfer coefficient (K_s) is assumed to be equal to K_m.

Canopy source height (h_a) is assumed to be equal to the center of action of r_b within the canopy as obtained from the solution of

$$\int_{z_1}^{h_a} L_d u^{1/2} dz = \int_{h_a}^{z_2} L_d u^{1/2} dz \tag{6.50}$$

The resistance between CAS and the reference height (z_m) can be described by integration of $K_s (= K_m)$ over the distance from h_a to z_m, which includes within-canopy (h_a to z_2), turbulent transition layer (z_2 to z_t) and log-linear profile (z_t to z_m) segments.

$$r_a = \int_{h_a}^{z_m} \frac{1}{K_s} dz = \int_{h_a}^{Z_2} \frac{1}{K_m} dz + \int_{Z_2}^{Z_t} \frac{1}{K_m} dz + \int_{Z_t}^{Z_m} \frac{1}{K_m} dz = \frac{C_3}{u_m} \tag{6.51}$$

The coefficients C_1, C_2, C_3 and the ratio $u_2 : u_m$ need only be calculated once for a given vegetation condition (type, geometry, LAI). The above expressions for r_a, r_b, r_d are adjusted to take acount of stability.

6.4.6 Surface resistance and canopy resistance

For bare soil evaporation, r_{surf} controls moisture flux from the top soil layer to the air and is expressed as follows.

$$r_{surf} = 30 + 3.5 W_1^{-2.3} \tag{6.52}$$

When $e_*(T_g) < e_a$, which is the condition of the dew formation (negative evaporation), r_{surf} is set to zero.

For vegetated surfaces, the additional resistance represents the control that 'stomata' act on transpiration. Stomata are microscopic pores on the leaves of plants that open and close in response to environmental conditions such as PAR, leaf temperature(T_c), vapor pressure deficit(δe), and leaf water potential(ψ_l). Broadly speaking, they seem to maximize rates of plant photosynthesis, while minimizing the risk of excessive transpiration rates.

The bulk canopy resistance (r_c) is thought to be equivalent to all the stomatal resistances of the individual leaves in the canopy "acting in parallel". The light-dependent stomatal resistance of an individual leaf is given by the following expression[7].

$$r_s = \frac{a_2}{b_2 + \mathbf{F}_\pi \cdot \mathbf{n}} + c_2 \tag{6.53}$$

$\mathbf{F}_\pi$ = photosynthetically active radiation (PAR) flux
$\mathbf{n}$ = vector of leaf normal

The dependence of r_c on different leaf angle distributions is discussed in Sellers (1985). However, it is convenient to use the average leaf projection to replace the leaf angle distribution function.

$$
\begin{aligned}
\frac{1}{r_c} &= V_c\, N_c\, f(T_c)\, f(\delta e)\, f(\psi_l) \int_0^{L_T} \frac{\overline{G(\mu)}}{r_s}\, dL && (6.54)\\
f(T_c) &= \frac{(T_c - T_l)(T_h - T_c)^{h_4}}{(T_o - T_l)(T_h - T_o)^{h_4}} \qquad h_4 = \frac{T_h - T_o}{T_o - T_l} && (6.55)\\
f(\delta e) &= 1 - h_5 \delta e = 1 - h_5[e_*(T_a) - e_a] && (6.56)\\
f(\psi_l) &= \frac{\psi_l - \psi_{c2}}{\psi_{c1} - \psi_{c2}} && (6.57)
\end{aligned}
$$

Of particular importance is the factor $f(\psi_l)$ which accounts for the effects of soil moisture stress and excessive evaporation demand. ψ_l is calculated by using a catenary model of the water transfer pathway from root zone to leaf (van der Honert, 1948).

$$\psi_l = \psi_r - h_a - \frac{E_{dc}}{\rho_w}(r_{plant} + r_{soil}) \qquad (6.58)$$

From eq.(6.58), the abstraction of soil moisture by transpiration from the ith soil layer ($E_{dc,i}$) is given by

$$E_{dc,i} = \frac{D_i}{D_r}\left(\frac{\psi_i - \psi_l - h_a}{r_{plant} + r_{soil}}\right)\rho_w \qquad (6.59)$$

Table 6.4: Fluxes, potential differences and resistances associated with the green area model

Flux	Potential difference	Resistance
H_c	$(T_c - T_a)\rho c_p$	r_b
H_g	$(T_g - T_a)\rho c_p$	r_d
$H_c + H_g$	$(T_a - T_m)\rho c_p$	r_a
λE_{dc}	$(e_*(T_c) - e_a)\rho c_p/\gamma$	$\frac{r_c + 2r_b}{1 - W_c}$
λE_{wc}	$(e_*(T_c) - e_a)\rho c_p/\gamma$	$2r_b/W_c$
λE_s	$(f_h e_*(T_g) - e_a)\rho c_p/\gamma$	$\frac{r_{surf} + r_d}{1 - W_g}$
λE_{wg}	$(e_*(T_g) - e_a)\rho c_p/\gamma$	r_d/W_g
$\lambda(E_c + E_g)$	$(e_a - e_m)\rho c_p/\gamma$	r_a

6.4.7 Sensible and latent heat fluxes

The fluxes of sensible and latent heat from each surface are described by an Ohm's law analogue form in which the fluxes are propotional to potential differences and inversely propotional to a (series of) resistance.

$$\text{flux} = \frac{\text{potential difference}}{\text{resistance}} \tag{6.60}$$

For the fluxes of sensible heat and latent heat, the potential differences are represented by temperatures and vapor pressures, respectively.

Figure 6.8(a) shows how sensible heat fluxes from the canopy (H_c) and the ground (H_g) must traverse the aerodynamic resistances r_b or r_d and r_a. Canopy water vapor flux must traverse an additional resistance (r_c). In addition, since it is assumed that water vapor exchange occurs from only one side of the leaf, the boundary-layer resistance is doubled for water vapor ($2r_b$). Evaporation from within the top soil layer E_g must cross the soil surface resistance (r_{surf}). Fluxes, potential differences, and resistances are summarized in Table 6.4.

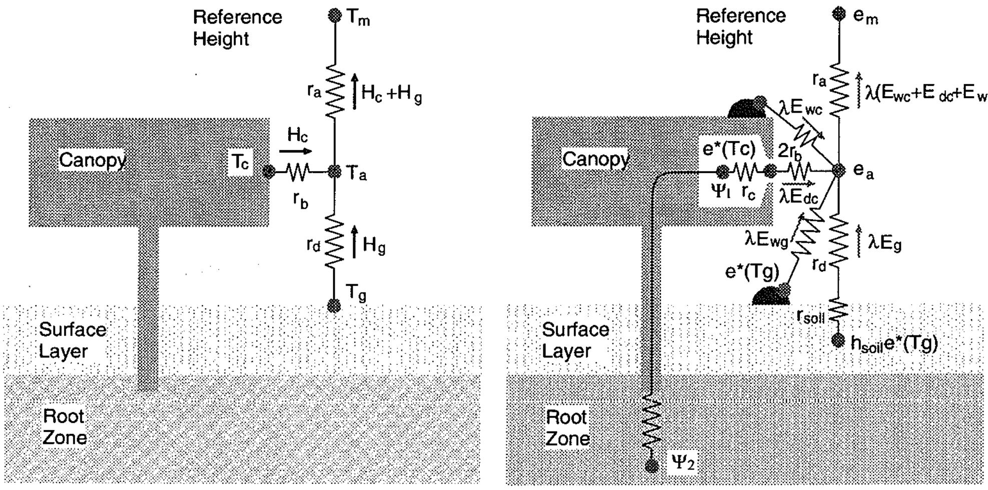

(a) Sensible heat flux (b) Latent heat flux

Figure 6.8: Transfer pathways as conceptualized in the green area model. (Reproduced from *Sellers et al.,1996*)

If we assume no storage of heat at any of the junctions of the resistance network shown in Figure 6.8(a), we can write the area-averaged sensible heat fluxes as follows.

$$\begin{aligned} H_c &= \frac{T_c - T_a}{r_b}\rho C_p = A(T_c - T_a), & A &= \rho C_p / r_b && (6.61)\\ H_g &= \frac{T_g - T_a}{r_d}\rho C_p = B(T_g - T_a), & B &= \rho C_p / r_d && (6.62)\\ H_c + H_g &= \frac{T_a - T_m}{r_a}\rho C_p = C(T_a - T_m), & C &= \rho C_p / r_a && (6.63) \end{aligned}$$

Air temperature within the canopy air space (CAS) can be eliminated from eq.(6.61) to (6.63).

$$T_a = \frac{A \cdot T_c + B \cdot T_g + C \cdot T_m}{A + B + C} \qquad (6.64)$$

Water vapor fluxes from the canopy (E_c) and the ground (E_g) have two components (E_{wc} and E_{dc}), (E_{wg} and E_s), respectively.

If we assume no storage of water vapor at any of the junctions of the resistance network shown in Figure 6.8(b), we can write the area-averaged latent heat fluxes as follows.

$$\lambda E_c = D(e_*(T_c) - e_a) \quad , \quad D = \frac{\rho C_p}{\gamma}\left(\frac{W_c}{2r_b} + \frac{1 - W_c}{r_c + 2r_b}\right) \qquad (6.65)$$

$$\lambda E_g = E(e_*(T_g) - e_a) \quad , \quad E = \frac{\rho C_p}{\gamma}\left(\frac{W_g}{r_d} + \frac{f_h e_*(T_g) - e_a}{(r_{surf} + r_d)(e_*(T_g) - e_a)}\right) \qquad (6.66)$$

$$\begin{aligned} \lambda E_c + \lambda E_g &= F(e_a - e_m), \quad F = \frac{\rho C_p}{\gamma r_a} && (6.67)\\ e_a &= \frac{D \cdot e_*(T_c) + E \cdot e_*(T_g) + F \cdot e_m}{D + E + F} && (6.68) \end{aligned}$$

6.4.8 Numerical solution of prognostic equations

In the numerical solution of the prognostic equations for temperatures, we make use of the fact that the storage terms are small relative to the energy fluxes. These values make eq. (6.8), (6.9) fast response equations so that changes in T_c, T_g, even over a time step as short as an hour, can have a significant feedback on the magnitude of the energy fluxes. The energy fluxes are explicit functions of atmospheric boundary conditions, prognostic variables, aerodynamic and surface resistances. Prognostic equations are solved by an implicit backward method using partial derivatives of each term.

First, considering the energy fluxes in prognostic equations as functions of temperature, partial derivatives are calculated. Then, prognostic equations are expressed in explicit backward-differencing form and a set of linear simultaneous equations regarding the changes in temperatures over a time step (Δt) are obtained.

Not only energy fluxes but also heat exchange terms are dependent on temperature. Prognostic equations can then be written in discrete-time form.

$$\begin{aligned}
C_c\frac{\Delta T_c}{\Delta t} &= Rn_c - H_c - \lambda E_c + \left(\frac{\partial Rn_c}{\partial T_c} - \frac{\partial H_c}{\partial T_c} - \frac{\partial \lambda E_c}{\partial T_c}\right)\Delta T_c \\
&+ \left(\frac{\partial Rn_c}{\partial T_g} - \frac{\partial H_c}{\partial T_g} - \frac{\partial \lambda E_c}{\partial T_g}\right)\Delta T_g \qquad (6.69) \\
C_g\frac{\Delta T_g}{\Delta t} &= Rn_g - H_g - \lambda E_g - \omega C_g(T_g - T_d) + \left(\frac{\partial Rn_g}{\partial T_c} - \frac{\partial H_g}{\partial T_c} - \frac{\partial \lambda E_g}{\partial T_c}\right)\Delta T_c \\
&+ \left(\frac{\partial Rn_g}{\partial T_g} - \frac{\partial H_g}{\partial T_g} - \frac{\partial \lambda E_g}{\partial T_g} - \omega C_g\right)\Delta T_g + \omega C_g \Delta T_d \qquad (6.70) \\
C_d\frac{\Delta T_d}{\Delta t} &= Rn_g - H_g - \lambda E_g + \left(\frac{\partial Rn_g}{\partial T_c} - \frac{\partial H_g}{\partial T_c} - \frac{\partial \lambda E_g}{\partial T_c}\right)\Delta T_c \\
&+ \left(\frac{\partial Rn_g}{\partial T_g} - \frac{\partial H_g}{\partial T_g} - \frac{\partial \lambda E_g}{\partial T_g}\right)\Delta T_g \qquad (6.71)
\end{aligned}$$

This can be written in matrix form,

$$KX = Y \qquad \longrightarrow \qquad X = K^{-1}Y$$

$$K = \begin{pmatrix} K_{1,1} & K_{1,2} & K_{1,3} \\ K_{2,1} & K_{2,2} & K_{2,3} \\ K_{3,1} & K_{3,2} & K_{3,3} \end{pmatrix} \qquad X = \begin{pmatrix} \Delta T_c \\ \Delta T_g \\ \Delta T_d \end{pmatrix}$$

The above equations can be solved in terms of temperature changes (ΔT_c, ΔT_g, ΔT_d). Each temperature is updated to the value at time $t_0+\Delta t$ by adding temperature change to the initial value at time t_0. Furthermore, energy fluxes are modified to show the values averaged over a time step (between time t_0 and time $t_0+\Delta t$).

$$Rn'_c = Rn_c + \frac{1}{2}\left(\frac{\partial Rn_c}{\partial T_c}\Delta T_c + \frac{\partial Rn_c}{\partial T_g}\Delta T_g\right) \qquad (6.72)$$

$$Rn'_g = Rn_g + \frac{1}{2}\left(\frac{\partial Rn_g}{\partial T_c}\Delta T_c + \frac{\partial Rn_g}{\partial T_g}\Delta T_g\right) \qquad (6.73)$$

$$H'_c = H_c + \frac{1}{2}\left(\frac{\partial H_c}{\partial T_c}\Delta T_c + \frac{\partial H_c}{\partial T_g}\Delta T_g\right) \qquad (6.74)$$

$$H'_g = H_g + \frac{1}{2}\left(\frac{\partial H_g}{\partial T_c}\Delta T_c + \frac{\partial H_g}{\partial T_g}\Delta T_g\right) \qquad (6.75)$$

$$\lambda E'_c = \lambda E_c + \frac{1}{2}\left(\frac{\partial \lambda E_c}{\partial T_c}\Delta T_c + \frac{\partial \lambda E_c}{\partial T_g}\Delta T_g\right) \qquad (6.76)$$

$$\lambda E'_g = \lambda E_g + \frac{1}{2}\left(\frac{\partial \lambda E_g}{\partial T_c}\Delta T_c + \frac{\partial \lambda E_g}{\partial T_g}\Delta T_g\right) \qquad (6.77)$$

6.5 Observation of land surface processes

6.5.1 Introduction of the Lake Biwa Project

The field observation has been carried out under the Japanese hydro- meteorological project called "Lake Biwa Project". A core activity of this project has been collaborative field observation synchronized with spaceborne and airborne remote sensing. This project has been developed and carried out by a Japanese group for investigating the hydrological cycle near land surface. This project aims to understand the hydrological cycle within the Lake Biwa Basin together with establishing ways of scaling up and down the hydrological model within the scale of 100 km × 100km. The targets of this project are

(1) validation of satellite remote sensing

(2) development of algorithms/models describing hydrological processes

(3) understanding land-atmosphere interactions

(4) evaluation of space/time scale effects in the hydrological cycle

(5) establishment of a land-atmosphere coupled model for the Lake Biwa Basin

The history of this project can be summarized as follows.

The first stage (from 1989 to 1994)

mainly focused on targets (1) and (2) with point in situ observations. The target area was mainly harvested paddy field and the largest target spatial and temporal scales were 1 km and 1 day.

The second stage (from 1995 to 2000)

has been mainly focusing on targets (3) and (4) by coupled numerical models developed by members. Currently, seasonal variation of energy and water cycle is gradually being added as one of the targets by combining the numerical model with operational information from satellite observation and established regular in situ measurement systems. Accordingly, the largest target spatial and temporal scales are shifted to 20 km and 1 week on the viewpoint of up scaling.

The third stage (from 2001 ~)

The third stage is now implemented to establish the target (5). Also, a new attempt has been executed for the direct observation of the areal flux by a great number of turbulent measurement systems.

6.5.2 Observation system at paddy field

Now four observation systems have been installed and operated regularly for different landuse conditions (paddy field, forest, lake, and urban area) within the Lake Biwa Basin. Among them, the observation system for the paddy field is introduced here.

Supposing that the purpose of the measurement is to monitor the energy budget itself, the following items are the minimum requirement.

net radiation, ground heat flux, air pressure,
air temperature(two levels), relative humidity(two levels)

If the observation is aimed for the development and validation of LSS, the following items are required to be observed together.

forcing variables, prognostic variables,
diagnostic variables(fluxes, and other related variables)

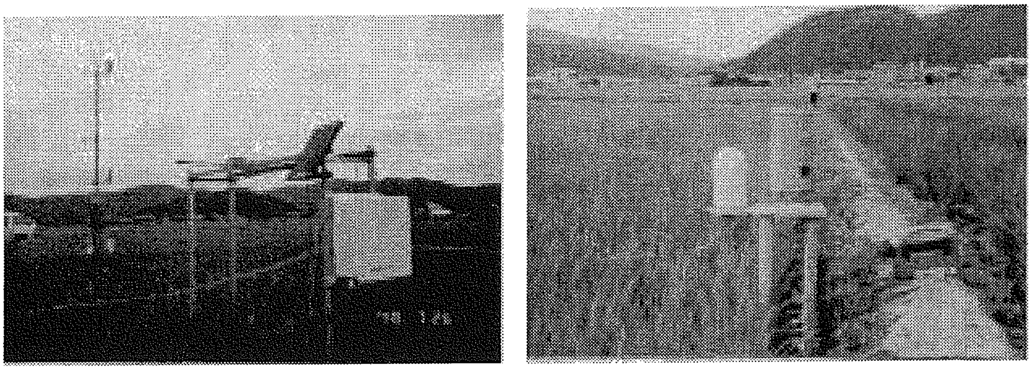

(a) whole system (b) raingauge and water gauge

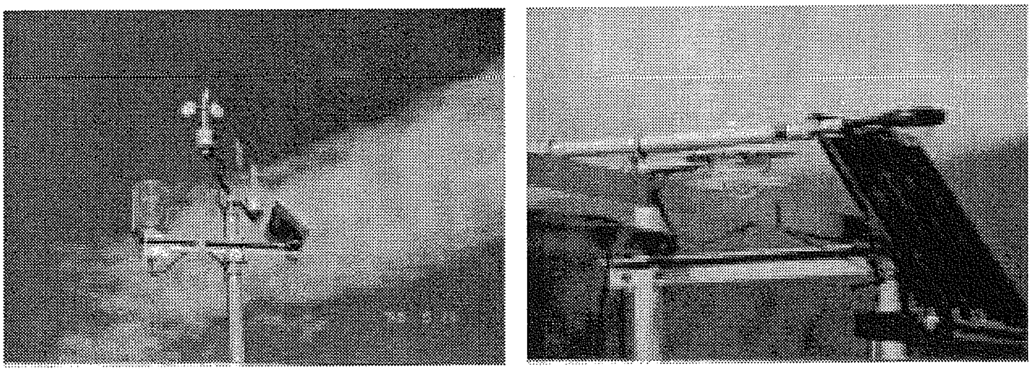

(c) meteorological sensors (d) radiation sensors

Figure 6.9: Heat budget observation system in paddy field

The flux measurement system for the paddy field was designed to meet the latter objective. The observation site is located at N35.49, E136.23. One tract of paddy field is about 30m width and 100m length, and this field belongs to a local farmer (Mr. Komori). This field has been treated and called an 'intensive field' since 1991. Regular operation of this system started in July 1998.

The system consists of two sub-systems (see Figure 6.9(a)). The vertical profile of atmospheric variables near the surface is recorded by the Grant data logger(SQ1021). Radiation and soil related variables are recorded by the Campbell data logger(CR10X). The power source for the system is solar panel (11.1W, 14.5W) with battery (18.0Ah, 13.5Ah). In addition to usual heat budget observation system, water temperature and water depth are also measured to know the status of water. Light quantum sensors were added to observe photosynthetic activity from June 1999. Observation items and sensors are listed in Table 6.5. Note that the leftmost column in Table 6.5 shows the purpose of the measurement. F, P, D refer to forcing, prognostic, diagnostic variables, respectively.

If one might seek ideal conditions for observation, the site might be located in the remote place where electricity and telephone lines are absent. Recently, the service area for mobile phone has extended day by day. Thus, mobile phone can be used as a communication tool between the office and the field. Owing to mobile phone, data can be collected easily, and the troubles can be resolved early.

Table 6.5: Observation items and sensors

note	item	sensor	height
F,D	air temp.	Vaisala VH-G-Z	507,264,111cm
F,D	humidity	Vaisala VH-G-Z	507,264,111cm
F,D	wind speed	Vector A100L2	523,266,116cm
F	wind direction	Vector W200	523cm
F	pressure	Vaisala PTB100	210cm
F,D	light quantum	Licor LI-190SA	200cm(up&down)
P	soil temp.	Campbell 107	-1,-10,-20cm
P	water temp.	Campbell 107	1cm
	net radiation	REBS Q7	195cm
D	soil heat	REBS HFT-3	-1cm
F,D	long-wave rad.	Eppley PIR	195cm(up&down)
F,D	short-wave rad.	Kipp&Zonen CM-14	195cm(up&down)
P	soil moisure	Campbell CS615	-5,-5,-20,-20cm
P,D	water depth	Ikeda KWH-4PHT	
F	precipitation	Ikeda RT-5	

6.5.3 Data analysis

Observed data are processed with Bowen ratio method to calculate energy fluxes. As for the heat storage term, it is the total of energy stored in both water and soil, when water exists on soil surface.

Diurnal variation

Figure 6.10 shows an example of observed data (energy budget, radiation budget, temperature, soil moisture, water depth, and albedo, respectively) on June 6th 2000. As water depth data shows, water existed on that day, and a significant part of net radiation energy was stored as ground heat flux. Clear diurnal variation in albedo data occurred for two reasons. One is dependancy of solar angle (low soil reflectance), and the other is photosynthesis activity.

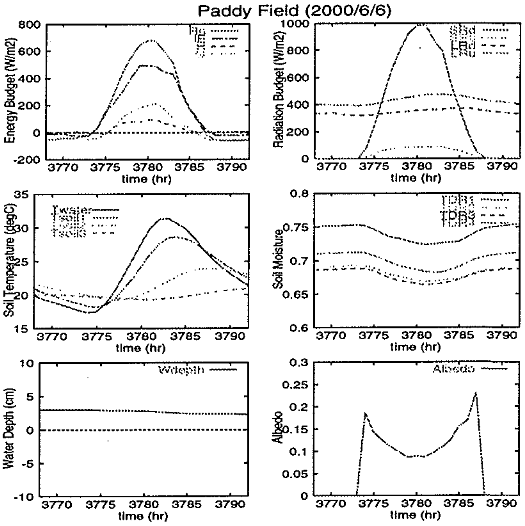

Figure 6.10: Diurnal variation of observed elements at paddy field (2000/6/6)

Seasonal variation

Table 6.6: Monthly average energy budget(Wm^{-2})

period	Rnet	G	H	lE
99/8/9~31	119.0	0.8	15.4	102.7
99/9/1~30	97.3	1.5	15.6	80.2
99/10/1~31	70.7	-8.1	14.2	64.6
99/11/1~30	35.9	-9.6	7.1	38.4
99/12/1~31	22.2	-12.2	2.3	32.1
00/1/1~31	28.9	-8.3	3.1	34.1
00/2/1~29	24.9	-10.0	0.4	34.5
00/3/1~25	67.4	-2.3	5.90	63.8
00/5/16~31	140.4	-2.7	16.9	126.2
00/6/1~30	109.2	9.1	11.5	88.6
00/7/1~/31	150.6	7.2	12.7	130.8
00/8/1~/17	172.1	5.9	21.0	145.2
average	78.6	-3.0	9.6	72.1

Monthly energy budget is listed in Table 6.6. Although there is much snow in winter (from middle of December to the end of Februaly), the observation system is not designed for snowcover. Therefore, the accuracy of the energy balance (especially for the heat storage term) in winter season may not be so good. Net radiation has its maximum in August and minimum in December. As for heat storage, the maximum value is in June. While net radiation increases from June to August, heat storage decreases. This tendency can be explained by the growing of rice crop and existence of water. Basically, the soil moisture value stays relatively high and the Bowen ratio is low (latent heat is dominent) throughout the year. This is due to winter precipitation and high field capacity of soil (clay).

6.6 Paddy field model

In the original version of the green area model, there is no framework to treat the rice paddy field (paddy field is treated the same as cropland). Through detailed analysis of the field data and the simulation results, it was found that the green area model is difficult to use for paddy field if the simulation period becomes longer. Another motivation for the development of the paddy field scheme is to treat the irrigation water.

Therefore, a water layer which has a temperature (T_w) and depth (D_w) is added to the green area model to treat the paddy field realistically.

6.6.1 Artificial water control

Water in paddy field is controlled/operated differently according to the growing stage of rice. The water depth control rule is basically expressed in three stages as follows (see Figure 6.11).

1. **ponding irrigation stage**
   Water is irrigated to keep the minimum water level(H_1).
2. **internal drain stage**
   Water is drained after T_2 and kept below zero for some period(T_3).
3. **intermittent irrigation stage**
   The water level is controlled repeatedly during the drying period(T_4).

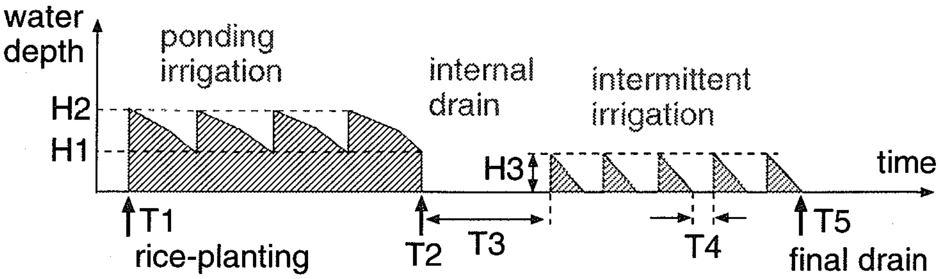

Figure 6.11: Water depth control rule

Parameters used in this basic water control rule are listed in Table 6.7. Although actual variation of water depth is very complicated due to rainfall, we could guess when artitifial water control occurred through detailed analysis of observed data. What has to be noticed is that the value of parameters are not constant. They are changable depending on weather conditions. In fact, the values for 1999 and 2000 are different.

Table 6.7: Parameters for artificial water control

definition	symbol	value
water irrigation rate	W_{in}	4.5mm/hr
water drainage rate	W_{out}	1.4mm/hr
rice-planting date	T_1	
internal drain start date	T_2	6/7
period of internal drain	T_3	27day
drain period for intermittent irrigation	T_4	3day
final drain date	T_5	
low level for ponding irrigation	H_1	20mm
high level for ponding irrigation	H_2	30mm
high level for intermittent irrigation	H_3	40mm

6.7 Application to the Lake Biwa Basin

The energy and water budget within the Lake Biwa Basin, Japan, is estimated using the land surface scheme (SiBUC). The atmospheric forcing mesh dataset needed to run SiBUC is created based on surface meteorological station (SDP) and AMeDAS data. The resolution of this mesh dataset is 3km in space and 1hr in time.

The downward shortwave radiation is corrected by the inclination and direction of the local topography. Radar AMeDAS Precipitation (Rap) is used for precipitation. As for the landuse/landcover dataset, KS202 (Japanese National Geographical Information) which has 100m resolution is used.

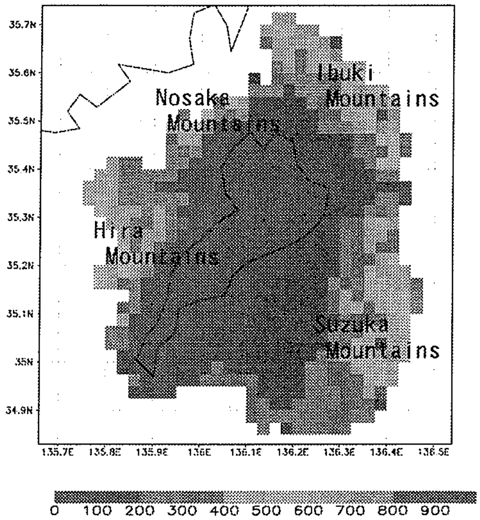

Figure6.12: Topography of the Lake Biwa Basin

In KS202, forest is expressed by one category since this dataset is aimed for landuse. Thus GLCC (USGS) is further used to divide the forest class into several kind of forest(evergreen/decidous, broad/needle leaf etc.). In this study, several kinds of vegetation (upper most 10 classes) are allowed to coexist in the same grid.

6.7.1 Validation at point scale

The energy and water budget is calculated using a 3km grid. At the point scale, energy budget observation data from the Lake Biwa Project is utilized. Three sites are chosen in order to check the performance of SiBUC model. The first one is the grid (Grid P) for the paddy field. The second one is the grid (Grid L) for the lake surface. The third one is the grid (Grid F) for the deciduos forest.

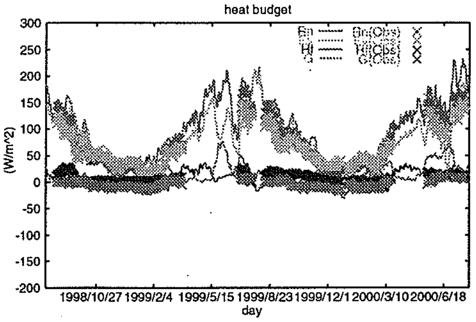

Figure 6.13: Energy budget at paddy field

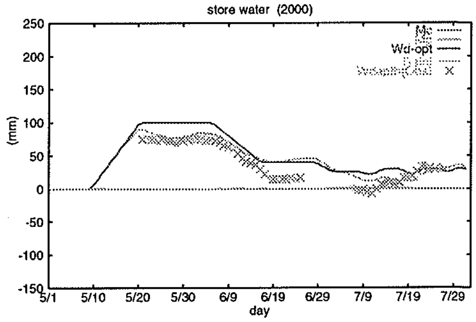

Figure 6.14: Water depth at paddy field

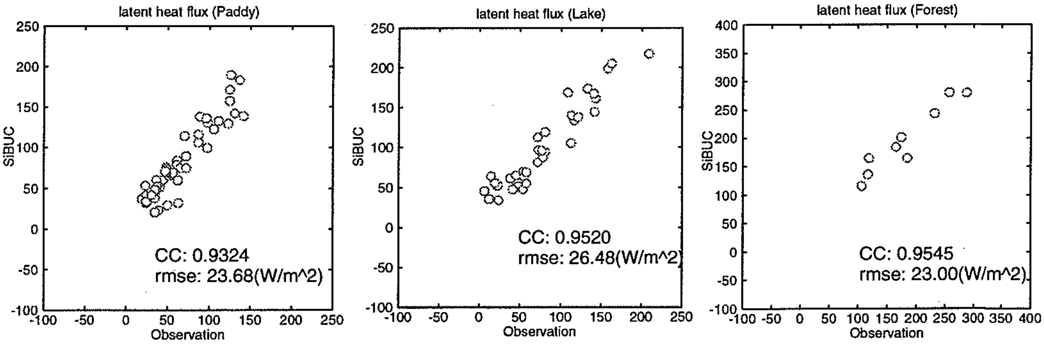

(a) paddy field (b) lake surface (c) forest

Figure 6.15: Scatter graphs of 10-day average latent heat for three landuses

Seasonal variation (10-day moving average) of energy budget components for paddy field are shown in Figure 6.13. Solid lines are simulated results, and observed values are plotted. It can be said from this figure that the SiBUC model can reproduce the seasonal cycle of the energy budget of paddy field. Time series (10-day moving average) of water depth is shown in Figure 6.14.

'Wd-opt' in this figure means an optimum water depth used in paddy field scheme. During May, water is operated to maintain high water depth, then water depth is maintained at a relatively low value. This feature expresses the paddy field scheme well if we see it in a moving averaged value.

10-day average latent heat flux for paddy field, lake surface, and forest are compared in scatter graphs (Figure 6.15). We can see that latent heat flux is simulated very well for all three sites. Considering that most of the Lake Biwa Basin is occupied by these three land-uses, simulated evapotranspiration within the Basin is expected to be highly accurate.

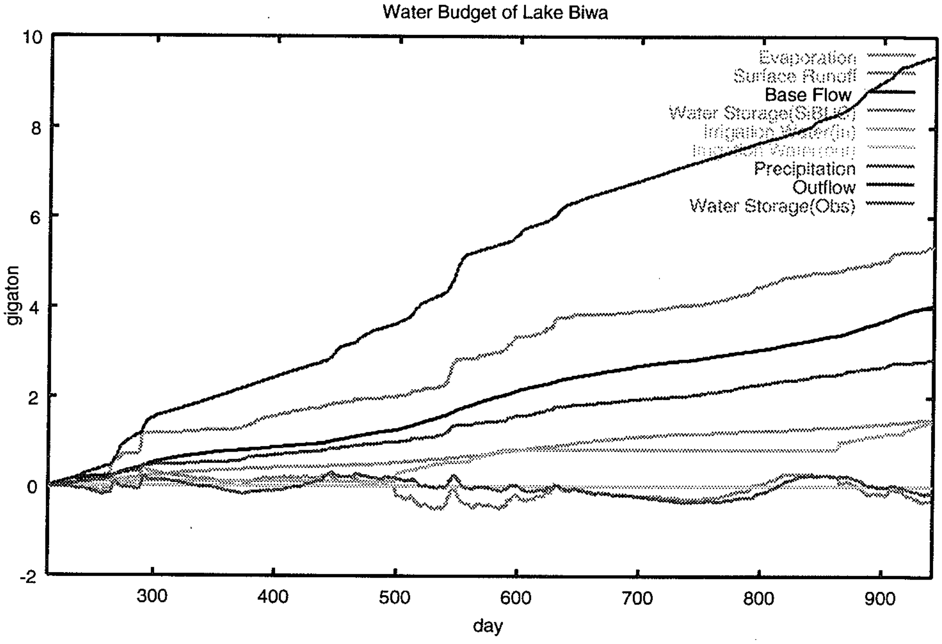

Figure 6.16: Time series of accumulated water budget components for Lake Biwa

To check the water budget at the basin scale, a basin mask and lake mask data set is also prepared. Aggrigating basin-mesh data and lake-mesh data, water budget of Lake Biwa is calculated. Figure 6.16 shows the time series of accumulated water budget components for Lake Biwa. The unit is in giga ton (Gt=10^9m^3). In this figure, 'Water Storage(obs)' was calculated from the observed water level and lake surface area. 'Water Storage(SiBUC)' means the storage change estimated from the simulation result and is calculated by the following water budget equation.

$$\Delta S = P_L - E_L - Q_{out} + Q_{surf} + Q_{base} - W_{in} + W_{out} \qquad (6.78)$$

where

ΔS : lake water storage change (simulation)
P_L : precipitation over the lake (observation)
E_L : evaporation from the lake (simulation)
Q_{out} : outflow from the Lake (observation)
Q_{surf} : surface runoff from the basin-mesh(simulation)
Q_{base} : baseflow from the basin-mesh(simulation)
W_{in} : irrigation water demand from paddy field(simulation)
W_{out} : forced water drainage from paddy field(simulation)

These two Water Storage terms are very close in value to each other. Consdering that the total amount of precipitation over the whole basin for two years is 13.58Gt, the water budget imbalance of 0.05Gt is regarded to be sufficiently small.

References

[1] Avissar,R. and R.Pielke, 1989 : A parameterization of heterogeneous land surfaces for atmospheric numerical models and its impact on regional meteorology, *Mon. Weather Rev.*, **117**, 2113-2136.

[2] Camillo,P. and T.J.Schmugge, 1981 : A computer program for the simulation of heat and moisture flow in soils. NASA Tech. Memo. 82121, National Aeronautics and Space Administration, Greenbelt, MD, 93pp.

[3] Clapp.R.B.,and G.M.Hornberger, 1978 : Empirical equations for some soil hydraulic properties.*WaterResour.Res.*, **14**(4),601-604.

[4] Deardorff,J.W., 1977 : Efficient prediction of ground surface temperature and moisture with inclusion of a layer of vegetation. *J.Geophys.Res.*, **83**, 1889-1903.

[5] Dickinson, R. E., 1983 : Land surface process and climate-surface albedos and energy balance. *Advances in Geophysics*, **25**, 305-353.

[6] Goudriaan, J., 1977 : Crop micrometeorology.Wageningen Center for Agricultural Publishing and Documentation, Wegeningen, the Netherlands, 249pp.

[7] Jarvis, P.G., 1976 : The interpretation of the variation in leaf water potential and stomatal conductance found in canopies in the field. *Philos. Trans. Roy. Soc. london, Ser B.*, **273**, 593-610.

[8] Kimura, F., 1989 : Heat Flux on Mixtures of Different Land-use Surface : Test of a New Parameterization Scheme. *J. Meteor. Soc. Jpn.*, **67**, 401-409.

[9] Michaud,J.D. and W.J.Shuttleworth, 1997 : Executive summary of the Tucson Aggregation Workshop, *J.Hydrol.*, **190**, 176-181.

[10] Sellers, P. J., 1985 : Canopy reflectance,photosynthesis and transpiration. *Int. J. remote Sens.*, **6**, 1335-1372.

[11] Sellers, P. J., Y. Mintz, Y. C. Sud and A. Dalcher, 1986 : A simple biosphere model(SiB) for use within general circulation models. *J. Atmos. Sci.*, **43**, 505-531.

[12] Sellers, P. J., and J. Dorman, 1987 : Testing the Simple Biosphere model(SiB) with point micrometeorological and biophysical data. *J. Climate Appl. Meteor.*, **26(5)**, 622-651.

[13] Sellers,P.J., J.W.Shuttleworth, J.L.Dorman, A.Dalcher, and J.M.Roberts, 1989 : Calibrating the simple biosphere model (SiB) for Amazonian tropical forest using field and remote sensing data. PartI: Average calibration with field data. *J.Appl.Meteor.*, **28**, 727-759

[14] Sellers,P.J., D.A.Randall, G.J.Collatz, J.A.Berry, C.B.Field, D.A.Dazlich, C. Zhang, G.D.Collelo, and L.Bounoua, 1996 : A revised land surface parameterization (SiB2) for atmospheric GCMs, Part I, Model formulation, *J.Clim.*,**9**, 676-705.

[15] Tanaka K. and Ikebuchi S.(1994) : Simple Biosphere Model Including Urban Canopy (SiBUC) for Regional or Basin-scale Land Surface Processes, Proceedings of the international study conference on GAME, 3.59-3.62.

[16] Thom, A. S., 1971 : Momentum absorption by vegetation. *Quart. J. Roy. Meteor. Soc.*, **97**, 414-428.

Chapter 7

Radar Hydrology

Eiichi Nakakita
Dept. of Global Environment Engineering, Kyoto University,
Yoshida Honmachi, Sakyo-ku, Kyoto, 606-8501, JAPAN
Phone/Fax: +81-75-753-5109
E-mail: nakakita@info.gee.kyoto-u.ac.jp

7.1 Introduction

7.1.1 Radar hydrology

What is "radar hydrology"? In a broad sense, this term refers to all kinds of topics for utilizing electromagnetic waves in the field of hydrology such as discharge measurements, detection of ground water and so on. In a limited sense, the term means "hydrological applications of weather radar" which still includes many topics such as,

- Estimation of precipitation using radar data,
- Prediction of precipitation using radar data,
- Distributed hydrologic modeling,
- Hydro-climatic studies based on radar data,
- Application of weather radars for hydrologic forecasting in different climates,
- Contributions of radar data to water management,
- Emerging radar technologies and their potential for hydrologic applications,
- Progress in application of polar-metric techniques,

- Space-borne radar,
- Operational experience in radar hydrology,
- Coupling meteorological and hydrological models assimilating radar data,
- Radar Hydrology in urban areas,
- Scale issues that radar observation can solve,
- Application for forecasting of dangerous hydrologic phenomena,
- Warning System,
- Mechanism of precipitation

Indeed, these were topics for the fifth international symposium on hydrological application of weather radar, which was held in Kyoto, in 2002. Among these, this paper focuses on topics that lie somewhere between meteorology and hydrology.

7.1.2 Short-term rainfall prediction

Rainfall distribution is greatly affected by topography. That is, dynamics and microphysics relate topography to features such as generation, growth, decay and lingering of rainfall areas. This is why, so far, no short-term rainfall prediction method using weather radar has been successful in predicting rainfall distribution on meso-β scale beyond approximately two hours ahead. This situation is severe in Japan because 70 percent of its land area is mountainous. Improving short-term rainfall prediction is necessary in order to increase the reliability of real-time flood forecasting. In this sense, utilizing radar information with basic meteorological equations is expected to improve the above situation. Many methods of short-term rainfall prediction using weather radar have been proposed in Japan and in other countries. Nakakita *et al.* (1996) and Browning and Collier (1989) review other methods including methods that use satellite measurements.

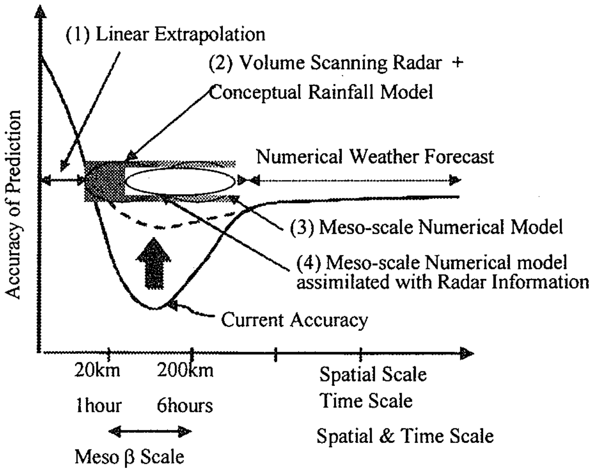

Figure 7.1: Schematic of present status of rainfall prediction.

As is schematically shown in Figure 7.1, operationally used short-term rainfall prediction methods can be classified into three categories; (1) methods based on the liner extrapolation of the movement pattern of horizontal rainfall distribution, (2) methods based on a conceptual rainfall model using the principles of water balance and thermodynamics; and (3) meso-scale numerical weather forecasting model. Most of the current short-term rainfall prediction methods that operationally use radar information belong to the first category and can practically be used for a only one-hour prediction lead-time. On the other hand, as the fourth category, operational meso-scale numerical predictions are now available in some countries and work well beyond a lead-time of several hours. However, it is a fact that the accuracy of prediction for lead-times of two to several hours is still low. In order to improve the accuracy for these lead-times, physically based prediction methods assimilated with radar information are required. In this sense, development of methods belonging to categories (2) and (3) have been expected to improve the accuracy.

A method belonging to the second category has been developed by Nakakita *et al.* (1991, 1992, 1996), and this is operationally used by the Yodo Dams Control Office of Ministry of Land, Infrastructure and Transportation, Japan. Kalman filtering theory was also introduced to this method to further its practical use (Sugimoto *et al.*, 2000). In this method, a conceptual rainfall model plays the role of bridging the gap between radar information and numerical weather prediction scales. However, this method has room to introduce dynamical concepts because the method assumes an unchanged wind field during the lead-time of prediction. Along this line, this paper shows relations between rainfall distribution and some dynamic indices that can be computed using a middle product of the prediction method. In other words, this paper shows the results of an investigation to determine how large a hidden potential the middle product has for introducing the dynamic concept into the prediction method.

7.1.3 Analysis of rainfall distribution over mountainous region

As mentioned above, it is very difficult to determine the properties of rainfall distribution in Japan, which is a mountainous region, due to the influence of topography. Additionally, due to physical restrictions, it is not possible to set up rain gauges at a large number of locations in such regions. As a result, rainfall distribution structures in mountainous regions are not yet obvious.

One of the common features of conventional studies is that the accumulation time scale of rainfall that is analyzed is relatively short, that is, the time scale of one or two rainfall events. Oki *et al.* (1990), for example, explained well the concept of the relation between topographic effect on accumulated rainfall distribution and its temporal-spatial scale, and reached the following conclusion. In the case that the accumulation time scale is a little longer than the temporal-spatial scale of an individual meteorological disturbance, that is to say, in the time scale of one rainfall event or daily rainfall, the topographic effect becomes very significant. The above conclusion is agreed with in this study. However if the rainfall distribution in such an accumulation time scale is paid attention to, it seems to be difficult to determine the properties of rainfall distribution as the topographic effect on rainfall varies significantly with each meteorological disturbance.

On the other hand, Nakakita *et al.* (1997), suggested the following. It may be possible to find a universal relation between rainfall and topography independently of the variation of rainfall with each disturbance, if the topographic effect over an even longer accumulation time scale is paid special attention to. That is to say, it is necessary to take such a long time scale into consideration that covers the scale of plural meteorological disturbances for the purpose of determining the universal properties of rainfall distribution.

In conventional studies the data obtained from ground-based rain gauges that are set at discrete locations are used as true rainfall data. However there seems to exist a limit of reproducibility of rainfall distribution in mountainous regions if it is analyzed by using such data, which doesn't have adequate observation density in mountainous regions.

In this study one of the properties of rainfall distribution, that is, a hierarchical time-scale structure in the dependence of rainfall distribution on topography is paid special attention to. It is attempted to determine the universal properties of the dependence on topography, and to make clear the rainfall distribution structure through the analysis of rainfall data observed by weather radars.

7.2 Short-term rainfall prediction by linear extrapolation

7.2.1 Development of short-term rainfall forecast with linear extrapolation in Japan

The first two methods in the area of the hydraulic engineering in Japan were proposed by Takeuchi (1978) and Shimogaki *et al.* (1978). It was just after the installation of the Akagiyama Radar in the Kanto District, which was the first operational radar of the Ministry of Construction. Takeuchi (1978), described the time variation of rainfall distribution by the strain tensor and used the judgment of man in identifying the time variation. In turn, Shimogaki *et al.* (1978) described the rainfall distribution by the normal probability density function with two variables and used the Kalman filtering theory in the prediction step. After those, Ohkura *et al.* (1983) proposed a method which uses a modified regression analysis in identifying movement of rainfall distribution, which is used in the operational forecast in the Ministry of Construction.

After the second operational radar named the Miyama Radar became operational in the Kinki District, Takasao *et al.* (1983); Shiiba *et al.* (1984); Takasao and Shiiba (1985) developed their own methods. At first, they proposed a method which identifies place dependent movement of rainfall distribution using a weighted regression analysis. They next proposed another method which uses the two dimensional translation equation in describing the time variation which will be outlined below. They have developed it as a method which can estimate the accuracy of prediction in real-time by introducing stochastic description in to the translation equation, which will be outlined in the next section. After those, Moriyama *et al.*

(1984), Jinno *et al.* (1990), and Kawamura *et al.* (1991) proposed methods which describe the time variation by the translation-diffusion equation aiming to predict rainfall distributions within a smaller observation area with a higher spatial observation resolution than those operational radars managed by the Ministry of Construction. Jinno *et al.* (1990) and Kawamura *et al.* (1991) investigated the prediction of rainfall distribution using a rainguage network which provides rainfall observations with high spatial and temporal resolution, too. Furthermore, they used stochastic description in the translation-diffusion equation in order to introduce stochastic characteristics of rainfall distribution. Finally, Hino (1985) proposed another method which uses the concept of the virtual load in describing rainfall distribution.

7.2.2 Outline of a method based on translation method

The short-term rainfall prediction method proposed by Shiiba *et al.* (1984) and Takasao and Shiiba (1985) is flexible in identifying the movement of horizontal rainfall distribution for operational purposes, and in introducing stochastic concepts into the method for evaluating the accuracy of prediction in real-time. The method and results are briefly outlined here.

7.2.2.1 Translation model

The method assumes that the time variation of the horizontal rainfall distribution $r(x,y,t)$ can be described by

$$\frac{\partial r}{\partial t} + u\frac{\partial r}{\partial x} + v\frac{\partial r}{\partial x} = w \tag{7.1}$$

according to the works by Tatehira and Makino, (1974). Here, (u,v) indicates the translation vector by which the horizontal rainfall distribution is assumed to be translated and w indicates the growth-decay rate, i.e. the rate of increase in rainfall strength along its movement. Note that (u,v) does not indicate the horizontal wind velocity and w does not indicates the vertical wind velocity either. A point of this method is that it is assumed that

$$\begin{cases} u(x,y) = c_1x + c_2y + c_3 \\ v(x,y) = c_4x + c_5y + c_6 \\ w(x,y) = c_7x + c_8y + c_9, \end{cases} \tag{7.2}$$

such that parameters $c_1,\ldots\ldots, c_9$ can be identified by the method of linear least squares using observed rainfall distribution, and that the translation vector can express the patterns of the movement of the distribution, other than uniform translation, such as rotation and shear strain. In addition to these, the prediction can be done fully analytically by the method of characteristics.

7.2.2.2 Identification of translation vector

We can identify u, v and w, i.e. c_1,....., c_9, by the method of linear least squares, using the difference equation of Eq.(7.1) approximated by the central difference scheme as follows.

Let the rectangular horizontal area covering a radar observation area be subdivided by rectangular sub-areas of $\Delta x \times \Delta y$ and let

$$\begin{cases} x_i = (i - \frac{1}{2})\Delta x, \ i = 1, \quad ,M \\ y_j = (j - \frac{1}{2})\Delta y, \ j = 1, \quad ,N \\ t_k = k\Delta t, \ k = 1, \quad ,K - 1. \end{cases} \tag{7.3}$$

Here, Δt is the time interval of the radar observation, M and N are the number of sub-areas along the x-axis and y-axis, respectively, and $(K+1)\Delta t$ is the duration over which the past rainfall distributions $r(x,y,t_0\text{-}K\Delta t)$,....., $r(x,y,t_0)$ are used for identifying the translation vector. The parameters c_1, ..., c_9 are identified so that

$$J_c = \sum_{k=-K}^{-1} \sum_{i=2}^{M-1} \sum_{j=2}^{N-1} \upsilon_{ijk}^2 \tag{7.4}$$

is minimized. Here,

$$\begin{aligned} \upsilon_{ijk} &= [\frac{\partial r}{\partial t}]_{ijk} + (c_1 x + c_2 y + c_3)[\frac{\partial r}{\partial x}]_{ijk} \\ &+ (c_4 x + c_5 y + c_6)[\frac{\partial r}{\partial y}]_{ijk} - (c_7 x + c_8 y + c_9) \end{aligned} \tag{7.5}$$

As mentioned before, values of the partial derivatives are approximated by the central difference scheme. Parameters are sequentially identified using the Square Root Information Filter, which was used in controlling rockets (Bireman (1977)).

7.2.2.3 Prediction of rainfall distribution

Assuming the translation vectors are time invariant for several hours, the prediction is performed by tracing backward along the characteristic curves of the simultaneous differential equations

$$\begin{cases} \frac{dx}{dt} = c_1 x + c_2 y + c_3 \\ \frac{dy}{dt} = c_4 x + c_5 y + c_6 \\ \frac{dr}{dt} = c_7 x + c_8 y + c_9, \end{cases} \tag{7.6}$$

which are equivalent to Eqs. (7.1) and (7.2). In other words, the prediction $r(x,y,t_0+t)$ can be obtained fully analytically by

$$\begin{aligned} r(x,y,t_0+t) &= r(x(t_0),\ y(t_0),\ t_0) - S(\tau; c_1, \cdots, c_9)\begin{bmatrix} x \\ y \\ 1 \end{bmatrix}, \\ \begin{bmatrix} x(t_0) \\ y(t_0) \end{bmatrix} &= R(-\tau; c_1, \cdots, c_6)\begin{bmatrix} x \\ y \\ 1 \end{bmatrix}, \end{aligned} \qquad (7.7)$$

where R and S are 2×3 and 3×3 matrices, respectively.

7.2.2.4 Example of the prediction

Figure 7.2 shows rainfall distributions at 17:00 JST, 18:00 JST and 19:00 JST on Aug. 1, 1982, which were observed by the Miyama radar rainguage located on the center of Kinki District, Japan, and managed by the Ministry of Construction. The radar observes rainfall every 5 minutes with a horizontal resolution of 3 km × 3 km. The rainfall event accompanied typhoon 8210. We can guess that the eye of the typhoon was located near the radar observation area judging from the shape of the curved rainbands which rotate counterclockwise.

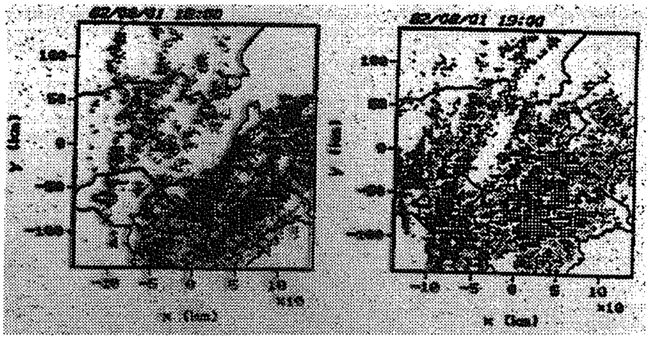

Radar Image

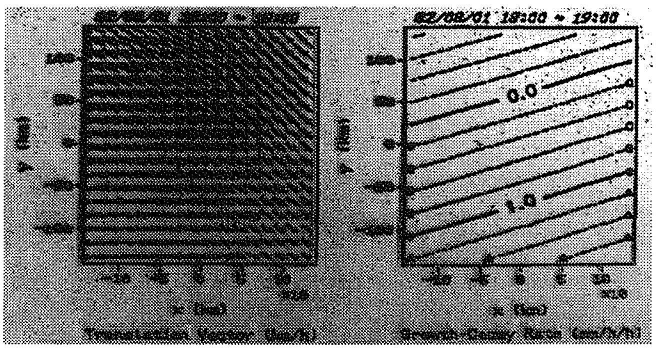

Translation vector and growth-decay rate

Figure 7.2: Observed rainfall and identified translation vector and growth-decay rate

Figure 7.2 also shows identified translation vector ((u,v)) and the growth-decay rate w. The upper and lower lines correspond to the identifications using every 5 minute rainfall distribution from 17:00 JST through 18:00 JST and from 18:00 JST through 19:00 JST, respectively. Notice that the identified translation vectors capture the features of the movement of rainfall distribution well, and that the time variation of the vectors is small. On the contrary, the time variation of the growth-decay rate w is large although the identified distribution for each period captures the features of growth and decay of rainfall distributions well.

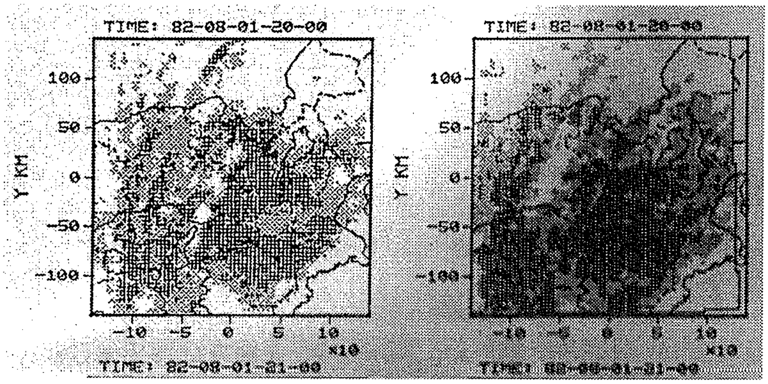

Observed Predicted

1 hour ahead

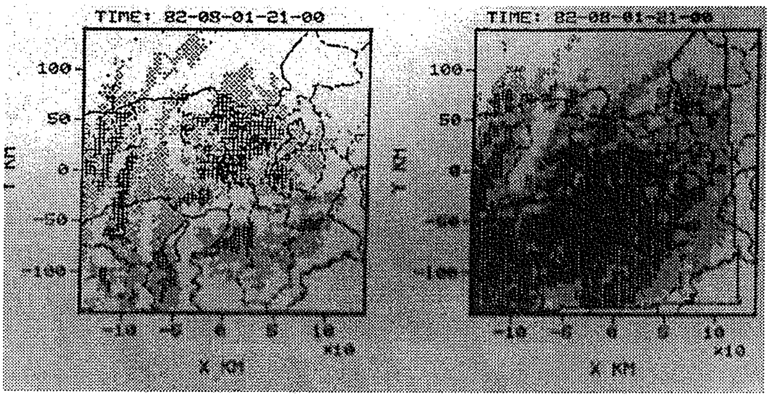

Observed Predicted

2 hour ahead

Figure 7.3: Observed rainfall and predicted rainfall

Figure 7.3 shows predicted rainfall with corresponding radar observed rainfall up to 2 hours ahead. The start time is 19:00 JST. Therefore, the translation vector (u,v) and the growth-decay rate w shown on the lower line in Figure 7.3 were used here. We can see that the movement of the spiral shaped rainbands are predicted fairly well. On the other hand, the predicted rainfall intensity is larger than the observed one. This can be said more for the 2 hour ahead prediction than for the 1 hour ahead prediction. This over prediction results from the fact that the growth-decay rate w is not time invariant.

To show the fact above and to examine the properties of changes with time in the translation vector and the growth-decay rate fields, we estimated the c_n values serially at 15-min. intervals. The time series data obtained for the components $u_0 = c_3$ and $v_0 = c_6$ of translation vector at the radar site, and the coefficients c_7, c_8, and c_9 in the expression for growth-decay rate show that, except for the coefficients in the expression for growth-decay rate, the time series are highly serially dependent. This gives us the basis for extrapolating the estimated rainfall pattern motion to the future, with the reservation that too long a data set should not be used for the parameter estimation because there are apparent trends in these time series. In contrast, the time series of the coefficients in the expression for the growth-decay rate can be thought of as almost random with zero means.

7.3 Short-term stochastic rainfall prediction

The short-term rainfall prediction method outlined above has been extended by Takasao, Shiiba, and Nakakita, (1994), to a stochastic method so that the method could provide in real-time the accuracy of the areal rainfall predicted using radar information. The extension was carried out based on an investigation of the stochastic properties of the prediction model's parameters. Here, a case study using actual rainfall distribution observed by a radar during a typhoon passage over Japan will be presented. The results show that we can predict the mean square error of predicted areal rainfall at least within 1 hour ahead using the method proposed here.

7.3.1 Introduction of random variable

Based on the fact that the time series of the coefficients in the expression for growth-decay rate can be thought of as almost random with zero means, they assume the Eq.(7.1) should be modified to

$$\frac{\partial r}{\partial t} + u\frac{\partial r}{\partial x} + v\frac{\partial r}{\partial x} = \varepsilon(x, y, t), \tag{7.8}$$

Here, $\varepsilon(x,y,t)$ is a random variable which satisfies the following conditions;

$$E[\varepsilon(x, y, t)] = 0, \quad E[\varepsilon(x, y, t)\varepsilon(x', y', t')] = Gf(x - x', y - y', t - t'), \tag{7.9}$$

where E means the expectation. Given the function f, we could identify the value of G using rainfall information which is used in identifying u, v, and w.

Let $S(x,y)$ be a $\Delta x \times \Delta y$ rectangular region, the center of which is placed at (x,y), and $\Delta r(x,y,t)$ be the deviation from the areal mean rainfall over the region $S(x,y)$ at the time $\underline{t}$. Then the variance of the predicted areal mean rainfall is the same as that of $\Delta r(x,y,t)$:

$$\Delta R\,(x, y, t) = \frac{1}{\Delta x \Delta y}\int_{S(x,\,y)} \Delta r\,(\xi, \eta, t)\, d\xi\, d\eta\,. \tag{7.10}$$

On the other hand, since $\Delta r(x,y,t)$ satisfies

$$\frac{\partial \Delta r}{\partial t} + u\frac{\partial \Delta r}{\partial x} + v\frac{\partial \Delta r}{\partial y} = \varepsilon(x, y, t), \tag{7.11}$$

therefore,

$$\Delta r(\xi, \eta, t) = \int_0^t \varepsilon(\xi_*(\xi, \eta, \tau), \eta_*(\xi, \eta, \tau), \tau)\, d\tau\,, \tag{7.12}$$

$$\begin{aligned} \frac{d\xi_*}{d\tau} &= u \quad (= c_{11}x + c_{12}y + c_{13}), \;\; \xi_*(t) = \xi\,, \\ \frac{d\eta_*}{d\tau} &= v \quad (= c_{21}x + c_{22}y + c_{23}), \;\; \eta_*(t) = \eta\,. \end{aligned} \tag{7.13}$$

Therefore, the variance of the error of the predicted areal rainfall can be predicted by the equation:

$$\begin{aligned} E[\Delta R(x, y, t)^2] &= \frac{1}{(\Delta x \Delta y)^2} E[\{\int_{S(x,\,y)} \int_0^t \varepsilon(\xi_*(\xi, \eta, \tau), \eta_*(\xi, \eta, \tau), \tau)\, d\tau d\xi d\eta\}^2\,] \\ &= \frac{G}{(\Delta x \Delta y)^2}\int_0^t \int_0^t \int_{S(x,\,y)} \int_{S(x,\,y)} f(\xi_* - \xi_*', \; \eta_* - \eta_*', \; \tau - \tau'\,)\, d\xi\, d\xi'\, d\eta\, d\eta'\, d\tau\, d\tau'\,, \end{aligned} \tag{7.14}$$

Here, notice that in the derivation of equations above, it is not necessary for the shape of region $S(x,y)$ to be rectangular.

7.3.2 Case study using radar information

This method was applied to the rainfall brought by typhoon T8210 which is the same event for which we showed the results of the prediction in the second section.

Firstly, we have to determine the function f based on real observations. Since w is a random process in time with a mean of 0 as shown in the second section, it would be quite reasonable if we assume that

$$f(x - x', \; y - y', \; t - t') = \delta(\,t - t'\,)\, g(\,x - x', \; y - y'\,)\,, \tag{7.15}$$

where $\delta(t)$ is Dirac's Delta function. Supposing that

$$\underline{\varepsilon}(x, y) = \int_{-T}^{0} \varepsilon(x, y, \tau)d\tau, \tag{7.16}$$

it follows that

$$E[\underline{\varepsilon}(x, y)\,\underline{\varepsilon}(x', y')] = G\,T\,g(x - x', y - y'). \tag{7.17}$$

Next we must find out whether the function g depends on only the distance between the two points concerned and what the shape of the function is. We examined these using the 5-minute interval rainfall distributions ranging from 18:00 JST through 19:00 JST on Aug. 1. 1982. This means $T = 1$ hour. Computing the results of the left-hand side of Eq. (7.16) in terms of various distances between two points inside the radar observation coverage, it is found that the function g has the form

$$g(x - x', y - y') = \exp[-\alpha\{(x - x')^2 + (y - y')^2\}^{1/2}] \tag{7.18}$$

and that G = 26.73[mm2/h3], α = 0.125[km-1]. The identification of the two parameters were carried out using the method of least squares. Because the correlation decreases as the distance of the two points concerned increases, the comments regarding the rate of increase of the variance from the previous section, could basically be applied to this case as well. Namely, Eq.(7.18) satisfies that $E[\varepsilon(x,y,t),\varepsilon(x',y',t')]$ is a monotonically decreasing function in terms of the distance between (x,y) and (x',y').

We carried out the integration in the right-hand side of Eq.(7.14) using the trapezoidal formula with intervals of 3km in space and 5 minutes in time, while we analytically solved Eq.(7.13). Notice that the predicted variance is independent of (x,y), i.e. the position of the center of the region $S(x,y)$. Here, we refer to the predicted variance as being a theoretical value. In the cases of $\Delta x=\Delta y=$6km, and $\Delta x=\Delta y=$12km, we compared the theoretical values and computed values which were obtained by direct computation of the left-hand side of Eq.(7.14) using observed and predicted rainfall distributions.

The results showed that the theoretical and calculated values coincide fairly well up to a lead time of 55 minutes, which indicates it is reasonable to predict the mean square error of predicted areal rainfall intensity within about 1 hour ahead. In addition, we can see that the values of the mean square error of both theoretical and calculated values increase proportionally with time in both cases. This means that both assumptions of Eq.(7.18) were reasonable. However, we can imagine the mismatching between the theoretical and calculated values beyond 1 hour ahead. We can guess the reason would be that the increase of the prediction error of the translation vector would collapse the assumption that $\varepsilon(x,y,t)$ is uncorrelated in terms of time. On the contrary, this means that we can predict the mean square error by the proposed method as far as the translation vectors are serially independent.

7.4 Short-term rainfall prediction using a conceptual rainfall model and volume scanning radar

7.4.1 Outline of the short-term prediction method

As a basic environmental meso-α scale field, distributions of air pressure, wind velocity, air temperature and water vapor are estimated using the grid point values from a numerical weather prediction. Grid point values (for three hourly intervals) from a numerical weather prediction are generated by the Regional Spectral Model developed by the Japan Meteorological Agency and are known as Grid Point Value data (GPV data). The estimated wind field is kept unchanged throughout the prediction process. At the initial time, three-dimensional distributions of water content and rainfall intensity, as meso-β scale information, are estimated from radar observations. Also the initial three-dimensional distribution of the conversion rate of water vapor is estimated as meso-β scale information using already estimated distributions. Next, based on these distributions, the three-dimensional distribution of parameters of the conceptual rainfall model is identified as meso-β scale information. After horizontally translating the above estimated parameter's distribution, three-dimensional distributions of the conversion rate and then the rainfall intensity are predicted. The reason for the simple translation of the parameter's distribution is that we strive for by parameter's distribution of a conceptual rainfall model, modeling a field not affected by topography.

It should be noted that the method does not use the predicted GPV rainfall itself. The horizontal and temporal resolutions of the GPV data are still low compared to those of radar information. Thus, the additional radar information allows the GPV subgrid variability of rainfall to be predicted. This subgrid variability is crucial to accurate flood forecasting during extreme events in mountainous topography. The physically-based model utilizes observations of a volume scanning radar as information on meso-β scale and predictions of a numerical weather model as meso-α scale information. The model parameters can be taken as a kind of index which shows degree of shortages of vertical vapor flux estimated by using basic meso-α wind field. Thus, the conceptual rainfall model plays the role of bridging the gap between radar information and numerical weather prediction scales.

Specifically, the following three conservation equations are used:

$$\frac{\partial \theta}{\partial t} + u\frac{\partial \theta}{\partial x} + v\frac{\partial r}{\partial y} + w\frac{\partial r}{\partial z} = \frac{LQ}{\rho_0 C_p}\left(\frac{1000}{p_0}\right)^{R_d/C_p} \tag{7.19}$$

$$\frac{\partial m_v}{\partial t}+u\frac{\partial m_v}{\partial x}+v\frac{\partial m_v}{\partial y}+w\frac{\partial m_v}{\partial z}=-\frac{Q}{\rho_0} \tag{7.20}$$

$$\frac{\partial m_l}{\partial t}+u\frac{\partial m_l}{\partial x}+v\frac{\partial m_l}{\partial y}+w\frac{\partial m_l}{\partial z}=\frac{Q}{\rho_0}+\frac{\rho_w}{\rho_0}\frac{\partial r}{\partial z} \tag{7.21}$$

while the following equation for estimating the rainfall intensity is adopted only for prediction stage:

$$r=\frac{\rho_w}{\rho_0}W_t\,m_l\,. \tag{7.22}$$

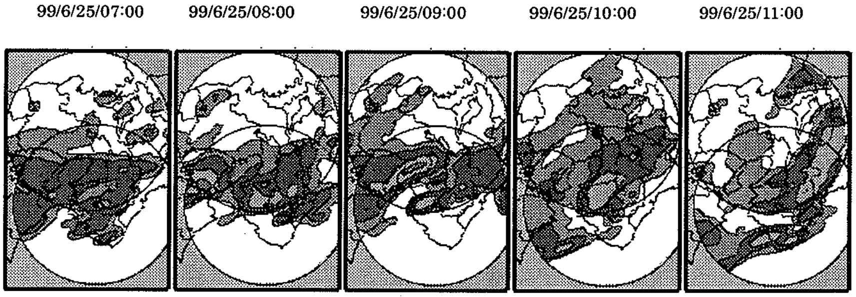

Observed Rainfall

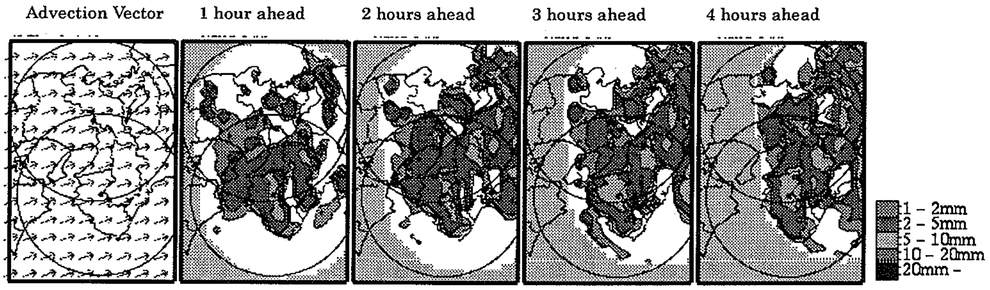

Predicted Rainfall

Figure 7.4: Rainfall distribution predicted using conceptual rainfall model assimilated by 3D radar information.

It should be noted that (7.19)-(7.22) are used in both conceptual rainfall models. In (7.19)-(7.22), (x,y,z) represents the Cartesian coordinate system, (u, v, w) is the wind vector, θ is the potential temperature, m_l and m_v are the mixing ratios of the liquid water content and water vapor respectively, r is the rainfall intensity, Q is the water vapor conversion rate, ρ and ρ_w are densities of the air and liquid water respectively, L is the latent heat of condensation, Cp is the specific heat at constant pressure, R_d is the individual gas constant for dry air, and p is the air pressure in hPa. Wt is the averaged relative fall velocity of water particles computed by the empirical equations of Ogura and Takahashi (1971).

The most important variable in (7.19)-(7.22) is the water vapor conversion rate Q because its prediction will in turn affect the predictions of other variables including rainfall intensity r. The "conversion rate" is defined as the amount of water vapor that is converted into precipitation particles per unit time and unit volume. The initial three-dimensional distribution of Q is estimated using the distributions of m_l and r based on the conservation equation (7.21). The conceptual rainfall model then predicts the time series of the distribution of Q, which results in rainfall prediction. It should be noted that there is no provision for prediction of clouds because conventional radars cannot detect cloud particles.

The Instability Field IF model is defined by the following equation:

$$\frac{\partial}{\partial t}\{(1-\alpha)m_s\}+u\frac{\partial}{\partial x}\{(1-\alpha)m_s\}+v\frac{\partial}{\partial y}\{(1-\alpha)m_s\}+w\frac{\partial}{\partial z}\{(1-\alpha)m_s\}=-\frac{Q}{\rho_0} \quad (7.23)$$

where, m_s is the saturation mixing ratio computed from air pressure and potential temperature using the empirical formula given by Murray (1967) and Pielke (1984).

With the radar estimated conversion rate Q we can then compute the initial three-dimensional distribution of $\alpha(x,y,z)$ from (7.23) when Q is not zero. Here, the three-dimensional distribution of the parameter α defines the instability field of the IF model. The relation $1-\alpha = m_v/m_s$ is found to hold only after α is identified. Using the past and present three-dimensional distributions of radar reflectivity, past and present instability fields can be identified.

Equation (7.23) assumes water vapor beyond a newly defined saturation mixing ratio, $(1-\alpha)m_s$, condenses to the precipitation particles (or precipitation particles evaporate when water vapor mixing ratio is less than $(1-\alpha)m_s$). In other words, domains with large values of parameter α are prone to relatively heavy rainfall. Therefore, the parameter α can be taken as a kind of index which shows the degree of shortages of vertical water vapor flux brought on by the used basic meso-α wind field. The reason for the shortages is that the used wind field, corresponding to the meso-α scale, is rather stratiform; this is in contrast with organized strong convection accompanied by the moisture, which is expected to exist in the cumulative clouds in the scale of meso-β.

7.4.2 Case study

Figure 7.4 shows radar-observed and predicted rainfall distributions for hourly intervals. The translation vector of IF (not that of rainfall distribution) is identified using time series of horizontal rainfall distributions for the past 30 minutes according to the operationally used method proposed by Takasao and Shiba (1985). The upper line shows the radar-observed distributions and the right column shows predicted distributions both for the height of 3.5km. The starting time of prediction is 07:00 JST, June 25 in 1999.

It can be seen that gradual expansion of the overall rainfall area and local growth of the rainfall area over the southern mountainous region are well predicted. These kinds of predictions have not been possible with liner extrapolation of radar echo pattern.

7.5 Hierarchical time-scale structure in the dependence of rainfall distribution on topography

7.5.1 Hierarchical time-scale structure of rainfall distribution

Spatial rainfall distributions at accumulation time scales of between 5 and 25 days are shown in Figure 7.5. Here, the radius of the target domain is 120 km and the resolutions of radar information are three km in space and five minutes in time. In this figure it is shown that the relation between rainfall distribution and topographic altitude becomes obvious as the accumulation time scale of rainfall increases. Additionally it is shown that the relation doesn't vary so significantly in the

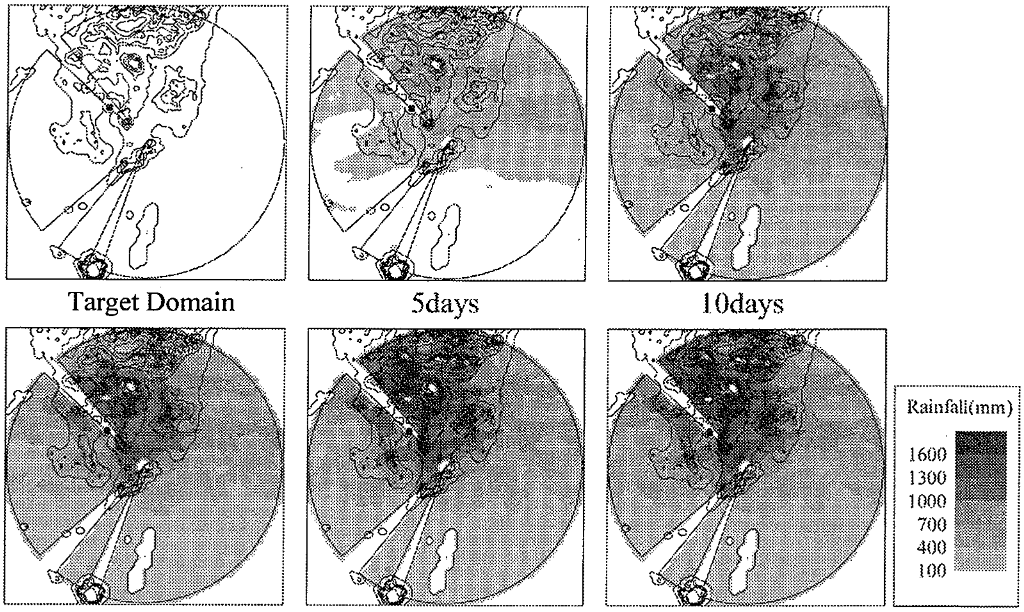

Target Domain 5days 10days

15days 20days 25days

Figure 7.5: Accumulated rainfall distributions at various time scales. (Southern Kyushu region, from August 1, 1993)

accumulation time scale longer than approximately 20 days, and appears to converge into a constant relation as the time scale increases.

The correlation coefficient (C.C) between *T*-days-accumulated rainfall distribution for each point, $R_T(x,y)$, and topographic altitude, $h(x,y)$, is then calculated

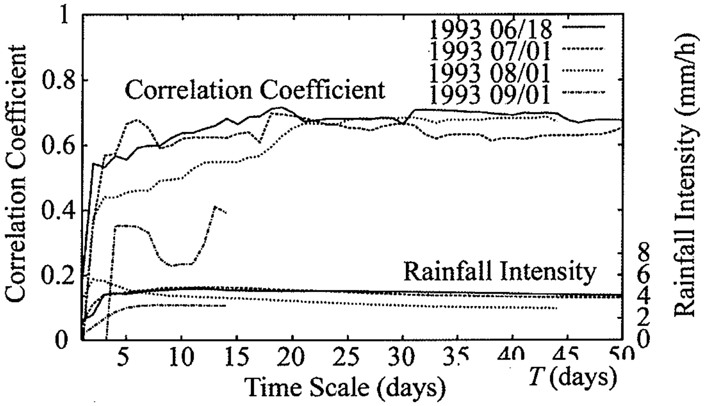

Figure 7.6: Correlation coefficient between *T*-days-accumulated rainfall R_T (x,y) and topographic altitude $h(x,y)$. (southern Kyushu region)

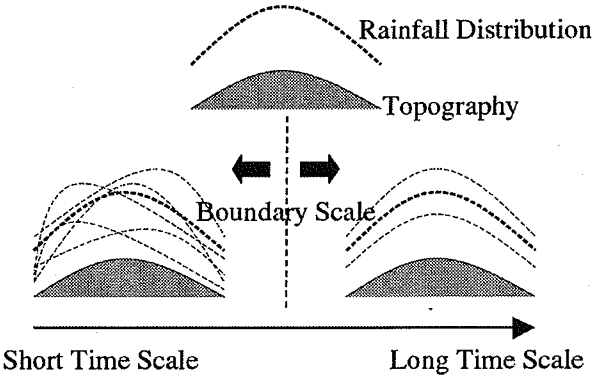

Figure 7.7: Schematic figure of the hierarchical time-scale structure of rainfall distribution.

while changing the accumulation time scale. The results are presented in Figure 7.6. This figure also demonstrates that the correlation coefficient increases as the accumulation time scale increases, and that after the time scale reaches approximately a month the value becomes almost constant.

These properties of rainfall distribution demonstrate the following. Although the relation between short time-scale rainfall distribution (ex. one-event rainfall distribution) and topography varies in a number of ways, predominant topographic effects and the universal relations can be found only if the relation between relatively long time-scale rainfall distribution (ex. one-week or one-month rainfall distribution) and topography is taken into consideration. This concept is represented in a schematic form in Figure 7.7.

In this study this feature of rainfall distribution is called" hierarchical time-scale structure in the dependence of rainfall distribution on topography". Drawing attention to this, an attempt is made to quantify the dependence of rainfall distribution on topography, which has been difficult in conventional studies.

7.5.2 Indices for the expression of the hierarchical time-scale structure

7.5.2.1 Properties of rainfall distribution in the Kinki region of Japan

In this section the properties of rainfall distribution in the Kinki region of Japan are investigated. 0.3 mm/h is chosen as a threshold value for the effective rainfall time *Te*. This investigation shows that the relation between rainfall distribution and topographic altitude becomes apparent as the accumulation time *Te* increases, as is observed with the rainfall distribution in southern Kyushu (Figure 7.5). Such a tendency is so outstanding around the Kii Mountains, which is based in the south of the Kinki region. However, unlike the southern Kyushu region, there exists some regions where the dependence of rainfall on topography is not apparent, for example the coastal regions of the Sea of Japan.

The correlation coefficient between *Te*-days-accumulated rainfall distribution

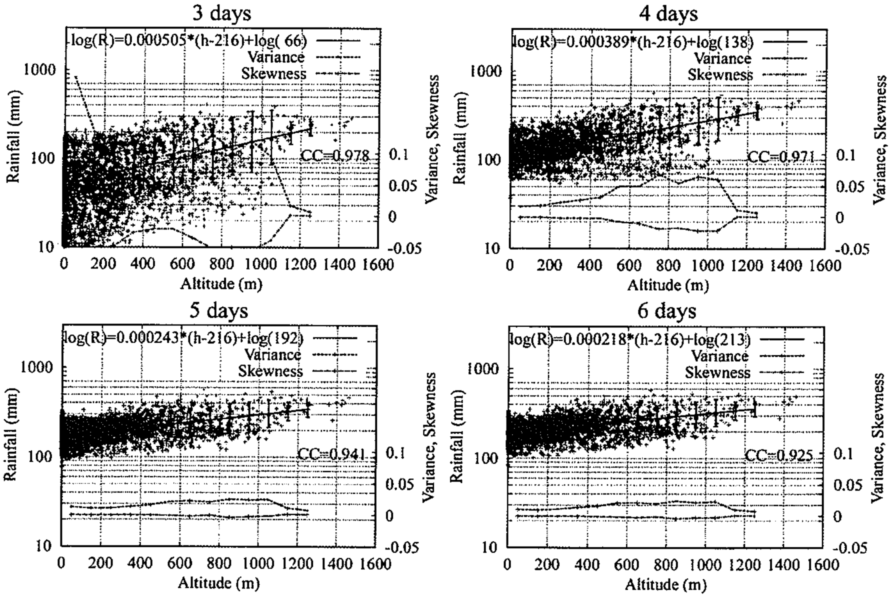

Te = 3 days : September 1～September 21　　*Te* = 4 days : September 1～September 24
Te = 5 days : September 1～September 25　　*Te* = 6 days : September 1～September 27

Figure 7.8: Accumulated rainfall and topographic altitude at each accumulation time scale *Te*. (Kinki region, from September 1, 1998)

and topographic altitude is calculated, as it was for Figure 7.6. When compared to the result in Figure 7.6, features different from those of the southern Kyushu region are found, that is, the correlation coefficient doesn't increase with rainfall accumulation and doesn't tend to converge to a constant value. As a result, it is necessary to use another index besides correlation coefficient so as to analyze the hierarchical time-scale structure of rainfall distribution in the Kinki region. In the following section another index is introduced.

7.5.2.2 Analysis of the hierarchical structure through classification of topographic altitude

The figures displayed in Figure 7.8 represent the relation between topographic altitude, on the horizontal axis, and *Te*-days-accumulated rainfall, on the vertical axis. In these figures all points in the target domain are plotted. Each figure represents a case with accumulation time scales *Te* of between 3 days and 6 days. In every case it is shown that accumulated rainfall tends to increase on the whole with the increase of topographic altitude. Although such a qualitative tendency has already been reported in conventional studies which used ground-based rain-gauge data, it remains one of the challenges to formulate such properties of rainfall distribution.

Here, the topographic altitude is classified at 100 m intervals, and then a regression line is made by using the special averages of accumulated rainfall for each class. The results are shown in Figure 7.8. These results demonstrate that it may be possible to determine the dependence of rainfall distribution on topography, since the correlation coefficient between the special averages of accumulated rainfall and topographic altitude for each class indicates a high value, which is over 0.9. Additionally in each class, the variance and skew ness of accumulated rainfall on a logarithmic axis, log(R), from the regression line are calculated. The results are also shown in Figure 7.8. These results show that the variance of accumulated rainfall in each class decreases with the increase of accumulation time, and converges into a constant value. That is to say, the relation between rainfall distribution and topographic altitude converges into a constant relation as rainfall accumulation time increases. This is the feature of hierarchical time-scale structure of rainfall distribution.

Even in these cases, the variance decreases as the accumulation time scale *Te* increases, and then converges into an almost constant value after the *Te* increases to be over about 5 days. This feature indicates the existence of a hierarchical time-scale structure and that 5 days of *Te* is one of the boundary time scales. Additionally the slope of the regression line also converges into an almost constant value at the point of about 5 days of *Te*. As described above, the slope of the regression line converges into an almost constant value, and the variance also converges into a constant value. That is to say, it is demonstrated that the dependence of rainfall distribution on topography can be quantified by using such statistical values as an index only if the accumulation time of rainfall distribution is over a certain value, since the regression line represents an expectation of accumulated rainfall distribution and forms the basis of this analysis.

7.6 Conclusion

As shown above, radar information can be effectively used for rainfall prediction and analysis of rainfall distribution. This distributed information with high resolution should find further use in other hydrological purposes such as analysis of scale effect of hydrological processes with the distributed hydrological modeling. Also improving design rainfall should be taken into consideration.

References

Bireman, G. L. (1977): Factorization method for discrete sequential estimation, Academic Press.

Browning, K. A. and C. G. Collier (1989): Nowcasting of precipitation systems, *Review of Geophysics*, 27 No.3, 658-664.

Georgakakos, K. P. and R. L. Bras (1984a): A hydrologically useful station precipitation model, Part I: Formulation, *Water Resour. Res.*, 20, No.11, 1585-1596.

Georgakakos, K. P. and R. L. Bras (1984b): A hydrologically useful station precipitation model, Part II: Applications, *Water Resour. Res.*, 20, No.11, 1597-1610.

Hino, M. (1985): Short-term rainfall prediction by "Virtual Load" method, Proc. 29th Japanese Conf. on Hydraulics, JSCE, pp.203-208 (in Japanese with English abstract).

Jinno, K., A. Kawamura, R. Berndtsson, M. Larson, and J. Niemczynowicz (1990): A convective dispersion model for real-time prediction of urban-scale rainfall, Proc. of 5th Int. Conf. on Urban Storm Drainage.

Kawamura, A., K. Jinno, J. Niemczynowicz, R. Berndtsson, and M. Larson (1991): On the temporal and spatial characteristics of short-term urban-scale rainfall and its real-time prediction, Proc. Hydraulic Engineering, JSCE, 35, pp.63-68 (in Japanese with English abstract).

Lee, T. H. and K. P. Georgakakos (1990): A two-dimensional stochastic-dynamical quantitative precipitation forecasting model, *J. Geophys. Res*, 95-D3, 2113-2126.

Moriyama, T., M. Hirano, T. Kawarada, and H. Hara (1984): Short-term rainfall prediction by use of a translation-diffusion model, Proc. 29th Japanese Conf. on Hydraulics, JSCE, pp.209-214 (in Japanese with English abstract).

Nakakita, E., T. Sugahara, N. Okada, and S. Ikebuchi (1997): Temporal-spatial rainfall distribution characteristics depending on topographical features (in Japanese with English abstract), Annuals of the Disaster Prevention Research Institute of Kyoto University, No.40 B-2, pp.275-287.

Rahuel, J.L., Holly, F.M., Jr., Chollet, J.P., Belleudy, P.J., and Yang, G. (1989). "Modeling of river bed evolution for bedload sediment mixtures." *J. Hydr. Engrg.*, ASCE, Vol. 115, No. 11, pp. 1521-1542.

Nakakita, E., M. Shiiba, S. Ikebuchi, and T. Takasao (1991): Advanced use into rainfall prediction of three-dimensionally scanning radar, Hydrological applications of weather radar, edited by I. C. Clukie and C. G. Collier, 391-408.

Nakakita, E., S. Ikebuchi, N. Sawada, M. Shiiba and T. Takasao (1992): A short-term rainfall prediction method using reflectivity detected by three-dimensionally scanning radar, *Preprints of 2nd Int. Symp. on Hydrological Applications of Weather Radar*, F1, Hannover, Germany, 10pages.

Nakakita, E, S. Ikebuchi, T. Nakamura, M. Kanmuri, M. Okuda and A. Yamaji (1996): Short-term rainfall prediction method using a volume scanning radar and grid point value data from numerical weather prediction, *J. Geophys. Res.*, 101-D21, 26,181-26-197.

Oki, T., K. Mushiake, and T. Koike (1990): Rainfall distribution at storm event estimated by orography and wind direction (in Japanese with English abstract), Journal of the Japan Society of Civil Engineers, Vol.417 II-13, pp.199-207.

Shiiba, M., T. Takasao, and E. Nakakita, (1984): Investigation of short-Term rainfall prediction method by a translation model, Proc. 28th Japanese Conf. on Hydraulics, JSCE, pp.423-428 (in Japanese).

Shimogaki, H., A. Murota, and T. Etho (1978) : Analysis and on-line prediction for spatial distribution of precipitation by pluviometoric radar systems, Proc. 22nd Japanese Conf. on Hydraulics, JSCE, pp.169-174 (in Japanese with English abstract).

Sugimoto, S., E. Nakakita, S. Ikebuchi (2001): A stochastic approach to short-term rainfall prediction using a physically based conceptual rainfall model, *J. Hydrol.*, 242, 137-155.

Suzuki, Y., E. Nakakita, and S. Ikebuchi (2002): Study on the dependence properties of rainfall distributions on topographic elevations, Journal of Hydroscience and Hydraulic Engineering, Vol.20, No.1.

Takasao, T. and Shiiba (1980): Flood forecasting by the state-space method, Annuals of Disaster Prevention Res. Inst., Kyoto Univ., No.23, B-2, pp.211-226 (in Japanese with English abstract).

Takasao, T., M. Shiiba and K. Takara (1982a): Building of a lumped runoff model and on-line runoff prediction techniques, Annuals of Disaster Prevention Res. Inst., Kyoto Univ., No.25, B-2, pp.221-243 (in Japanese with English abstract).

Takasao, T., M. Shiiba and K. Takara (1982b): A basic study on real-time runoff prediction by a storage model, Annuals of Disaster Prevention Res. Inst., Kyoto Univ., No.25, B-2, 245-267 (in Japanese with English abstract).

Takasao, T., M. Shiiba and E. Nakakita (1983): Short-term rainfall prediction by a radar rainguage. Annuals, Disaster Prevention Res. Inst., Kyoto Univ., No.26-B-2, pp.165-179 (in Japanese with English abstract).

Resources Systems, pp.117-132. Proc. 22nd Japanese Conf. on Hydraulics, JSCE, 161-168 (in Japanese with English abstract).

Takasao, T. and M. Shiiba (1985): Development of techniques for on-line forecasting of rainfall and runoff, Natural Disaster Science, 6, No.2, pp.83-112.

Takasao, T., M. Shiiba and E. Nakakita (1994): A real-time estimation of the accuracy of short-term rainfall prediction using radar, Stochastic and Statistical Methods in Hydrology and Environmental Engineering, edited by K.W. Hipel, Volume 2, Kluwer Academic Publishers, pp.339-351.

Takeuchi, K., (1978): Short time forecast of determination of the precipitation area and its intensity distribution, Proc. 22nd Japanese Conf. on Hydraulics, JSCE, pp.161-168 (in·Japanese with English abstract).

Tatehira, R., and Y. Makino (1974): Use of digitized echo patterns for rainfall forecasting, J. Met. Res., Japan Met. Agency, No.26, pp.187-199 (in Japanese with English abstract).

Chapter 8

Water Resources Management and Planning

Tomoharu Hori
Graduate School of Global Environmental Studies, Kyoto Univ.
Yoshida Honmachi, Sakyo-ku, Kyoto 606-8501, JAPAN
Phone: +81-75-753-5095, fax: +81-75-753-4907
E-mail: hori@wr.kuciv.kyoto-u.ac.jp

8.1 Introduction

It is said that 1.4 billion km^3 of water exists on the earth. Most of it, 97.5 %, exists in the ocean as salty, water and fresh water makes up 2.5 %. Most of the fresh water exists as ice in Arctic and Antarctic regions, while inland fresh water accounts for only 0.8 % of all fresh water. The major part of inland water, however, is ground water and only 0.01 % of that water on the earth remains in rivers and lakes, and is accessible to us. It is needless to say that we cannot utilize all of the 0.01 % of the accessible water. It is a surprising fact that we live depending on such a small amount of water resources.

The key characteristic of water is that it is a circulating resource. In contrast to from fossil fuel, water dose not disappear when people use it. Thus although the available amount of water resources is limited for a fixed period, we can use it enduringly unless our utilization system becomes inappropriate. But it should be emphasized that the circulation of water is uneven in time and space. Techniques of water resources engineering have been developed so far to dissolve the resulting mal-distribution and produce stable accessible water. Dam reservoirs are designed to flatter the temporal distribution of river flows resulting in the development of new water resources. Water distribution systems consist of pipes and channel networks, and have made it possible for people to live in places sepaerated from water source areas.

Another characteristic of water to be emphasized is that it is an environmental resource. No creature on earth can live without water. Rivers and lakes are important places for a lot of creatures and provide biological diversity. The waterfront is a basic region for human beings to enjoy wonderful and precious nature. In development and management of water resources, we must consider preservation of water quantity and quality as well as the total ecosystem.

Circumstances surrounding water resources are now greatly uncertainty. Water circulation systems on regional and global scale inherently contain uncertainty. But we have to note that in recent years global climate change has brought about a large impact on the water circulation system, which has increased the uncertainty in water resources systems. IPCC concluded in its third assessment report (IPCC, 2001) that most global warming observed during the past five decades has been a result of human activities, and that many physical and eco-systems on the earth have begun to be affected by recent warming. No clear evidence to indicate a significant change in precipitation has been detected yet. Meanwhile it is said that global climate change may make the unevenness of the distribution of water resources in time and space worse. Therefore efforts should be devoted to increase the reliability of existing facilities or to utilize them in more efficient ways. In this course, from the viewpoint of effective use of water resources, some basic concepts and techniques for water resources development and management are presented.

8.2 Water resources development

8.2.1 Basic design scheme of a reservoir

A reservoir is a fundamental facility to smoothen the temporal variability of water flow in a river. Since available water in the natural condition is constrained by the minimum flow discharge, reservoirs are designed to store the excess flow, and to release it when the natural flow comes under the demand level. In the design of a reservoir for water supply, how much capacity is reasonable is of the primary interest.

Let us take as an example the simple single reservoir system shown in Figure 8.1. Deficit discharge $q_d(t)$ and excess discharge $q_e(t)$ at the reference point are given by the following equations:

$$q_d(t) = \max(q_n(t) - q_r(t), 0) \quad \text{and}$$

$$q_e(t) = \max(q_r(t) - q_n(t), 0)$$

where $q_n(t)$ and $q_r(t)$ denote the demand and natural discharges at the reference point respectively and t denotes the time. The discharge the reservoir should resupply is given by q_d and possible storage at time t, $q_v(t)$, is given by

$$q_v(t) = \min(q_{in}(t), q_e(t))$$

where $q_{in}(t)$ denotes inflow to the reservoir. Then the reservoir storage necessary to satisfy the water demand from the beginning to time t, $S(t)$, is calculated by

$$S(t) = S(t-\Delta t) + \int_{t-\Delta t}^{t} (q_d(\xi) - q_v(\xi))d\xi$$

where Δt is time interval of computation, with a five-day interval adopted in many cases.

Given $q_n(t)$, $q_r(t)$ and $q_{in}(t)$, the water balance simulation for the reservoir according to the above equations produces the capacity diagram over time. If reliability corresponding to a return period of 10 years, the largest value is adopted as a design capacity, and in the case of 20 years, the second largest is adopted. It is insufficient, however, to run the balancing simulation for actual flow data since inflow discharge varies from year to year. Stochastic simulation of river flow should be incorporated into the design process.

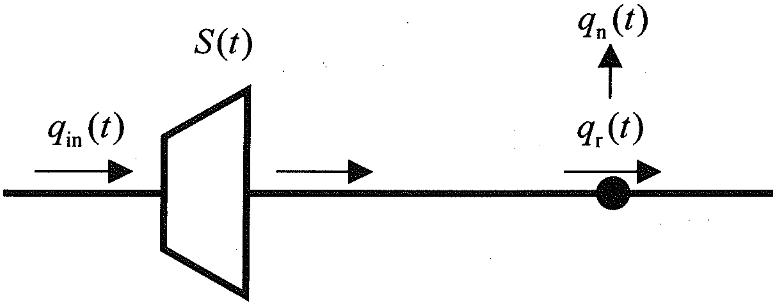

Figure 8.1: Simple reservoir system

8.2.2 Optimal design scheme of water control facilities

If a water resource system with multiple reservoirs and multiple intake facilities is taken into account, the major interest is to obtain site and scale plan of those facilities which minimizes the construction cost. In this section, the formulation of water resources system design is discussed by the use of linear mixed integer programming. Let us consider a water resources system with M possible reservoirs, N possible intake facilities and L demand blocks. In this system, water volume newly developed by reservoir i, q_i, depends on its capacity v_i and capacities of other reservoirs and can be expressed as follows:

$$q_i = f_i(v_i, V_i), \quad V_i = \{v_j \mid j \in I_i\} \quad (i = 1, 2, \ldots, M)$$

where I_i denotes the set of reservoirs which affect the newly developed water of reservoir i. Reservoirs that are located upstream of reservoir i may belong to I_i. We can take either of two choices, namely, to construct or not to construct reservoir i and intake facility j. But in the case of constructing the facility, its scale is restricted by predefined minimum and maximum values. Namely,

$$v_i = 0 \quad \text{or} \quad v_i^{\min} \le v_i \le v_i^{\max} \quad (i = 1, 2, \ldots, M)$$

$$w_j = 0 \quad \text{or} \quad w_j^{\min} \le w_j \le w_j^{\max} \quad (j = 1, 2, \ldots, L)$$

where w_j denotes the intake volume by facility j and $v_i^{\min}$ and others are the upper and lower limit of capacities. Flow discharge at intake point j, Q_j, is expressed by

$$Q_j = \sum_{k \in E_j} q_k - \sum_{k \in H_j} w_k \quad (j = 1, 2, \ldots, N).$$

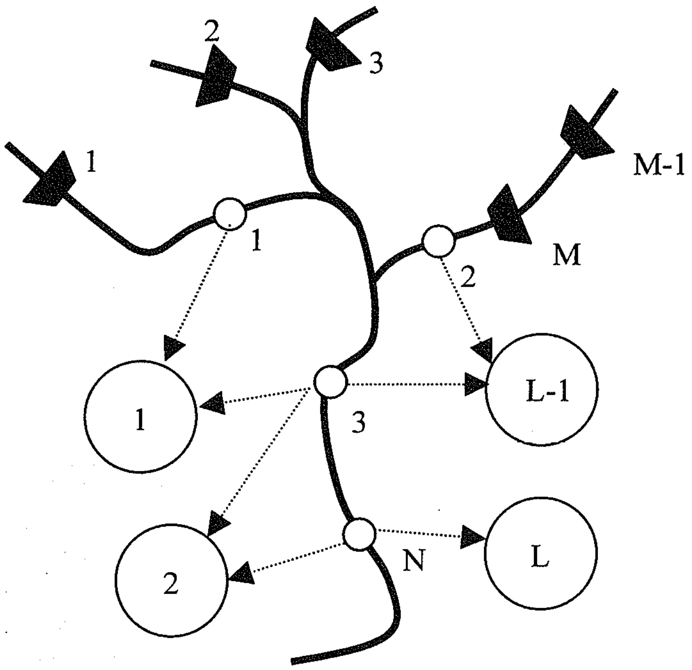

Figure 8.2: Water Resources Development System

The symbol E_j and H_j denote the set of reservoirs and intake facilities upstream of point j and q_j^M is the predefined allowable minimum discharge to maintain the river environment at point j. The flow discharge at point j must be larger than the intake water and the allowable minimum discharge. Then

$$Q_j = \sum_{k \in E_j} q_k - \sum_{k \in H_j} w_k \geq w_j + q_j^M \quad (j = 1, 2, \cdots, N)$$

should hold.

Water is supplied through the diversion network to satisfy the demand of each consumption block. Then

$$w_j = \sum_{k \in G_j} x_{jk} \quad (j = 1, 2, \cdots, N)$$

$$d_k = \sum_{j \in F_k} x_{jk} \quad (k = 1, 2, \cdots, L)$$

where x_{jk} denotes water supply from intake facility j to consumption block k, d_k: water demand at block k, G_j: set of consumption blocks taken care of by intake facility j, F_k: set of intake facilities which can provide water to block k. Construction cost is zero when a facility is not selected to be constructed and depends on its capacity when it is constructed, namely,

$$C_i^D = \begin{cases} 0 & \text{when not constructed} \\ g_i(v_i) & \text{when constructed} \end{cases} \quad (i = 1, 2, \cdots, M)$$

$$C_i^W = \begin{cases} 0 & \text{when not constructed} \\ h_i(v_i) & \text{when constructed} \end{cases} \quad (j = 1, 2, \cdots, N)$$

where C_i^D and C_j^W are the costs to construct reservoir i and intake facility j respectively. The objective is to obtain the combination of reservoirs and intake facilities which minimize the total cost $\sum_{i=1}^{M} C_i^D + \sum_{j=1}^{N} C_j^W$.

Now we have obtained the mathematical expressions of this water resources development problem. But they are given in a rather general way and are not expressed in a suitable form for mathematical programming, which is crucial to obtain the optimal solution. Nakagawa (1984) developed a systematic approach to solve a site and scale planning problem of this type by the use of mixed integer programming. Let us have a look how the water resources system design can be transformed into the integer-programming problem below.

First let us introduce complementary integer variables μ_i and ε_j which denote the state of construction of possible facilities. Each variable takes the value of zero when the reservoir or intake facility is constructed and takes one when constructed. Making the use of digital variables μ_i and ε_j, the water resources system design problem is rewritten as follows:

$$\sum_{i=1}^{M} C_i^D + \sum_{j=1}^{N} C_j^W = \sum_{i=1}^{M} \mu_i \cdot g_i(v_i) + \sum_{j=1}^{N} \varepsilon_j \cdot h_j(w_j) \quad \rightarrow \quad \min$$

$$q_i = f_i(v_i, V_i) \quad (i = 1, 2, \ldots, M)$$

$$v_i^{\min} \cdot \mu_i \le v_i \le v_i^{\max} \cdot \mu_i \quad (i = 1, 2, \ldots, M)$$

$$w_j^{\min} \cdot \varepsilon_j \le w_j \le w_j^{\max} \cdot \varepsilon_j \quad (j = 1, 2, \ldots, M)$$

$$Q_j = \sum_{k \in E_j} q_k - \sum_{k \in H_j} w_k \ge w_j + q_j^M \quad (j = 1, 2, \ldots, N)$$

$$w_j = \sum_{k \in G_j} x_{jk} \quad (j = 1, 2, \ldots, N)$$

$$d_k = \sum_{j \in F_k} x_{jk} \quad (k = 1, 2, \ldots, L)$$

$$\mu_i, \varepsilon_j \equiv 0 \,(\bmod 1) \quad (i = 1, 2, \ldots, M, \quad j = 1, 2, \ldots, N).$$

The decision variables are μ_i, ε_j, which denote whether to construct it or not, capacities of reservoir i and intake facility j: v_i, w_j, and water supply from intake point j to demand block k: x_{jk}. Since decision variables μ_i and ε_j take integer value and the functions $g_i(v_i)$, $h_j(w_j)$ and $f_i(v_i, V_i)$ are non-linear, the problem described by the above equations is a mixed-integer programming problem with non-linear functions. Unfortunately, however, an effective algorithm is not developed to solve a mixed-integer programming problem with non-linear functions. Therefore we have to introduce linearization to obtain the optimal solution for the problem.

The reservoir construction cost functions can be linearized by the use of pre-computed class values and interpolation. Let $(\overline{v}_i^0, \overline{v}_i^1, \ldots, \overline{v}_i^{n_i})$ be some class values of possible reservoir capacity and $(\overline{a}_i^0, \overline{a}_i^1, \ldots, \overline{a}_i^{n_i})$ be their associated costs, the cost function can be expressed in linear manner as follows by introducing auxiliary integer variable δ_i^l which takes the value of zero or one:

$$v_i = \sum_{l=0}^{n_i} \lambda_i^l \cdot \overline{v}_i^l$$

$$g_i(v_i) = \sum_{l=0}^{n_i} \lambda_i^l \cdot \overline{a}_i^l$$

$$\sum_{l=0}^{n_i} \lambda_i^l = 1, \lambda_i^l \geq 0$$

$$\begin{cases} \lambda_i^0 & \leq & \delta_i^l \\ \lambda_i^l & \leq & \delta_i^{l-1} + \delta_i^l \quad (l = 1, 2, \ldots, n_i - 1) \\ \lambda_i^{n_i} & \leq & \delta_i^{n_i - 1} \end{cases}$$

$$\begin{cases} \sum_{l=0}^{n_i} \delta_i^l = 1 \\ \delta_i^l \equiv 0 \, (\mathrm{mod}\, 1) \quad (l = 0, 1, \ldots, n_i - 1) \end{cases} .$$

We can easily imagine that the intake facility cost functions $h_j(w_j)$ can be linearized by the same technique. Assuming that the construction cost series $(\overline{b}_j^0, \overline{b}_j^1, \ldots, \overline{b}_j^{m_j})$ is pre-computed for the representative values of intake facility capacities $(\overline{w}_j^0, \overline{w}_j^1, \ldots, \overline{w}_j^{m_j})$. The cost functions of possible intake facilities can be expressed as follows:

$$w_j = \sum_{l=0}^{m_j} \xi_j^l \cdot \overline{w}_j^l$$

$$h_j(w_j) = \sum_{l=0}^{m_j} \xi_j^l \cdot \overline{b}_j^l$$

$$\sum_{l=0}^{m_j} \xi_j^l = 1, \xi_j^l \geq 0$$

$$\begin{cases} \xi_j^0 & \leq & \varsigma_j^l \\ \xi_j^l & \leq & \varsigma_j^{l-1} + \varsigma_j^l \quad (l = 1, 2, \ldots, m_j - 1) \\ \xi_j^{n_j} & \leq & \varsigma_j^{m_j - 1} \end{cases}$$

$$\begin{cases} \sum_{l=0}^{m_j} \varsigma_j^l = 1 \\ \varsigma_j^l \equiv 0 \, (\mathrm{mod}\, 1) \quad (l = 0, 1, \ldots, m_j - 1) \end{cases} .$$

The capacity and developed water relation, $f_i(v_i, v_j)$, is rewritten using the pre-computed developed water amount $\overline{q}_i^{kl}$ for the combinations of the sample values of v_i and v_j, namely $\overline{v}_i^k$ and $\overline{v}_j^l$, as the following equation:

$$q_i = f_i(v_i, v_j) = \sum_{k=0}^{n_i}\sum_{l=0}^{n_j} \lambda_i^k \bar{q}_i^{kl} \lambda_j^l .$$

This equation, however, contains the quadratic form and then we cannot use linear mixed integer programming. In order to cope with this problem, let us assume that the capacity of reservoir j, which affects the water amount newly developed by reservoir i, takes only one of the discrete values $\bar{v}_j^l$ $(l = 1, 2, \ldots, n_j)$ and introduce the auxiliary integer variable η_j^l. The equation above can be rewritten into the following form:

$$\sum_{k=0}^{n_j} \lambda_i^k \cdot \bar{q}_i^{kl} - (1 - \eta_j^l) \cdot M \le q_i \le \sum_{k=0}^{n_j} \lambda_i^k \cdot \bar{q}_i^{kl} + (1 - \eta_j^l) \cdot M$$

$$(l = 1, 2, \ldots, n_j)$$

$$\begin{cases} \displaystyle\sum_{l=1}^{n_j} \eta_j^l = 1 \\ \eta_j^l = \begin{cases} 0 & \text{when } v_j \ne \bar{v}_j^l \\ 1 & \text{when } v_j = \bar{v}_j^l . \end{cases} \end{cases}$$

where M is a suitably large number.

Using the liniearization described above, we have obtained the new objective function:

$$\sum_{i=1}^{M}\sum_{l=0}^{n_j} \lambda_i^l \cdot \bar{a}_i^l + \sum_{j=1}^{N}\sum_{l=0}^{m_j} \xi_j^l \cdot \bar{b}_j^l \quad \to \quad \min .$$

from which we can obtain the optimal solution through the algorithm developed for a linear mixed-integer programming.

8.3 Water resources management

Management is also one of the key topics in water resources engineering. For example, if a reservoir is operated in an inappropriate manner, it cannot bring out the functions expected in the design process. On the other hand when it is operated in an effective way, it could supply even more water than expected.

Reservoir operation problems have been studied intensively for these five decades especially from the optimization viewpoint. Readers can refer to Yeh (1985) for a state-of-the-art review of reservoir operation techniques. Here fundamental schemes of optimum reservoir operation are introduced.

8.3.1 Water quantity control by a reservoir based on deterministic dynamic programming

Let us consider a discrete time system with a reservoir shown in Figure 8.2. The continuity equation is given by

$$s_{i+1} = s_i + q_i - r_i - e_i$$

where s_i denotes the storage volume of the reservoir at the beginning of time step i, q_i the inflow to the reservoir during time step i, r_i the release discharge and e_i loss from the reservoir due to evaporation or seepage. The storage s_i is constrained by

$$s_{\min} \leq s_i \leq s_{\max}$$

where $s_{\min}$ and $s_{\max}$ denote maximum and minimum storage of the reservoir. The purpose of reservoir operation is to maximize the total benefit during the time period to be considered. The objective can be formulated as follows:

$$\sum_{i=1}^{I} g_i(r_i, \overline{s}_i) \quad \rightarrow \quad \max.$$

where $g_i(\cdot)$ represents benefit in time step i, which depends on the initial storage and release discharge, $\overline{s}$ is the mean storage at the beginning and at the end of time step i and I is the end of the reference time period. The objective function may be defined by loss in case of flood protection. In those cases, operation can be formulated as a minimization problem or $g_i(\cdot)$ can be defined to give negative values.

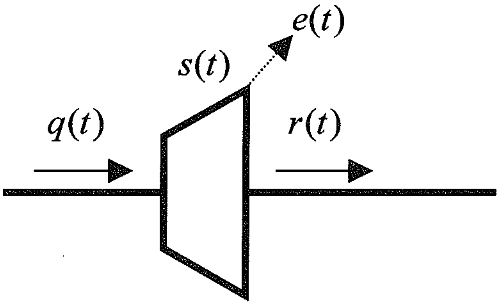

Figure 8.3: Single reservoir control system

Suppose here thatl the inflow discharge and loss from the reservoir are known. When the benefit function $g_i(\cdot)$ is linear, the operation problem can be solved by linear programming since the constraints given by the equations are linear. But readers can easily imagine that the number of constraints become larger as the reference time period is longer. It is well known that linear programming problems become harder to solve when the number of constraints increase. Moreover, the benefit function is not linear in many cases and is not expressed in an analytical form. In the case of flood control for example, $g_i(\cdot)$ may be the damage caused by floods and include runoff and inundation simulation.

For these reasons, dynamic programming has been introduced to solve the reservoir operation problems. The objective function can be rewritten as follows:

$$\max_{r_1,\ldots,r_I}\{\sum_{i=1}^{I} g_i(r_i,\overline{s}_i)\} = \max_{r_1,\ldots,r_I}\{\sum_{i=1}^{I-1} g_i(r_i,\overline{s}_i) + g_I(r_I,\overline{s}_I)\}.$$

Considering state transition from the beginning to the end of step I, when the value of storage at the beginning of time step I, s_I, is fixed, $g_I(r_I,\overline{s}_I)$ comes to be a function only of r_I because $\overline{s}_I$ can be expressed in terms of r_I by the continuity equation. Note that here the value of r_I to maximize $g_I(r_I,\overline{s}_I)$ gives the maximum value of the right side of the equation according to the fixed value of s_i. Thus we can obtain:

$$\begin{aligned}\max_{r_1,\ldots,r_I}\{\sum_{i=1}^{I} g_i(r_i,\overline{s}_i)\} &= \max_{r_1,\ldots,r_{I-1}}[\sum_{i=1}^{I-1} g_i(r_i,\overline{s}_i) + \max_{r_I}\{g_I(r_I,\overline{s}_I)\}]\\ &= \max_{r_1,\ldots,r_{I-1}}\{\sum_{i=1}^{I-1} g_i(r_i,\overline{s}_i) + f_I(s_I)\}\end{aligned}$$

where $f_I(s_I) = \max_{r_I}\{g_I(r_I,\overline{s}_I)\}$. In the same way, the objective function can be rewritten as:

$$\max_{r_1,\ldots,r_I}\{\sum_{i=1}^{I} g_i(r_i,\overline{s}_i)\} = \max_{r_1,\ldots,r-2}[\sum_{i=1}^{I-2} g_i(r_i,\overline{s}_i) + \max_{r_{I-1}}\{g_{I-1}(r_{I-1},\overline{s}_{I-1}) + f_I(s_I)\}]$$

and $f_{I-1}(s_{I-1})$ is defined by:

$$f_{I-1}(s_{I-1}) = \max_{r_{I-1}}\{g_{I-1}(r_{I-1},\overline{s}_{I-1}) + f_I(s_I)\}.$$

Performing this operation from the end of the reference period to the beginning, the following recursive equation holds:

$$f_{I-i}(s_{I-i}) = \max_{r_{I-i}}\{g_{I-i}(r_{I-i},\overline{s}_{I-i}) + f_{I-i+1}(s_{I-i+1})\},\quad i = 0,1,\ldots,I-1$$

where $f_{I+1}(s_{I+1}) = 0$. By applying the recursive functions from the end of the reference period, the optimal release discharges at all the time steps are determined as functions of the initial storage. If the storage volume at step 0 is given, all the release series are fixed.

8.3.2 Incorporating stochastic characteristics of inflow discharge

The deterministic dynamic programming approach is a simple and powerful tool to study reservoir operation problems. However, it cannot consider the stochastic properties of inflow series, which is essential to reservoir management. Therefore stochastic dynamic programming was developed to handle Markov process type inflows.

Consider the case where an inflow discharge series follows a single order Markov chain. In this case, only by fixing the value of the initial storage at each time step, we cannot determine the optimal release at the present step independently because the probability of inflow discharge differs according to the inflow at the previous step. Thus the combination of initial storage at each time step and inflow discharge at the previous step should be taken as a state variable.

The objective function can be expressed in terms of the expected value of total benefit or loss. Let $f_{I-i}(s_{I-i}, q_{I-i})$ be the optimal value of the objective function for the period from the end to time step $I-i$. The recursive function can be expressed as follows:

$$f_{I-i}(r_{I-i}, q_{I-i-1}) = \max_{r_{I-i}}\{ \sum_{r_{I-i-1}=0}^{r_{I-i-1}^{\max}} \mathrm{P}[r_{I-i} \mid r_{I-i-1}](g_{I-i}(r_{I-i}, \overline{s}_{I-i}) + f_{I-i+1}(r_{I-i+1}, q_{I-i}))\}$$

where $\mathrm{P}[\bullet \mid \bullet]$ denotes the conditional probability and $r_{I-i-1}^{\max}$ is the maximum level of conditional inflow discharge.

8.3.3 Real time operation

The deterministic and stochastic dynamic programming approaches require the inflow series itself or its conditional probability to be known. This assumption is satisfied when the optimal release policy is computed for the past inflow data, which is usually done to get reservoir operation rules during the designing process of water resources systems. These operations are called "off-line control". On the contrary, in-situ operation is called "on-line" or "real-time" control.

In real time control, the most simple method of operation is to use inflow predictions in the recursive equations of the deterministic dynamic programming model. In the case of a stochastic dynamic programming model, you have only to use current storage volume if the conditional probabilities of inflow discharge are given. In both cases, only the release discharge at the first period is adopted for actual operation because when the time passes and you move to the next time step you will get another observation.

In real-time control, the method of assessment and consideration of uncertainty of predictions is very important, and many studies are devoted to formulate and solve for better solutions. The reader can easily find papers on this topic in well-known academic journals. A comprehensive state-of-the-art of reservoir operation is summarized by Yeh (1985).

8.4 Concluding remarks

Since water resources are unevenly distributed in time and space, we have to control these distributions by artificial means in order to transform natural water distributions into resources. We have looked at the basic concept to do that in this chapter from the viewpoint of system optimization. Closing this chapter, I would like to point out that water resource problems has have both local and global aspects.

Even if we can design the water resources supply systems or operation systems, those systems can improve the water availability only in limited regions. We cannot transport water resources between continents. In larger or smaller regions, people can only intake the water that is in rivers or lakes nearby. In this sense, water resource problems are local issues.

On the other hand, when we think about the impact of global climate change on our water resources, the target area is extended to the global scale. When you want to know its impact on a specific limited area, the knowledge about global circulation is necessary. We should not forget that the water brought by the nature to local areas is controlled by global water circulation systems. We also note that we do not live on the goods which are produced in the local area we live. We live mutually depending on the products of foreign countries through the global trade network. When you eat some fruits imported from another country, it means that you used the water to produce those fruits in that country for you. In a highly networked environment, water problems that occur in other limited regions may bring large impacts on other areas through the economic network. In this sense also, water resources problems have a global aspect.

In order to know the recent world trends on water resources, web sites of international organizations are useful. The world water council, an international world water think tank established in 1996, gives a large amount of documents including world water vision on its web site (http://www.worldwatercouncil.org). The global water partnership (http://www.gwpforum.org) gives various samples of water management in different areas in its toolbox. You can also know the detail about the third World Water Forum on the site http://www.world.water-forum3.com.

References

Ikebuchi, S.: Water resources Engineering, Morikita Shuppan Co. Ltd., 2001 (in Japanese).

Nakagawa, H.: A systems approach to Water Resources Development and Distribution, Ph.D. Thesis, Kyoto University, 1984 (in Japanese).

Watson, R.T. and the Core Writing Team (Eds.): IPCC Third Assessment Report: Climate Change 2001, IPCC, Geneva, Switzerland, 2001.

Yeh, W.: Reservoir Management and Operations Models: A State-of-the-Art Review, Water Resources Research, Vol..21, No.12, pp.1797 - 1818, 1985.

Chapter 9

Catchment Hydrology

Yasuto TACHIKAWA
Disaster Prevention Research Institute, Kyoto University
Gokasho Uji, Kyoto 611-0011, Japan
Phone: +81-774-38-4126, Fax: +81-774-38-4130
E-mail: tachikawa@mbox.kudpc.kyoto-u.ac.jp

9.1 Introduction

The methods for flood disaster prevention and reduction are usually grouped into two categories. One is to cope with floods through the use of structural facilities such as dams and levees. The other involves the use of non-structural measures such as flood warning systems and flood hazard maps.

In order to provide structural and non-structural counter-measures against flood hazards, the construction of an accurate flood runoff simulation model and the development of a reliable real-time runoff prediction system are essential. In this chapter, conceptual catchment hydrologic models and their applications to large catchments are presented. A real-time flood prediction method is also described.

The chapter is organized as follows: in Section 9.2, the tank model and the storage function method, which are typical conceptual models developed and frequently used in Japan, and a simplified Xinanjiang model originally developed in China, are described. River routing models are also briefly presented. Then, based on the simplified Xinanjiang model, a catchment hydrologic model is applied to the Chao Phraya River basin in Thailand (110,000 km^2) and the Huaihe River basin in China (132,000km^2). In Section 9.3, a real-time flood runoff prediction method and its application to the Tsuno River basin in Japan (724km^2) is presented. The real-time flood runoff prediction method is based on

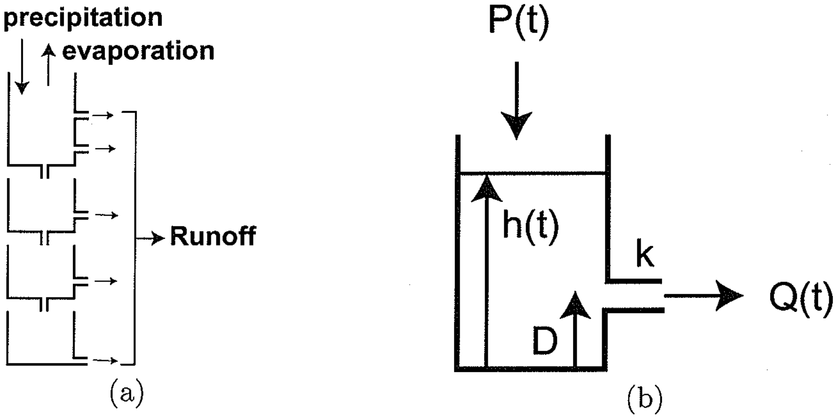

Figure 9.1: Schematic drawing of the tank model.

the storage function method combined with the filtering and prediction theory developed by Kalman and others (eg. Kalman, 1960; Jazwinski, 1970; Bierman, 1977). Finally in Section 9.4, current research topics are briefly introduced. Recent advancements of physically-based distributed hydrological models are presented in Chapter 10.

9.2 Catchment hydrologic modeling

9.2.1 Runoff process model

Tank model

The tank model is a simple rainfall-runoff model developed by Sugawara (1976, 1995), which is usually composed of four tanks as shown in Figure 9.1(a). Precipitation is provided to the top tank and evaporation is subtracted from the top tank. Discharges from the side outlets correspond to surface, sub-surface and groundwater discharges. Figure 9.1(b) shows a single tank model, which is represented by the following equations

$$\frac{d}{dt}h(t) = P(t) - Q(t), \quad Q(t) = \begin{cases} k(h(t) - D) & , \text{ when } h(t) \geq D \\ 0 & , \text{ when } 0 \leq h(t) < D \end{cases} \tag{9.1}$$

Tank models with various combinations of tanks are also expressed as the combinations of Eq.9.1, which are represented by simultaneous differential equations. When the structure of tanks and model parameters are well defined, the tank model performs well for long and short term runoff simulations.

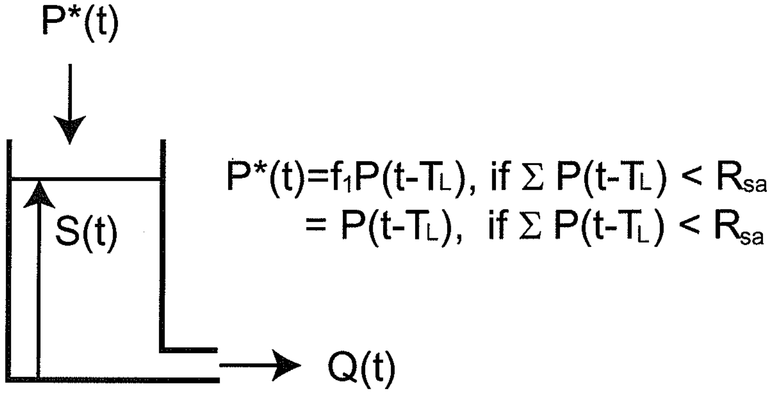

Figure 9.2: Schematic drawing of the storage function method.

Storage function method

The rainfall runoff model based on Kimura's storage function method (1960) is represented as

$$\frac{d}{dt}S(t) = P^*(t) - Q(t), \quad S(t) = KQ(t)^p \tag{9.2}$$

where $P^*(t)$ is effective rainfall intensity defined by

$$P^*(t) = \begin{cases} f_1 P(t - T_L) & , \text{when } \sum_{\tau=0}^{t-T_L} P(\tau) < R_{SA} \\ P(t - T_L) & , \text{when } \sum_{\tau=0}^{t-T_L} P(\tau) \geq R_{SA} \end{cases} \tag{9.3}$$

In the equations, $S(t)$ is water storage height, $Q(t)$ is runoff height, and f_1, T_L, R_{SA}, K and p are constant model parameters. The value for f_1 takes a constant value less than 1.0 when accumulated rainfall from the beginning of a flood is less than R_{sa}. R_{sa} represents the amount of accumulated rainfall when all of the watershed area is in saturation. T_L represents a lag time parameter. The value for K depends on topographic attributes and so on and is sometimes determined from catchment area. The value for p depends on flow conditions and so on and is sometimes fixed to 0.6.

Although the model is quite simple, it reproduces flood hydrographs well, and as such the model is frequently used for engineering purposes in Japan. The problem is that the optimal set of model parameters differs depending on the flood being simulated. In Section 9.3, a real-time runoff prediction scheme based on the storage function method is represented, which takes into account the uncertainty of model parameters.

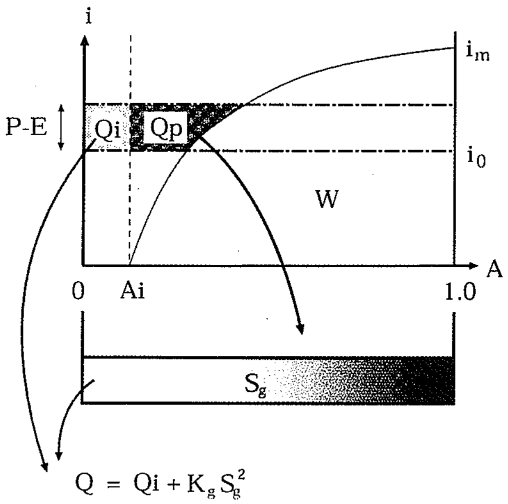

Figure 9.3: Schematic drawing of a simplified Xinanjiang model.

Simplefied Xinanjiang model

A simple hydrologic model (Nirupama *et al.*, 1996) based on the Xinanjiang model (Zhao, 1992; Zhao and Liu, 1995) is an extension of the tank model, which takes into account a spatial distribution of soil water capacity. As shown in Figure 9.3, runoff generation occurs when the soil water storage reaches its capacity. The spatial distribution of soil water storage capacity i over a basin is defined as

$$i(A) = i_m \left\{ 1 - \left(1 - \frac{A - A_i}{1 - A_i} \right)^{1/b} \right\} \tag{9.4}$$

when $A_i < A \leq 1.0$. If $0 < A \leq A_i$, $i = 0$, where i_m is the maximum soil water storage height, A is the areal fraction of a basin which takes a value between 0 and 1, A_i is the impervious proportion of a basin, and b is a model parameter which determines the shape of the distribution of soil water storage capacity. A runoff depth Q_i occurs over impervious areas, and is represented as

$$Q_i = A_i(P - E) \tag{9.5}$$

where P is precipitation and E is evapotranspiration. Runoff depth from the pervious area Q_p is given by the following equation when $i_m < i_o + P - E$,

$$Q_p = (P - E)(1 - A_i) - W_m + W \tag{9.6}$$

If $i_m \geq i_o + P - E$,

$$Q_p = (P - E)(1 - A_i) - W_m + W + W_m \left(1 - \frac{i_o + P - E}{i_m} \right)^{1+b} \tag{9.7}$$

where W is current soil water storage (in depth unit), i_0 is current storage height in unsaturated area, and W_m is the maximum water storage capacity over a basin (in depth unit) expressed as

$$W_m = \frac{i_m}{1+b}(1 - A_i) \tag{9.8}$$

W is considered to be the soil water storage which only contributes to evapotranspiration. Q_p is added to groundwater storage S_g and total runoff Q is computed as

$$Q = Q_i + k_g S_g^2 \tag{9.9}$$

Model parameters of the runoff element model are A_i, b, W_m and k_g.

9.2.2 Channel routing process model

When the study area is more than several hundred square km, the watershed is usually subdivided into several sub-basins and a flood routing model which links the sub-basin hydrologic models is introduced.

Channel routing models are classified into distributed routing models and lumped routing models. Distributed routing models Ffequently used are the dynamic wave model, the diffusion wave model and the kinematic wave model, whose momentum equations are shown as

$$\underbrace{\frac{\partial v}{\partial t} + v\frac{\partial v}{\partial x} + \underbrace{g\frac{\partial h}{\partial x} - \underbrace{g(S_o - S_f) = 0}_{\text{Kinematic wave}}}_{\text{Diffsion wave}}}_{\text{Dynamic wave}} \tag{9.10}$$

where v is velocity, h is depth, S_o is bed slope, and S_f is friction slope.

When a catchment is subdivided into several sub-basins, the channel routing in each sub-basin is sometimes represented using a lumped routing model. The Muskingum method and the Muskingum-Cunge method are frequently used lumped routing models. Recently, Shiiba *et al.* (1996) developed a new lumped stream kinematic wave model. The model calculates discharges at the lower ends of river segments by setting the assumption that river discharge varies linearly along each river segment at each time step instead of routing flows of each computational cross section. This method realizes to route river flow physically with high computational efficiency. Assuming the cross sections of river segments are wide rectangle, the model parameters are Manning's roughness coefficient and channel width. The channel routing method is used in the following application models.

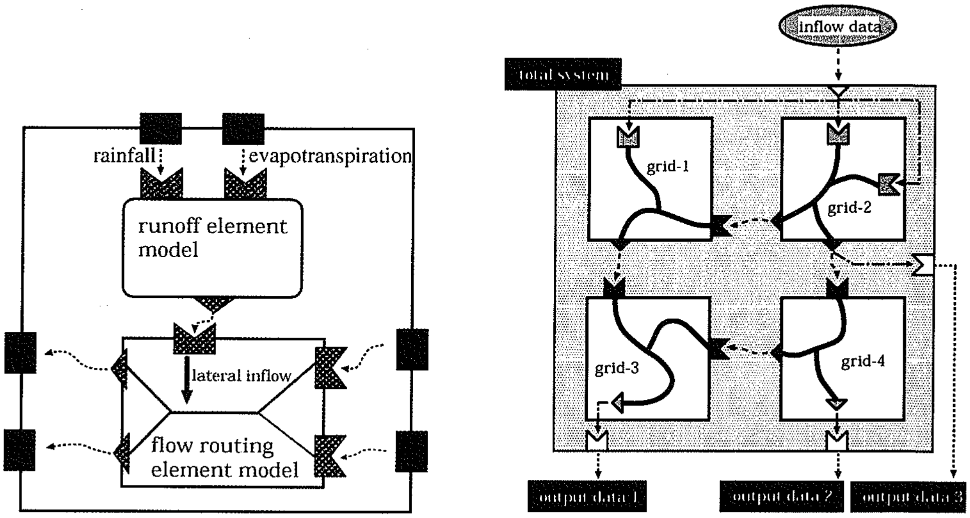

(a) (b)

Figure 9.4: (a) Structure of a sub-system model. (b) Structure of a total simulation system-model consisting of sub-system models.

9.2.3 Building catchment hydrologic model

Basic framework for building a catchment hydrological model is as follows:

1) Division of a study basin into several sub-basins.
2) Modeling of hydrological processes in each sub-basin (runoff element modeling, Figure 9.4(a)).
3) Modeling of channel flow routing in each sub-basin (flow routing element modeling, Figure 9.4(a)).
4) Building a total simulation model by connecting subsystem models composed of the runoff element models and the flow routing element models (Figure 9.4(b)).

For each sub-basin, a sub-model composed of a runoff element model and a flow routing element model is usually constructed. The runoff element model represents hydrological processes within a sub-basin, which computes discharge to the channel network within the sub-basin. The flow routing element model gets discharge from the runoff element model and river inflows from the upper reaches in the adjacent sub-basins, and it calculates river outflows to lower reaches within the adjacent sub-basins. By using the connection relationship of sub-basins, sub-models are linked together and a total runoff simulation model is constructed.

Recently, several hydrologic modeling software packages have been developed, which enable easy and systematic connections of hydrologic element mod-

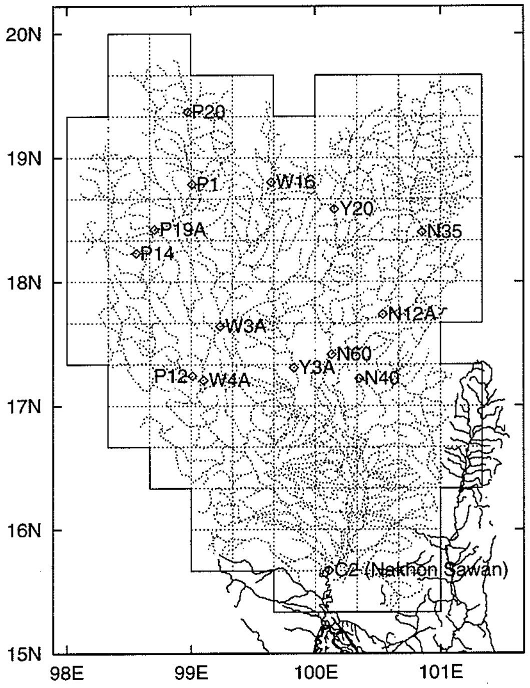

Discharge Stations	Catchment Area(km^2)
P1	6,355
P12	26,363
P14	3,853
P19A	14,023
P20	1,355
W3A	8,985
W4A	10,507
W16	1,284
Y3A	13,583
Y20	5,410
N12A	15,718
N35	10,335
N40	4,340
N60	18,692
C2	110,569

Figure 9.5: Channel network and grid division for the Chao Phraya River basin. Dotted lines show the channel network above Nakhon Sawan (C2 station).

els. Runoff simulation models presented in next sections are developed using Object-oriented Hydrological Modeling System, OHyMoS (Takasao *et al.*, 1996a; Ichikawa *et al.*, 2000). In OHyMoS, basic common functions such as setting model parameter values, initializing computational variables, exchanging data between element models and setting computation time steps for each element model are implemented as functions of the abstract base class. It is possible to set different time steps for each element model depending on the rate of a hydrological response. The system automatically accumulates calculated values before they are passed from one element model to another element model and calculated values are transferred when the lower element model requests the values.

9.2.4 Application to the Chao Phraya River basin in Thailand

Model settings

Figure 9.5 shows the channel network for the Chao Phraya River above Nakhon Sawan, the outlet of the 110,000km^2 study area. At first, the channel network

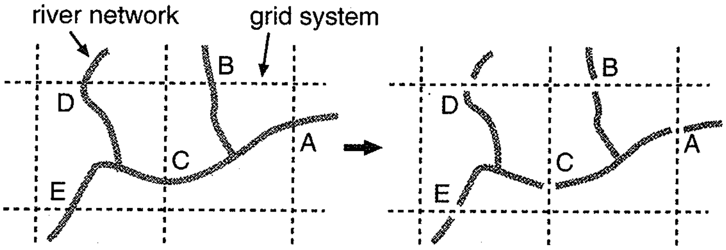

Figure 9.6: Division of a river network by grid boxes.

Table 9.1: Values of model parameters.

runoff element model			
A_i	b	W_m (mm)	kg (mm-s unit)
0.0	1.0	620.0	0.00011

flow routing element model		
B (m)	n (m-s unit)	P
100.0	0.05	0.6

data set was generated from the river network data sets stored in the DCW (Digital Chart of the World) and the GLOBE (Global Land One-km Base Elevation) data sets. In this model, a watershed basin is subdivided into grid boxes according to a grid system of a meso-scale atmospheric model with $1/3 \times 1/3$ degree as shown in Figure 9.6 to incorporate atmospheric model outputs.

After subdividing the watershed basin into subbasins (grid boxes), each grid box hydrological process was modeled using the simplified Xinanjiang model (Nirupama *et al.*, 1996) and flow routing was modeled using the lumped kinematic wave routing model (Shiiba *et al.*, 1996). Flow routing element models were then linked together to make a total runoff simulation model. Hydrological modeling procedures are automatically processed using functions in OHyMoS library.

Model parameters shown Table 9.1 were identified at the watershed of the P20 station (1,355km^2) and applied to all the element models. The reason to determine the model parameters at the watershed is that its catchment area is nearly equal to the size of one grid box.

Model performances were evaluated using observed precipitation data. Precipitation values given to each grid box were obtained by simply averaging the precipitation values observed within each grid box. There were no observed or simulated evapotranspiration data sets, thus evapotranspiration values were determined from precipitation and discharge data sets. The value is supposed to take the same value every day.

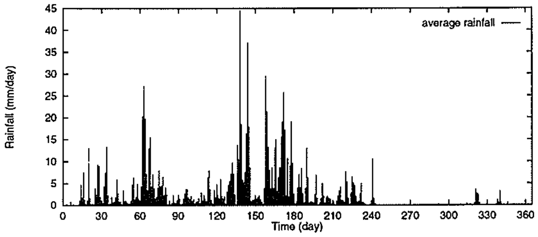

Figure 9.7: Basin average precipitation from April 1 in 1987 to March 31 in 1988.

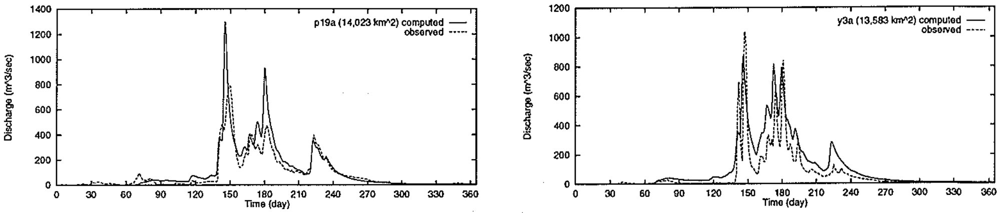

(a) P19A station

(b) Y3A station

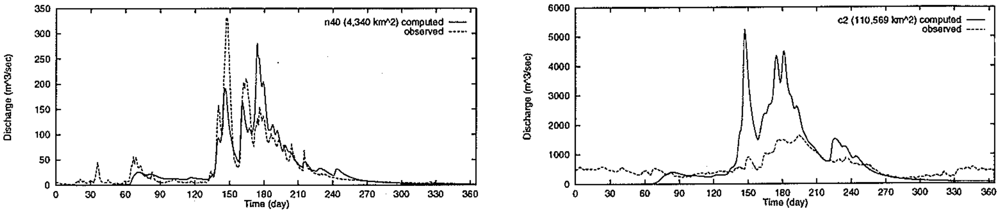

(c) N40 station

(d) C2 station

Figure 9.8: Observed and simulated discharges from April 1 in 1987 to March 31 in 1988.

Application results

The simulation period used is from April 1, 1987 to March 31, 1988. The basin average rainfall is shown in Figure 9.7. Some simulation results are shown in Figure 9.8. The results at P19A station, N40 station and Y3A station show good agreement with the observed discharges. These discharge stations are located at the upper reaches of the Bhumiphol dam and the Sirikit dam. Simulations for other stations at upper reaches of the dams also showed good results. However at the stations located at the lower reaches of the dams, there were significant differences between simulated discharges and observed ones. Figure 9.8(d) shows computed discharge at Nakhon Sawan (110,000km^2), the outlet of the study area. This shows that dam controls give a great effect on the hydrological cycle in the study basin.

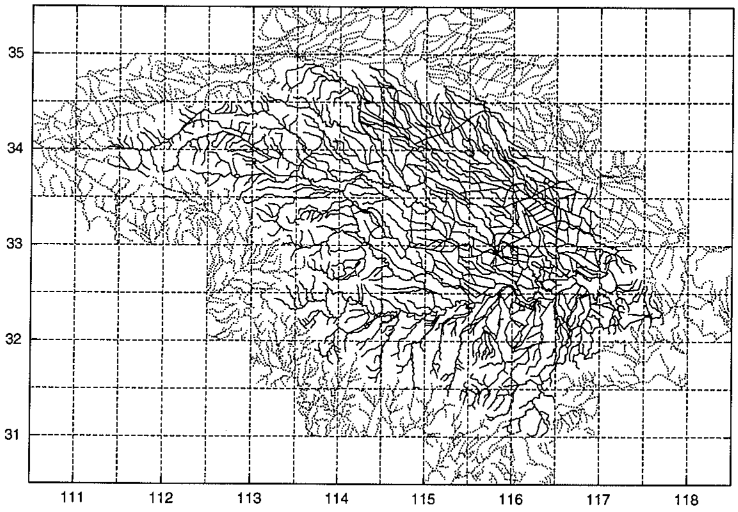

Figure 9.9: Generated channel network data for the Huaihe River. Solid lines show the channel reaches of the Huaihe River for the upper part of Bengbu.

9.2.5 Application to the Huaihe River basin in China

Model settings

The same model was applied to the the Huaihe River basin in China. Figure 9.9 shows the channel network for the Huaihe River above Bengbu, the outlet of the 132,350km^2 study area. The channel network data were generated from the 1:500,000 scale Tactical Pilotage Chart (TPC) series and the Global Land One-km Base Elevation (GLOBE) data set, then the channel network data was subdivided into 10 minute grid boxes.

The runoff element model parameters were identified by using hydrological data sets observed in the Shigan River basin during the GAME HUBEX IOP in 1998 (Tachikawa *et al.*, 2000). For routing element model parameters, Manning's roughness coefficient was set to 0.05 m$^{-1/3}$s for all the river segments and the channel width $B(x)$ at x along a channel reach was set by using the relation

$$B(x) = B_u + (B_l - B_u) \times \left(\frac{A(x)}{A_l}\right)^c \tag{9.11}$$

where $A(x)$ is upstream catchment area (km^2), A_l is the catchment area at Bengbu (132,350 km^2), B_u is the channel width at the upper ends (10 m), B_l is the channel width at Bengbu (600 m), and $c = 0.3$. The value of c was determined using the cross section data and catchment area in the Huaihe River basin.

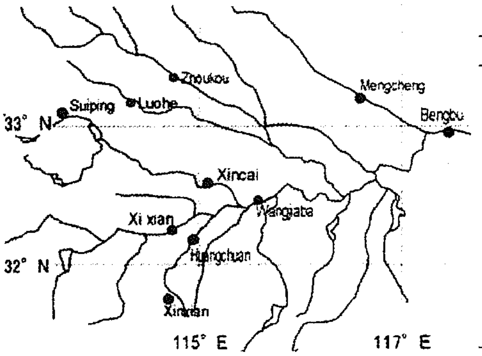

Station	Lon.	Lat.	Area(km^2)
Bengbu	117 23	32 56	132,350
Wangjiaba	115 36	32 26	29,844
Zhoukou	114 39	33 38	24,733
Mengcheng	116 33	33 17	12,245
Xi xian	114 44	32 20	10,133
Luohe	114 02	33 36	8,097
Xincai	114 59	32 46	5,702
Suiping	113 58	33 08	2,093
Huangchuan	115 03	32 08	1,553
Xinxian	114 52	31 37	293

Figure 9.10: Generated channel network data for the Huaihe River. Solid lines show the channel reaches of the Huaihe River for the upper part of Bengbu.

The input data for the model is time and spatial distributed evapotranspiration and precipitation data. Two different data sets were used as input data. One is a five-minute grid resolution data set created for Estimation of Energy and Water Budget (EEWB) in the Huaihe River basin (Kozan *et al.*, 2001), which was generated from the GAME HUBEX IOP observed data sets with a land surface hydrological model, the SiBUC model (Tanaka *et al.*, 1994). Another is GAME Reanalysis Product (version 1.1) with 1.25 grid resolution data (Japan Meteorological Agency, 2000) produced by using JMA 4DDA system in a cooperative study of JMA and NASDA. The data set has an advantage of including the GAME special observation of radio-sonde data set. By using these data sets, river discharges during the GAME HUBEX Intensive Observation Period, from May 1 in 1998 to August 31 in 1998, were simulated.

Application results

To simulate river discharges, hourly precipitation and evapotranspiration data with ten minute spatial resolution were generated from HUBEX IOP EEWB data and GAME Reanalysis 1.25 data. Figure 9.10 presents the locations of discharge stations where comparisons of simulated and observed discharges are conducted. Figure 9.11 shows the simulated and observed discharges using GAME Reanalysis 1.25 data from May 1 to August 31 in 1998. In the Wangjiaba and Suiping catchments, simulated discharges were underestimated. In general, to simulate a river discharge for small catchments, input data with smaller grid size are requested. A preliminary result suggests that the ratio of catchment size to input data resolution should be more than 10 (Roshan *et al.*, 2002). For the Wangjiaba and Suiping catchments, the grid size of GAME Reanalysis data may be too coarse for the runoff simulation. While at Bengbu, the simulated discharge using GAME Reanalysis data gives a better result. This is because the input resolution is compatible with the Bengbu simulation, and also the

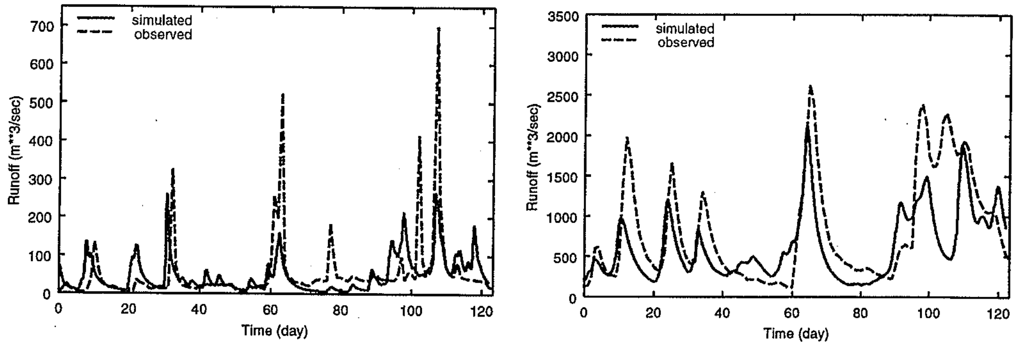

(a) Suiping (2,093 km^2) (b) Wangjiaba (29,844 km^2)

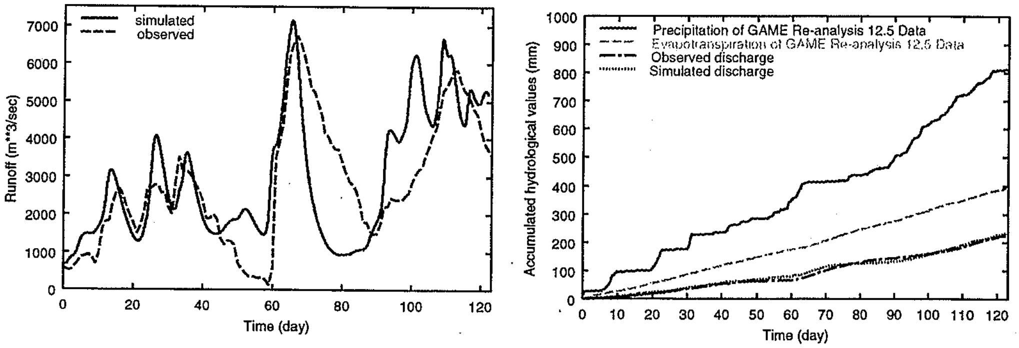

(c) Bengbu (132,350 km^2) (d) Accumulated Water Budget at Bengbu

Figure 9.11: Observed and simulated hydrographs from May 1 to August 31 in 1998 by using GAME Reanalysis 1.25 Data.

estimated precipitation and evapotranspiration data for the entire study area included in GAME Reanalysis data might be a good estimation. Figure 9.11(d) shows the accumulated water budget for the upper part of Bengbu from May 1 to August 31 in 1998 using GAME Reanalysis 1.25 data. When using GAME Reanalysis data, accumulated values of simulated and observed discharge show quite good agreement.

In the basin a number of dams are in operation, but the model does not consider the discharge manipulation due to the dam operation. The effect of flood plain to the river discharge is also not considered. This may be because the recession period after the largest peak discharge around 70th day in Figure 9.11(c) is not well simulated. To incorporate human activities on a hydrological cycle, such as dam controls, reservoir regulations, and water intakes for irrigation are quite important to represent the hydrological cycle in the catchment.

9.3 Real-time runoff prediction

Real-time flood forecasting is quite important to prevent or reduce damage due to floods. In Japan, the storage function method developed by Kimura (1960) is often used for short term flood runoff simulations. Although it is a very simple rainfall runoff model, it has a high ability to represent the nonlinearity of flood runoff phenomena. So far, some on-line flood runoff prediction methods which couple the storage function method with the filtering and prediction theory developed by Kalman and others have been developed and improved by several researchers (Shiiba and Takasao, 1980; Takara *et al.*, 1983; Takasao and Shiiba, 1984).

One of the shortcomings of the storage function method is that the best fitted model parameters differ depending on the flood being simulated. To cope with it, a real-time runoff prediction method considering the uncertainty of parameters of the storage function method was devised to improve the prediction accuracy (Takasao *et al.*, 1993, 1994a, 1995, 1996b) In the method, a number of filters with different model parameters run simultaneously. The values of probability distribution density assigned to these filters and state variables are updated by using Kalman filtering with real-time observation data.

In the section, a basic theory of a real-time runoff prediction method using the storage function method with the Kalman filter and its extention are described. Then some simulation results applied to the Tsuno River basin in Japan (724km^2) are represented, that shows a treatment of the uncertainty of model parameters enhances the prediction accuracy.

9.3.1 Basic idea of real-time runoff prediction method

Figure 9.12 shows the schematic drawing of real-time runoff prediction method presented here. Let's assume that the current time is 14:00. When we obtain a one-hour ahead rainfall prediction, flood runoff prediction and its error variance at 15:00 is calculated using the prediction scheme. When the current time becomes 15:00, we observe the discharge. In the filtering scheme, the value of the model state variables are estimated by using the predicted value, the observed value and their error variances. After updating state variables at 15:00, the discharge at 16:00 is again predicted using the estimated values of the model state variables.

Thus, for each time step, prediction, observation and updating state variables are performed recursively to obtain predicted values with its uncertainty.

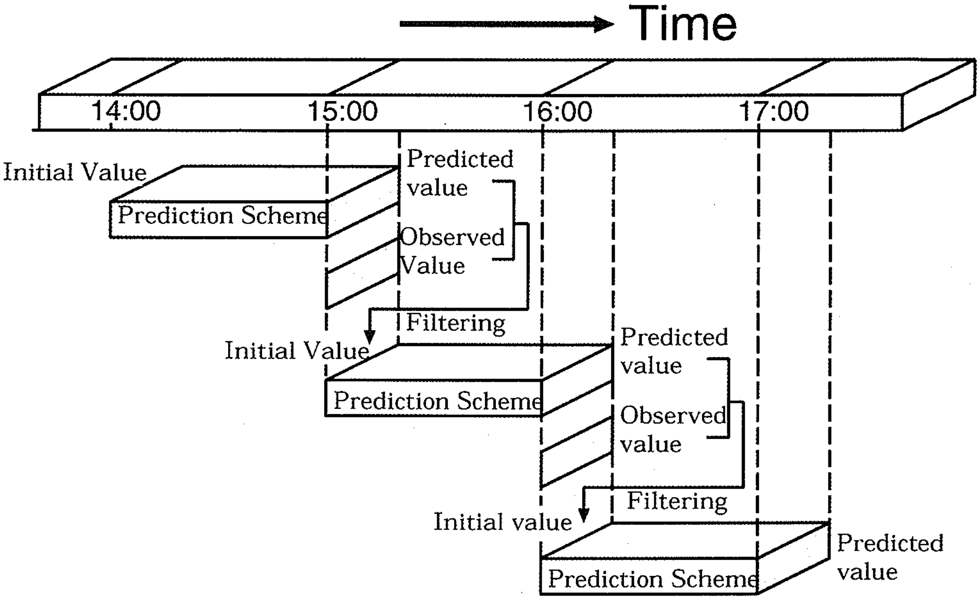

Figure 9.12: Schematic drawing of real-time runoff prediction scheme.

9.3.2 Real-time runoff prediction method with single filter

State-space representation of runoff system

The rainfall runoff model based on Kimura's storage function method is represented as a state–space model for $t_k \leq t < t_{k+1}$:

$$\frac{d}{dt}x(t) = f_1 r(t - T_L) - (x(t)/K)^{1/p} + w(t) \tag{9.12}$$

$$y_k = (x_k/K)^{1/p} + v_k \tag{9.13}$$

where t = time, $x(t)$ = state variable (water storage height), $r(t)$ = input variable (mean rainfall intensity between t_k and t_{k+1}), x_k = state variable at time t_k, y_k = output variable (runoff height) at time t_k, and f_1, T_L, K, and p = constant model parameters.

The value for f_1 takes a constant value less than 1.0 when accumulated rainfall is less than R_{sa}. R_{sa} represents the amount of accumulated rainfall when all of the watershed area is saturated. T_L represents a lag time parameter. The value for K depends on topographic attributes and so on and is sometimes determined from catchment area. The value for p depends on flow conditions and so on and is sometimes fixed to 0.6.

A continuous system noise term $w(t)$ and a discrete observation noise term v_k are represented as follows:

$$E[w(t)] = 0, \ E[w(t)w(\tau)] = Q\delta(t-\tau) \tag{9.14}$$

$$E[v_k] = 0, \ E[v_k v_l] = R\delta_{k,l} \tag{9.15}$$

where Q = variance of system noise, R = variance of observation noise, $\delta(t-\tau)$ = the Dirac delta function, and $\delta_{i,j}$ = the Kronecker delta function. It is also assumed that the system noise, the observation noise and the state variables are uncorrelated with one another.

Equations 9.12 to 9.15 are generally represented as follows:

$$\frac{d}{dt}\mathbf{x}(t) = \mathbf{f}(\mathbf{x}(t), \mathbf{r}_k) + F\mathbf{w}(t) \tag{9.16}$$

$$\mathbf{y}_k = \mathbf{g}(\mathbf{x}_k) + G\mathbf{v}_k \tag{9.17}$$

$$E[\mathbf{w}(t)] = 0, \ E[\mathbf{w}(t)\mathbf{w}(\tau)^T] = Q\delta(t-\tau) \tag{9.18}$$

$$E[\mathbf{v}_k] = 0, \ E[\mathbf{v}_k\mathbf{v}_n^T] = R\delta_{k,l} \tag{9.19}$$

where $\mathbf{r}_k$ = input variable vector between t_k and t_{k+1}, $\mathbf{x}_k$ = state variable vector at time t_k, $\mathbf{y}_k$ = output variable vector at time t_k, $\mathbf{f}$ and $\mathbf{g}$ = nonlinear vector functions, F and G = coefficient matrices, $\mathbf{w}(t)$ = continuous system noise vector, $\mathbf{v}_k$ = discrete observation noise vector, Q = covariance matrix of system noise, and R = covariance matrix of observation noise.

Since Eqs. 9.16 and 9.17 are nonlinear, it is difficult to calculate exactly the transition of the probability distribution of the state variable $\mathbf{x}$. Therefore we suppose $\mathbf{x}$ is Gaussian and solve the stochastic differential equation by an iterative difference method with the aid of a statistical linearization technique (Takasao and Shiiba, 1984).

Prediction scheme

At time t_k, the following procedures are carried out to obtain the one-step-ahead state prediction $\widetilde{\mathbf{x}}_{k+1} = \widetilde{\mathbf{x}}(t_{k+1})$ and the error covariance matrix $\widetilde{P}_{k+1} = \widetilde{P}(t_{k+1})$, ($t_{k+1} = t_k + \Delta T$ and ΔT = time increment of discharge observation).

First, by linearizing statistically the right-hand side in Eq. 9.16 at time t ($t_k \leq t < t_{k+1}$),

$$\frac{d}{dt}\mathbf{x}(t) = A\mathbf{x}(t) + \mathbf{b} + F\mathbf{w}(t) \tag{9.20}$$

is obtained, where A and b are non-probabilistic constant matrix and vector respectively. Discretizing Eq. 9.20 yields

$$\mathbf{x}(t+\Delta t) = \Phi\mathbf{x}(t) + \Gamma\mathbf{b} + \Gamma F\mathbf{w}_t \tag{9.21}$$

where Δt is computation time increment, and $\mathbf{w}_t$ is a noise term with

$$E[\mathbf{w}_t] = 0,\ E[\mathbf{w}_t\mathbf{w}_t^T] = Q_t = Q/\Delta t.$$

Φ and Γ are non-probabilistic matrices determined by A and Δt. To get Φ and Γ, the Padé approximation for e^{tA} can be applied:

$$\Phi = \left[1 - \frac{\Delta t}{2}A + \frac{\Delta t^2}{12}A^2\right]^{-1} \times \left[1 + \frac{\Delta t}{2}A + \frac{\Delta t^2}{12}A^2\right]$$

$$\Gamma = \left[1 - \frac{\Delta t}{2}A + \frac{\Delta t^2}{12}A^2\right]^{-1} \Delta t$$

From Eq. 9.21,

$$\widetilde{\mathbf{x}}(t + \Delta t) = \Phi\widetilde{\mathbf{x}}(t) + \Gamma\mathbf{b} \tag{9.22}$$

$$\widetilde{P}(t + \Delta t) = \Phi\widetilde{P}(t)\Phi^T + \Gamma F Q_t F^T \Gamma^T \tag{9.23}$$

are derived. Iterating these procedures until time t_{k+1}, we get the one-step-ahead state prediction vector $\widetilde{\mathbf{x}}_{k+1}$ and the error covariance matrix $\widetilde{P}_{k+1}$.

Finally, to get the probability distribution of $\mathbf{y}$, by linearizing Eq. 9.17 at time t_{k+1},

$$\mathbf{y}_{k+1} = H\mathbf{x}(t_{k+1}) + d + G\mathbf{v}_{k+1} \tag{9.24}$$

is obtained, where H and d are non-probabilistic matrix and vector. The estimate of output $\widetilde{\mathbf{y}}_{k+1}$ and the error covariance matrix $\widetilde{Y}_{k+1}$ are computed from

$$\widetilde{\mathbf{y}}_{k+1} = H\widetilde{\mathbf{x}}_{k+1} + d \tag{9.25}$$

$$\widetilde{Y}_{k+1} = H\widetilde{P}_{k+1}H^T + GRG^T \tag{9.26}$$

Filtering scheme

When $\mathbf{y}_{k+1}$ is observed at time t_{k+1}, $\widetilde{\mathbf{x}}_{k+1}$ and $\widetilde{P}_{k+1}$ are updated and the filtered state estimate vector $\widehat{\mathbf{x}}_{k+1}$ and the error covariance matrix $\widehat{P}_{k+1}$ are obtained by using the Kalman filter:

$$\widehat{\mathbf{x}}_{k+1} = \widetilde{\mathbf{x}}_{k+1} + K(\mathbf{y}_{k+1} - \widetilde{\mathbf{y}}_{k+1}) \tag{9.27}$$

$$\begin{aligned} \widehat{P}_{k+1} &= (I - KH)\widetilde{P}_{k+1} \\ &= (I - KH)\widetilde{P}_{k+1}(I - KH)^T + KGRG^TK^T \end{aligned} \tag{9.28}$$

where K is the Kalman gain given by

$$K = \widetilde{P}_{k+1}H^T(H\widetilde{P}_{k+1}H^T + GRG^T)^{-1}$$

The $\widehat{x}_{k+1}$ and $\widehat{P}_{k+1}$ are used as the initial state vector and the error covariance matrix for the next prediction procedure.

9.3.3 Treatment of uncertainty of runoff model parameters

The storage function method has five model parameters, f_1, R_{sa}, T_L, K and p. Among these parameters, f_1, R_{sa} and T_L take various values depending on a flood. Thereby the parameters f_1, R_{sa} and T_L are assumed to be constant within each flood duration but differ according to floods. The value for K is determined by catchment area (Nagai *et al.*, 1982) and p is fixed to 0.6.

To consider the uncertainty of the model parameters, a number of filters with different model parameters are run simultaneously, and the probability distribution assigned to these filters is updated by using the Kalman filtering with real-time observation data. A prediction algorithm for the procedure is as follows:

1) Suppose that the model parameters f_1, R_{sa} and T_L take p, q and r discrete different values $f_{1,i}$, $i = 1, \cdots, p$, $R_{sa,j}$, $j = 1, \cdots, q$, $T_{L,k}$, $k = 1, \cdots, r$, respectively.

2) Set $p \times q \times r$ filters having different model parameters. The i, j, k-th filter has model parameters $f_{1,i}$, $R_{sa,j}$ and $T_{L,k}$.

3) Set initial probability density D_{ijk} for each filter with model parameters $f_1 = f_{1,i}$, $R_{sa} = R_{sa,j}$ and $T_L = T_{L,k}$.

4) Run these filters simultaneously. For each filter get an updated state estimate $\widehat{x}_{ijk}(t_m)$, its error variance $\widehat{P}_{ijk}(t_m)$, a one step ahead state prediction $\widetilde{x}_{ijk}(t_m + \Delta T)$, and its error variance $\widetilde{P}_{ijk}(t_m + \Delta T)$, where t_m is the current time and ΔT is the lead time of prediction.

5) Calculate the value of probability density of observed discharge $y(t_m)$ for each filter using

$$\begin{aligned} g_{ijk}(t_m) &= g(y(t_m)|f_1 = f_{1,i}, R_{sa} = R_{sa,j}, T_L = T_{L,k}) \\ &= \frac{1}{\sqrt{2\pi \widehat{Y}_{ijk}(t_m)}} \times \exp\left[-\frac{(\widehat{y}_{ijk}(t_m) - y(t_m))^2}{2\widehat{Y}_{ijk}(t_m)} \right] \end{aligned}$$

where $\widehat{y}_{ijk}(t_m)$ is an updated discharge estimate and $\widehat{Y}_{ijk}(t_m)$ is its updated error variance at time t_m.

6) Update the probability density D_{ijk} assigned to the filters by

$$D_{ijk}(t_m) = \frac{g_{ijk}(t_m) D_{ijk}(t_{m-1})}{\sum_{i=1}^{p} \sum_{j=1}^{q} \sum_{k=1}^{r} g_{ijk}(t_m) D_{ijk}(t_{m-1})}$$

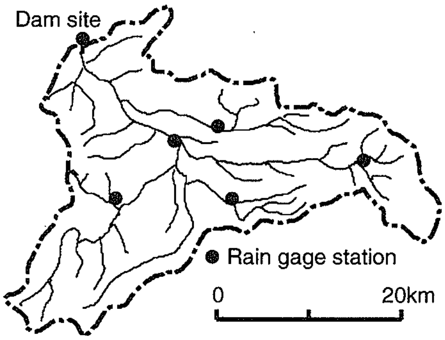

Figure 9.13: Tsuno River Basin (724.0 km^2).

7) Using the one step ahead discharge prediction $\widetilde{y}_{ijk}(t_m + \Delta T)$ and probability density $D_{ijk}(t_m)$, obtain the most probable prediction $\check{y}(t_k + \Delta T)$ as

$$\check{y}(t_k + \Delta T) = \sum_{i=1}^{p} \sum_{j=1}^{q} \sum_{k=1}^{r} D_{ijk}(t_m) \widetilde{y}_{ijk}(t_m + \Delta T)$$

8) At time t_{m+1}, go to step 4) and repeat this procedure.

9.3.4 Applications and results

The method is applied to the Tsuno River basin (724.0 km^2) which is located in the upper part of the Zintsuu River basin in the Chuubu district, Japan (Figure 9.13). In the following prediction simulation, the rainfall is assumed to be known by the predictor, that is, rainfall forecasting is not carried out to test the performances of our prediction method.

Frequency distribution of model parameters

The values of the best fitted model parameters were determined for each of 20 floods which happened in the Tsuno River basin. The model parameters f_1, R_{sa} and T_L are supposed to take different discrete values at intervals of 0.1, 10 mm and 0.5 hr respectively. The value for p is fixed to 0.6 and K is fixed to 13.0 (mm–hr unit). The parameters were obtained by minimizing the difference between an observed and its simulated discharge.

The distributions of identified parameter values of f_1, T_L and R_{sa} are shown in Figure 9.14. The values of an ordinate represent the number of floods fit for the model parameters. In these figures, thick lines represent marginal distributions of f_1, T_L and R_{sa}. It can be seen that the model parameters are widely distributed.

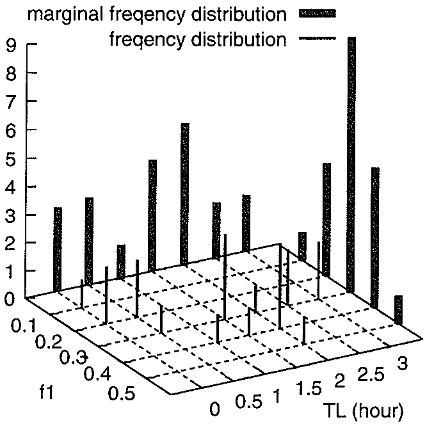

(a) f_1 and T_L

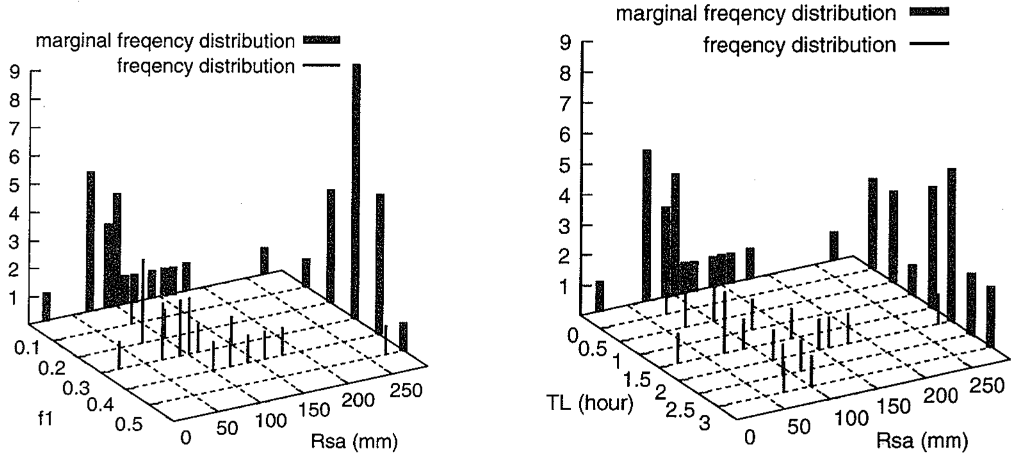

(b) f_1 and R_{sa}

(c) T_L and R_{sa}

Figure 9.14: Distribution of identified model parameter values for f_1, T_L and R_{sa} for the Tsuno River basin.

Comparisons of predictions

To investigate the performances of the prediction method, we compare the four cases of discharge predictions:

Case 1 One-hour-ahead discharge prediction by a single filtering system with the best fitted model parameters to the flood.

Case 2 One-hour-ahead discharge prediction by a single filtering system with the best fitted model parameters to the other flood.

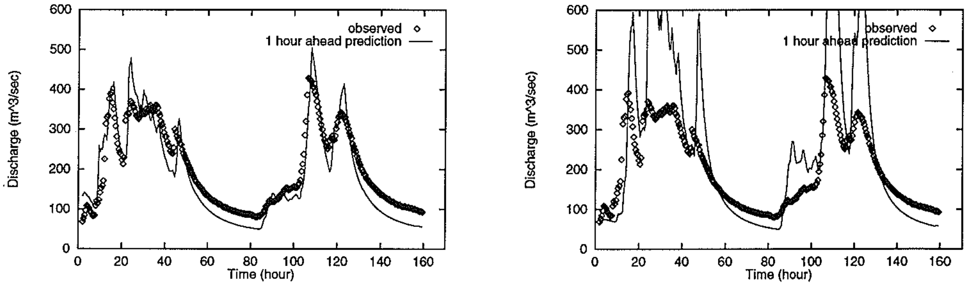

(a) Case 1 (b) Case 2

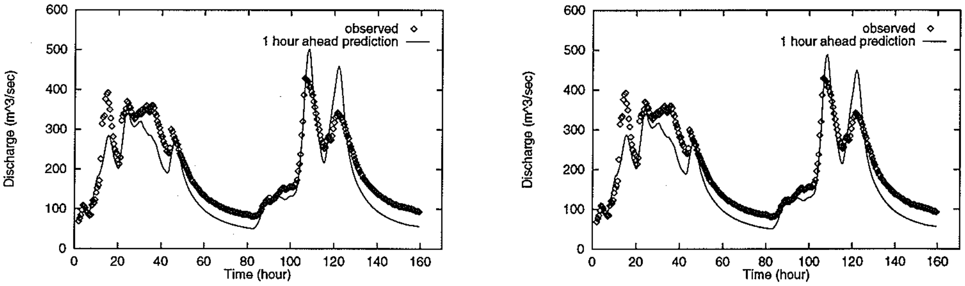

(c) Case 3 (d) Case 4

Figure 9.15: One-hour-ahead discharge prediction for the flood during September 1 to 8 in 1989 with different methods.

Case 3 One-hour-ahead discharge prediction by a number of filtering systems with different model parameters which are run simultaneously. In the case, 1050 kinds of filtering systems are run and initial probability distribution assigned to filtering systems are set evenly.

Case 4 One-hour-ahead discharge prediction by a number of filtering systems with different model parameters which are run simultaneously. In the case, 1050 kinds of filtering systems are run and initial probability distribution assigned to filtering systems are set according to the frequency distribution of the model parameters.

All the cases, the variance of the system noise and the observation noise are set to 10 $\mathrm{mm}^2/\mathrm{hr}^2$.

Discussions

Figure 9.15 shows the one-hour-ahead discharge predictions of the flood during September 1 to 8 in 1989 for the case 1 to 4 respectively. The best fitted model parameters to the flood are $f_1 = 0.5$, $R_{sa} = 270$ mm and $T_L = 2.0$ hr. The prediction result shown in Figure 9.15(b) represents that it is dangerous to make a prediction by a single filtering system with fixed model parameters.

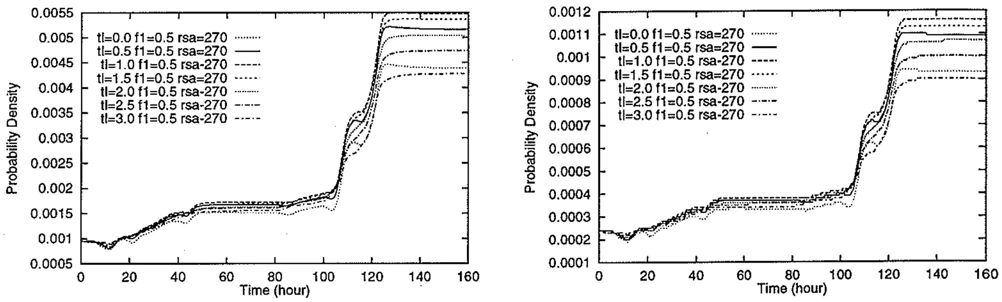

(a) Case 3 (b) Case 4

Figure 9.16: Changes of the probability density assigned to filtering systems.

The discharge prediction shown in Figure 9.15(c) is obtained by 1050 kinds of single filtering systems which run simultaneously. In the case, R_{sa} was assumed to take 30 kinds of discrete values from 10 mm to 300 mm at intervals of 10 mm, f_1 was assumed to take five kinds discrete values from 0.1 to 0.5 at intervals of 0.1, and T_L was assumed to take seven kinds of discrete values from 0.0 hr to 3.0 hr at intervals of 0.5 hr. The initial values of probability distribution density assigned to filtering systems were set evenly. The prediction result underestimates the first peak discharge but shows a quite better result than the one of the case 2. The discharge prediction shown in Figure 9.15(d) is also obtained by 1050 kinds of single filtering systems which run simultaneously. In the case, the initial values of probability distribution density assigned to the filtering systems were set according to the distribution of model parameters shown in Figure 9.14.

Figure 9.16 shows the changes of probability density assigned to the filters with $R_{sa} = 270$ mm and $f_1 = 0.5$, which are the best fitted R_{sa} and f_1 to the flood. It can be seen that for both cases the probability density values show large values as the time passes. This indicates that the filters suitable for the flood have larger weight as the time passes and the prediction systems of cases 3 and 4 adapt to the flood effectively.

9.4 Summary and further works

To develop a reliable flood runoff model and real-time runoff prediction method is the most fundamental work to prevent and reduce flood disasters. In Section 9.2, the tank model and the storage function method, developed and frequently used in Japan, were presented. A simple Xinanjiang model, originally developed in China, was also shown. Next, based on the simplified Xinanjiang model, a catchment hydrologic model was applied to the Chao Phraya River basin in Thailand (110,000 km^2) and the Huaihe River basin in China (140,000km^2).

In Section 9.3, a real-time runoff prediction method taking account of the uncertainty of runoff model parameters was described. In the method, a number of filters with different model parameters run simultaneously and the probability density values assigned to these filters are updated by using Kalman filtering with real-time observation data. Application results show that the method enhances the prediction accuracy and stability.

Currently, most river catchments in Japan are covered with weather radar rainfall measurement systems, with information disseminated in real time to watershed administration offices. Ground based rainfall and river discharge measurement systems also provide hydrological data through Internet in real time. Using such information, the development of a flood warning system based on a distributed rainfall-runoff model and radar rainfall measurements is one of the most important research works. To develop such a system, the following issues are important research topics:

- a flood forecasting using radar and distributed hydrological model
- distributed hydrological model assimilated with radar information
- precipitation field analysis related to scale issues of flood runoff system
- propagation of error of rainfall forecast and/or rainfall estimation through distributed hydrological model
- tradeoff between the lower accuracy and the higher density of measurements achieved by radar
- flood potential map and warning system with radar and distributed hydrological models

References

Bierman, G. J. (1977) “Factrization methods for discrete sequential estimation”, Academic Press, New York.

Ichikawa, Y., M. Shiiba, Y. Tachikawa and K. Takara (2000). “Object-oriented hydrological modeling system”, *HydroInformatics 2000*, Iowa, USA, CDROM.

Jazwinski, A. H. (1970). “Stochastic process and filtering theory”, Academic Press.

Japan Meteorological Agency (2000). GAME-IOP Reanalysis Data (Version 1.1), ftp://hydro.iis.u-tokyo.ac.jp/GAME/GAIN/GAME-REANL/

Kimura, T. (1960). “Research on the estimation of flood runoff (1) –A study of the storage function– (in Japanese).” *Journal of Research of Public Works Research Institute*, Ministry of Construction, Japan, Vol. 4, No. 5, pp. 1–21.

Kalman, R. E. (1960). "A new approach to linear filtering and prediction problems", *Trans. ASME, J. of Basic Eng., 82 (Series D)*, pp. 35–45

Kozan, O., K. Tanaka, and S. Ikebuchi (2001). "Estimation of energy and water budget in the Huaihe River Basin, China", *Proc. of the International Workshop on GAME-AAN/Radiation*, pp. 32–35.

Nagai, A., M. Kadoya, H. Sugiyama, and K. Suzuki (1982). "Synthesizing storage function model for flood runoff analysis (in Japanese)." *Annuals of Disaster Prevention Research Institute, Kyoto Univ.*, No. 25, B-2, pp. 207-220 (in Japanese).

Nirupama, Y. Tachikawa, M. Shiiba and T. Takasao (1996). "A simple water balance model for a mesoscale catchment based on heterogeneous soil water storage capacity", *Bulletin of Disaster Prevention Research Institute, Kyoto Univ.*, 45, pp. 61-83.

Shrestha, R. K., Y. Tachikawa and K. Takara (2002). "IC ratio concept in distributed hydrological modeling for optimal performance", *Proc. of International Symp. on Comparative Regional Hydrology and Mission for IHP Phase VI of UNESCO*, Kuala Lumpur, Oct. 2002, pp. 127–137, CDROM.

Shiiba, M. and T. Takasao (1980). "Filtering and prediction of runoff system." In: *Proc. of the Third International Symposium on Stochastic Hydraulics* (ed. by H. Kikkawa and Y. Iwasa), Tokyo, Japan, pp.83-93.

Shiiba, M., Y. Ichikawa, S. Ikebuchi, Y. Tachikawa and T. Takasao (1996). "Scale-up of a runoff model using GIS and an object-oriented hydrological modeling system", *IAHS Publ.*, 235, pp. 63–70.

Sugawara, M, E. Ozaki, I. Watanabe and Y. Katsuyama. (1976). "On a method of forecasting the daily discharge of the Mae Nam Chao Phraya and its tributaries at several points by means of Tank Model", *Research Notes of the National Research Center for Disaster Prevention*, no. 24, pp. 1–47.

Sugawara, M. (1995). "Tank Model", Chapter 6 in "Computer Models of Watershed Hydrology", ed. V. P. Singh, Water Resources Publications, pp. 165–214.

Tachikawa, Y., K. Takara, Y. Ichikawa and M. Shiiba (2000). "Test Simulation of a macro grid scale distributed hydrological model for the Huaihe River Basin in China", *Proc. of the International GAME/HUBEX Workshop, Sapporo*, pp. 139-146.

Tachikawa, Y., K. Takara, K. Takara, Y. Ichikawa and M. Shiiba (2001). "Simulation of river discharge in the Huaihe River Basin in China", *Proc. of the 5th International Study Conference on GEWEX in Asia and GAME, Nagoya*, vol. 3, pp. 734-737.

Takara, K., M. Shiiba and T. Takasao (1983). "A stochastic method of realtime flood prediction in a basin consisting of several sub-basin." *Journal of Hydroscience and Hydraulic Engineering*, Japan Society of Civil Engineers, 1(2), pp. 93-111.

Takasao, T. and M. Shiiba (1984). “Development of techniques for on-line forecasting of rainfall and flood runoff.” *Journal of Japan Society for Natural Disaster Science*, 6(2), pp. 83–112.

Takasao, T., M. Shiiba and Y. Tachikawa (1993). “Real–time Integrated operating system of retarding basin sluice ways”, IAHS Publ., no. 213, pp. 403–410.

Takasao, T., M. Shiiba and Y. Tachikawa (1994a). “Development of a real-time stage prediction system and its application to the upstream Kizu River Basin (in Japanese).” *Journal of Hydraulic, coastal and Environmental Engineering*, Japan Society of Civil Engineers, 503/II-29, pp. 19–27.

Takasao, T., M. Shiiba and E. Nakakita (1994b). “A real-time estimation of the accuracy of short-term rainfall prediction using radar.” *Stochastic and statistical methods in hydrology and environment engineering*, Kulwer Academic Publishers, 2, pp. 339–351.

Takasao, T., M. Shiiba and Y. Tachikawa (1995). “Operating system for retarding basin sluice ways using real-time stage prediction”, *Journal of Hydroscience an Hydraulic Engineering*, vol. 13(1), pp, 63–70.

Takasao, T., M. Shiiba and Y. Ichikawa (1996a). “A runoff simulation with structural hydrological modeling System”, *Journal of Hydroscience and Hydraulic Engineering*, Japan Society of Civil Engineers, 14(2), pp. 47–55.

Takasao, T., M. Shiiba and Y. Tachikawa (1996b). “A real-time flood runoff prediction method considering the uncertainty of parameters of the storage function method (in Japanese).” *Annual Journal of Hydraulic Engineering*, Japan Society of Civil Engineers, 40, pp. 317–322.

Tanaka, K. and S. Ikebuchi (1994). "Simple biosphere model including urban area and water body, and its application to the basin of Biwa Lake", *Annuals of Disaster Prevention Research Institute, Kyoto Univ.*, 37, pp. 299-313.

Zhao, R. J. (1992). “The Xinanjiang model applied in China”, *Journal of Hydrology*, 135, pp. 371–381.

Zhao, R. J. and X. R. Liu (1995). “The Xinanjiang Model”, Chapter 7 in "Computer Models of Watershed Hydrology", ed. V. P. Singh, Water Resources Publications, pp. 215–232.

Chapter 10

Distributed Runoff Modeling

Yutaka Ichikawa
Graduate School of Global Environmental Studies, Kyoto University
Yoshida-honmachi, Sakyo-ku, Kyoto 606-8501, JAPAN
phone: +81-75-753-5096, fax: +81-75-753-4907
e-mail: ichikawa@wr.kuciv.kyoto-u.ac.jp

10.1 Introduction

Rainfall-runoff processes are water flow phenomena that occur on and beneath the ground surface, and can be modeled using differential equations to describe movement of flowing water. For example, water flow in porous soil is described by combining Darcy's law and the continuity equation. Also, water flow on the ground surface is described by the Navier-Stokes equation and the continuity equation. A distributed runoff model is the model which describes spatio-temporal variations of hydrological variables on the basis of differential equations for physical water movement. Because it is generally difficult to analytically solve the differential equations of water movement, they are usually solved by using numerical techniques that discretize the equations and the spatio-temporal domain of the problem. The spatio-temporal variations of hydrological variables are simulated on grid points or cells placed on the spatial domain at each time step. The grid points or cells are also used to consider spatial distributions of geographical and vegetational properties in a catchment, which give considerable effects on rainfall-runoff processes. Using a distributed runoff model, hydrological variables can be calculated at any points and possible changes of runoff characteristics due to changes of climate or land use can be predicted.

There are several fundamental distributed runoff models such as the kinematic wave model, diffusion wave model, dynamic wave model, and unsaturated-saturated flow model (Richards' equation). Also, there are a large number of practical distributed runoff models created by combining or extending the fundamental models. The purpose of this chapter is to introduce the basic theory of the kinematic wave model as an example of a distributed runoff model and to give lumping techniques of kinematic wave models. A hydrological modeling system will also be discussed as a practical application of distributed runoff modeling.

10.2 Basic theory of the kinematic wave model

The kinematic wave model is an unsteady open channel flow wave model which is often used in engineering hydrology. The kinematic wave model was originally developed for river routing, but later was applied to catchment rainfall-runoff modeling and several variations of the kinematic wave model were developed.

The basic form of the kinematic wave equation is

$$\frac{\partial A}{\partial t} + \frac{\partial Q}{\partial x} = q_L(x,t) \tag{10.1}$$

$$Q(x,t) = \beta A(x,t)^m \tag{10.2}$$

where $A(x,t)$ is the flow cross-sectional area, $Q(x,t)$ is the flow discharge, $q_L(x,t)$ is the lateral inflow discharge per unit length, and β and m are constants. $A(x,t)$ and $Q(x,t)$ are abbreviated to A and Q, respectively in Eq. 10.1.

Equation 10.1 is the continuity equation and is derived from the principle of mass conservation within a control volume, and Eq. 10.2 is derived from Manning's or Chezy's laws, which are flow resistance laws of open channel uniform flow. Manning's law is described as:

$$v = \frac{1}{n} R^{2/3} I^{1/2} \tag{10.3}$$

in which v is the average flow velocity, n is Manning's friction coefficient, R is the hydraulic radius, and I is the friction slope. By assuming that R can be generally expressed as $z_1 A^{z_2}$ (z_1 and z_2 are constants), we can easily obtain the expression of Eq. 10.2.

10.3 Numerical solutions of the kinematic wave model

10.3.1 An overview of numerical solutions

The combination of Eq. 10.1 and Eq. 10.2 is a nonlinear first-order partial differential equation which describes the change of Q and A in time and space. This equation can be solved by using numerical methods. Several methods are available, for example, the finite difference method, the finite element method, and the finite volume method. In this section, the finite difference methods are used to solve this equation because it is easy to understand them and to write computer programs to implement them.

Finite difference methods are classified into two types: explicit and implicit. Explicit methods evaluate all spatial derivatives in a partial differential equation at the time level where the solution is known. Implicit methods evaluate all spatial derivatives at the time level where the solution is unknown. Generally speaking, implicit methods are more complex than explicit ones, however the former is superior in numerical stability to the latter. Both methods are explained below.

10.3.2 Explicit method

The Lax-Wendroff scheme is explained as an example of an explicit method. Figure 10.1 shows the discretized $x-t$ plane, the grid system, and the variables defined at the grid points. The subscripts i and j denote incremented space and time levels, respectively. This scheme calculates $A_{i,j+1}$ from $A_{i-1,j}$, $A_{i,j}$, and $A_{i+1,j}$ as stated below.

Expanding $A(x, t+\Delta t)$ using the Taylor's series up to the second order, we can obtain:

$$A(x,t+\Delta t) = A(x,t) + \Delta t\frac{\partial A}{\partial t} + \frac{(\Delta t)^2}{2}\frac{\partial^2 A}{\partial t^2} \tag{10.4}$$

Equation 10.1 can be rewritten as:

$$\frac{\partial A}{\partial t} = q_L - \frac{\partial Q}{\partial x} \tag{10.5}$$

Using this expression, $\partial^2 A/\partial t^2$ can also be rewritten as:

$$\begin{aligned}\frac{\partial^2 A}{\partial t^2} &= \frac{\partial}{\partial t}\left(q_L - \frac{\partial Q}{\partial x}\right)\\ &= \frac{\partial q_L}{\partial t} - \frac{\partial}{\partial t}\left(\frac{\partial Q}{\partial x}\right)\\ &= \frac{\partial q_L}{\partial t} - \frac{\partial}{\partial x}\left(\frac{\partial Q}{\partial t}\right)\end{aligned}$$

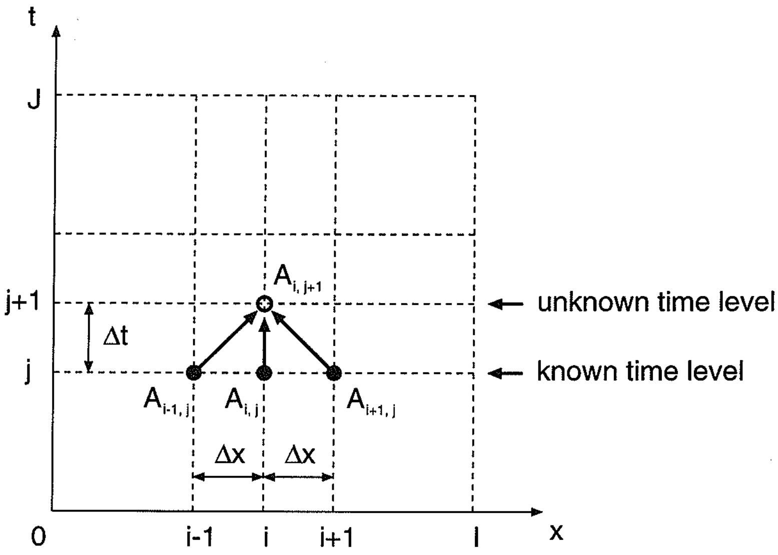

Figure 10.1: Discretization of $x - t$ plane

$$
\begin{aligned}
&= \frac{\partial q_L}{\partial t} - \frac{\partial}{\partial x}\left(\frac{\partial A}{\partial t}\frac{dQ}{dA}\right) \\
&= \frac{\partial q_L}{\partial t} - \frac{\partial}{\partial x}\left\{\left(q_L - \frac{\partial Q}{\partial x}\right)\frac{dQ}{dA}\right\} \qquad (10.6)
\end{aligned}
$$

in which $dQ/dA = \beta m Q^{m-1}$.

These expressions (Eq. 10.5 and Eq. 10.6) do not include any derivatives of Q and A with respect to time. We replace all derivatives in these expressions by difference operators:

$$\frac{\partial A}{\partial t} \simeq q_{Li,j} - \frac{Q_{i+1,j} - Q_{i-1,j}}{2\Delta x} \qquad (10.7)$$

$$
\begin{aligned}
\frac{\partial^2 A}{\partial t^2} \simeq \frac{q_{Li,j+1} - q_{Li,j}}{\Delta t} - \frac{1}{\Delta x}\left\{\left(q_{Li+1/2,j} - \frac{Q_{i+1,j} - Q_{i,j}}{\Delta x}\right)\cdot\right. \\
\left.\beta m A^{m-1}_{i+1/2,j} - \left(q_{Li-1/2,j} - \frac{Q_{i,j} - Q_{i-1,j}}{\Delta x}\right)\cdot \beta m A^{m-1}_{i-1/2,j}\right\} \qquad (10.8)
\end{aligned}
$$

in which

$$q_{Li\pm1/2,j} = \frac{q_{Li,j} + q_{Li\pm1,j}}{2} \qquad (10.9)$$

$$A_{i\pm1/2,j} = \frac{A_{i,j} + A_{i\pm1,j}}{2} \qquad (10.10)$$

$$Q_{i,j} = \beta A_{i,j}^m \tag{10.11}$$

Let the right hand side of Eq. 10.7 be A_1 and that of Eq. 10.8 be A_2, then we obtain:

$$A_{i,j+1} = A_{i,j} + \Delta t A_1 + \frac{(\Delta t)^2}{2} A_2 \tag{10.12}$$

This equation means $A_{i,j+1}$ (and also $Q_{i,j+1}$) can be calculated from $A_{i-1,j}$, $A_{i,j}$, $A_{i+1,j}$, $q_{Li-1,j}$, $q_{Li,j}$, $q_{Li+1,j}$, and $q_{Li,j+1}$. If the values of $A_{i,0}$ (or $Q_{i,0}$) $(i = 0, 1, \cdots I)$ are given as the initial conditions and the values of $A_{0,j}$ (or $Q_{0,j}$) $(j = 0, 1, \cdots J)$ and $q_{Li,j}$ $(i = 0, 1, \cdots I,\ j = 0, 1, \cdots J)$ are given as the boundary conditions, $A_{i,j+1}$ can be calculated sequentially.

10.3.3 Implicit method

Equations 10.1 and 10.2 can be rewritten as

$$\frac{\partial Q}{\partial t} + c\frac{\partial Q}{\partial x} = cq_L \quad \left(c = \frac{dQ}{dA} = \beta m A^{m-1}\right) \tag{10.13}$$

where c is the kinematic wave velocity.

The discretization of Eq. 10.13 on the $x - t$ plane by using the scheme developed by Beven[1] leads to:

$$\frac{Q_{i,j+1} - Q_{i,j}}{\Delta t} + \theta c_{i-1/2,j+1}\left(\frac{Q_{i,j+1} - Q_{i-1,j+1}}{\Delta x} - q_{Li-1/2,j+1}\right) +$$
$$(1-\theta)\ c_{i-1/2,j}\left(\frac{Q_{i,j} - Q_{i-1,j}}{\Delta x} - q_{Li-1/2,j}\right) = 0 \tag{10.14}$$

in which Δx is the distance between two adjacent grid points, Δt is the time step size, and θ is the time weighting parameter. $c_{i-1/2}$ is evaluated as $0.5(c_i + c_{i+1})$.

In this equation, the unknown variable is $Q_{i,j+1}$. Collecting unknown terms to the left hand side of the equation, we obtain

$$\left(1 + \theta c_{i-1/2,j+1}\frac{\Delta t}{\Delta x}\right) Q_{i,j+1} =$$
$$Q_{i,j} + \theta c_{i-1/2,j+1}\Delta t\left(\frac{Q_{i-1,j+1}}{\Delta x} + q_{Li-1/2,j+1}\right) -$$
$$(1-\theta)c_{i-1/2,j}\Delta t\left(\frac{Q_{i,j} - Q_{i-1,j}}{\Delta x} - q_{Li-1/2,j}\right) \tag{10.15}$$

Equation 10.15 is a nonlinear equation of $Q_{i,j+1}$ because $c_{i-1/2,j+1}$ is dependent on the value of $Q_{i,j+1}$. To solve this equation, two methods are available. One is the method that treats the value of $c_{i-1/2,j+1}$ as constant by assuming that the nonlinearity of Eq. 10.15 is not so strong. In this method, Eq. 10.15 is considered as a linear equation. The other is the iterative method, which uses the following procedures:

step 1: Let $\hat{Q}_{i,j+1}$ be the estimate of $Q_{i,j+1}$. Give the initial value to $\hat{Q}_{i,j+1}$.

step 2: Calculate $c_{i-1/2,j+1}$ by substituting the value of $\hat{Q}_{i,j+1}$ into $\beta m Q^{m-1}$.

step 3: Calculate $Q_{i,j+1}$ by taking $\left(1 + \theta c_{i-1/2,j+1} \Delta t/\Delta x\right)$ to be constant.

step 4: If $|Q_{i,j+1} - \hat{Q}_{i,j+1}| \leq \epsilon$ (tolerance level), go to calculation of $Q_{i+1,j+1}$. Otherwise, consider $Q_{i,j+1}$ obtained in the step 3 as the new estimate value and go back to the step 2.

10.4 Various kinematic wave models

The kinematic wave concept was originally developed for river routing, but it is also applicable to catchment routing. For this purpose, several variations of the kinematic wave models have been developed. They involve the ability to consider the complex flow mechanism, the characteristics of soil, and its spatial distribution within a catchment. The solution technique for them is basically the same as that for the original kinematic wave model. This section describes the theoretical background of the kinematic wave models for catchment routing, but does not deal with the solution techniques for them.

10.4.1 Kinematic wave model for shallow water flow on a rectangular plane

A catchment is often modeled as a rectangular plane or a set of rectangular planes, and runoff flow from a catchment is modeled as shallow water flow on a rectangular plane (or rectangular planes).

The hydraulic radius of shallow water flow can be approximated by the water depth, h. Then, Eq. 10.3 (Manning's law) can be rewritten as:

$$v = \frac{1}{n} h^{2/3} I^{1/2} \tag{10.16}$$

Therefore the discharge per unit width, q, can be expressed as:

$$\begin{aligned} q &= vh \\ &= \frac{\sqrt{I}}{n} h^{5/3} \\ &= \alpha h^m \end{aligned} \tag{10.17}$$

in which $\alpha = \sqrt{I}/n$, $m = 5/3$. This equation is the kinematic wave equation for shallow water flow on a rectangular plane.

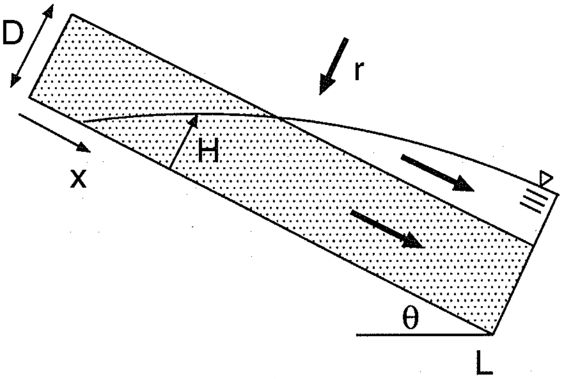

Figure 10.2: Schematic representation of surface-subsurface flow on a hillslope

By dividing both sides of Eq. 10.1 by the width of a rectangular plane, B, we can obtain a different form of the continuity equation:

$$\frac{\partial h}{\partial t} + \frac{\partial q}{\partial x} = r \quad (= q_L/B) \tag{10.18}$$

in which r is rainfall intensity.

The value of I is usually approximated as the slope gradient of the rectangular plane, and the value of n is calibrated from observation or specified empirically.

10.4.2 Kinematic wave model for surface-subsurface flow[2, 3]

The kinematic wave model described in **10.4.1** can be applied to infiltration excess overland flow (Hortonian overland flow), but is not applicable to saturation excess overland flow, because the model does not consider the water flow in a surface soil layer (subsurface flow). Takasao *et al.*[2] developed a kinematic wave model which considered both surface and subsurface flow, and its interaction. This model can describe a saturation excess overland flow mechanism.

They assumed that hillslope surface was covered by a soil layer with high surface infiltration capacity and permeability, which is illustrated in Figure10.2. In this figure, D is the depth of the soil layer, L is the length of the hillslope, H is the depth of water flow, and r is the rainfall intensity. Let γ be the porosity of the soil layer and be spatially constant. Then the depth of the effective pore of the soil layer, d, becomes γD. Also, the actual water depth (water volume in height), h, becomes γH $(0 \leq H < D)$ or $H - D + \gamma D$ $(H \geq D)$. Takasao *et al.* derived the following piecewise relation between h and q from Darcy's law and Manning's law:

$$q = \begin{cases} ah & (0 \le h < d) \\ \alpha(h-d)^m + ah & (h \ge d) \end{cases} \tag{10.19}$$

where a $(= k\sin\theta/\gamma)$ is the velocity of water which flows in the soil layer, k is the hydraulic conductivity, and α and m are $\sqrt{\sin\theta}/n$ and 5/3, respectively. The upper relation given in Eq. 10.19 is used for the case where only subsurface flow occurs, and the lower relation in Eq. 10.19 is used for the case where saturation excess overland flow occurs.

10.4.3 Kinematic wave model considering field capacity

The kinematic wave models described in **10.4.1** and **10.4.2** are basically used to simulate flood runoff which occurs in heavy rainfall events where the gravity force is dominant as a driving force of water flow. However these models can not be used in drier conditions because the capillary force of soil particles can not be negligible in comparison with the gravity force in such conditions. This fact means that we can not conduct long term runoff simulations from dry seasons to humid seasons continuously using a single runoff model.

To solve this problem, Shiiba *et al.*[4] developed a new kinematic wave model by which both flood and low flow simulation can be conducted by introducing a concept of field capacity of hillslope soil layer to the kinematic wave model for surface-subsurface flows. This new kinematic wave model enables a runoff simulation to be connected continuously from flood period to low flow period, or conversely from low flow period to flood period. This model assumes that a part of water which infiltrates into a surface soil layer is mainly captured by the capillary force of soil particles and lateral water flow occurs when water content exceeds the field capacity of the soil.

The kinematic wave equation considering field capacity is as follows:

$$q = \begin{cases} ah_f & (0 \le h_f < d) \\ \alpha(h_f-d)^m + ah_f & (h_f \ge d) \end{cases} \tag{10.20}$$

$$h = \begin{cases} h_f + h_c\left(1 - \left(\dfrac{d-h_f}{d}\right)^N\right)^{1/N} & (0 \le h_f < d) \\ h_f + h_c \quad (h_f \ge d) \end{cases} \tag{10.21}$$

where q is the discharge per unit width, h is the total water content, h_f is the free water content, a $(= k\sin\theta/\gamma_e)$ is the water flow velocity in a surface soil layer, k is the hydraulic conductivity, γ_e is the effective porosity of a surface soil layer, d $(= \gamma_e D)$ is the depth of pore contained in a surface soil layer, D is the depth of a surface soil layer, $\alpha = \sqrt{\sin\theta}/n$, θ is the slope gradient, n is the Manning roughness coefficient, m is a constant (> 1), N is a constant (> 1), $h_c = \gamma_c D$, and γ_c is the field capacity of a surface soil layer.

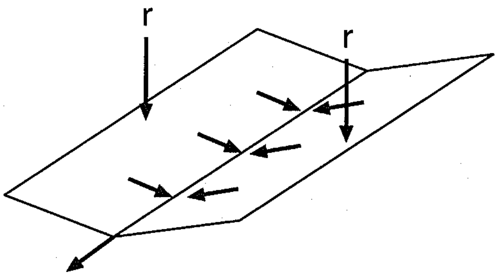

Figure 10.3: Schematic representation of an open-book catchment model

10.5 Applications of kinematic wave models

10.5.1 Using an open-book catchment model

The simplest application of the kinematic wave model is to apply the model to an open-book catchment model. Figure 10.3 shows a schematic representation of an open-book catchment model. As its name implies, an open-book catchment model consists of two rectangular planes and a stream. Rain water flows on the planes and drains into the stream. The streamflow drains out of the catchment outlet. The flows on the rectangular planes and the stream are routed using the kinematic wave model. This is the simplest approximation of catchment hydrology using a kinematic wave model, and a more complex structure of a catchment can be modeled as a cascade of the open-book catchment model.

10.5.2 Using a digital elevation model

In recent years, digital elevation maps have become available at a resolution fine enough to clearly describe the topography of catchments (50 m in the UK, France and Japan; 30 m in the USA; 25 m in Switzerland)[5]. Using these data, a number of digital elevation models (DEMs) have been developed to precisely and efficiently represent catchment topography. Digital elevation models can be grouped into three types: 1) contour-based models; 2) triangular irregular network models; and 3) grid-based models. Each model has been used as the basis for a number of distributed runoff models. For example, TAPES-C[6, 7] is based on a contour-based model, and Tachikawa *et al.*[8], Palacios-Velez *et al.*[9], Vieux[10] and Goodrich *et al.*[11] developed distributed hydrological models based on triangular irregular network models. TOPMODEL[12], which is one of the most famous rainfall-runoff models, relied upon manual topographic analysis in the early days, but it now uses a grid-based DEM and a computerized technique to derive the topographic index of the catchments[13]. SHE[14, 15] also has a grid-based structure and uses its structure directly for computing

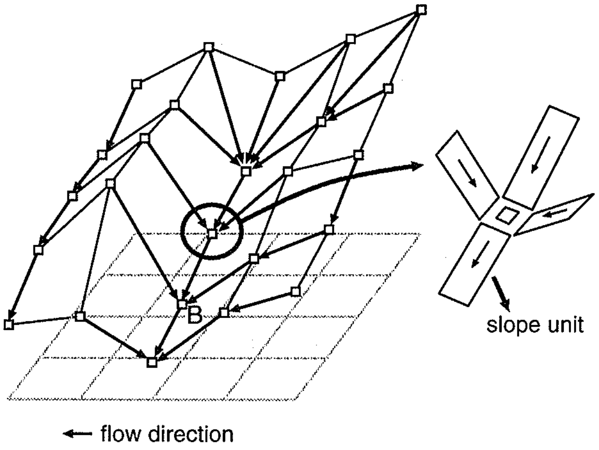

Figure 10.4: Schematic representation of the grid-based DEM

hydrological phenomena. Besides these two models, there are many other hydrological models which are based on grid-based DEMs because the grid-based DEMs have structures which are simple and suitable for hydrological modelings.

Ichikawa *et al.*[16] applied the kinematic wave model considering field capacity to a grid-based DEM[17]. Figure 10.4 shows a schematic representation of the grid-based DEM which they used. In this figure two adjacent grid points are connected by a rectangular plane. They call this rectangular plane "a slope unit". Catchment topography is represented by a set of slope units. For each slope unit, its area, length and gradient can be easily calculated. They applied the kinematic wave model considering field capacity to all the slope units comprising the catchment topographic model and routed water flows from upstream slope units to downstream slope units. The outflow discharge from the catchment was used as the lateral inflow condition of a river routing model. Figure 10.5 shows observed and predicted discharges for the Daido River basin (180 km^2), using the kinematic wave model applied on the grid-based DEM. The peak values of discharge are overestimated in the upper figure, but the simulated hydrograph gives a good result in the lower figure, particularly in the recession stage. This fact means the kinematic wave model considering field capacity has high applicability to low flow periods.

10.6 Lumping of distributed runoff models

The distributed runoff models, such as the kinematic wave models, have the advantage that they are based on the physical processes of flowing water. However, generally speaking, they require much computation time and resources.

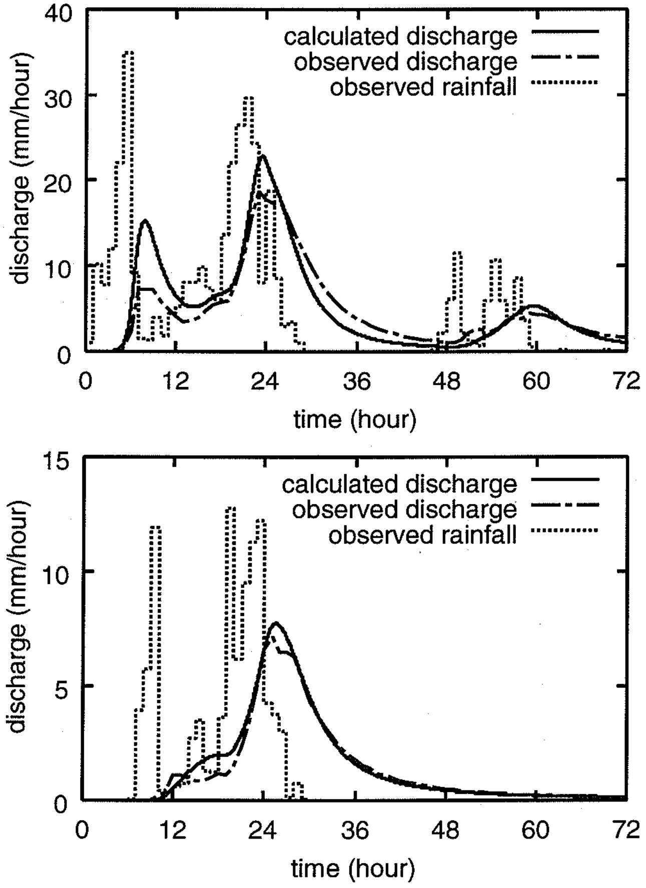

Figure 10.5: Observed and predicted discharge using the kinematic wave model considering field capacity

In this section, lumped kinematic wave runoff models are derived by spatially integrating the kinematic wave models described in **10.2**, **10.4.2** and **10.4.3** in order to reduce the computational burden of water flow routing. These lumped models have a physical basis and the parameter values are calculated using topographic variables obtained from the DEM.

10.6.1 Lumping of the original kinematic wave model

In this section, the kinematic wave model, $A = KQ^P$ (A: flow cross-sectional area, Q: flow discharge, K and P: constants), is used to describe shallow water flow on a rectangular plane instead of $q = \alpha h^m$ derived in **10.4.1**. These equations are different expressions of the kinematic wave model for shallow water flow.

The main purpose of this section is to derive a steady-state relation between storage volume and outflow discharge of a rectangular plane by spatially integrating the kinematic wave model. When a rainfall-runoff system reaches a steady condition, the discharge at some point, Q, is expressed as $r \times M$, in which r is the rainfall intensity and M is the upslope contributing area at the point.

Suppose that a catchment is represented by N slope units. Let us consider the ith slope unit ($i = 1, 2, ..., N$). Let L_i be the length, B_i the width, M_i the area, θ_i the gradient, and K_i and P_i the kinematic constants K and P, of the ith slope unit. K_i is expressed as:

$$K_i = \begin{cases} \left(\dfrac{n_i B_i^{\frac{1}{P_i}-1}}{\sqrt{\sin\theta_i}} \right)^{P_i} & \text{(for surface flow)} \\ \dfrac{\gamma_i}{k_i \sin\theta_i} & \text{(for subsurface flow)} \end{cases} \qquad (10.22)$$

where n_i is the Manning's coefficient, k_i is the hydraulic conductivity, and γ_i is the effective porosity. Also let U_i be the upslope contributing area at the upper end of the ith slope unit. If the ith slope unit is located on the upper boundary of a catchment, $U_i = 0$.

Let $A_i(x)$ be the flow cross-sectional area and $Q_i(x)$ the flow discharge at the distance x from the upper end of the ith slope unit. Since a slope unit is a rectangular plane, the upslope contributing area at the distance x from its upper end of the ith slope unit, $M_i(x)$, is expressed as:

$$M_i(x) = \frac{M_i}{L_i} x + U_i \qquad (10.23)$$

Then we can obtain

$$Q_i(x) = r \left(\frac{M_i}{L_i} x + U_i \right) \qquad (10.24)$$

and from the kinematic wave equation, we have

$$A_i(x) = K_i r^{P_i} \left(\frac{M_i}{L_i} x + U_i \right)^{P_i} \tag{10.25}$$

Spatially integrating $A_i(x)$, we can obtain the storage volume of the ith slope unit, s_i

$$s_i = \int_0^{L_i} A_i(x) dx = \frac{r^{P_i}}{P_i + 1} \frac{K_i L_i}{M_i} \left\{ (M_i + U_i)^{P_i+1} - (U_i)^{P_i+1} \right\} \tag{10.26}$$

Summing up s_i, we can obtain the total storage volume of the catchment, S

$$S = \sum_{i=1}^{N} s_i = \sum_{i=1}^{N} \frac{1}{P_i + 1} \frac{K_i L_i}{M_i} \left\{ (M_i + U_i)^{P_i+1} - (U_i)^{P_i+1} \right\} r^{P_i} \tag{10.27}$$

If we assume that the constant in the kinematic wave model, P_i, is spatially uniform and rewrite P_i as P, Eq. 10.27 can be further simplified as:

$$S = \frac{r^P}{P+1} \sum_{i=1}^{N} \frac{K_i L_i}{M_i} \left\{ (M_i + U_i)^{P+1} - (U_i)^{P+1} \right\} = E r^P \tag{10.28}$$

where

$$E = \frac{1}{P+1} \sum_{i=1}^{N} \frac{K_i L_i}{M_i} \left\{ (M_i + U_i)^{P+1} - (U_i)^{P+1} \right\} \tag{10.29}$$

Let O be the outflow discharge from the catchment. Under the steady-state condition, $O = r \times \sum_{i=1}^{N} M_i$, rearranged for,

$$r = \frac{O}{\sum_{i=1}^{N} M_i} \tag{10.30}$$

Substituting Eq. 10.30 into Eq. 10.28, we can obtain

$$S = E \left(\frac{O}{\sum_{i=1}^{N} M_i} \right)^P = F O^P \tag{10.31}$$

where $F = E / (\sum_{i=1}^{N} M_i)^P$.

Equation 10.31 gives the steady-state relation between the storage volume and outflow discharge of a catchment. However we use this relation to calculate outflow discharge for the unsteady condition, that is, time variant rainfall case. Thus we have the relationship between storage and outflow as follows:

$$S(t) = F O(t)^P \tag{10.32}$$

The continuity equation of storage volume is given by

$$\frac{dS}{dt} = Q_L(t) - O(t) = Q_L(t) - \left(\frac{S(t)}{F}\right)^{1/P} \tag{10.33}$$

where $Q_L(t) = r(t) \times \sum_{i=1}^{N} M_i$. Since Eq. 10.33 is an ordinary differential equation for $S(t)$, we numerically solve this equation by using Runge-Kutta method. We call the model derived here as "the lumped kinematic wave model". The value of F in Eq. 10.31 can be calculated from the topographic quantities and kinematic constants. This means that the lumped kinematic wave model is a lumped model but the parameters can be specified on a physical basis.

To validate the performance of the lumped kinematic wave model, we apply it to catchment modeling and compare simulated results with those of the distributed kinematic wave model and observed discharges. Figure 10.6 shows predicted discharges of the lumped kinematic wave model and the distributed kinematic wave model. The upper discharge hydrographs were obtained on the condition that only surface flow occurred in the catchment and the following parameter values were used: Manning's coefficient, n: 0.3 `[m-s]`, kinematic constant, P: 0.6. The lower discharge hydrographs were obtained on the condition that only subsurface flow occurred and hydraulic conductivity k: 0.2 `[m/s]`, effective porosity γ: 0.1, kinematic coefficient P: 1.0. For all simulations, any rainfall losses (evapotranspiration, infiltration to ground water, interception and depression storage) were not taken into account, and the values of model parameters were considered to be uniform in space.

It can be seen from this figure that the discharges simulated by the two models are very similar in all simulations. The computation time of the lumped model was about 2 seconds while that of the distributed model was about 5 hours, using Sun Ultra-SPARC Work Station (clock frequency: 167 MHz, memory: 256 Mbytes). This fact suggests that the lumped kinematic wave model can be used as a substitutional model of the distributed kinematic wave model when computation speed is given high priority and we can accept some lumping errors.

We now compare the discharges calculated by the lumped kinematic wave model with observed discharges. Figure 10.7 shows the predicted and observed discharges. The upper and lower discharges were obtained for 1–2 August 1982 and 19–20 September 1990, respectively. All simulations were conducted on the condition that only subsurface flow occurred and any rainfall losses were not taken into account. The upper graph shows that the calculated discharge is less than the observed one at the peak. This seems to be caused by the fact that only subsurface flow was considered in the simulation while there was a high possibility that the surface flow occurred in the catchment due to heavy precipitation in the upper case. The lower graph shows relatively good agreement between the calculated and observed discharges. Because there was

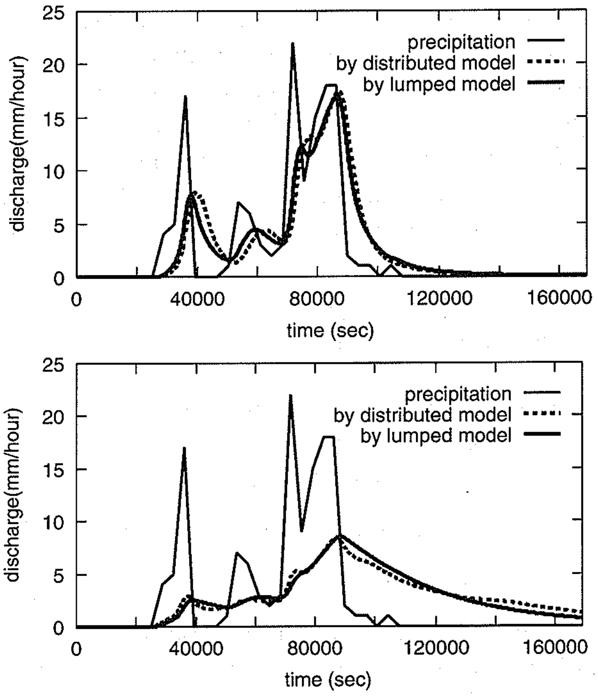

Figure 10.6: Predicted discharges of the lumped kinematic wave model and the distributed kinematic wave model

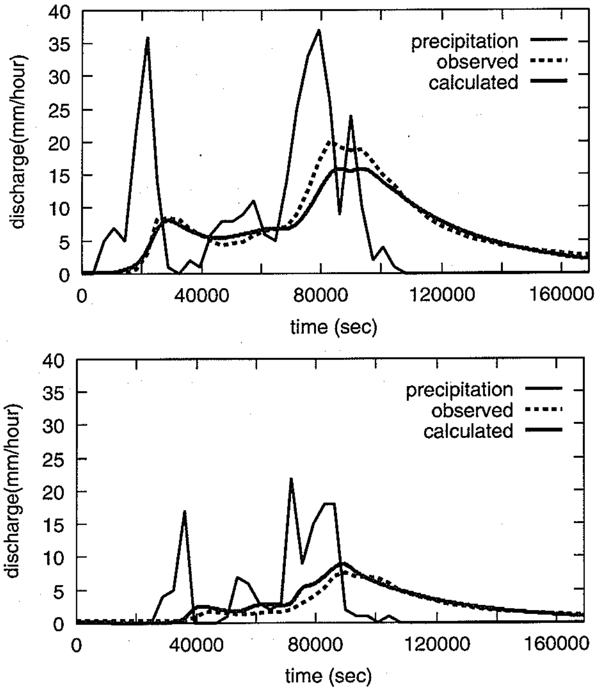

Figure 10.7: Predicted and observed discharges

less precipitation in the lower case than the upper case, subsurface flow was considered to be a dominant runoff process in the lower case, as assumed in the simulation. This seems to cause the better result in the lower case.

These comparisons suggest that the lumped kinematic wave model can be used as a substitutional model of a distributed runoff model but further improvements are required so that the model can consider the spatial heterogeneity of runoff processes in order to reproduce observed discharges with high accuracy.

10.6.2 Lumping of the kinematic wave model for surface-subsurface flow[18]

The key point of the lumping method shown in the previous section is spatial integration of the flow cross-sectional area ($\int A(x)dx$). Therefore, this lumping method is not applicable to a kinematic wave equation in which:

- A (or h) is not explicitly described by Q (or q).
- A (or h) is not integrable with Q (or q).

This means that this lumping method can not be used for lumping of the kinematic wave model for surface-subsurface flow. A lumping method for the kinematic wave model for surface-subsurface flow is shown here.

Let us express a general kinematic wave equation as $q = g(h)$ and suppose that q is integrable with h. Also, let us express an equation obtained by solving the above equation for h as $h = f(q)$. f can not be always given explicitly. Assume that the rainfall-runoff process of a slope system reaches steady state with spatially uniform rainfall input. From this assumption, discharge flux in the slope system can be expressed as the product of (spatially uniform) rainfall intensity and the upslope contributing area.

Storage volume of a slope unit, s, is given below:

$$s = \int_0^L A(x)dx = \int_0^L w(x)h(x)dx \tag{10.34}$$

where x is the distance from the upstream end of a slope unit, L is the length of the slope unit, $A(x)$ is the flow cross-sectional area, $w(x)$ is the width of the slope unit, and $h(x)$ is total water content. Based on the above assumption, discharge in a slope unit can be given as:

$$Q(x) = Q(0) + \bar{r}\int_0^x w(x')dx' = \bar{r}U + \bar{r}\int_0^x w(x')dx' \tag{10.35}$$

where $\bar{r}$ is the rainfall intensity and U is the upslope contributing area of the slope unit. U for each slope unit in the slope system can be easily calculated by summing up areas of the slope units located on the upstream region of the slope unit.

Because a slope unit is rectangular, the width of the slope unit is constant within the unit. Then Eq. 10.34 and Eq. 10.35 can be rewritten as Eq. 10.36 and Eq. 10.37 respectively by replacing $w(x)$ with $\bar{w}$ (constant):

$$s = \bar{w} \int_0^L h(x)dx \tag{10.36}$$

$$Q(x) = \bar{r}U + \bar{r}\bar{w} \int_0^x dx' = \bar{r}U + \bar{r}\bar{w}x \tag{10.37}$$

$$q(x) = Q(x)/\bar{w} = \bar{r}U/\bar{w} + \bar{r}x \tag{10.38}$$

To calculate storage volume of a slope unit, integration of Eq. 10.36 is needed. However, f is not always given explicitly. Then we transform Eq. 10.36 to Eq. 10.39 by changing a variable of integration from x to q using the relationship given by Eq. 10.38:

$$s = \bar{w}/\bar{r} \int_{q(0)}^{q(L)} f(q)dq = \bar{w}/\bar{r}\ [F(q(L)) - F(q(0))] \tag{10.39}$$

where $dF/dq = f$.

Figure 10.8 schematically shows a relationship between f, g and F. If f is explicitly given as a function of q and can be analytically integrated with q, F can be easily obtained. However f is not always given as an explicit function of q since q is generally a function of h. Then F can not be analytically obtained. However it is assumed that g is a function of h and can be analytically integrated with h. From this assumption, if a value of $h(x)$ can be obtained from g, $F(q(x))$ can be calculated as:

$$F(q(x)) = q(x)h(x) - \int_0^{h(x)} g(h)dh \tag{10.40}$$

Based on the above discussion, we determine a series of procedures to get a relationship between storage volume and discharge of a slope system as follows:

step 1 Assign a value to $\bar{r}$.

step 2 Calculate discharge per unit width at the upstream and downstream ends of a slope unit, $q(0)$ and $q(L)$, using Eq. 10.38 with $\bar{r}$ given in step 1.

step 3 Calculate $h(0)$ and $h(L)$ numerically using $q = g(h)$ with $q(0)$ and $q(L)$ obtained in step 2.

step 4 Calculate $F(q(0))$ and $F(q(L))$ using Eq. 10.40 and calculate s using Eq. 10.39 with $F(q(0))$ and $F(q(L))$.

step 5 Repeat the procedures from step 2 to step 4 for all the slope units contained in the slope system.

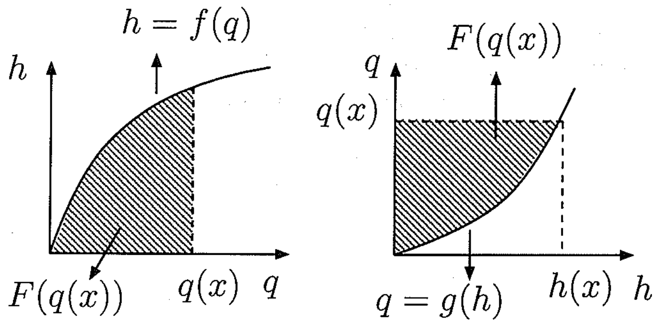

Figure 10.8: Relationship between f, g and F

step 6 Sum up storage volumes of all the slope units.

step 7 Calculate discharge from the slope system by multiplying $\bar{r}$ by total area of the slope system.

step 8 Repeat the procedures from step 1 to step 7 with new value of $\bar{r}$.

Runoff calculation is conducted by using a discrete relationship between storage volume and discharge of the slope system obtained from the above procedures and equation of continuity.

The crucial part of this method is Eq. 10.40. If we know the form of $F(q(x))$ for a kinematic wave model, we can derive the relationship between storage volume and discharge by using $F(q(x))$. The momentum equation of the kinematic wave model for surface-subsurface flow is:

$$q = g(h) = \begin{cases} ah & (0 < h < d) \\ \alpha(h-d)^m + ah & (h \geq d) \end{cases} \tag{10.41}$$

For simplicity, the notation of $q' \equiv q(x)$ and $h' \equiv h(x)$ will be used in the following. In the case of $h(x) < d$ (Figure 10.9), $h' = q'/a$. Then $F(q')$ can be easily obtained as follows:

$$F(q') = \frac{1}{2} \cdot q' \cdot \frac{q'}{a} = \frac{q'^2}{2a} \tag{10.42}$$

In case of $h' \geq d$ (Figure 10.10), $F(q')$ can be rewritten as:

$$F(q') = q'h' - G1 - G2 \tag{10.43}$$

$$G1 = ad^2/2 \tag{10.44}$$

$$\begin{aligned} G_2 &= \int_d^{h'} \{\alpha(h-d)^m + ah\} dh \\ &= \frac{\alpha}{m+1}(h'-d)^{m+1} + \frac{a}{2}(h'^2 - d^2) \end{aligned} \tag{10.45}$$

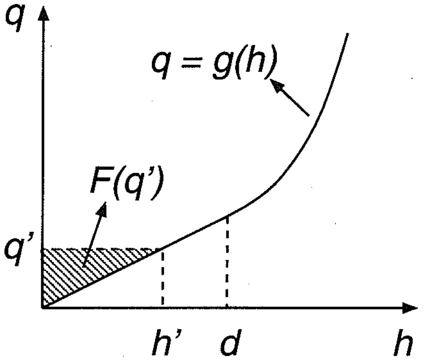

Figure 10.9: $F(q(x))$ for the case of $h(x) < d$

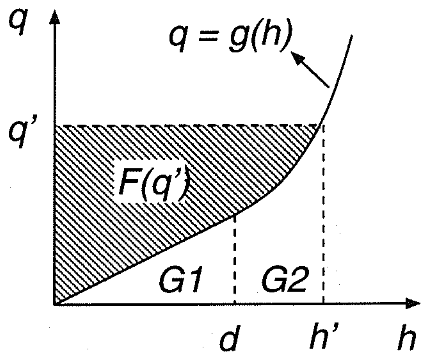

Figure10.10: $F(q(x))$ for the case of $h(x) \geq d$

Rearranging the above equations, we finally get:

$$F(q') = q'h' - \frac{\alpha}{m+1}(h' - d)^{m+1} - \frac{ah'^2}{2} \tag{10.46}$$

We thus know the form of $F(q(x))$ for the kinematic wave model for surface-subsurface flow. Then we can derive the relationship between storage volume and discharge by using the procedure which was shown above.

Figure10.11 gives the results computed by the lumped kinematic wave model for surface-subsurface flow. The observed discharges and the results by the (distributed) kinematic wave model for surface-subsurface flow are also shown in the figure. The study area and application period are the same as those for the applications of the (original) lumped kinematic wave model. By comparing this figure with Figure10.7, we can see that the lumped kinematic model for surface-subsurface flow gives better agreements than the (original) lumped kinematic wave model.

10.6.3 Lumping of the kinematic wave model considering field capacity[19]

The kinematic wave equation considering field capacity, which is given again as Eq. 10.47 and 10.48 contains the variable describing free water content h_f in addition to the variables of discharge per unit width q and total water content h. Thus the lumping method for the kinematic wave model for surface-subsurface flow can not be applied to this equation as it is.

$$q = g(h_f) = \begin{cases} ah_f & (0 \leq h_f < d) \\ \alpha(h_f - d)^m + ah_f & (h_f \geq d) \end{cases} \tag{10.47}$$

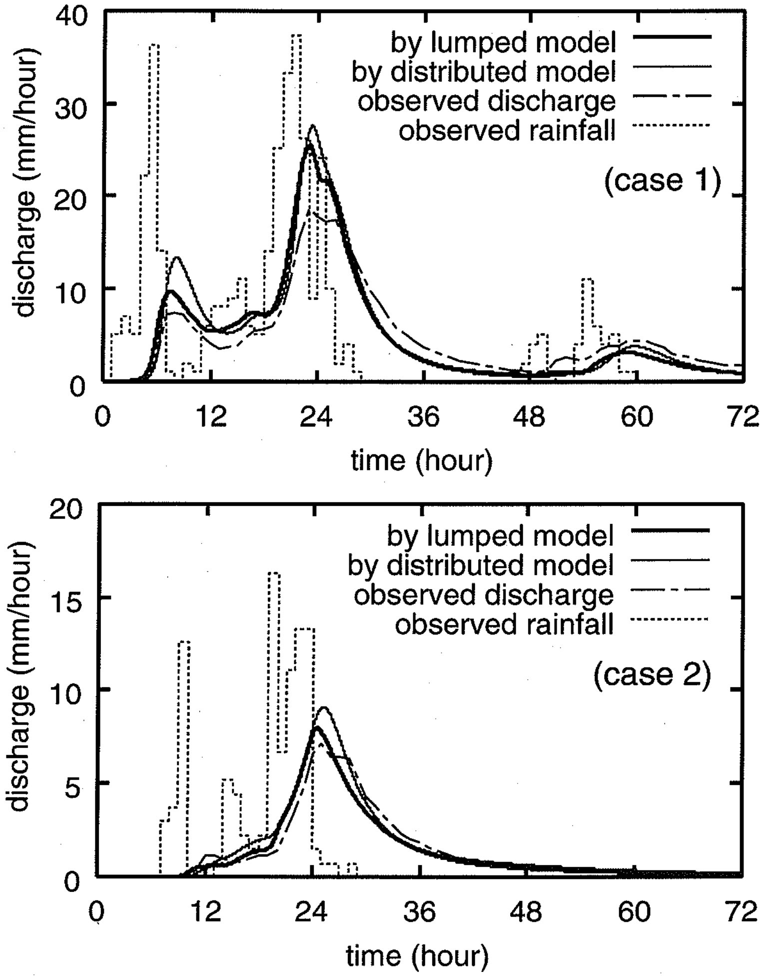

Figure 10.11: Simulation using the lumped kinematic model for surface-subsurface flow: top: Aug. 1982, bottom: Sept. 1990

$$h = u(h_f) = \begin{cases} h_f + h_c \left(1 - \left(\dfrac{d - h_f}{d}\right)^N\right)^{1/N} & (0 \leq h_f < d) \\ h_f + h_c \quad (h_f \geq d) \end{cases} \tag{10.48}$$

Eq. 10.40 can be rewritten as Eq. 10.49 by changing the variable of integration from h to h_f:

$$\begin{aligned} F(q(x)) &= q(x)h(x) - \int_0^{h_f(x)} g(h_f) \frac{dh}{dh_f} \, dh_f \\ &= q(x)h(x) - \int_0^{h_f(x)} g(h_f)u'(h_f)dh_f \end{aligned} \tag{10.49}$$

where $h_f(x)$ is free water content corresponding to $h(x)$, $g(h_f)$ and $u(h_f)$ are given by Eq. 10.20 and Eq. 10.21 respectively, and $'$ (dash) refers to differentiation with respect to h_f.

In the case that a surface soil layer is unsaturated, Eq. 10.49 can be further transformed as:

$$\begin{aligned} F(q(x)) &= q(x)h(x) - \int_0^{h_f(x)} g(h_f)u'(h_f)dh_f \\ &= q(x)h(x) - [g(h_f)u(h_f)]_0^{h_f(x)} + \int_0^{h_f(x)} g'(h_f)u(h_f)dh_f \\ &= \int_0^{h_f(x)} g'(h_f)u(h_f)dh_f \end{aligned} \tag{10.50}$$

Because $g'(h_f)$ is a in this case, we can obtain the following equation by substituting $g'(h_f)$ ($= a$) and $u(h_f(x))$ Eq. 10.21 into Eq. 10.50:

$$F(q(x)) = \frac{1}{2} a h_f(x)^2 + a h_c \frac{d}{N} \cdot B_{1-c^N}\left(\frac{1}{N} + 1, \frac{1}{N}\right) \tag{10.51}$$

where $B_{1-c^N}\left(\frac{1}{N} + 1, \frac{1}{N}\right)$ is the product of the beta function $B\left(\frac{1}{N} + 1, \frac{1}{N}\right)$ and the incomplete beta function $I_{1-c^N}\left(\frac{1}{N} + 1, \frac{1}{N}\right)$.

In the case that a surface soil layer is completely saturated, we can get the following expression of $F(q(x))$ by dividing the interval of integration of the second term in Eq. 10.49 into $[0 \sim d]$ and $[d \sim h_f(x)]$ and by substituting $u'(h_f)$ into Eq. 10.49:

$$\begin{aligned} F(q(x)) &= q(x)\,h(x) - adh_c + ah_c \frac{d}{N} \cdot B\left(\frac{1}{N} + 1, \frac{1}{N}\right) \\ &\quad - \frac{\alpha}{m+1}(h_f(x) - d)^{m+1} - \frac{1}{2} a h_f(x)^2 \end{aligned} \tag{10.52}$$

Figure10.12 gives the results computed by the lumped kinematic wave model considering field capacity. The observed discharges and the results using the (distributed) kinematic wave model considering field capacity are also shown in the figure. The study area and application period are the same as those for the applications of the (original) lumped kinematic wave model and the lumped model for surface-subsurface flow. This figure shows that the lumped model considering field capacity gives reasonable simulation results compared with the observed discharge and the results simulated by the distributed kinematic wave model considering field capacity.

10.7 Hydrological modeling system

Hydrological systems are generally considered as a set of hydrological elements. Precipitation, evapotranspiration, water flow on the slope systems, river network flow, water storage in the dam reservoirs, and many element models have been developed. It is therefore quite natural that there has been a demand for a hydrological modeling system which builds a catchment model by combining the element models. Such systems have been developed and used as powerful tools to build hydrological models. However, the existing hydrological modeling systems have a problem that a user-defined element model can not be easily used with the modeling systems. In order to solve this problem, a new hydrological modeling system was developed, which is called the Object-oriented Hydrological Modeling System (OHyMoS)[20, 21]. OHyMoS is designed on the basis of object-oriented programming concepts and it allows the users to easily develop their own element models and easily build a catchment model by combining element models.

10.7.1 Existing modeling systems

HEC–HMS, developed by the US Army Corps of Engineers Hydrologic Engineering Center[22], is one of the most famous hydrological modeling systems. The current version is 2.2 as of February, 2003. It provides seven types of hydrological element models: subbasin, routing reach, junction, reservoir, source, sink and diversion. The users are allowed to construct basin hydrological models by selecting and connecting these elements. Also each element has several options for hydrological computation, and the users can choose an appropriate option for each element. This type of modeling system has the advantage that the users are free from the laborious work of writing the codes of the element models if they use the element models provided in the modeling system. This type of modeling system, however, has a defect that it is practically difficult for the users to develop their own element models because they have to know the details of the modeling system, which is usually a huge and complex software.

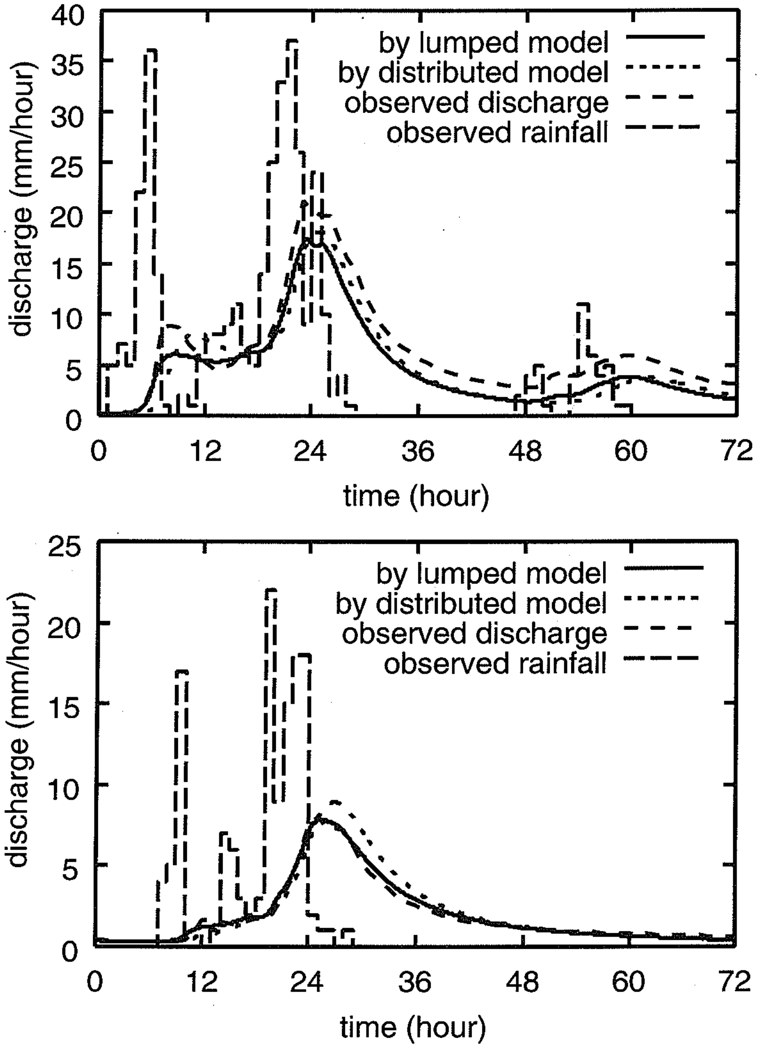

Figure 10.12: Simulation by the lumped kinematic model considering field capacity: top: Aug. 1982, bottom: Sept. 1990

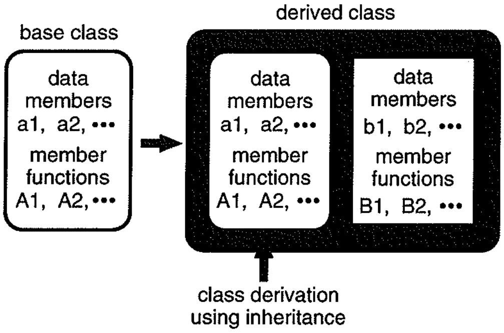

Figure 10.13: Creating a new class using inheritance

10.7.2 Design concept of OHyMoS

In order to solve the defect of the existing modeling systems, we use the object-oriented programming concept to develop a new hydrological modeling system, namely, OHyMoS. The object-oriented programming concept is the technical term used in contrast with the procedure-oriented programming concept.

In OHyMoS, a hydrological element is regarded as *a class*, which is a main feature of the object-oriented programming. A class is a template that describes both the data variables and the valid functions for the data variables. The data variables are called *data members* and the functions are called *member functions.* Because a hydrological element model executes computations by operating state variables and parameters in the hydrological equations, it can be expressed as a class by regarding the state variables and the parameters as the data members and the equations as the member functions.

The object-oriented programming also has a mechanism that new classes can be built from old ones through *inheritance* (Figure 10.13). A new class, referred to as a derived class, can inherit the data members and the member functions of the original or *base class.* The new class can add data members and member functions to those it inherits from its base class. A base class is often used to describe a common and abstract structure of some objects and a derived class is used to describe the specific structure of individual object. In OHyMoS, we provide the base element model as a base class which has common and indispensable member functions such as the functions to initialize state variables and drive the computations. An user of OHyMoS is allowed to derive a new element model from the base element model by using inheritance. The new element model inherits the common and indispensable functions provided in the base element model, and the user can readily use the functions and also can add new data members and member functions if necessary. The inheritance brings us another important benefit. All the element models will have a common

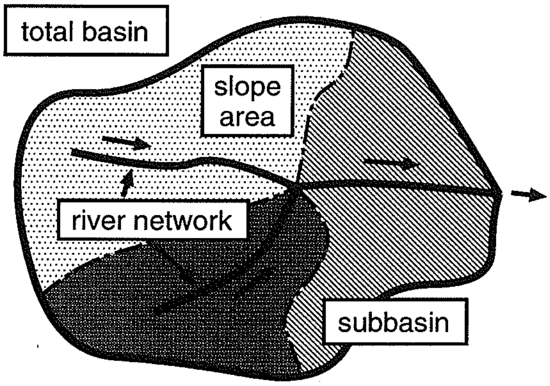

Figure 10.14: Basin structure

structure because they are all derived from the base element model. This fact implies that all the element models can be operated using the same function calls.

The inheritance is used when a new class will have the same member functions as the base class. However the new class may have the same member functions with the different implementations, i.e. the member functions whose purposes are same but whose methods are different. Object-oriented programming provides for this by using *polymorphism.* Polymorphism enables us to implement the inherited member functions differently from those of the base class. For example, all the hydrological element models must have the member function to simulate hydrological phenomena. It is therefore quite natural that this member function should be defined in the base element model and all the element model should have this function by using inheritance from the base element model. However each element model needs to implement this function uniquely according to each feature. To solve this dilemma, we use polymorphism. Polymorphism allows an inherited function within a derived model to have a different form from that of the original function defined in the base element model.

10.7.3 Element model, subsystem model, and total system model

OHyMoS provides a structure of *a subsystem model* and *a total system model* in addition to an element model. A subsystem model is a set of element models and a total system model is a set of subsystem models and element models. For example, suppose that a basin consists of three subbasins and each subbasin consists of a slope area and a river network as shown in Figure 10.14. OHyMoS

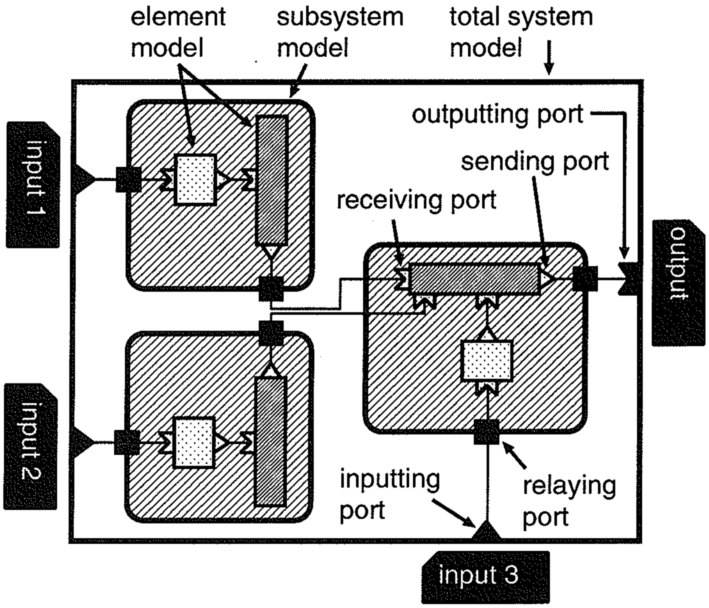

Figure 10.15: Model structure using OHyMoS

allows the slope area and the river network to be modeled as the element models. These element models are derived from the base element model. Also, OHyMoS allows the subbasins to be modeled as subsystem models by connecting the element models for a slope area and a river network, and allows the basin to be modeled as the total system model by connecting the three subsystem models (Figure 10.15).

An element model conducts actual hydrological computations according to the hydrological characteristics, and a subsystem model and a total system model work as managers of the element models and/or the subsystem models; they issue several commands to operate the subordinate models. Also, a total system model is used for communicating with a user interactively through command line inputs and dealing with data files.

10.7.4 Data transfer

OHyMoS also provides the model for communicating (sending and receiving data) between element models. This model allows an user to send or receive data from an element model to other element models according to the relations among element models defined by the user without writing program codes to transfer data. The model for sending data from an element model is called *a data sending port* and the model for receiving data from another element model is called *a data receiving port.* A subsystem model has *a data relaying port* for transferring data from/to the outside of the model. A total system model has *a data inputting port* to read a data file (rainfall, temperature, etc) and *a data outputting port* to write calculation results (discharge, water depth, etc) to a file. The data transferred through the ports is modeled as *a data pack* which contains time and some numerical value(s). The port models and the data pack model also have the object-oriented hierarchies whose roots are *the base port model* and *the base data pack model*, respectively.

10.7.5 Application

OHyMoS was applied to the Huaihe River basin in China (145,000 km^2) in order to simulate rainfall-runoff processes. Figure 10.16 shows Huaihe River basin. The basin was divided into 1478 subbasins using 10' × 10' grid boxes. Each subbasin was modeled as a subsystem model which consisted of the Xinanjiang model[23] representing runoff processes from the slope area and the lumped kinematic stream network model[24] representing the flood wave in the river network (Figure 10.17). The whole basin was modeled by connecting the subsystem models (Figure10.18). For details of these models, refer to Tachikawa *et al.*[25]. Figure 10.19 shows the simulation result.

References

[1] Beven, K., 1979: On the Generalized Kinematic Routing Method, Water Resources Research, Vol. 15, No. 5, 1238–1242.

[2] Takasao, T., M. Shiiba and H. Kitamura, 1976: A distributed runoff model and lumping scale of a river basin, Proc. 31st Annu. Conf. JSCE, 2-86, 163 (in Japanese).

[3] Takasao, T. and M. Shiiba, 1988: Incorporation of the effect of concentration of flow into the kinematic wave equations and its applications to runoff system lumping, *J. Hydrol.*, 102, 301–322.

[4] Shiiba, M., Y. Tachikawa, Y. Ichikawa, T. Hori and K. Tanaka, 1998: Development of slope runoff models which consider field capacity and pipe flows (in Japanese), Annuals of Disas. Prev. Res. Inst., Kyoto Univ., 41, B–2, 229–235.

[5] Beven, K. J., 2000: Rainfall-runoff modeling, John Wiley & Sons, LTD, 360p.

[6] O'Loughlin, E., 1986: Prediction of surface saturation zones in natural catchments by topographic analysis, Water Resources Research, 22, 794–804.

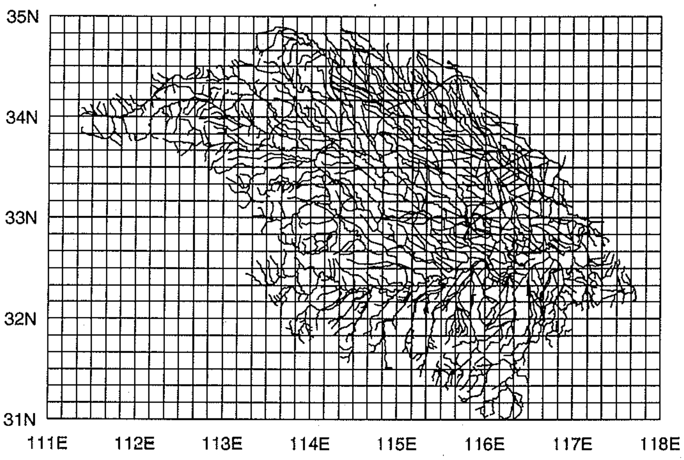

Figure 10.16: Huaihe River basin

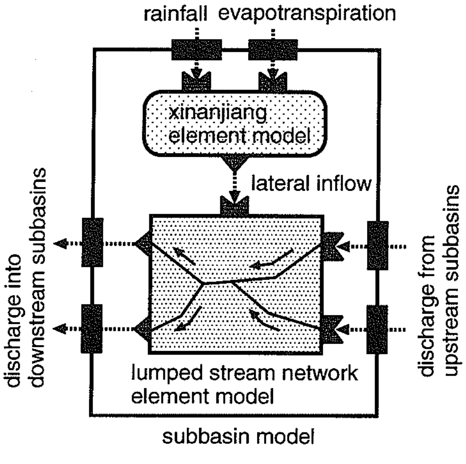

Figure 10.17: Element models and subsystem model

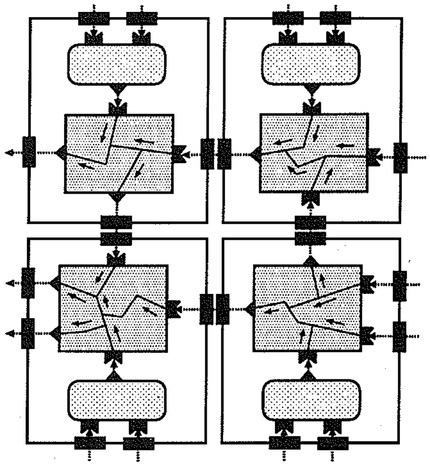

Figure 10.18: Total system model

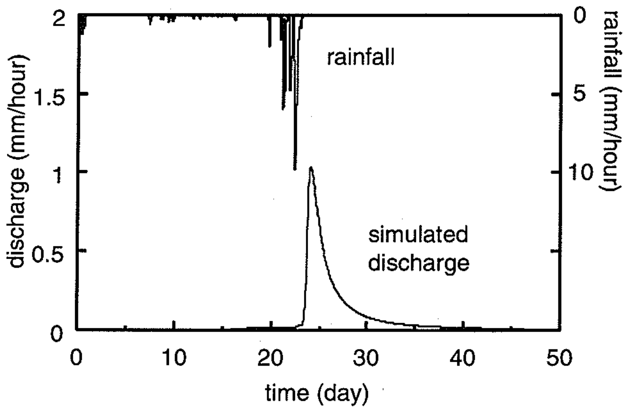

Figure 10.19: Simulation result

[7] Grayson, R. B., Bloschl, G. and Moore, I. D., 1995: Distributed parameter hydrologic modelling using vector elevation data: THALES and TAPES-c, In Singh V. P. (ed) Computer Models of Watershed Hydrology, Water Resource Publications Highlands Ranch, CO, 669–696.

[8] Tachikawa, Y., M. Shiiba, and T. Takasao, 1994: Development of a basin geomorphic information system using a TIN-DEM data structure, Wat. Resour. Bull., 30, 1, 9–17.

[9] Palacios-Velez, O. L., Gandoy-Bernasconi, W. and Cuevas-Renaud B., 1998: Geometric analysis of surface runoff and the computation order of unit elements in distributed hydrological models, Journal of Hydrology, 211, 266–274.

[10] Vieux, B. E., 1991: Geographic information systems and non-point source water quality and quantity modeling, Hydrological Processes, 5, 1, 101–113.

[11] Goodrich, D. C., D. A. Woolhiser and T. O. Keefer, 1991: Kinematic routing using finite elements on a triangular irregular network, Water Resources Research, 27, 6, 995–1003.

[12] Beven, K. J. and M. J. Kirkby, 1979: A physically based, variable contributing area model of basin hydrology, Hydrological Sciences Bulletin, 24, 1, 43–69.

[13] Quinn, P. F., K. J. Beven and R. Lamb, 1995: The $\ln(a/\tan\beta)$ index: how to calculate it and how to use it in the TOPMODEL framework, Hydrological Processes, 9, 161–182.

[14] Abbott, M. B., J. C. Bathurst, J. A. Cunge, P. E. O'Connell and J. Rasmussen, 1986: An introduction to the European Hydrological System – Systeme Hydrologique Europeen, SHE. 1. History and philosophy of a physically-based, distributed modelling system, Journal of Hydrology, 87, 45–59.

[15] Abbott, M. B., J. C. Bathurst, J. A. Cunge, P. E. O'Connell and J. Rasmussen, 1986: An introduction to the European Hydrological System – Systeme Hydrologique Europeen, SHE. 2. Structure of a physically-based, distributed modelling system, Journal of Hydrology, 87, 61–77.

[16] Ichikawa, Y., M. Murakami, Y. Tachikawa and M. Shiiba, 2001: Development of a basin runoff simulation system based on a new digital topographic model, Journal of Hydraulic, coastal and environmental engineering, 691/II-57, 43–52 (in Japanese).

[17] Shiiba, M., Y. Ichikawa, T. Sakakibara and Y. Tachikawa, 1999: A new numerical representation form of basin topography, Journal of Hydraulic, coastal and environmental engineering, 621/II-47, 1–9 (in Japanese).

[18] Ichikawa, Y., T. Ogura, Y. Tachikawa, M. Shiiba and K. Takara, 2000: Lumping general kinematic wave equation of slope runoff system, Annual Journal of Hydraulic Engineering, JSCE, 44, 145–150 (in Japanese).

[19] Ichikawa, Y. and M. Shiiba, 2002: Lumping of kinematic wave equation considering field capacity, Proc. 3rd International Conference on Water Resources and Environment Research, Dresden, Germany, Vol. 1, 56–60.

[20] Ichikawa, Y., Y. Ichikawa, K. Takara and M. Shiiba, 2000: Object-oriented hydrological modeling system, Proc. of Hydroinformatics 2000 (CD-ROM).

[21] http://hywr.kuciv.kyoto-u.ac.jp/ohymos.html :
Web site of Object-oriented Hydrological Modeling System.

[22] http://www.hec.usace.army.mil/default.html : Web site of US Army Corps of Engineers Hydrologic Engineering Center.

[23] Zhao, R. J., Y. L. Zhang, L. R. Fang, X. R. Liu and Q. S. Zhang, 1980: The Xinanjiang model, Proc. of the Oxford Symposium on Hydrological Forecasting, IAHS Publ., 129, 351–356.

[24] Shiiba, M., Y. Ichikawa, S. Ikebuchi, Y. Tachikawa, and T. Takasao, 1996: Scale-up of a runoff model using GIS and object-oriented hydrological modeling system, Application of Geographic Information Systems in Hydrology and Water Resources Management, IAHS Publ., 235, 63–70.

[25] Tachikawa, Y., Y. Ichikawa, K. Takara and M. Shiiba, 2000: Development of a macro scale distributed hydrological model using an object-oriented hydrological modeling system, Proc. of Hydroinformatics 2000 (CD-ROM).

Practice 1

Execution of a Cloud Resolving Model

Taro Shinoda
Hydroshperic Atmospheric Research Center, Nagoya University
Furo-cho, Chikusa-Ku, Nagoya, 464-8601, Japan
Phone: +81-52-789-3494, fax: +81-52-789-3436
E-mail: shinoda@ihas.nagoya-u.ac.jp

1.1 Purpose

The purpose of this practice is to try the execution of a meteorological numerical simulation and watch some figures drawn by yourself from the results of this simulation. We will execute the ***CReSS*** (Cloud Resolving Storm Simulator) developed by Prof. Tsuboki and Mr. Sakakibara (Tsuboki and Sakakibara 2001).

1.2 Initial setup

First, you check your computer name (from "G1" to "G7"). After you login your computer, move the directory into your computer name (e.g., "g1"). You can see "cress1.4m.ihp.tar" in your directory. This file is an archived and compressed file of ***CReSS***. You expand this archive file by "tar" command.

Third, compile the solver as follows. The dimension of the calculation is defined in the user configuration file “user.conf.***” and include files are produced automatically. It is, therefore, not necessary to change the source code of the solver.

```
[ihp@master]        ./compile.csh solver user.conf.***
```

When the compilation is completed, the executable file **solver.exe** is generated. We confirm the existence of **solver.exe** and its date of generation and its file size in order to check whether the compilation is successfully or not. The “***” means the name of the experiment and we specify this name by the parameter “exprim” in the “user.conf.***.”

Forth, we can execute the solver while reading the use configuration file **user.conf.***** from the standard input and outputting *****.out** to the standard output.

```
[ihp@master] mpirun1 ./solver.exe < user.conf.*** > ***.out
```

If the calculation is terminated normally, ***CReSS*** leaves the message **“This program stopped normally.”** at the end of the standard output “*****.out**” and the history dump files (the names include **dmp**), the geographic information file (the names include **geography**) and restart files (the names include **res**) are produced. The standard output includes the history of the calculation and the maximum and minimum of the prognostic variables. These files will be used when we analyze the results of the simulation. We can view the results of the simulation by drawing horizontal/vertical cross-sections and time series easily using graphical software “***grads.***”

1.4 Results of some sample experiments

1.4.1 Results of the Kelvin-Helmholtz billows experiment

Summaries of the model setting are as follows.

Name of numerical experiment	“catseye”
Numbers of grid points	99×4×139
Grid intervals	10×10×5 [m]
Time intervals of the large time step	0.4 [s]
Time intervals of the small time step	0.02 [s]
Time of the termination of calculation	480.0[s]
Initial wind and potential temperature	Vertical shear is the hyperbolic tangent type.
Initial perturbation of potential temperature	0.4 [K] (maximum)

The results will show a clear cats eye structure of the Kelvin-Helmholtz billows in the stream lines of the *u* and *w* components and the overturning of potential temperature associated with the billows (Fig. 6 and 7 in Chapter 5). You can make the same figure using graphical software “***grads***” in this practice session.

1.4.2 Results of the mountain waves experiment

Summaries of the model setting are as follows.

Name of numerical experiment	"mountainwave"
Numbers of grid points	363×4×147
Grid intervals	400×400×125 [m]
Time intervals of the large time step	10.0 [s]
Time intervals of the small time step	1.0 [s]
Time of the termination of calculation	9000.0 [s]
Shape of mountain	bell-shaped mountain
Height of mountain	500 [m]
Half width of mountain	2000 [m]
Initial horizontal wind	10 [m/s] (whole of the model domain)
Initial stratification	N = 0.01 [/s] (N: Brunt-Vaisala angular frequency) Vertical shear is the hyperbolic tangent type.

The results will show upward and downward propagating mountain waves developing with time (Fig. 8 in Chapter 5). You can make the same figure using graphical software "***grads***" in this practice session.

1.4.3 Results of squall line experiment

Summaries of the model setting are as follows.

In this case, the number of grid points and integration time are very large. The calculating time is too long to execute in this practice session. Therefore, we will watch the results of calculation, which had been run previously, instead of executing it now.

The results will show that the squall line extends from northwest to southeast and moves northeastward (Fig. 15 in Chapter 5). You can make the same figure using graphical software "***grads***" in this practice session.

Name of numerical experiment	“test”
Numbers of grid points	583×411×53
Grid intervals	300×300×300 [m]
Time intervals of the large time step	3.0 [s]
Time intervals of the small time step	0.2 [s]
Time of the termination of calculation	7200.0 [s]
Initial condition	Doppler radar data Sounding data

Part II

Outline of the Training Course in 2002

Outline

As a part of the Japanese contribution to the International Hydrological Programme (IHP), a short course for participants from the Asia-Pacific region is going to be conducted on precipitation and water resources, from 23 February to 8 March, 2003, at Hydrospheric Atmospheric Research Center, Nagoya University, Nagoya, and Graduate School of Engineering (Department of Global Environment Engineering and Department of Civil Engineering Systems) and Disaster Prevention Research Institute, Kyoto University, Kyoto, Japan. The course includes a series of lectures in English, practice sessions and technical tours to in-situ observation site, national offices and facilities concerned with precipitation and water resources.

Objectives

The general aim of the IHP short course is to help participants to develop their basic knowledge of hydrological systems and their sensitivity to climate changes and to contribute to solve current global environmental problems. Water resource is one of the biggest problems for not only developing countries but also developed countries. In 2003, after this IHP short course, the Third Water Forum will be held in Kyoto, Japan. In the Forum, the problem of heavy rainfall and flood will be also focused on as one of vital problems in the field of water resources. Under this circumstance, this IHP short course will focus on understanding mechanism and prediction of heavy rainfall and flood runoff including river basin management. The topic on draught in senses of phenomena and management will be included as a typical topic of water resources.

The problems of water resources and ways of solving them depend much on features of nature and human activity in the field people are living. In this sense, participants can get essential and comprehensive idea of ways of planning, managing and monitoring problems on water resources of their own countries including precipitation.

Course Contents (convenors: E. Nakakita and H. Uyeda)

Lecturers

T. Hori (Department of Civil Engineering Systems, Kyoto University)
Y. Ichikawa (Department of Civil Engineering Systems, Kyoto University)
E. Nakakita (Department of Global Environment Engineering, Kyoto University)
K. Nakamura (Hydrospheric Atmospheric Research Center, Nagoya University)
T. Shinoda (Hydrospheric Atmospheric Research Center, Nagoya University)
Y. Tachikawa (Disaster Prevention Research Institute, Kyoto University)
I. Tamagawa (River Basin Research Center, Gifu University)
K. Tanaka (Disaster Prevention Research Institute, Kyoto University)
K. Tsuboki (Hydrospheric Atmospheric Research Center, Nagoya University)
H. Uyeda (Hydrospheric Atmospheric Research Center, Nagoya University)

OUTLINE OF THE TRAINING COURSE 2002

Lectures

L1 Basics of Meteorology on Precipitation..........................H. Uyeda

Basic equations on meteorology and treatment of precipitation phenomena Some of basis on cloud physics for the preparation of studies on radar meteorology

L2 Basics on Mesoscale Meteorology and Radar Meteorology .... H. Uyeda

Basics of mesoscale meteorology
Weather radar application for revealing mesoscale phenomena

L3 Boundary Layer ....I. Tamagawa

Introduction of boundary layer
Structure of boundary layer
Turbulent transport
Parameterization of turbulence

L4 Rain Observation from Satellites .... K. Nakamura

Principles of satellite remote sensing
Microwave and visible/infrared radiometer observation
Active microwave rain observation techniques
Results of spaceborne rain radar observation of rain

L5 Basics on Numerical Simulation ....K. Tsuboki

Fundamental aspects on numerical simulation
Basics of cloud resolving numerical model in comparison with numerical weather forecastings

L6 Land Surface Processes ....K. Tanaka

Land surface processes
Land surface model
Observation of land surface processes

L7 Radar Hydrology ....E. Nakakita

Radar-rainfall estimation
Potential of utilizing radar into planning and real time managing of water resources
Short-time rainfall prediction using radar and its accuracy

L8 Water Resources Planning and Management ....T. Hori

Distribution of water resources and water balance
Water resources development and planning, from the viewpoint of optimization
Management and operation in water resources systems, focusing on reservoir operation
Draught and safety measures of water resources systems

L9 Catchment Hydrology .... Y. Tachikawa

Instruction of conceptual runoff simulation models such as Tank model, storage function method, and Xinanjiang Model
Instruction of lumped river flow routing
A real time flood prediction method with Kalman filter theory

L10 Distributed Runoff Modeling ....Y. Ichikawa

Basic concept of distributed runoff modeling
Instruction of kinematic wave theory
Lumping of distributed runoff models
Hydrological modeling system

Practices

P1 Cloud Resolving Model ....T. Shinoda

Explanation of results of numerical simulation with a cloud resolving model
Practice to run a cloud resolving model on a rain case

P2 Short-term Rainfall Prediction Using Radar ....E. Nakakita

Explanation of algorithm of a short-term rainfall prediction method
Practice to run the prediction method

P3 Flood Runoff Prediction ....Y. Tachikawa

Processing DEMs for distributed runoff modeling
Construction of distributed rainfall-runoff model based on kinematic wave theory
Runoff simulation

Technical Tours

T1 Meteorological Office & Observatory............................H. Uyeda

Visit to a meteorological office and observatory in Nagoya

T2 In-situ Observation sites for Land Surface Processes ....K. Tanaka and I. Tamagawa

Visit to permanent in-situ observation sites in the Lake Biwa basin

T3 Offices and Facilities for River Basin Management ....E. Nakakita

Visit to dam control offices and some historical facilities for river basin management in the Yodo River basin.

Schedule (23 February -8 March, 2003)

23 (Sunday) Feb., 2003	Arrival at Nagoya	Stay in Nagoya
24 (Monday)	Guidance, Lectures 1 & 2, Reception at Nagoya University	Stay in Nagoya
25 (Tuesday)	Lectures 3 & 4,	Stay in Nagoya
26 (Wednesday)	Lecture 5 and Practice 1	Stay in Nagoya
27 (Thursday)	Practice 1 (cont'd) and Technical Tour 1	Stay in Nagoya
28 (Friday)	Writing report and Lecture 6	Stay in Nagoya
1 (Saturday) March	Technical Tour 2 on the way to Kyoto	Stay in Kyoto
2 (Sunday)	Japanese culture introduction and Free time	Stay in Kyoto
3 (Monday)	Lectures 7 & 8	Stay in Kyoto
4 (Tuesday)	Practice 2	Stay in Kyoto
5 (Wednesday)	Lectures 9 & 10	Stay in Kyoto
6 (Thursday)	Practice 3	Stay in Kyoto
7 (Friday)	Technical Tour 3 and Closing ceremony	Stay in Kyoto
8 (Saturday)	Departure from Kansai (Osaka) Air Port	

Part III

Past Activities of the IHP Training Course

Past activities of the IHP Training Course (1991- 2001)

The IHP Training Course in Asia and the Pacific Region has been executed since 1991by the Working Group for IHP Training Course, under the direction of the Sub-Committee for IHP, Japanese National Commission for UNESCO. The Training Course was aimed at giving participants an opportunity to learn observation technology of hydrology and to have practical experience in hydrological observation in the field.

In the First to Sixth-sessions of the Training Course, the training began with two or three preliminary lectures to introduce the subjects to be studied throughout the remainder of the course schedule. After this introduction, students have been taken around to several specialized institutes in the days following, to hear about what was actually done there, and to see modern instrumentation in general hydrology. It has been found, however, that this training approach possibly encourages passiveness on a part of the students because they spend an inordinate amount of time traveling daily to the host institutions where they can only listen and observe rather than participate actively.

Some innovations, therefore, were made at the Seventh-session, both in the educational content and in the schedule. Firstly, we decided to focus the training course on more clearly denned targets, and the first Year's programme concentrated on Snow Hydrology. Secondly, we decided to include practice sessions such as a field programme to allow the students, themselves, the opportunity to carry out experiments and make relevant observations/analyses. Finally, we decided to prepare a newly edited textbook for the participants in the training course.

Some innovations, therefore, were made at the Seventh-session, both in the educational content and in the schedule. Firstly, we decided to focus the training course on more clearly denned targets, and the first Year's programme concentrated on Snow Hydrology. Secondly, we decided to include practice sessions such as a field programme to allow the students, themselves, the opportunity to carry out experiments and make relevant observations/analyses. Finally, we decided to prepare a newly edited textbook for the participants in the training course.

1. The First IHP Training Course, 1991

1.1 Participants

Ms. Zhao Ling (China), Student of the Special Program of Sciences of Atmosphere and Hydrosphere, Graduate School of Science, Nagoya Univ., Japan
Mr. Zhao Jing (China), ibid.
Ms. Hidbjat Bernadia Irawati Tjandradewi (Indonesia), ibid.
Mr. Geng Biao (China), Student of Sciences of Atmosphere and Hydrosphere, Graduate School of Science, Nagoya Univ., Japan
Ms. Sri Mulat Yuningsih (Indonesia), Res. Inst. for Water
Mr. Roslan BinSahat (Malaysia), Resources Development, Dept. of Public Works Hydrology Branch, Dept. of Drainage and Irrigation

1.2 Schedule and Lectures

Mar. 2-3	Water Res. Inst., Nagoya Univ. (Nagoya) • Lecture on runoff processes in river watersheds(Prof. F. Takagi,Water Res. Inst., Nagoya Univ.) • Lecture and practice session on precipitation and water resources in Asia(Assoc. Prof. Y. Fujiyoshi, Asst.. Prof. K. Kato, Assoc. Prof. Y. Ishizaka, Water Res. Inst. Nagoya Univ.) • Lecture and practice session on the matter cycle and water quality in the hydrosphere(Prof. M. Sakamoto, Prof: N. Handa, Assoc. Prof. K. Ohta, Water Res. Inst. , Nagoya Univ.)
Mar. 4-6	Chubu Regional Construction Bureau, Min. of Construction (Chubu Region) • Technical tour of hydrological facilities for river control
Mar. 7-8	(Sat - Sun): holidays
Mar. 9	Water Resources Res. Center, Disaster Prevention Res. Inst., Kyoto Univ. • Laboratory experiment on evaporation from bare soil
Mar. 10	Kiryu Experimental catchment, Faculty of Agriculture, Kyoto Univ. • Meteorological and hydrological observations at a small catchment in hilly terrain
Mar. 11	(Kyoto to Tsukuba)
Mar. 12	Forestry & Forest Products Res. Inst., Min. of Agriculture, Forestry & Fisheries(Hitachi-Ohta) • Training on evaporation and soil moisture measurements,and hydrological observation
Mar. 13	National Inst. for Environmental Studies, Environment Agency (Tsukuba)

- Technical tour of research facilities for water quality conservation

Mar. 14-15 (Sat-Sun) : holidays

Mar. 16-17 Public Works Res. Inst., Min. of Construction (Tsukuba)

- Lectures on hydrological observations and models of water discharge

Mar. 18 Forecast Dept. & Observation Dept., Japan Meteorological Agency (Tokyo)

- Lecture and technical tour concerning Short-range precipitation forecasting using radar and the AMeDAS (automated meteorological data acquisition system)

Mar. 19 Meteorological Satellite Cente, Japan Meteorological Agency (Kiyose)

- Technical tour of Meteorological Satellite Center

2. The Second IHP Training Course, 1992

2.1 Participants

Ms. Zhao Ling (China), Student of the Special Program of Sciences of Atmosphere and Hydrosphere, Graduate School of Science, Nagoya Univ., Japan

Ms. Thapa,Arati (Nepal), Student of Special Program of Sciences of Atmosphere and Hydrosphere, Graduate School of Science, Nagoya Univ., Japan

Mr. Kayastha, Rijan Bhakta (Nepal), ibid.

Mr. Sarwono, Pitoyo Sudibyo (Indonesia), ibid.

Mr. Le Cong Thanh (Vietnam), ibid.

Mr. Xu Guangxiang (China), ibid.

Mr. Adisak, Suriyavanagul (Thailand), Electricity Generating Authority

Mr. Pham Van Tan (Vietnam), Network Operation Dept., Hydrometeorological Service

Mr. Ekanayaka M. Wimalasena (Sri Lanka), Investigation Section, National Water Supply and Drainage Board

Mr. S. Mahmoud Borghei (Iran), Asst.. Prof., Dept. of Civil Engineering Sharif Univ. of Technology

2.2 Schedule and Lectures

Mar.1-2 Water Res. Inst., Nagoya Univ. (Nagoya)

- Lecture and practice session on precipitation and water resources in Asia (Asst. Prof. T. Ohta, Asst. Prof. K. Kato,Assoc. Prof. Y. Ishizaka, Water Res. Inst., Nagoya Univ.)
- Lecture and practice session on the material cycle and
- water quality in the hydrosphere (Assoc. Prof.H.Terai, Water Res.

Inst., Nagoya Univ.)
- Technical tour

Mar. 3-5 Kanto Regional Construction Bureau, Min. of Construction (Nagoya to Tokyo, Kanto Region)
- Technical tour of hydrological facilities for river control

Mar. 6-7 (Sat-Sun): holidays

Mar. 8-9 Environmental Res. Center, Univ. of Tsukuba (Tsukuba) Observation and data analysis of evapotranspiration

Mar. 10-11 National Res. Inst. for Earth Science&Disaster Prevention, Science&Technology Agency (Tsukuba-Ichihara, Chiba) Laboratory experiment of rainfall
- Technical tour of an experimental hydrological catchment

Mar. 12-14 (Fri-Sun): holidays

Mar. 15-16 National Res. Inst. of Agricultural Engineering, Min. of Agriculture, Forestry & Fisheries (Tsukuba) Analysis of irrigation and drainage Study of experimental ground water facilities

Mar. 17 Forecast Dept. & Observation Dept., Japan Meteorological Agency (Tokyo)
- Lecture and technical tour for short-range Precipitation for casting using radar and the AMeDAS

Mar. 18 Meteorological Satellite Center, Japan Meteorological Agency (Kiyose)
- Technical tour of Meteorological Satellite Center

3. The Third IHP Training Course, 1993

3.1 Participants

Mr. Kamal, Md. Syeeduzzaman (Bangladesh), Student of the Special Program of Sciences of Atmosphere and Hydrosphere, Graduate School of Science, Nagoya Univ., Japan

Ms. Sipayung, SintaBerliana (Indonesia), ibid.

Ms. HeKaiqing (China), ibid.

Mr. ZhuYan (China), Dept. of Hydrology, Hohai Univ.

Mr. Wu Yongxiang (China), Nanjing Inst. of Hydrology & Water Resources, Min. of Water Resources

Ms. Suva, Imelda Manalastas (Philippines), Bureau of Res. & Standards, Dept. of Public Works & Highways

Mr. Dwivedi, AshokKumar (India), Hydrological investigations Division, National Inst. of Hydrology, Roorkee

Mr. Ahmad, Bashir (Pakistan), Centre of Excellence in Water Resources Englneerlng, Univ. of Englneering & Technology, Lahore

3.2 Schedule and Lectures

Aug.16-17 Institute for Hydrospheric-Atmospheric Sciences (IHAS), Nagoya Univ.(Nagoya)

- Lectures on multi-scale cloud distributions in monsoon regions of Asia (Asst. Prof. K. Kato)
- Lectures on cloud physics and chemistry in Climate studies (Prof. H. Tanaka)
- Lectures on Asian cryosphere and changes in water Resources (Prof. Y. Ageta)
- Lectures on water cycle and stableisotopes (Assoc. Prof. M. Nakawo)

Aug. 18-20 Chubu Regional Construction Bureau, Min. of Construction (Chubu Region)

- Technical tour of hydrological facilities for river control

Aug. 21-22 (Sat-Sun): holidays

Aug. 23 Water Resources Res. Center,Disaster Prevention Res. Inst., Kyoto Univ.

- Lecture on control of run-off water

Aug. 24 Kiryu Experimental Catchment, Faculty of Agriculture, Kyoto Univ.

- Meteorological and hydrological observations at a small

Aug. 25 (Kyoto to Tsukuba)

Aug. 26 Forestry & Forest Products Res. Inst., Min. of Agriculture, Forestry & Fisheries (Hitachi-Ohta)

- Training on evaporation and soil moisture measurements, and hydrological observation

Aug. 27 Public Works Res. Inst., Min. of Construction (Tsukuba)

- Lectures on hydrological observations and models of water discharge

Aug. 28-29 (Sat-Sun): holidays

Aug. 30 Public Works Res. Inst., Min. of Construction (Tsukuba)

- Lectures on hydrological observations and models of water discharge

Aug. 31 National Inst. for Environmental Studies, Environment Agency (Tsukuba)

- Technical tour of research facilities for water quality conservation

Sep. 1 Meteorological Satellite Center, Japan Meteorological Agency (Kiyose)

- Technical tour of Meteorological Satellite Center

Sep. 2 Forecast Dept. &observation Dept., Japan Meteorological Agency (Tokyo)

- Lecture and technical tour concerning short-range precipitation forecasting using radar and the AMeDAS

4. The Fourth IHP Training Course, 1994

4.1 Participants

Mr. Sunil Adhikary (Nepal), Student of the Special Program of Sciences of Atmosphere and Hydrosphere, Graduate School of Science, Nagoya Univ., Japan
Mr. Zhang Wan Chang (China), ibid.
Mr. Mohammad Rezwanul Islam (Bangladesh), ibid.
Mr. BirbalRana (Nepal), Student of Stiences of Atmosphere and Hydrosphere,Graduate School of Science,Nagoya Univ., Japan
Ms. Y. K. Handapangoda (SriLanka), Teaching Asst.. in Civil Engineering, Univ. of Peradenlya, Peradenlya
Ms. Byambaagiin Oyunchimeg (Mongolia), Min. of Nature and Environment, Inst. of Water Problems,Ulaan Baatar
Mr. M. Fakhruddin (Indonesia), Puslitbang Limnology,LIPI,Bogor
Ms. Gadis Sri Haryani Bengen (Indonesia), Res. and Development Center for Limnology,Indonesian Inst. of Sciences, Bogor

4.2 Schedule and Lectures

Aug. 15-16 IHAS, Nagoya Univ. (Nagoya)
- Lecture on Asian monsoon and water cycle (Asst. Prf. K. Kato)
- Lecture on carbon cycling with water cycle (Prof. N. Handa)
- Lecture on aquatic micro-organisms and water quality (Assoc. Prof. H. Terai)

Aug. 17-19 Kanto Regional Construction Bureau,Min.of Construction (Nagoya to Tokyo,Kanto Region)
- Technical tour of hydrological facilities for river control

Aug. 20-21 (Sat-Sun) : holidays

Aug. 22-23 Environmental Res. Center, Univ. of Tsukuba (Tsukuba)
- Observation and data analysis of evapotranspiration

Aug. 24-25 National Res. Inst. of Agricultural Engineering, Min. of Agriculture, Forestry & Fisheries (Tsukuba)
- Analysis of irrigation and drainage
- Study of experimental facilities for ground water

Aug. 26 National Inst. for Environmental Studies, Environment Agency (Tsukuba)

- Technical tour of Res. facilities for water quality conservation

Aug. 27-28 (Sat-Sun): holidays

Aug. 29-30 National Res. Inst. for Earth Science &Disaster Prevention, Science & Technology Agency(Tsukuba-Chiba Pref.)

- Large scale rainfall experiment
- Technical tour of an experimental hydrological catchment

Aug. 31 Forecast Dept. &observation Dept., Japan Meteorological Agency (Tokyo)

- Lecture and technical tour concerning short-range Precipitation forecasting using radar and the AMeDAS

Sep. 1 Meteorological Satellite Center, Japan Meteorological Agency (Kiyose)

- Technical tour of Meteorological Satellite Center

5. The Fifth IHP Training Course,1995

5.1 Participants

Ms. Meng Xiao(China), Student of the Special Program of Sciences of Atmosphere and Hydrosphere, Graduate School of Sciences, Nagoya Univ., Japan
Mr. Talukder Abul Bashar MD. Alauddin(Bangladesh), ibid.
Mr. Liu Jing Shi(China), ibid.
Mr. Begkhutod Perapol(Thailand), ibid.
Mr. Bhatt Maya Prakash(Nepal), ibid.
Mr. Ma Xieyao(China), Student of Sciences of Atmosphere and Hydrosphere,Graduate School of Science,Nagoya Univ., Japan

5.2 Schedule and Lectures

<Part 1 : Chubu Region>

Dec. 13-15 Chubu Regional Construction Bureau, Min. of Construction (Aichi and Gifu)

- Technical tour of hydrological facilities for river control

<Part 2 : Kinki Region>

Feb. 13 Lake Biwa Res. Inst., Shiga Pref. (Otsu)

- Lecture and technical tour for Lake Biwa

Feb. 14 Branch Office of Kinki District of Public Works, Min. of Construction (Otsu)

- Lecture and technical tour for mountain conservation

Dept. of Forestry, Kyoto Univ. (Otsu)

- Lecture and technical tour of an experimental basin

Feb. 15 Disaster Prevention Res. Inst., Kyoto Univ. (Uji)

- Lecture and technical tour on disaster prevention

Hirakata Operation Center, Min. of Construction(Hirakata)

- Lecture on river water control

Feb. 16 Section of River Management, Kyoto Pref. (Kyoto)

- Technical tour concerning river management

<Part3 : Kanto Region>

Mar. 11 Inst. for Forestry and Forest Products, Min. of Agriculture, Forestry and Fisheries (Hitachi-Ohta)

- Training on evaporation and soil moisture measurement, and on making hydrological observation

Mar. 12 National Inst. for Environmental Studies, Environment Agency (Tsukuba)

- Technical tour of research facilities for water quality conservation

Mar.13 Public Works Res. Inst., Min. of Construction (Tsukuba)

- Lecture on hydrological observation and models of water discharge

Mar.14 Forecast Dept. & observation Dept., Japan Meteorological Agency(Tokyo)

- Lecture and technical tour concerning Short-range Precipitation forecasting using radar and the AMeDAS

Mar. 15 Meteorological Satellite Center, Japan Meteorological Agency (Kiyose)

- Technical tour of Meteorological Satellite Center

6. The Sixth IHP Training Course

6.1 Participants

Mr. Zulkefle bin Ghazali(Malaysia), Hydrology Division, Dept. of Irrigation and Drainage

Mr. Rhoel C. Villa(Philippines), National Hydraulic Res. Center, U. P. College of Englneerlng

Mr. Luong Tuan Anh(Vietnam), Inst. of Meteorology and Hydrology, Hanoi Hydrometeorological Service of Vietnam

Mr. Atthaporn Buddhapolit(Thailand), Hydrology Division, Royal Irrigation Dept.

Ms. Rungkarn Krishnamra(Thailand), Soil and Water Conservation Division, Land Development Dept.

6.2 Schedule and Lectures

Aug. 19-20 IHAS, Nagoya Univ. (Nagoya)

- Lecture on hydrological characteristics of tropical forests (Prof. K. Kuraji, Univ. of Tokyo)
- Lecture on remote sensing from space (Prof. K. Nakamura, IHAS, Nagoya Univ.)
- Lecture on development of distributed rainfall-runoff model by using digital elevation models (Prof. Y. Tachikawa, Kyoto Univ.)
- Lecture on the new thrust of IHP activities in Southeast Asia and Pacific, Asian/Pacific FRIEND (Flow Regimes from International Experimental and Network Data)(Prof. K. Takeuchi, Yamanashi Univ.)

Aug. 21-23 Kanto Regional Construction Bureau, Min. of Construction (Kanto Region)

- Technical tour of hydrological facilities for river control

Aug. 24-25 (Sat-Sun): holidays

Aug. 26-27 Environmental Res. Center, Tsukuba Univ. (Tsukuba)

- Lecture and practice session on evapotranspiration measurements
- Lecture on the role of the biosphere for climate systems

Aug. 28-29 National Res. Inst. of Agricultural Engineering, Min. of Agriculture, Forestry & Fisheries (Tsukuba)

- Analysis of irrigation and drainage
- Technical tour to an irrigated paddy field

Aug. 30 Public Works Res. Inst., Min. of Construction (Tsukuba)

- Technical tour of research facilities for water quality conservation

Aug. 31-Sep. 1(Sat-Sun): holidays

Sep. 2-3 National Res. Inst. for Earth Science &Disaster Prevention Environment Agency (Chiba Pref.)

- Large-scale rainfall experiment
- Technical tour to the hydrological catchment basin

Sep. 4 Forecast Dept. & Observation Dept., Japan Meteorological Agency (Tokyo)

- Lecture and technical tour concerning short-range Precipitation forecasting using radar and the AMeDAS

Sep. 5 Meteorological Satellite Center, Japan Meteorological Agency (Kiyose)

- Technical tour of Meteorological Satellite Center

7. The Seventh IHP Training Course on "Snow Hydrology", 1998

The general aim of the IHP short course is to help participants develop their basic knowledge of hydrological systems and of their sensitivity to climate changes as well as to contribute to solving current global environmental problems. The cryosphere is most vulnerable to the projected global warming trend that has recently become a major concern in many countries. The seventh training course focuses on snow hydrology.

The topics covered range from basic knowledge of the role of the cryosphere in the global environment to technical applications, including observations and measurements in snow packs.

7.1 participants

Mr. D. B. Ch ettri(Bhutan), Executive Engineer, Meteorology Unit, Div. Power, Min. of Trade and Industry
Mr. Liang, Zhongmin(China), Teacher, Dept. Hydrology, Hohai Univ.
Mr. Om Ratna Bajracharya(Nepal), Senior Hydrologist, Dept. Hydrology and Meteorology, Min. of Science and Technology
Mr. Shiva Bhakta Prajapati(Nepal), Hydrologist, Dept. Hydrology and Meteorology, Min. of Science and Technology
Mr. Aurangzeb Khattak(Pakistan), Asst. Director, WRRC
Mr. Edvin Aldrian(Indonesia), M2, IHP Student, IHAS, Nagoya Univ.
Mr. DangXuanPhong(Vietnam), M2, IHP Student, IHAS, Nagoya Univ., Japan
Mr. Li, Jianjun(China), M2, IHP Student, IHAS, Nagoya Univ., Japan
Mr. Yudi Iman Tauhid(Indonesia), M2, IHP Student, IHAS, Nagoya Univ., Japan
Mr. Bhuwan Chandra Bhatt(Nepal), Ml, IHP Student, IHAS, Nagoya Univ., Japan
Mr. Zhou Shiqiao(China), Ml, IHP Student, IHAS, Nagoya Univ., Japan
Mr. Kayastha Rijan Bhakta(Nepal), Res. Fellow, IHAS, Nagoya Univ., Japan
Mr. Suresh Chandra Pradhan(Nepal), Hydrological Asst., Dept. Hydrology and Meteorology, Min. of Science and Technology
Mr. Keshav Raj Sharma(Nepal), Hydrological Asst., Dept. Hydrology and Meteorology, Min. of Science and Technology
Mr. Chok Bahadur Gurung(Nepal), Hydrological Asst., Dept. Hydrology and Meteorology, Min. of Science and Technology
Dr. Dodi Wangdu, Head(Bhutan), Division of Geology and Mines
Ms. Diraagiin Erdenetsetseg(Mongolia), Expert, Centre for Climate and

Environmental Change, Inst. of Meteorology and Hydrology
Mr. Nozomu Naito(Japan), D3, Graduate Student, IHAS, Nagoya Univ.
Mr. Fumio Nakazawa(Japan), Ml, Graduate Student IHAS, Nagoya Univ.
Mr. Yosihiro Yoshioka(Japan), M2, Graduate Student, Nagaoka Univ. of Technology

7.2 Schedule and Lectures

Lecturers

Y. Ageta, IHAS, Nagoya Univ.
T. Aoki, Meteorological Res. Inst.
K. Goto-Azuma, Nagaoka Inst. of Snow and Ice Studies, National Res. Inst. for Earth Science and Disaster Prevention
N. Hayakawa, Dept. of Civil and Environmental Engineering, Nagaoka Univ. of Technology
H. Iida, Sediment Control Division, Dept. of Civil Engineering, Toyama Prefectural Government
I. Kamiishi, Centre of Snow and Ice Technology, ARGOS Co. Ltd.
S. Kobayashi, Res. Inst. for Hazards in Snowy Areas, Niigata Univ.
M. Lu, Dept. of Civil and Environmental Engineering, Nagaoka Univ. of Technology
H. Mizuno, Meteorological College
M. Nakawo, IHAS, Nagoya Univ.
H. Ohno, Japan International Res. Centre for Agricultural Sciences
K. Satow, Civil Engineering, Nagaoka National College of Technology
T. Takeda, IHAS, Nagoya Univ.
Y. Takeuchi, Nagaoka Inst. of Snow and Ice Studies, National Res. Inst. for Earth Sciences and Disaster Prevention
K. Yokoyama, Hokuriku National Agricultural Experiment Station

Schedule (9 March, 1998-22 March,1998)

Mar. 9 Arrival at Nagoya, Japan
Mar. 10 (IHAS, Nagoya Univ.)

- Guidance
- Lecture on glaciers and the water cycle
- Lecture on precipitation process
- Lecture on synoptic conditions and snowfall precipitation process
- Icebreaker reception in the evening

Mar. 11 (IHAS, Nagoya Univ.)

- Technical tour

	Move from Nagoya to Myoko (4 hour train ride)
Mar. 12	· Lecture on water circulation over the earth : the roles of snow and ice · Radiation processes and remote sensing of snow · Practice session for spectral albedo observations on a snow field
Mar. 13	· Lecture on snowmelt hydrology · Practice session for hydrographical observations · Fabrication of the Endo-type snow-water content meter(1)
Mar. 14	Lecture on metamorphism of deposited snow · Lecture on snow changes in snow pack and melt water chemistry during snowmelt · Lecture on heat budget of a snow pack
Mar. 15	Technical bus tour to Niigata Experiment Laboratory, Public Works Res. Inst., Tohkamachi Experiment Station, Forestry and Forest Products Res. Inst., Nagaoka Inst. of Snow and Ice Studies, National Res. Inst. for Earth Science and Disaster Prevention(Stay overnight at a spa, Yomogihira Hot Spring, in the snow region)
Mar. 16	Technical bus tour continues to Myoken Weir, Shinano River · Facilities for snow removal by melting in Nagaoka City · Shinano River Work office, Hokuriku Regional Construction Bureau · Oukouzu Division Work, Shinano River and the Division Work Museum · Arai Weir, Shinano River · Fabrication of the Endo-type snow-water content meter(2)
Mar. 17	Practice session for heat exchange over a snow surface
Mar. 18	Practice session for snow pit observations
Mar. 19	Data handling exercise(reception in the evening)
Mar. 20	Report preparation Move from Myoko to Nagoya(train ride)
Mar. 21	Closing ceremony
Mar. 22	Departure from Nagoya

8. The Eighth IHP Training Course on "Remote Sensing", 1999

Recently, the environmental problems attracts strong attentions. The spatial scales of the problems range from very local one to global one. Environmental problems have close connection to atmospheric and hydrospheric phenomena. For the atmospheric and hydrospheric sciences, satellite remote sensing is very useful and essential because of its capability to observe the atmosphere and hydrosphere in a big scale. For example, recently launched TRMM (TropicalRainfallMeasuringMission) is providing us a unique three-dimensional rain structures regardless of the location over tropical and a part of mid latitude regions. ADEOS (Advanced Earth Observing Satellite) gave us beautiful images of global phytoplankton distribution over global ocean.

Ground-based remote sensing Which includes radars and lidars is also useful for the atmospheric observation.

The lectures give the basic theory of remote sensing, technology and applications, and current Earth observation satellites, etc.

8.1 Participants

Mr. Limsakul Atsamon(Thailand), IHAS, Nagoya Univ., Japan

Ms. Jiang Cuiling(China), IHAS, Nagoya Univ., Japan
Mr. Aryal Deepak(Nepal), IHAS, Nagoya Univ., Japan
Ms. Aranya Fuangswasdi(Thailand), Ground Water Division, Dept. of Mineral Resources
Ms. Zainab Hashim(Malaysia), Hydrology Division, Dept. of Irrigation and Drainage
Mr. Wibowo Hendro(Indonesia), Puslitbang Limnologi-LIPI
Dr. Cheng Ming(China),Nanjing Inst. of Hydrology and Water Resources, Min. of Water Resources
Mr. Te Navuth(Cambodia), Min. of Water Resources and Meteorology
Ms. Yuko Ogawa(Japan), Global Information and Early Warning Service, Food and Agriculture Organization of the United Nations, Italy
Mr. Thongdum Pengyai(Thailand), Hydrometeorology Division, Meteorological Dept.
Mr. Chhetri B. Tek(Nepal), IHAS, Nagoya Univ., Japan
Mr. Haryoko Urip(Indonesia), Meteorological and Geophysical Agency
Ms. Li Zhuxiao(China), IHAS, Nagoya Univ., Japan

8.2 Schedule and Lectures

Lecturers and lecture titles

Y. Honda, Chiba Univ. : Global vegetation observation Ⅱ
T. Iguchi, Communications Res. Laboratory(CRL), Min. of Posts and Telecommunications : Active microwave measurement of rain and

clouds from space I
T. Itabe, Communications Res. Laboratory, Min. of Posts and Telecommunications : Lidar proving of the atmosphere
K. Kajiwara, Chiba Univ. : Global vegetation observationI
T. Koike, Nagaoka Univ. of Technology : soil wetness measurement from satellite micro wave remote sensing
T. Kozu, Communications Res. Laboratory, Min. of Posts and Telecommunications : Active microwave measurement of rain and Clouds from space II
K. Nakamura, IHAS, Nagoya Univ. : Observation of atmosphere by radar
T. Saino, IHAS, Nagoya Univ.: Ocean color observation by satellite
H. Shimoda, Tokai Univ.: Current remote sensing technology for global warming monitoring
D. Short, IHAS, Nagoya Univ.: The Tropical Rainfall Measuring Mission
K. Tsuboki, IHAS, Nagoya Univ.: Radar measurement of precipitation processes
S. Uratsuka, Communications Res. Laboratory, Min. of Post and Telecommunications: Synthetic aperture radar and its applications

Scbedule

Mar. 8	Arrival at Nagoya, Japan
Mar. 9	Guidance, lectures and reception at IHAS, Nagoya Univ.
Mar. 10	Lectures and technical tour in IHAS, Nagoya Univ.
Mar. 11	Lecture and guidance of data analysis training
Mar. 12	Data analysis training
Mar. 13	Data analysis training (continued)
Mar. 14	Move to CRL at Koganei, Tokyo
Mar. 15	Lectures
Mar. 16	Lectures and technical touratCRL
Mar. 17	Move to Tokai Univ. and lectures／move to Chiba Univ.
Mar. 18	Lectures
Mar. 19	Lectures and move to Nagoya
Mar. 20	Free day
Mar. 21	Departure from Nagoya

9. The Ninth IHP Training Course on "Limnology" 1999 summer

Limnology is a field of study on terrestrial water ecosystems such as lakes, rivers, reservoirs, ground waters and wetland. Human activities have been linked very closely to those water ecosystems and changed them directly or indirectly through global environmental changes. We have to learn basic limnological processes and how to manage and conserve those water ecosystems with sustainable development through the next century.

Limnological studies in Japan only began in 1899 and we are celebrating their centennial history. The following Programs have been prepared to welcome trainees of the IHP training course in limnology In the summer of 1999.

9.1 Participants

Mr. Abung Rachmann (Indonesia), Res. Inst. for Water Resources Development
Dr. Arveti Nagaraju (India), Dept. of Geology, Sri Venkateswara Univ.
Dr. Chen Yuaufang(China), College of Water Resources and Environment, Hohai Univ.
Ms. Daram S. Enkhtsetseg (Mongolia), Inst. of Meteorology and Hydrology
Mr. Hossain Md Anawar (Bangladesh), IHP student in IHAS, Nagoya Univ., Japan
Ms. Lythi M. Hai (Vietnam), Dept. of Water Resources and Environment, Inst. of Geography
Mr. Mohd. Talha Mohd. Zaharon (Malaysia), Environmental Health Section, Engineering Services Division, Min. of Health
Ms. Sirisampan Satiraporn (Thailand), IHP student in IHAS, Nagoya Univ.,Japan

9.2 Schedule and Lectures

Lecturers and lecture titles

H. Terai, IHAS, Nagoya Univ.: Material cycling in deep and shallow water ecosystems
K. Ichino, Faculty of International Communication, Aichi Univ.: Low-cost water treatment systems using constructed wetlands
T. Yoshioka, IHAS, Nagoya Univ. Current technology in limnology (1) Stable isotope ecology
T. Okino, Faculty of Sciences, Shinshu Univ.: A historical review of limnology in Japan and a case study on Lake Suwa
K. Kato, School of Allied Medical Sciences, Shinshu Univ.: Current technology in limnology (2) Microbial ecology
T. Hanazato, Suwa Hydrobiological Station, Shinshu Univ.: global environment and lake ecosystems
H. Fushiml, School of Environmental Sciences, The Univ. of Shiga Pref.: water resources and environmental problems of Lake Biwa
M. Sakamoto, School of Environmental Sciences, The Univ. of Shiga Pref.: Eutrophication and management of freshwater environments
M. Nakamura, Lake Biwa Res. Inst. Shiga Pref. Lake Biwa-Yodo River water systems: Evolving issues on integrated management of water

quality

M. Kumagai, Lake Biwa Res. Inst., Shiga Pref.: Ecological in homogeneity due to dynamic variability in Lake Biwa

T. Nakajima, Lake Biwa Museum, Shiga Pref.: Evolution and distribution of cyprinid fish in East Asia during Neogene, and formation of the cyprinid fauna in Lake Biwa

R. F. Walker, Lake Biwa Res. Inst., Shiga Pref.: Current technology in limnology (3) Algal species classification by image processing

N. Nakamoto, Faculty of Textile Science and Technology, Shinshu Univ.: Misunderstanding of slow sand filtration in Japan and the biological mechanism of its system

M. Overmars, UNESCO, Jakarta Office: Special Lecture Current IHP activities in Asia Pacinc Region

Schedule

Jul. 26	Arrival at Nagoya, Japan
Jul. 27	Guidance and lectures at IHAS (icebreaker reception in the evening)
Jul. 28	Move to Suwa Hydrobiological Laboratory, guidance and lecture
Jul. 29	Field trip on Lake Suwa, observation and sampling
Jul. 30	Chemical and biological analysis of water and sediment samples
Jul. 31	Field trip to Lake Shirakoma, observation and sampling (reception in the evening)
Aug. 1	Technical bus tour to Kurobe Reservoir and Nishina sub alpine lakes
Aug. 2	Lake Kizaki Laboratory, travel to Hikone by train
Aug. 3	Lecture at the Univ. of Shiga Pref., Visit Limnological Laboratory, move to Otsu
Aug. 4	Lecture and technical tour at Lake Biwa Res. Inst.
Aug. 5	Field trip to Lake Biwa on there search vessel "Hakken"
Aug. 6	Technical tour to Lake Biwa Museum, back to Nagoya
Aug. 7	Closing Ceremony and reception
Aug. 8	Departure from Nagoya

10. The Tenth IHP Training Course on “Hydrlogy related to Head Water Management” 2000 summer

“Head Water Area” is understood as both supplying a source of clean water and assisting in the prevention of flood/sediment disasters for living people downstream. Over-cutting of trees or industrial pollution sometimes damages to the surrounding environment of "Head Water". Japan has experiences such failures 100 years ago. In this training course, we would like to focus on hydrological impacts of non-vegetation, and on the effects of both reforestation in steep slope and erosion control works in river-bed. The watersheds, we focus on, are damaged in the past with sulphurous acid gas caused by the refining factory of copper. Lectures are provided as the Faculty of Technology, Gunma University, Kiryu-city, Gunma Prefecture, and field training is to be done in the basin of the Watarase River, a tributary of the Tone River which is very important for Tokyo Metropolitan.

10.1 Participants

Mr. Evandri Ahmad (Indonesia):R & D Center for Informatic and Computer Science
Mr. Yuebo Xi (P. R. China): Hohai Univ.
Mr. Suy Sovann (Cambodia): Min. of Water Resources and Meteorology
Mr. Monoloth Soukhanouvong (Laos PDR): Dept. of Meteorology and Hydrology(DMH) Min. of Agriculture and Forestry(MAF)
Ms. Stephanie Bowis (New Zealand): West Coast Regional Council
Ms. Ubolwan Jenphanitsub (Thiland): Office of the National Water Resources Committee
Mr. Nguyen Kim Tuyen (Vietnam): Hydrometeorological Service of Vietnam
Mr. Birendra Raj Adhikari (Nepal): M1, IHP Student, IHAS Nagoya Univ.
Mr. Karma(Bhutan): M1, IHP Student, IHAS Nagoya Univ.

10.2 Schedule and Lectures

Lecturers and lecture titles

T. Ohta, Graduate School of life and Agriculture, Univ. of Tokyo, : Typology of erosion processes and watershed management, Effect of human activities on head water
S. Kobatake, Gunma Univ.,: History of mountain devastation in the Watarase River, Runoff analysis of head water
Y. Fukushima, Nagoya Univ.,: Hydrological processes in headwater
Y. Kawano, Min. of Agriculture, Forest conservation project in headwater areas
Y. Nakamura, Min. of Construction, : Sediment disaster preventive works in Japan
K. Honda, Asian Inst. of Technology, Thailand, : Evaluation of Erosion Control Work using Remote Sensing and GIS
T. Tsujimoto, Nagoya Univ.,: Sediment Transport and River Management
H. Tanji, Min. of Agriculture, Irrigation system and watershed management
H. Kawashima, Graduate School of life and Agriculture, Univ. of Tokyo, : River basin management and water quarity

G. Takahashi, Toyama Prefectural Univ. of Agriculture, Watershed management and conservation of ecosystem

Schedule

Jul. 24	Arrival at Narita Airport and move to Kiryu-city by limousine
Jul. 25	Guidance and lecture at the campus of Gunma Univ.
Jul. 26	Lecture
Jul. 27	Lecture
Jul. 28	Technical tour to Ashio
Jul. 29	Technical tour to Mt. Nsntai
Jul. 30	Inspect sights of Nikko
Jul. 31	Lecture and Practice
Aug. 1	Lecture and Practice
Aug. 2	Technical tour to the integrated Dam Control Office
Aug. 3	Lecture
Aug. 4	Technical tour to the Watarase Retarding Basin and Tone-Oozeki Barrage
Aug. 5	Move to Tokyo
Aug. 6	Departure from Narita

11. The Eleventh IHP Training Course on "Hydrogen and Oxygen Isotopes in Hydrology" 2001 summer

Stable isotopes of hydrogen and oxygen, and tritium of hydrological waters, have been used to trace water circulation in various scale in time and space. They have been revealed to be good parameters for understanding the hydrological systems and solving the hydrological problems. Fundamentals for sampling, determination, data analysis, and transport models of water isotopes will be briefly lectured about seawater, water vapor, precipitation water, snow, ice, surface water, soil water, ground water, and volcanic and hydrothermal water. Participants can get comprehensive idea of the application of hydrogen and oxygen isotopes in hydrology by practice to collect various kings of hydrological samples, determine their isotope ratios, and analyze their data by themselves.

11.1 Participants

Dr. Chague-Goff, Catherine (New Zealand): National Inst. of Water & Atmospheric Research (NIWA)

Mr. Deris, Mohammad (Malaysia): Hydrology and Water Resources Division, Dept. of Irrigation and Drainage Malaysia
Ms. Kemanuntagosorn, Naowarat (Thailand): Applied Hydrology Section Water Resources Management Dept. Hydro Power Survey and Land Division
Ms. Ngo, Van Anh Thi (Vietnam): Water and Air Environmental Research Center, Inst. of Meteorology and Hydrology
Ms. Po, Salina (Cambodia): Water Quality Analysis in Department of Hydrology and Riverworks of Min. of Water Resources and Meteorology
Mr. Putuhena, William Marcus (Indonesia): Research Institute for Water Resources, Min. of Settlement and Regional Infrastructure
Mr. Hankin, Stuart Ian (Australia): Australian Nuclear Science and Technology Organisation
Dr. Hughes, Catherine Imily (Australia): Australian Nuclear Science and Technology Organisation
Mr. Rafu, Aryal (Nepal): Graduate student of IHP special course at Nagoya Univ.
Mr. Zhu, Xuesong (China): Graduate student of IHP special course at Nagoya Univ.
Mr. Hashimoto, Shigemasa(Japan): Graduate student of Science, Nagoya Univ.
Mr. Uemura, Ryu(Japan): Graduate student of Environmental Science and Technology, Tokyo Inst. of Technology

11.2 Schedule and Lectures

Lecturers and lecture titles

N. Yoshida, Tokyo Inst. of Technology: Fundamentals of hydrologen and oxygen isotopes in hydrology
O. Matsubara, Akita Uinv. : General feature on the hydrologen and oxygen isotopes rations of natural water
A. Numaguti, Hokakido Univ.: Large-scale transport of water vapor and isotope variability
A. Sugiamoto, Kyoto Univ.: Water circulation in regional scale
M. Nakawo, Nagoya Univ.: Isotopes in snow and ice
H.Satake, Toyama Univ.: Tritium in precipitation and surface waters
M. Tsujimura, Tsukuba Univ.: Stable isotopic composition in soil water
M. Yasuhara, Geological Survey of Japan.: Environmental isotopes in groundwaters
J.Shimada, Kumamoto Univ.: Use of Environmental isotope tracers to reveal groundwater flow system
H. Wushiki, Japan International Cooperation Agency.: Water in arid lands
M. Kusakabe, Okayama Univ.: Volcanic and hydrothermal waters

Schedule

Sep. 9	Arrival at Nagoya
Sep. 10	Guidance and lectures at Nagoya Univ. (icebreaker reception in the evening)
Sep. 11	Lecture and laboratory tour at IHAS, Nagoya Univ.
Sep. 12	Move to Volcanic Fluid Research Center, Tokyo Institute of Technology at Kusatsu-Shirane
Sep. 13	Lecture and Practical, Sampling of Hydrothermal water etc. and laboratory tour at the center
Sep. 14	Move to Tokyo
Sep. 15	Lectures at National Olympic Memorial Youth Center
Sep. 16	Lectures and practice
Sep. 17	Move to Chiba Experimental Forest, University of Tokyo, Lecture and practice, sampling of stream water etc.
Sep. 18	Move to Tokyo, lecture and practice
Sep. 19	Lecture and practice, Measurement of samples at Yokohama Campus of Tokyo Institute of Technology
Sep. 20	Lecture and practice, Simulation training, and Discussion
Sep. 21	Closing ceremony, Free time
Sep. 22	Departure from Narita Air Port